Effects of ultra-oxidized graphene oxide on the hydration of cement

Taimur Mazhar Sheikh

A thesis presented for the degree of
Doctor of Philosophy

Department of Civil Engineering
Faculty of Science and Engineering
University of Nottingham Malaysia
December 17, 2021

Acknowledgments

I would like to thank my parents for their unflinching support in allowing me to pursue my doctorate studies. I would not have been able to perform any research without their ceaseless encouragement. I would also like to thank my wife for bearing with my indifferent companionship as an unfortunate consequence of my focus on research, and to continue providing more than her share of support during these times.

I would not have pursued my Ph.D if my supervisor Professor Jayaprakash Jaganathan had not seen this potential in me, and initiated me on my academic journey. Despite logistical issues, over the years he has continued to find pathways for my academic development and spurred me to overstep interdisciplinary fields and think outside the box to truly research something niche, and as such I am indebted to him. Associate Professor Kasturi Muthoosamy, my co-supervisor, has also shown tremendous patience and resolve in understanding a field she is not familiar with, and conversely helping me understand a field I knew nothing of. She has significantly streamlined my research and experimentation process with her expertise and resourcefulness, and I am very grateful to be taught by her. I would also like to extend my gratitude to Associate Professor Mohammed Parvez Anwar, who stepped up as my primary supervisor after Professor Jayaprakash could not supervise me in person. Despite the steep barrier of our different research fields, Dr. Anwar has always been in immediate contact, and has facilitated every request I have asked for with utmost quickness. Professor Andy Chan and Assistant Professor Abdullahi Ali Mo-

hamed also provided essential academic support to me as my co-supervisors.

I would also like to thank Mr. Adzarudin, Mr. Elias and Mr. Fatani, the lab technicians at Civil and Mixing lab who bore with me during the confusing lockdowns to keep the lab open, and to source materials for me in these troubling times. I am thankful to: Mr. Fareez, Ms. Fatihah from the Analytical lab and Ms. Khairini from the SEM lab for their crucial help in capturing and processing my research experiments. Finally, M.Eng students Elvira Ryanto, Khoo Seng Him, and Woo Chee Zheng showed great support by conducting GO-concrete related research for their Full Year Projects, and their results helped clear many variables I would not have time to conduct on my own.

Effects of ultra-oxidized graphene oxide on the hydration of cement

Taimur Mazhar Sheikh

Primary supervisor: Mohammed Parvez Anwar

Co-supervisors: Jayaprakash Jaganathan, Kasturi Muthoosamy, Andy Chan, Abdullahi Ali Mohamed

Abstract

While the use of concrete is widespread in the construction industry, cement's poor flexural capacity and tendency to form cracks limit the potential strength development of concrete structures. Of late, concrete nanoreinforcement has gained attention, as it mitigates crack formation at the nanoscale, allowing for construction of more durable and stronger structures. Graphene oxide (GO) is a highly promising nanoreinforcement candidate due to its ease of dispersion in water, and subsequently the concrete mix. However, recent research has suggested that GO cement reinforcement is not only physical but chemical, as the hydrophilic GO provides water seeding points for cement hydration, leading to a denser microstructure which increases the flexural capacity of concrete. This research investigates the chemical interactions of GO and water, with the premise that if GO is synthesized with varying functional groups, its ability to seed water to cement will be altered. If the GO reinforcement to cement is chemical, then the physical properties of concrete with the different GO functional groups will be significantly altered. As such, four variants of GO were synthesized with varying chemical properties, but similar physical prop-

erties such as sheet sizes and thicknesses. The chemical difference between all GOs were confirmed via analytical characterization tests. Incorporation of these GOs in cement, mortar, and concrete confirmed significant impacts on strength, workability, and durability. Ultra-oxidized GOs, i.e. GOs with high presence of hydroxyl and epoxide groups showed >50% concrete mix workability, 30% increase in 28-day compressive strength, > 50% increase in 28-day flexural strength and a 42% reduction in 24 hour pore size development with respect to control concrete. Furthermore, different superplasticizer treatments to ultra-oxidized GO concretes showed consistently improved performance as well. Conversely, low hydroxyl GOs showed inconsistent results, with reduced workability and lower 28-day compressive strength of concrete with respect to control. The results confirm that GO nanoreinforcement is primarily a chemical interaction with concrete, incumbent on the presence of hydroxyl groups on the GO sheets. This research presents high potential for future implementation with physical reinforcement such as fibers or rebars. However, greater research must be undertaken to ensure GO nanoreinforcement does not impact or is not impacted by chemical admixtures in concrete.

Contents

List of Figures

List of Tables

Nomenclature

AFM atomic force microscopy

AFt ettringite

B-GO Brodie's graphene oxide

BET Brunaur-Emmett-Teller porosity test

bwoc by weight of cement

cGO carboxyl dominant graphene oxide

CH calcium hydroxide (lime)

CHM cement hybrid material

CNF carbon nano fibers

CNT carbon nanotubes

CONT control sample

CSH/C-S-H calium silicate hydrate

CT computerized tomography

CVD chemical vapour deposition

DSM dynamic structural model

DTG differential thermogravimetry

fCNT functionalized carbon nanotubes

FTIR fourier transform infrared spectroscopy

GC graphene oxide based cement/concrete composite

GC+p graphene oxide based cement/concrete composite with superplasticizer

GCp pretreated graphene oxide-superplasticizer based cement/concrete composite

GO graphene oxide

H-GO Hummer's graphene oxide

HGC Ultra-oxidized hydroxyl-rich graphene oxide based cement/concrete

HGC+p Ultra-oxidized water-based graphene oxide based cement/concrete with superplasticizer

HGCp Ultra-oxidized water-based pretreated graphene oxide-superplasticizer based cement/concrete

HGO Ultra-oxidized water-based graphene oxide

hGO hydroxyl/oxyl dominant graphene oxide

ITZ interfacial transition zone

LGC Ultra-oxidized novel graphene oxide based cement/concrete

LGC+p Ultra-oxidized novel graphene oxide based cement/concrete with superplasticizer

LGCp Ultra-oxidized novel graphene oxide-superplasticizer cement/concrete composites

LGO Ultra-oxidized novel graphene oxide

MC methylcellulose

MIP mercury intrusion porosimetry

MLG multi-layer graphene

MWCNT multi-walled carbon nanotubes

OGC Ordinary graphene oxide based cement/concrete

OGC+p Ordinary graphene oxide based cement/concrete with superplasticizer

OGCp Ordinary pretreated graphene oxide-superplasticizer based cement/concrete

oGO ordinary graphene oxide

PC polycarboxylate

PEO polyethylene oxide

PPO polypropylene oxide

RCPT rapid chlorine penetration test

rGO reduced graphene oxide

SEM scanning electron microscope

SWCNT single-walled carbon nanotubes

TEM transmission electron micrscopy

TGA thermo-gravimetric analysis

UV-VIS ultra-violet/ visual spectroscopy

wrt with respect to

XGC Thermally reduced defective graphene oxide based cement/concrete

XGC+p Thermally reduced defective graphene oxide based cement/concrete with superplasticizer

XGCp Thermally reduced defective pretreated graphene oxide-superplasticizer based cement/concrete

XGO Thermally reduced defective graphene oxide

XPS X-ray photoelectron spectroscopy

XRD X-ray diffraction

Chapter 1: Introduction

Concrete is a mixture comprising of aggregates, cement and water . Upon contact with water, cement powder reacts to form a cementitious matrix that holds the fine and coarse aggregates together, allowing an efficient transfer of compressive loading to the stronger aggregates throughout the whole mix (Neville 2019, Li 2011). This makes concrete a durable and economical building material. However, cementitious bonding suffers from poor tensile and flexural capacity, leading to immediate failure via cracking hence requiring steel reinforcement (rebars), or, at the micrometer level, fiber reinforcement and/or high mix packing density (Neville 2019, Li 2011). This increases the building and serviceability cost of concrete, but has been always considered a necessary burden to bear in the construction industry (Neville 2019, Li 2011). The underlying cause of these flaws is the hydration reaction of cement itself: calcium hydroxide (CH), ettringite crystals (AFt), and calcium silicate hydrate (C-S-H) are the main products of Ordinary Portland Cement hydration, and while C-S-H provides the bonding nature of the cement matrix, AFt and CH are relatively larger sized crystals and do not contribute to any bonding development, introducing a weak interfacial transition zone (ITZ) between the aggregates and host matrix (Ollivier et al. 1995), as seen in Figure 1.0.1.

ITZ contributes to crack propagation and provides pathways for water to seep out (creep/shrinkage), and/or chlorides and corrosive chemicals to seep in (Neville 2019). While micro reinforcement certainly improves the strength and durability of concrete, it is a mitigative measure rather than a preventa-

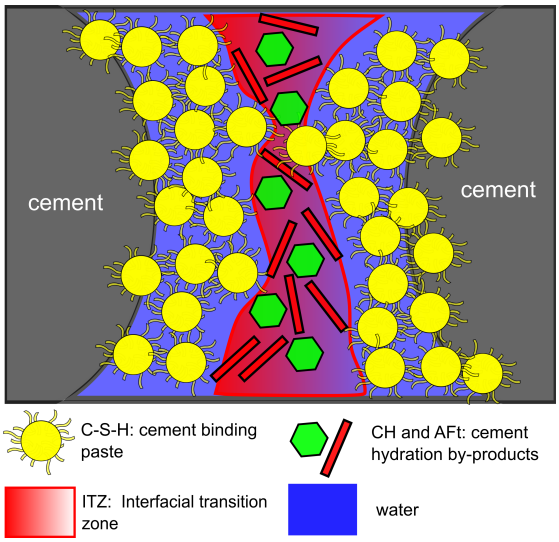

Figure 1.0.1: Visual schematic of the Interfacial Transition Zone (ITZ).

tive one, while also making concrete production more costly and complicated. Conversely, nanoreinforcement prevents crack growth by bridging and deflecting any weak zones at the earliest possible onset (Chuah et al. 2014). Figure 1.0.2 shows the size distributions of common admixtures and ingredients in concrete compositions; it should be noted that C-S-H gel is not listed in the aforementioned figure, however it's mean particle diameter size is found to be approximately 3.5 nm (Skinner et al. 2010).

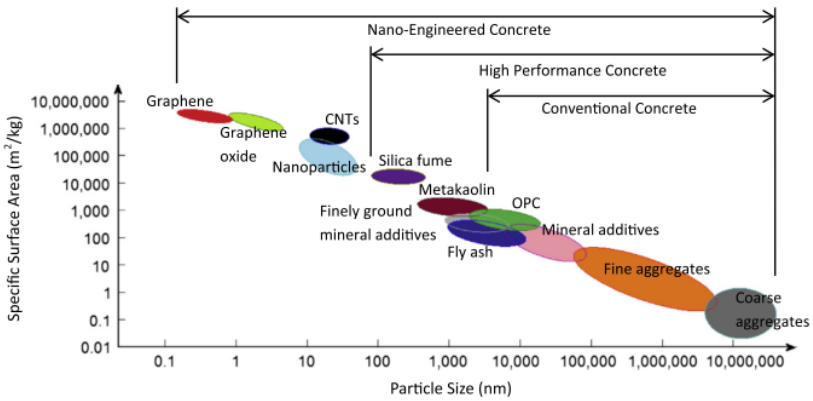

Figure 1.0.2: Size distributions of concrete's ingredients and admixtures. Abridged image by Chuah et al. (2014). Original image by Sanchez & Sobolev (2010).

1.1 Research Background

Despite the extensive use of concrete in industry, its poor flexural strength, low chloride resistance, cracking due to creep/shrinkage, and not to mention the high amounts of unreacted cement during hydration all contribute to a very inefficient, limited structural use. Subsequently, steel/fiber reinforcement and maintenance duties of concrete structures are required throughout their lifetime. Recently, reinforcing concrete with nanomaterials such as graphene, graphene oxide (GO) and carbon nanotubes (CNT) have shown highly promising results: significantly improving flexural strength of concrete by 200%, as well as durability enhancements by reducing chloride penetration in cement matrix up to 100%. These improvements occur with only minute additions of 0.02%-0.50% nanomaterials by weigh of cement, leading to higher tortuosity and greater structural interlock at the nanoscale. However, reasons for the improved performance of nano-reinforced concrete are still unclear. This research aims to explore the microstructural interactions of GO nanoreinforced concrete and develop a better understanding and application of this technology, leading to more cost-effective and sustainable concrete mix design.

1.2 Problem Statement

For GO concrete nanoreinforcement, the most significant hurdle is lack of knowledge of GO's specific interactions with the cement matrix in the mixture, hence it's research is pertinent for optimal contribution in concrete (Chuah et al. 2014). Determining the specific roles that each functional group of GO plays once initially dispersed is essential (Li, Li, Chen, Liu, Duan & Shah 2017). It is, fur-

thermore, important to ensure re-agglomeration does not take place as the GO solutions are being inserted into the cement matrix (Zhao et al. 2017). Finally, even small dosages of any GO can cause significant reduction in the flow of concrete (Li, Liu, Li, Li, Sanjayan, Duan & Li 2017). These issues have currently been mitigated by proper functionalization and ultrasonication of GO to ensure initial dispersion, followed by addition of certain plasticizers to improve workability, allowing the nanoparticles to stay dispersed in aqueous solutions for longer time periods (Zhao et al. 2016). However, it is still not known how the plasticizers and GO are specifically interacting with cement and its hydration products in the host matrix, and as such the strength and durability improvements of GO cannot be satisfactorily predicted. Additionally, the effects of GO have not yet been thoroughly investigated on concrete (as opposed to cement and mortar mixes), and it is essential to see if the improvements are being translated significantly despite the addition of coarse aggregates.

1.3 Aims and Objective(s) of the Research

The overall aim of this research is to understand how GO is chemically interacting with cement, and if the GO can be synthesized in a manner that allows for the best cement microstructural development, accounting for necessary admixtures such as plasticizers.

1. Determine whether the polycarboxylate superplasticizer interacts with GO in the concrete mix, and how this interaction impacts cement and concrete mix workability and strength development, with respect to GO with varying functional group ratios.

2. Custom tune the ratios of specific functional groups on GO nanoparticles, and observe subsequent change in their chemical interactions in water.

3. Incorporate GO with different functional groups in cement and concrete, to assess how functional groups of GO impact cement hydration, strength, and microstructural development.

4. Propose an underlying mechanism dictating the relationship between GO's functional groups and cement hydration development.

1.4 Research Hypotheses

This research is undertaken with the following hypotheses:

1. GO is hydrophilic and will interact with the sterically hindering plasticizers, hence GO with different functional group ratios will react differently with the same plasticizer.

2. Higher presence of specific functional groups will improve or reduce GO hydrophilicity.

3. Higher presence of specific functional groups on GO results in better performance of GO-cement composites with respect to strength, workability and durability.

4. The beneficial effects of GO incorporation to concrete are primary chemical, and the physical strength of GO is not necessarily translated to hydrated cement.

1.5 Research Questions

Based on the aforementioned research hypotheses, the research aims to answer the below queries:

1. How do the functional groups of GO affect its improvement to cement hydration and strength in the presence of plasticizers?
2. Do specific GO functional groups result in different interactions in water?
3. How is strength, durability and workability of the cement matrix affected, over time, by the respective oxidation and functional group tuning of GO?
4. Which functional groups of GO are responsible for its improvement, or lack of improvement, to cement hydration?

1.6 Scope of Research

As nanomaterial/cement chemistry research is in its stages of infancy, there are numerous hypotheses being researched globally, and as such there is no strong established foundation that may be used to predict results beforehand. Therefore, the aim of this research is to help construct the aforementioned foundation that can be used for future dissertations. Most investigations by far have presented different explanations for GO's behaviour in concrete, however all are hypothetical. Hence, this research takes a deep dive in the manufacturing of GO and verifying it's modifications accurately before proceeding to implement it in cement. As such, this research is not aimed at producing the strongest or most durable GO-cement composite, but rather identifying what could be

the chemical interactions in the GO-cement matrix that dictate how the cement develops. Once a reliable, consistent application of nanoreinforcement is achieved, only then can the framework be used to develop nanoreinforced concrete tailored to strength or durability attributes, or with other additives.

1.7 Significance and Potential Impact of Research

Results from this research can be used to spur the use of nanoreinforced concrete in niche structural design. As previous research has suggested, GO and other nanoreinforced cement mix fundamentally strengthens the C-S-H paste via pozzolanic effects, and the produced concrete is shown to be significantly stronger, resistant to salt diffusion, resistant to corrosive acids and resistant to creep and shrinkage effects. As a result, less concrete may be needed for the same strength requirements, which will also require less lifetime maintenance, and will be more resistant to seawater penetration, or toxic sewage erosion.

Highly oxidized GO is easier to bulk produce and store compared to it's more valued counterpart, graphene or reduced graphene oxide. However, if GO's functional groups are the primary donors to C-S-H's improved strength, then the physical integrity of GO sheets (which are a much more difficult and costly goal to address) are not high priority, streamlining nanomaterial application in cement. Additionally, only minute amounts of nanomaterials would be needed to initiate chemical improvement.

GO and other nanomaterials are proving to be viable for various industrial uses. The costs of obtaining graphene worldwide is reducing and more avenues for mass producing graphene are being explored. Demand of nano-

materials in the infrastructure industry will spur local production , allowing for more streamlined nanomaterial incorporation in cement and concrete. With nanoreinforcement, less concrete may be used to obtain the same design requirements, with fewer serviceability requirements and a reduced need for specialized admixtures. This results in a more cost effective, sustainable environment, due to less production of carbon dioxide as a consequence of reduced demand for OPC concrete.

1.8 Outline of Research

The following is an outline of each chapter in the thesis:

- Chapter 1 - Introduction: provides a brief introduction and background on cement and its shortcomings, and how nanoreinforcement may mitigate these aforementioned drawbacks. The problem statement, aims and objectives of this research are stated, as well as its scope and significance in the civil engineering industry.

- Chapter 2 - Literature Review: summarizes previous research performed on cement nanoreinforcement and why GO is an ideal reinforcement candidate. A primer is given on how GO is synthesized, and its relevant chemical properties that aid in cement incorporation. Furthermore, the chemistry of cement hydration is expounded to present a clearer picture for how GO can chemically interact with it.

- Chapter 3 - Methodology: the materials used for this research are detailed in this section. Sample preparation of both GO and cement for their respective analytical and/or strength and workability tests are explained.

A brief explanation for the analytical tests performed for this research is also presented.

- Chapter 4 - Results and Discussion: The results of GO and GO-cement analytical tests and GO-concrete strength/workability tests are submitted, and discussed in detail. A relationship between the strength analytical tests is established, and a new chemical interaction model is made explaining the particular development of the GO-cement microstructure.

- Chapter 5 - Conclusions: The research findings are summarized and used to address the previously set aims and objectives of the thesis. Concluding remarks are stated, and recommendations are provided for future research in this field.

Chapter 2: Literature Review

This chapter provides a detailed background and summary of nanoreinforcement in cement, specifically with carbon based nanomaterials such as graphene, CNT or GO. Previous progress and setbacks of cement carbon nanoreinforcement is discussed. and new perspective is provided about the chemical nature of GO and it's potential interactions with cement during the hydration process. An outline of this chapter is illustrated in Figure 2.0.1.

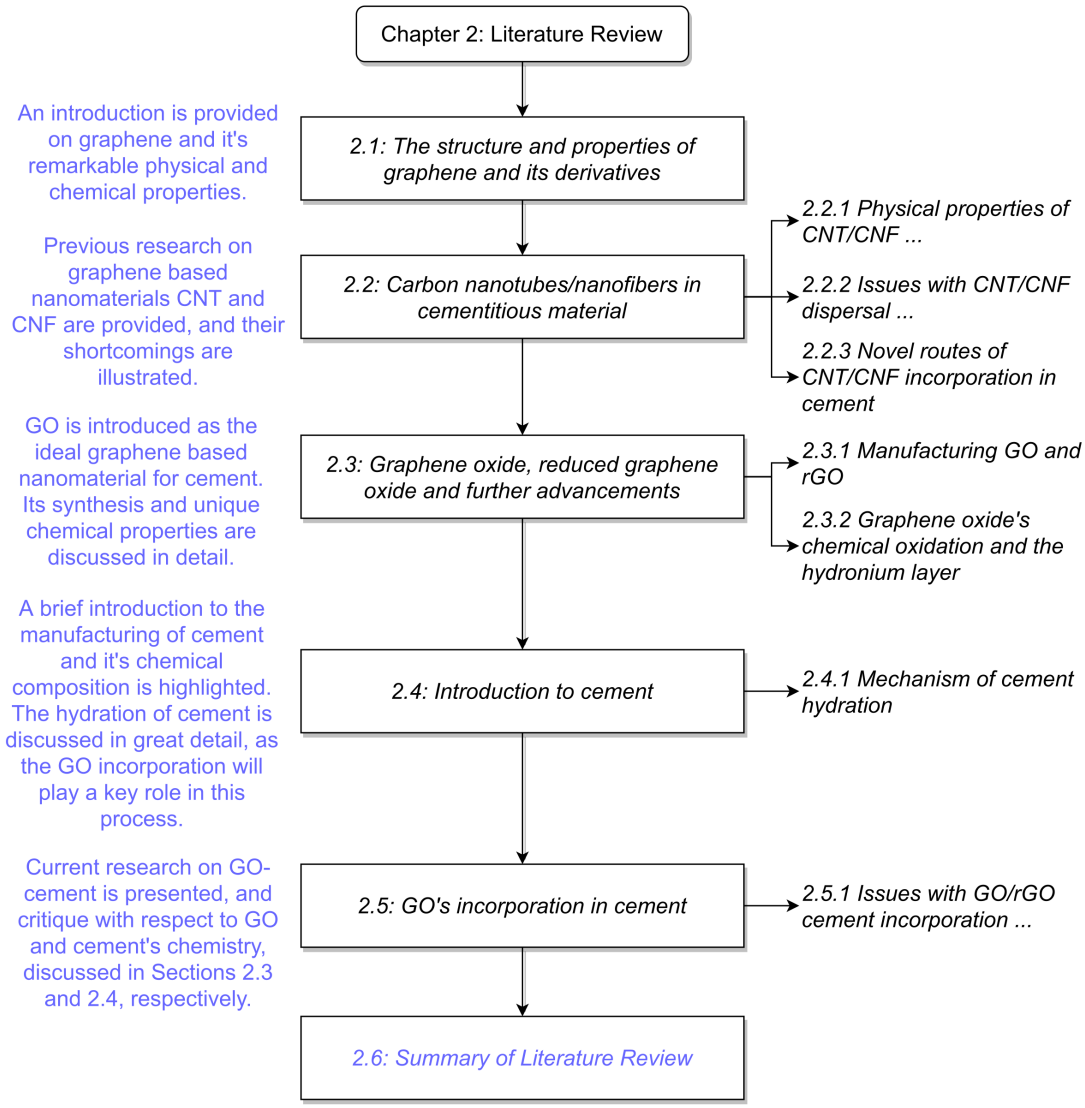

Figure 2.0.1: Flowchart outlining the section layout of Chapter 2: Literature Review

Recently, nanomaterials such as graphene, GO, nano-SiO_2 and CNT have seen an immense rise in their industrial engineering applications (Sharon & Sharon 2015*a*, Chuah et al. 2014). This literature review primarily focuses on graphene and GO as nanoreinforcement materials for concrete, due to extremely limited research on any other nanomaterial reinforcement (e.g. nano-SiO_2, TiO_2, chromium oxide, etc). However, some research on CNTs is also expounded, as their functionalization and interactions with cement are similar to GO, both being carbon based nanomaterials.

2.1 The structure and properties of graphene and its derivatives

Graphene is an allotrope of carbon, having a planar sheet structure comprising of one carbon atom being bonded to the three adjacent carbon atoms in a hexagonal honey-combed packing (Sharon et al. 2015). As such, the structure is mainly two dimensional, referred to as monolayer graphene. Several graphene sheets stacked on one another make multilayer graphene (MLG) or graphene nanoplatelets (GNP), and bulk stacking of graphene sheets form graphite. Sheets rolled into tubes (either single or multilayer) are termed carbon nanotubes (CNTs). Sheets wrapping into a spherical shape form Fullerene, as can be seen in Figure 2.1.1. The hexagonal building block has intra-planar carbon atom distance of 0.142 nm, while the interplanar distance between pure graphene sheets is 0.335 nm, visualized in Figure 2.1.2. The nanoscale thickness of the hexagonal sheet allows for possible physical interactions with C-S-H during hydration, which will be explained in Chapter 2.5 (Wang, Wang, Yao, Farhan,

Zheng & Du 2016, Peyvandi et al. 2013, Li, Lu, Chuah, Li, Liu, Duan & Li 2017, Sharma & Kothiyal 2015*b*). In its unique shape the carbon atoms are arranged in an sp^2 bonding configuration, with extremely strong σ-bonds holding the atoms together in a single planar sheet (Sharon et al. 2015). The remaining electron in the p orbital exists outside of the sheet plane, thus forming the weak, interplanar Van Der Waal π-bonds which attempt to hold the sheets of graphene together, albeit weakly, as shown in Figure 2.1.3. The σ-bonds contribute to the high strength of the graphene sheet, while the weak π-bonds give graphite/graphene the ability to have sheets slide over one another, e.g. in the use of graphite lead in pencils. The out of plane p orbitals and their resultant π-bonds allow the electrons to 'jump' between these clouds, forming conduction and valence bands, which result in the material's excellent electrical conductivity properties (Sharon et al. 2015), also visualized in Figure 2.1.3.

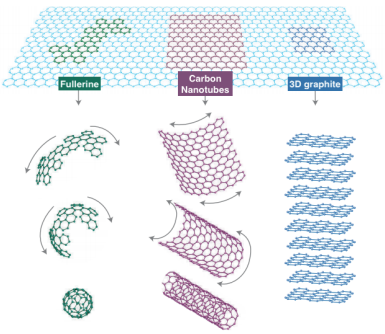

Figure 2.1.1: Graphene and its structural derivatives. (Sharon et al. 2015).

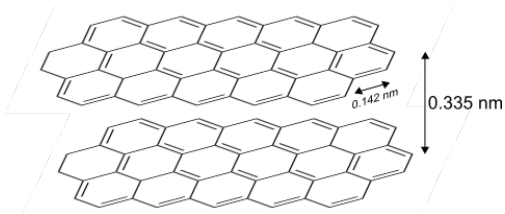

Figure 2.1.2: Dimensions and spacing of carbon atoms in graphene.

Graphene is estimated to have a Young's Modulus of 1 TPa and an intrinsic bulk strength exceeding 130 GPa (Lee et al. 2008), which is approximately 200x stronger than steel. As such, it is an ideal nanoreinforcement candidate for concrete structures (Chuah et al. 2014, Sharon et al. 2015). It also has unmatched

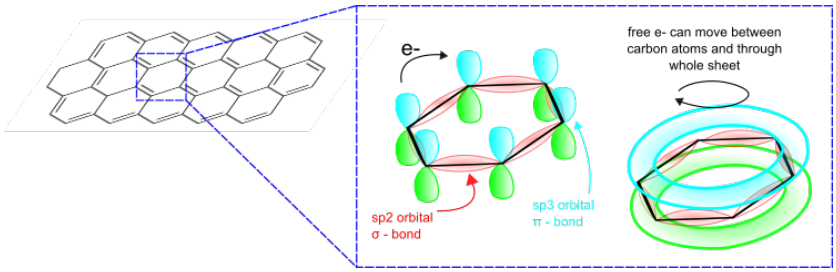

Figure 2.1.3: σ and π bond intervals, and electron hopping in graphene.

electrical and thermal conductivity (potentially enabling its use as a piezoresistive smart sensor) and is transparent, enabling optical use in photonic devices (Sharon et al. 2015). As their demand for use in industry increases, the manufacturing costs are decreasing and hence their use becoming more viable (Sharon & Sharon 2015*b*, Xu et al. 2018). However, from research done on graphene, MLG (multilayer graphene), CNT and CNF (carbon nanofibers), there are several difficulties in implementing these nanomaterials effectively and economically in concrete: one major compatibility issue arises due to their hydrophobic nature. (Chuah et al. 2014, Korayem et al. 2017, Norhasri et al. 2017, Parveen et al. 2013, Silvestre et al. 2016). Due to the presence of attractive Van Der Waal's (VDW) forces, graphene, CNTs and CNFs tend to agglomerate together, which results in no improvement to concrete's strength, and may even interfere with the hydration process to weaken the final material (Chuah et al. 2014, Korayem et al. 2017, Norhasri et al. 2017, Parveen et al. 2013, Silvestre et al. 2016).

2.2 Carbon nanotubes/nanofibers in cementitious material

2.2.1 Physical properties of CNT/CNF and their respective effects

Konsta-Gdoutos et al. (2010) examined the effects of short and long CNT at different concentrations. It was found that smaller concentrations of longer multi-walled CNTs (MWCNTs), with an aspect ratio of 1600 and surface area 250-300 m^2/g, exhibited similar mechanical contributions to higher concentrations of shorter MWCNTs, which possessed an aspect ratio of 700 and surface area 110 m^2/g. As such lower quantities of long MWCNTs may be used to provide the necessary reinforcement (Konsta-Gdoutos et al. 2010). However, it should be noted that 'short' and 'long' are subjective terms, as only two aspect ratios were tested, and results may vary for larger differences in aspect ratios of the CNTs. Abu Al-Rub's experiment (Abu Al-Rub et al. 2012) showed 0.2% 'short' MWCNT, with aspect ratio of 150, surface area 250-300 m^2/g) achieved a flexural strength of 12 MPa, as compared to 5 MPa of 0.1% 'long' MWCNT with aspect ratio 1250-3750 and surface area >500 m^2/g), and 3.2 MPa of the control mix. It is also observed that the MWCNT in Abu Al-Rub's study (Abu Al-Rub et al. 2012) had diameters of 9 nm or less, closer to the 3 nm theoretical diameter of pure SWCNTs, as opposed to the 20-40 nm in Konsta-Gdoutos et al. (2010) study, which indicates the latter's multiple stacking of walls.

2.2.2 Issues with CNT/CNF dispersal and mitigative measures

In their review, Parveen et al. (2013) summarized several mitigative measures used to effectively disperse CNT/CNF in the cement matrix; unlike tra-

ditional shear mixers, which are ineffective in this particular case, CNTs require an initial uniform dispersal in water, which is then mixed with cement. To ensure dispersion of CNTs in water, both physical and chemical solutions have been proposed, and/or a combination of them. The primary physical technique is ultrasonication, where voltage is transformed into high frequency shock waves through the solvent, hence disentangling and dispersing any CNT solutes (Parveen et al. 2013). However, while this solves the dispersal issue of hydrophobic nanomaterials in water, it does not ensure that the nanomaterials will stay uniformly dispersed as the water is mixed with the cement (Parveen et al. 2013); this issue has been verified by recent review papers from Korayem (2017) and Chuah(2014). Care also needs to be taken to not overdo the intensity and duration of the ultrasonicating, as that may lead to permanent damage and rupture of the CNT themselves (Parveen et al. 2013, Chuah et al. 2014, Korayem et al. 2017). Chemical treatments include the addition of surfactants, admixtures and the functionalization of the nanomaterials themselves (Parveen et al. 2013, Chuah et al. 2014, Korayem et al. 2017). By lowering the interfacial tension of water, surfactants like methylcellulose (MC) were found to assist MWCNTs in stable dispersions at optimum surfactant:CNT ratios of 4 and 6.25 (Parveen et al. 2013) for 0.16 wt% MWCNT, provided the suspension had been pre-stirred using ultrasonication or magnetic stirring; this can be seen in Figure 2.2.1. Using a lower ratio was not effective, while higher amounts of surfactants cause interference by blocking the possible interactions and embedding of CNTs in the production of C-S-H (Parveen et al. 2013). Similarly, for admixtures, a mixture of an air-entraining agent, a polycarboxylate (PC) superplas-

ticizer and low concentrations of lignosulfate can maintain a stable dispersion for up to 9 days (Parveen et al. 2013). PC superplasticizers by itself has been shown to aid in stable dispersions of CNTs in almost all studies; however high dosages, especially without the presence of defoaming agents, will lead to the retardation of the hydration process, and impact cement negatively (Parveen et al. 2013, Chuah et al. 2014, Korayem et al. 2017).

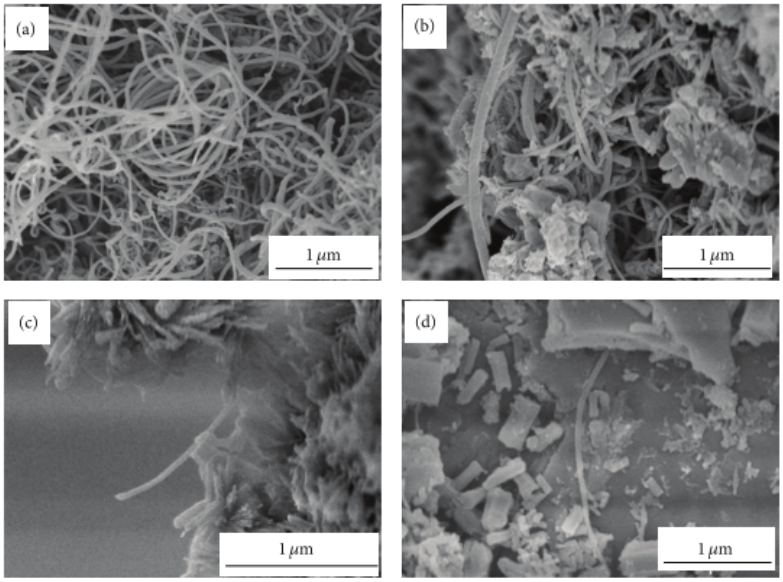

Figure 2.2.1: Effects of adding surfactant to CNT in ratios of (a) 0, (b) 1.5, (c) 4, and (d) 6.25 on the final dispersion of MWCNTs in cement matrix. (Parveen et al. 2013).

Finally, surface treatment of CNTs to increase their hydrophilicity has been experimented with success (Parveen et al. 2013, Chuah et al. 2014, Korayem et al. 2017): the steric repulsion provided by PC superplasticizers or certain surfactants arise due to their polar nature, having large hydrophobic 'end' chains with a hydrophilic 'head'. By subjecting CNTs/CNFs to strong acids, the nanomaterials get oxidized, and various carboxyl and hydroxyl groups can get grafted on the surface of these CNTs (Parveen et al. 2013). Figure 2.2.2 shows these functionalized CNTs (fCNTS), which can repel each other and hence can stay dispersed in water or an alkaline solvent for longer periods of time. In ad-

dition to the above, the carboxyl (-COOH) and hydroxyl (-OH) grafted groups can react with the C-S-H to be finely intertwined in the cement matrix, ensuring its excellent mechanical contributions to the overall material while also reducing porosity, resulting in a denser and more durable, crack resistant microstructure (Parveen et al. 2013, Chuah et al. 2014, Korayem et al. 2017).

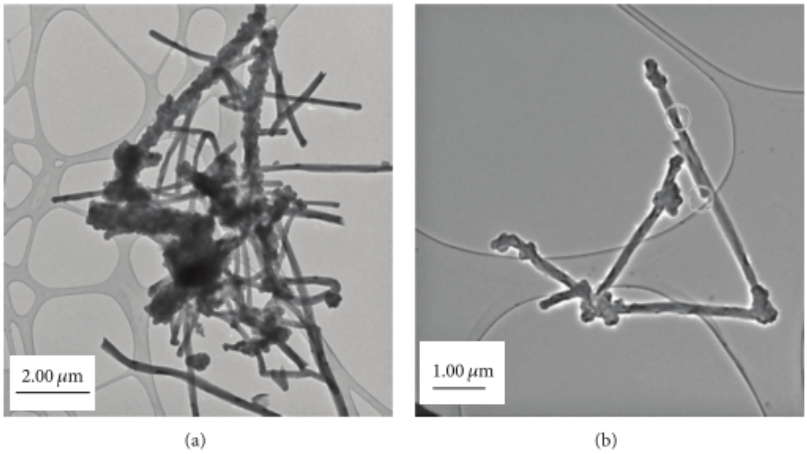

Figure 2.2.2: The improvement in dispersion (a) with and (b) without grafting acrylic acid polymer on CNTs. (Cwirzen et al. 2008).

Yazdanbakhsh et al. (2012) and Metaxa et al. (2013) have attempted to implement CNF in the cement matrix; CNFs are larger nanomaterials, having a diameter of 200 nm as opposed to the 20 nm average for CNTs (Metaxa et al. 2013). Yazdanbakhsh et al. (2012) found that the CNF mix with the least w/c ratio (0.25), and the highest CNF (1% by wt. cement) and superplasticizer (0.85 wrt cement) ratios displayed the highest flexural strength at 13.62 MPa, compared to 1.91 MPa of the control mix without superplasticizer (at w/c ratio of 0.40), and 9.87 MPa with superplasticizer (0.66 ratio wrt cement). Unlike CNTs steric hindrance effect, in Yazdanbakhsh's study a higher amount of CNF continues to improve the cement mix (2012). The factors affecting CNTs/CNFs mechanical contribution are complex and multi-faceted; for instance, in Metaxa et al.

(2013) research, ultrasonication dispersal @ 2800 kJ/I was found to result in a greater 28 day flexural strength (7.2 MPa) compared to 3500 kJ/I (6.9 MPa) or 2100kJ/I (6.6 MPa). In addition, Metaxa et al. (2013) also found that the CNFs with the rougher planar surfaces tend to contribute higher to the cement mixes; a possible reason for this could lie in the higher pullout force required to remove rougher fibers in the cement matrix (Metaxa et al. 2013).

2.2.3 Novel routes of CNT/CNF incorporation in cement

Nasibulin et al. (2009) introduced a unique method of growing the CNTs on the cement particles directly via chemical vapour deposition (CVD), using an inexpensive, custom built continuous feeding furnace reactor to avoid separate catalyst preparation (Nasibulin et al. 2009). An illustration of this growing can be seen in Figure 2.2.3. Results showed >100% increase in 28 day compressive strength of the material (55 MPa versus 25 MPa), and significantly lower electrical resistivity (1.3 MΩ cm vs 9.7 MΩ cm), however the 7 day compressive strength showed a >100% decrease for 30% CHM based cement mix (24 MPa vs. 49 MPa of the control mix), keeping in mind that the synthesis conditions were different for both 7-day and 28-day samples (Nasibulin et al. 2009). As such, it remains to be seen whether this approach can be consistent in producing improved nanoreinforced concrete.

Parveen et al. (2015) presented a CNT dispersion route using Pluronic F-127 as a dispersing agent (with the inclusion of a defoaming agent to ensure low air entrapment in the mixes), as opposed to more common surfactants (specifically sodium dodecylbenzene or SDBS), for both single-walled and multiwalled CNTs (SWCNT, MWCNT) and their functionalized counterparts (fSWCNT,

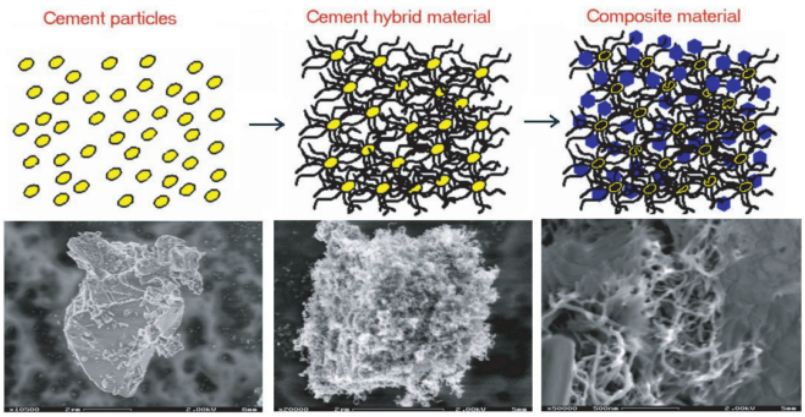

Figure 2.2.3: Illustrating the ideal mixing of CNT with cement matrix into a new composite material. (Nasibulin et al. 2009).

fMWCNT). Pluronic shares the same polyethylene oxide (PEO) side chain molecules found in polycarboxylate (PC) superplasticizers, but is used in biomedical fields for its low toxicity (Parveen et al. 2015). Previous research has shown Pluronic being effective at dispersion of CNT in water, provided it is at low concentrations relative to CNTs, and is preheated and pre-stirred before sonication (Ciofani et al. 2009). For Parveen et al. (2015), 28 day flexural strength varied considerably throughout all the mixes, and did not increase significantly for any of the nanoreinforced samples (the highest being a 6.7% improvement for 0.1% non-functionalized SWCNT: 7.6 MPa versus 7.15 MPa. The lowest was a decrease of 27.1% for 0.1% MWCNT @ 5.21 MPa), however the flexural modulus showed uniformly stiffer samples, a possible indication that the CNT have been dispersed sufficiently in the cement mixes (maximum 72% improvement for 0.1% f-SWCNT, 15.8 GPa vs.15 GPa) (Parveen et al. 2015). For 28 day compressive strength, 0.08% SWCNT with 3% Pluronic F-127 showed the most improvement at 15.4%, 41.1 MPa versus 35.6 MPa of the control mix. However, 0.1% MWCNT showed a decrease of 42.7% in strength at 20.4 MPa (Parveen et al. 2015). In general, SWCNT showed better mechanical contri-

butions than MWCNT, while the change in Pluronic F-127 concentration did not affect the mechanical strength of the mixes by itself for either SWCNT or MWCNT. The difference in the ratio of surfactant:defoaming agent also shows a pattern: 2:1 respective ratio generally outperformed (or rather performed less negatively) than the lower 3:1 ratios for MWCNT, while SWCNT did not require high amounts of defoaming agents in their dispersion. In addition, UV-Vis spectroscopy tests were initially carried to quantify the dispersion of Pluronic F-127 + MWCNT/SWCNT: fSWCNT showed the highest dispersion, while fMWCNT showed the least dispersion (Parveen et al. 2015). The low dispersion of MWCNT from Pluronic F-127 may further suggest their generally worse/negative impact on the cement mixes (Parveen et al. 2015).

An interesting route was taken by Balasubramaniam et al. (2017) by functionalizing the surface of CNTs with PC superplasticizer via ultrasonication. From their X ray diffraction (XRD) tests, all fCNTs underwent sufficient dispersal and effective mixing with the hydration constituents, verified by SEM imaging, whereby non-functionalized CNTs and control mixes showed agglomeration and heavy pore formation during the first day of the hydration process. As a result, compressive strength of fCNTs are significantly higher than both their non-functionalized versions (nfCNT), and the control mixes (with or without superplasticizers): for 0.025 wt% cement, fCNT @ 28 day strength is at 52 MPa, nfCNT is at 45 MPa, while for 0.05 wt% cement, fCNT @ 28 day strength is at 63 MPa, nfCNT is at 40 MPa and the control mixes are at roughly 47-48 MPa. Increasing the CNT amount to 0.5 wt% cement impacted the mixes negatively due to a steric hindrance effect (more difficult to isolate the nanomateri-

als at higher concentrations). Split tensile strength showed a similar trend, with 0.025% CNTs being stronger than higher concentrations for both functionalized and non-functionalized. However, it should be noted that the initial dispersion was not quantified via any methods, and this particular surface treatment required high dilution of the CNT/PC colloidal dispersion (Balasubramaniam et al. 2017), ultimately having relatively high w/c ratios of 0.56 for 0.025%, 0.68 for 0.05% and 0.80 for 0.5% nfCNTs, compared to 0.35, 0.40, 0.45 for their respective fCNT counterparts. As such, the sub-par strength performance can be owed to these high w/c ratios, and not solely the implementations of the CNT themselves (Neville 1996, Li 2011).

From the above studies, it is clear that a proper implementation of CNT can significantly improve the strength and durability of concrete. However, as indicated in past research, the uniform dispersion of CNTs remains a tricky endeavour; complex, multi-step dispersion routes do not seem feasible on a large scale, and large scale production of CNTs is expensive and not sustainable (Korayem et al. 2017, Norhasri et al. 2017). From the above referenced studies, results do not seem consistent, among other research suggesting CNT incorporation had primarily negative impacts to the samples (Musso et al. 2009), and more research is required to uncover the complex interactions of the C-S-H cement matrix, the alkaline/water solvent medium, and the properties and structural specifics of CNT themselves. In specific, testing parameters such as (i) purity of the CNTs, (ii) their aspect ratios, (iii) their single walled/multi walled nature, while employing strict quantified methods to describe their dispersion in water/alkaline mediums. Characterization tests such as UV-Vis spectroscopy

and zeta potential may provide enough information to organize and explain the high variability in its performance as a concrete nanoreinforcement material (Sindu et al. 2014). It should also be noted that not much research has been done on the effects of CNT incorporation in concrete samples, only cement paste or mortar.

2.3 Graphene oxide, reduced graphene oxide and further advancements

As seen above, functionalized CNTs were more hydrophilic, and while pristine graphene offers similar implementation difficulties as nfCNTs, graphene oxide (GO) is by comparison significantly easier to disperse in both water and organic solvents (Chuah et al. 2014, Korayem et al. 2017, Parades et al. 2008, Gao 2015). Initially GO was seen as a necessary intermediary step towards obtaining reduced graphene oxide (rGO), a graphene-like material used in various engineering and biomedical fields (Zhu et al. 2010, Gao 2015). To produce GO, graphite flakes are exfoliated, followed by oxidation using strong acids similar to the functionalization of CNT. Functional groups such as carboxyl (O=C-OH), carbonyl (C=O), epoxy(C-O-C) and hydroxyl(C-OH) groups are added to the carbon sheet structure, as shown in Figure 2.3.1 (Szabó et al. 2006, Fasolino et al. 2007, Zhu et al. 2010, Rattana et al. 2012, Medhekar et al. 2010, Zhao et al. 2014, Gao 2015, Papageorgiou et al. 2017). Carboxyl groups are attached at the edges of the graphene sheet, as they demand 3 bonds from the carbon atom, but hydroxyl, carbonyl and epoxy groups can be at the edges of sheet or on the basal planes (perpendicular, jutting out of the sheet) as well, with oxygen's charged

nature buckling the sheet and contributing to its 'rippled' look (Szabó et al. 2006, Fasolino et al. 2007, Zhu et al. 2010, Rattana et al. 2012, Medhekar et al. 2010, Zhao et al. 2014, Gao 2015, Papageorgiou et al. 2017). As stated before, pristine graphene is expected to have an interlayer spacing of approximately 0.335 nm; however graphene oxide, due to the basal functional groups, may have layers spaced out to 0.6 - 1.2 nm (Buchsteiner et al. 2006, Vorobiev et al. 2014). In molecular simulations by Medhekar et al. (2010), it is shown that a water content of 0.9% can increase the interlayer spacing to 0.51 nm. However, increasing the water content to 25.4% increases the interlayer spacing to 0.9 nm (see Figure 2.3.2). Due to the polarity of the oxygen in the hydroxyl and epoxy functional groups, the polar water molecules get attracted to them (hence the hydrophilicity) and form a hydrogen bond network in between the layers (see Figure 2.3.4); the water molecules hence end up bunching between the layers and increasing its interlayer spacing (see Figure 2.3.3) (Medhekar et al. 2010).

However, as a result of its functionalization, GO's overall surface area, mechanical strength, thermal and electrical conductivity is reduced from its parent graphene (Sharon & Sharon 2015*a*, Silvestre et al. 2016, Gao 2015, Papageorgiou et al. 2017). To overcome this issue GO can be further reduced to rGO, where the single bond functional groups (hydroxyl, epoxy) in the basal planes are removed, hence 'flattening' the sheets and obtaining a graphene-similar material (see Figure 2.3.1) (Zhu et al. 2010, Gao 2015, Chuah et al. 2014, Korayem et al. 2017, Zhao et al. 2014). It should be noted, as a preface, that GO nanoreinforced cement composites are a new field, and different research have interchangeably used GO and multilayer graphene (MLG) to refer to graphite oxide, graphene

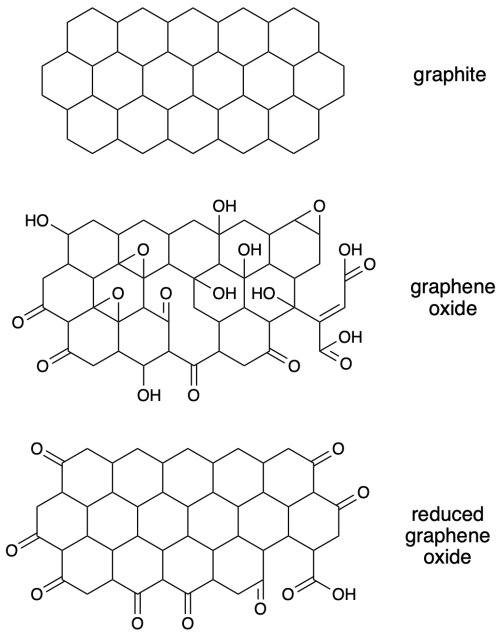

Figure 2.3.1: Commonly accepted structure models of graphene, GO and rGO, displaying the presence and location of oxidized functional groups.

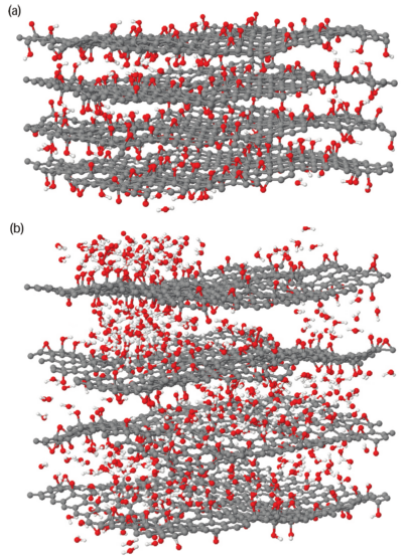

Figure 2.3.2: ReaxFF simulation of interlayer spacing of GO at (a) 0.9% and (b) 25.4% water content. Layers are 3.4 x 3 nm. Grey being carbon, red oxygen and white hydrogen atoms. (Medhekar et al. 2010).

oxide, and/or reduced graphene oxide with no clear standardization and references. Hence, it is of utmost importance to keep different chemical and molecular properties of GO for each research in mind, as minor differences in purity, the C:O ratio, the interlayer spacing, lateral length of GO layers and number of GO layers can significantly affect their performance as a cementitious composite (Wick et al. 2014), elucidated in Chapter 2.5. To mitigate these issues, Wick et al. (2014) have prescribed a helpful nomenclature as shown in Figure 2.3.5.

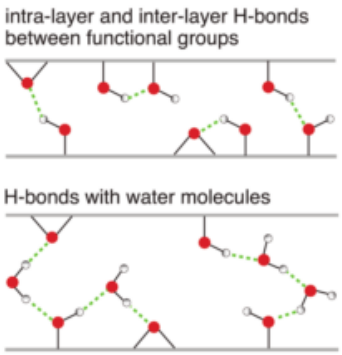

Figure 2.3.3: H-bond network and GO interlayer spacing illustrated in a simulation. (Medhekar et al. 2010).

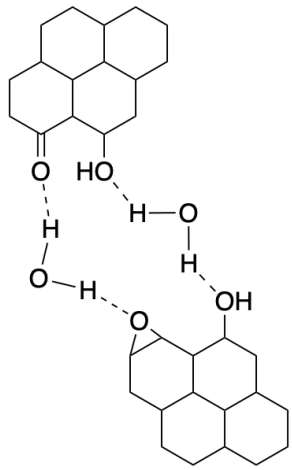

Figure 2.3.4: H-bond network bonds sketch.

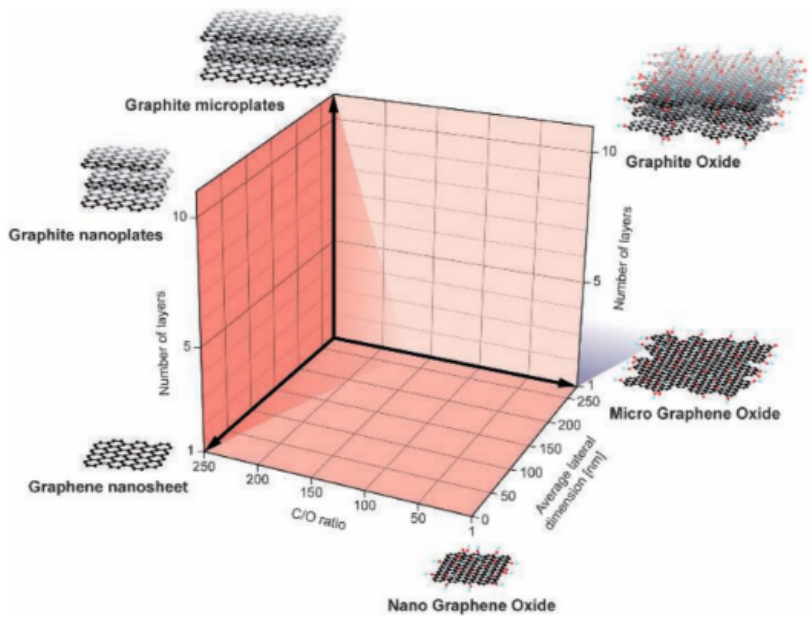

Figure 2.3.5: Guide for establishing GO nomenclature. (Wick et al. 2014).

2.3.1 Manufacturing GO and rGO

In the Introduction of Chapter 2.3, it can be observed that most CNT samples are not manufactured directly, but are procured from various suppliers. However, for several of the GO papers studied in this review, GO is synthesized from flaky graphite using chemical reactions akin to the functionalization procedure of CNTs. It is essential to dedicate a section explaining the typical production of GO, as that can offer key insight into their mechanical properties and contributions to the C-S-H cement matrix, as well as provide perspective for the large scale production viability of such composites.

The earliest well documented process of manufacturing GO was discovered by B. C. Brodie in 1859 and is known as the Brodie method (Gao 2015). It involved a mix of graphite slurry and nitric acid (HNO_3), to which potassium chlorate ($KClO_3$) was added, and the oxidation process was repeated multiple times (Gao 2015). An increase in mass was reported, due to the increase in the interlayer spacing as a result of the oxidation, and the resulting GO could disperse in water or alkaline mediums as opposed to its parental material and had a C:O ratio of approximately 2.19:1 (Gao 2015). Brodie's process was improved by L. Staudenmaier by replacing some of the nitric acid with sulphuric acid (H_2SO_4) and adding potassium in multiple fractions over the whole reaction period, a safer approach with less propensity for explosions (Gao 2015, Marcano et al. 2010, You et al. 2013, Yu et al. 2016). Regardless, these oxidizing agents are extremely dangerous, and are still at risk of minor explosions while the complete oxidation process took place over 3-4 days (Gao 2015, Qiu et al. 2014, You et al. 2013, Yu et al. 2016, Zaaba et al. 2017). In 1958 Hummers

and Offerman introduced what is now known as the Hummers method, where graphite is oxidized by a mix of sodium nitrate ($NaNO_3$), potassium permanganate ($KMnO_4$) and sulphuric acid, replacing the dangerous potassium chlorate completely and reducing the total time taken to only several hours (Gao 2015, Marcano et al. 2010, You et al. 2013, Yu et al. 2016, Zaaba et al. 2017). The active oxidizing ingredient in this case is diamanganese heptoxide (Mn_2O_7), formed as indicated in following reactions (Emiru & Ayele 2017):

$$KMnO_4 + 3H_2SO_4 \rightarrow K^+ + MnO_3^+ + H_3O^+ + 3HSO_4^- \tag{1}$$

whereby the manganese oxide and ions react,

$$MnO_4^- + MnO_3^+ \rightarrow Mn_2O_7 \tag{2}$$

which causes the oxidation of carbon in graphite to form GO and its functional groups (Emiru & Ayele 2017),

$$Mn_2O_7 + H_2SO_4 + C(graphite) \rightarrow \begin{pmatrix} C-O-C \\ C-OH \\ C=O \\ O=C-OH \end{pmatrix} + MnO_5 + H_2O + SO_4^{-2} \tag{3}$$

However, the manganese ions directly responsible for the graphite oxidation are still under contention and are discussed in a following section. From You et al. (2013) research, it is apparent that the method of production (Brodie, B-GO or Hummers H-GO) significantly affects the characteristics of the GO be-

ing produced. In their research, using XPS analysis, B-GO was found to have a C:O atomic ratio of 2.85:1 while H-GO was at 2.47, showing higher oxidation via Hummer preparation (You et al. 2013). Theoretically, Brodie's method results in purer output due to the absence of contamination by potassium, sulphur or manganese, albeit the reaction process is more dangerous (You et al. 2013). Via XRD tests, interlayer spacing for H-GO were found to be consistently higher than B-GO by 0.4-0.5 nm, slightly larger than the diameter of a water molecule at 0.3-0.35 nm: this suggests intercalation of more than one layer of water molecules, which are attracted to the O containing functional groups on the basal planes of GO sheets (You et al. 2013). Similar results were shown in other solvents (such as methanol) as well; additionally, B-GO showed higher exfoliation temperatures than H-GO, correlating to a better sheet structure and verifying its theoretically higher expected purity (You et al. 2013).

Despite the relative safety of Hummer's method, it is important to note that the use of sodium nitrate in both Brodie and Hummer's processes ensure production of toxic gases such as NO_2 and N_2O_4. Additionally Mn_2O_7 is a strong oxidizing agent, and may cause detonation at temperatures >55° Celsius (Gao 2015). Other retaining issues include low yield, low purity and/or large scale production feasibility, and several techniques have been proposed to address these problems (Shahriary & Athawale 2014, Ghorbani et al. 2015, Emiru & Ayele 2017, Marcano et al. 2010, You et al. 2013, Yu et al. 2016, Zaaba et al. 2017). Arguably the most notable improvement to Hummer's method was by Marcano et al. (2010) in 2010, in which the $NaNO_3$ was completely excluded, amount of $KMnO_4$ was increased and phosphoric acid (H_3PO_4) was added in

a ratio of 1:9 parts per sulphuric acid, as summarised in Figure 2.3.6. It was discovered that the improved Hummer's method exuded no toxic fumes, and gave a higher yield than the original method, even if the increased $KMnO_4$ is taken into account (Marcano et al. 2010). The new product also appeared to have better structural regularity, and it was easier to keep the exothermic temperature in check during the reaction process. However, the new yield exhibited a greater degree of oxidation (Marcano et al. 2010), not ideal for certain electrical/biomedical applications of GO which require a more pristine graphene like material. This does not impact and may actually prove beneficial for GO's use as a cementitious nanocomposite, as will be discussed later. Yu et al. (2016) presented a more efficient and economical synthesis method, substituting part of $KMnO_4$ with K_2FeO_4, and reducing the amount of concentrated H_2SO_4, the whole process is summarized in Figure 2.3.7. Alternatively, Chen et al. (2016) improved Hummer's method by introducing water enhanced oxidation with the ability to control the oxidation and functionalization degree (see Figure 2.3.8). Chen et al. (2016) discovered that the addition of 4 mL water per gram of graphite, and maintenance of GO-oxidant solution at low temperatures of 0° Celsius for 48 hours ensured 60 times the yield of highly oxidized GO. Additionally, the higher yield was of improved structural integrity to GO synthesized using the original Hummer's method, said integrity inferred from the significantly higher electrical conductivity of its reduced version compared to the original (Chen et al. 2016). However, it should be noted that while Chen (2016) also prepared 'carboxyl rich' GO, it was thermally reduced GO and their research was primarily focused on 'hydroxyl-rich' GO. As will be discussed

later, both carboxyl and hydroxyl groups have different or perhaps even no direct roles to play in their interactions with the cement matrix. Chen's (2016) methods were modified and implemented in this research, however the high yield was not reproducible and a new perspective on graphene oxide's chemical properties is detailed and justified. Lastly, in the aforementioned research it was found that high temperature oxidation of graphite can lead to destructive effects and permanent damages to the resultant GO, also seen as the missing C-C bonds in Figure 2.3.8 (Chen et al. 2016).

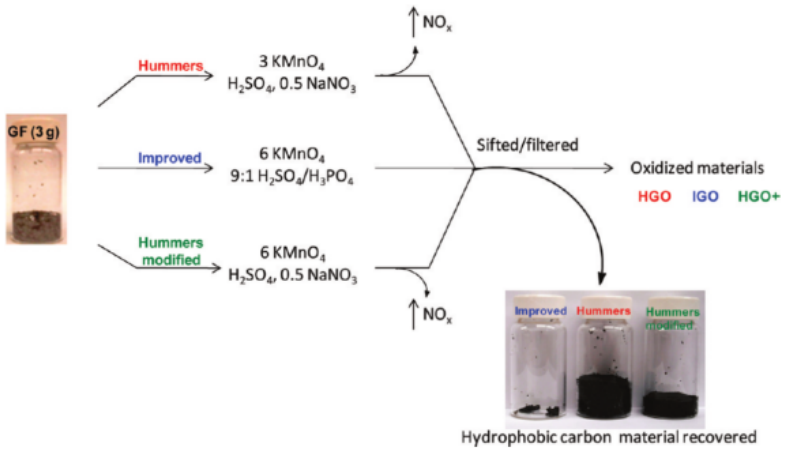

Figure 2.3.6: Hummers and Modified Hummers method of producing GO. (Marcano et al. 2010).

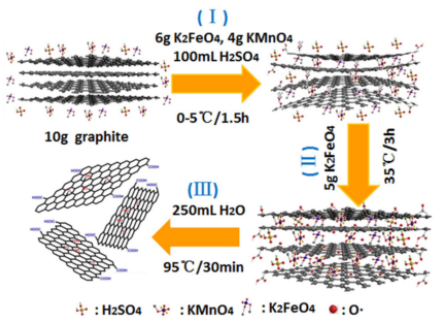

Figure 2.3.7: Newly improved Hummers method. (Yu et al. 2016).

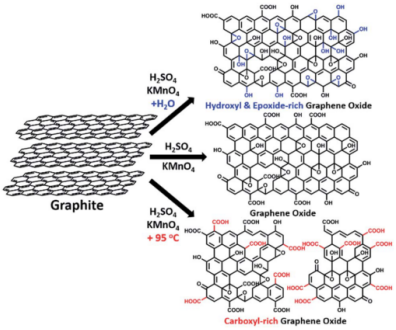

Figure 2.3.8: Water enhanced oxidation. (Chen et al. 2016).

As stated before, in many electrical, fluid and biomedical applications GO is seen as an intermediary product due to its ease of use and endless poten-

tial for modification, but it is relatively impure and electrically insulating compared to its reduced counterpart, rGO (Gao 2015, Zhao et al. 2014). To highlight their differences, the average thickness of a GO sheet would be approximately 1 nm, while an rGO sheet is only 0.34 nm thick, due to the absence of functional groups on the basal plane (Zhao et al. 2014). GO can be reduced to rGO through a myriad of electrochemical, microwave, biodegradable and thermal techniques (Ghorbani et al. 2015, Gao 2015, Emiru & Ayele 2017, Zhao et al. 2014), but, in the case for cement nano-reinforcement, the 'drawbacks' of GO are seemingly inconsequential, while their benefits (especially hydrophilicity) are too useful, and ensure greater large scale production viability for cementitious composites. However, in most cementitious incorporations of GO, not enough attention has been paid to the chemistry of the nanomaterial itself, perhaps understandably so as it's physical attributes are being focused on. However, it is hypothesized that GO's contributions are mostly chemical, and as such the following review subsections go in depth on the chemical inceptions and mechanisms of both the graphene oxide and cement hydration respectively, to provide a complete background that can satisfyingly describe how the nanomaterial is strengthening hydrated cement.

2.3.2 Graphene oxide's chemical oxidation and the hydronium layer

In Chapter 2.3.1, an introduction to different synthesis methods of GO is provided. This section further delves into how the layers of graphite are oxidized. Chemical oxidation of graphite to GO, either via Modified Hummer's method or Brodies method, typically follows a 5 step procedure (Lowe & Zhong 2016): 1) Intercalation of graphite into single or multi-layer graphene sheets (a tem-

porary state), 2) Oxidation of its sheets into GO via a strong oxidant, usually $KMnO_4$, 3) Termination of the process by introducing H_2O_2 and H2O 4) Decontamination of the mix by successive centrifuging and washing, often with dilute HCl and deionized water, and 5) dispersion of GO in solution via ultrasonication.

Graphite can be intercalated by various oxidizers (e.g., H_2SO_4, H_3PO_4) or reducers (KCL, KOH) (Kovtyukhova et al. 2014) except for Na^+ based compounds due to its lower ionic radius (Moriwake et al. 2017). Once intercalated, the GO-acid mix will stay exfoliated for months provided the acid is not diluted. Dimiev et al (Dimiev & Tour 2014) found that GO oxidation is diffuse-controlled, i.e., the rate GO oxidation is much higher than the rate of the oxidizing agent diffusing into the graphite layers, hence early intercalation is necessary to facilitate the oxidative process. H_2SO_4 does not initiate intercalation unless it is provided some energy, typically via stirring and/or heating the graphite-sulphuric acid mix (Higginbotham et al. 2010). It should be noted that H_2SO_4 also oxidizes the graphite, but its analogous compounds are removed upon hydrolysis (see Figure 2.3.9 for an illustration of this process). In addition, the ionic order of the added oxidizing acids matters: e.g. an HNO_3/H_2SO_4 mix would result in graphite sulphate compounds, while H_3PO_4/H_2SO_4 would not (Hofmann & Structure 1938).

$KMnO_4$ is the preferred oxidant for Modified Hummer's methods, however which of its intermediate ions contributes to the oxidation of graphite is still under debate. Li (2020) has argued that as the oxidation process is self-regulating, the manganese oxide cannot be neutral or electrophilic, as that would react

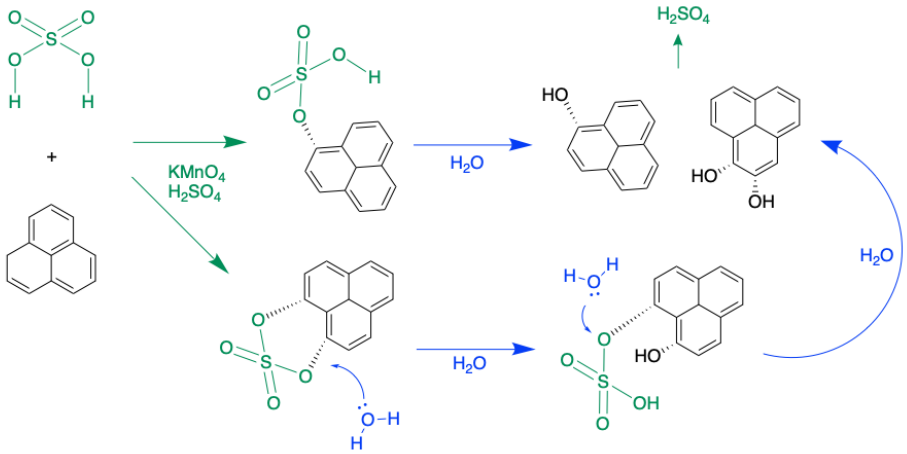

Figure 2.3.9: The oxidation and hydrolysis of analogous sulphate bonds in GO from addition and removal of sulphuric acid.

violently with the conjugated acid of H_2SO_4 and cannot be self-regulated. In addition, grafting of neutral radicals (O3,.O., HO.) on the carbon sheets would be randomized, unlike the localized aromatic and functionalized domains in actual GO sheets. Hence, MnO_3^+ is the most likely oxidant for GO, which itself is a temporary ion formed by dissociation of Mn_2O_7 (Li et al. 2020). Typically, $KMnO_4$ cannot be used in excess of 4-5wt. equivalent of graphite (Dimiev, Kosynkin, Alemany, Chaguine & Tour 2012) although this may vary depending on the acid combination and/or concentration used for oxidizing. Introducing a second acid in the mix (e.g. H_3PO_4), as long as the ionic order is appropriate, doesn't affect the $H_2SO_4/KMnO_4$ reaction, but actually improves the propagation rate and increases intake of $KMnO_4$ for GO oxidation (Higginbotham et al. 2010, Dimiev, Bachilo, Saito & Tour 2012, Marcano et al. 2010).

For cement development, water is essential in the hydration process. It is then important to also note the particular interactions of GO with water, and how that makes quantitative determination of GO functional groups complex. In Rourke's 2011 paper the 'oxidative debris' was noted to adhere to GO after

its creation, removed by base wash but also reducing the GO (2011). However, Dimiev et al (2013) in their excellent paper made a strong case for the dynamic structural model (DSM) for GO, where they asserted that the hydroxyl (phenol) and carbonyl groups on the basal planes of GO sheets protonate any water molecules in contact to form a hydronium (H_3O^+) layer. This hydronium layer (also referred to as the DSM layer in later discussions) contributes to the high acidity of GO, while ensuring stable dispersion by positive charge repulsion between GO sheets in aqueous suspension. However, the 'tug of war' of charges between the positively charged H_3O^+ and negatively charged COO^- or CO^- open bonds can result in constant opening and closing of bonds along the functionalized domains of the GO sheet (illustrated in Figure 2.3.10). This is further enhanced by vinylogous activity through the functionalized carbon sheets, production of vicinal diols by unzipping of epoxide groups, and vice versa, ultimately resulting in constant dynamic interactions of GO suspensions. Recent simulations (Mouhat et al. 2020) have also lent credence to the dynamic protonation by GO, while other models propose new phenol functional groups that may facilitate these surface charges (Aliyev et al. 2019, Szabó et al. 2006). Simplified GO-DSM illustrations of the above activities are shown in Figure 2.3.11 and Figure 2.3.12.

The GO-DSM model is compatible with all conventional theories regarding GO functionalization behavior, while also emphasizing its self-regulating interactions while in suspension. This emphasis is greatly overlooked and can result in erroneous conclusions from correctly performed analytical characterizations of GO. The H_3O^+ film is very difficult to remove, and extreme mea-

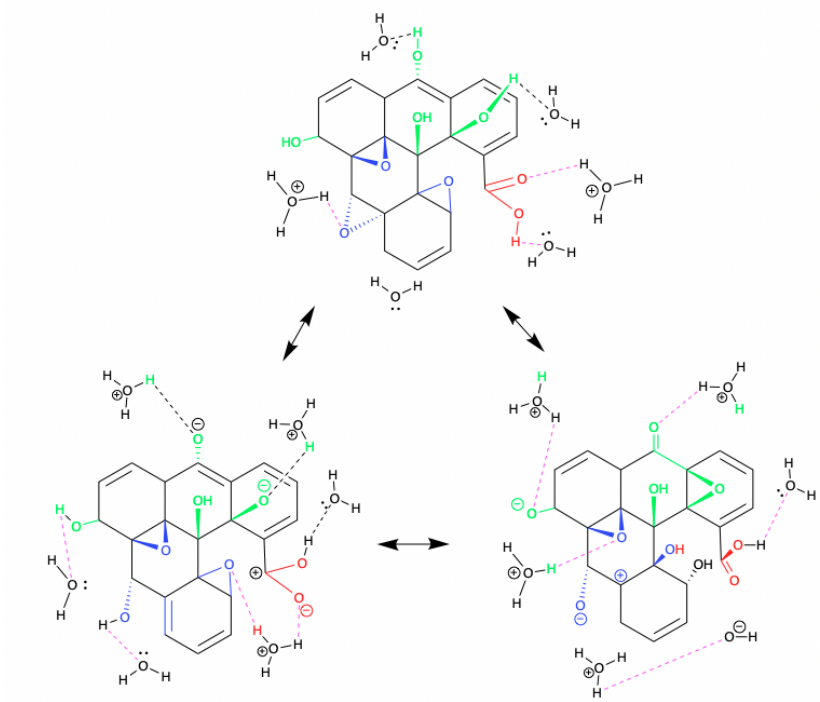

Figure 2.3.10: The creation and interchange of water/hydronium molecules by GO in dynamic structural (DSM) model.

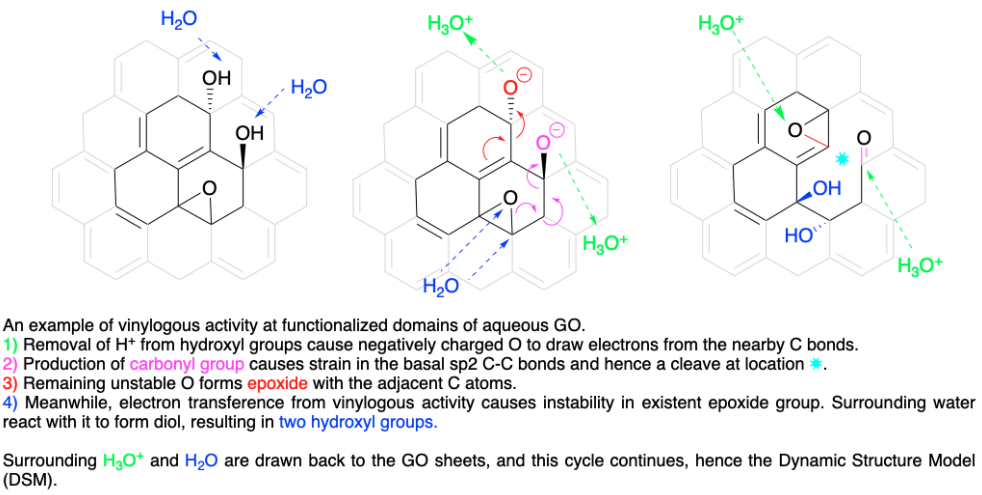

Figure 2.3.11: Illustrating the vinylogous activity in GO DSM.

sures such as freeze drying or intense heating may remove the layer, but also destroy the functional groups on the GO surface and cause sheet tearing, as shown in Section 4.2.3 of this PhD research. Furthermore, the O-H bonds from the hydronium layer can also overlap when analyzing IR spectra or XPS peak fitting, leading to inaccurate C/O ratio estimations from XPS spectra (as well

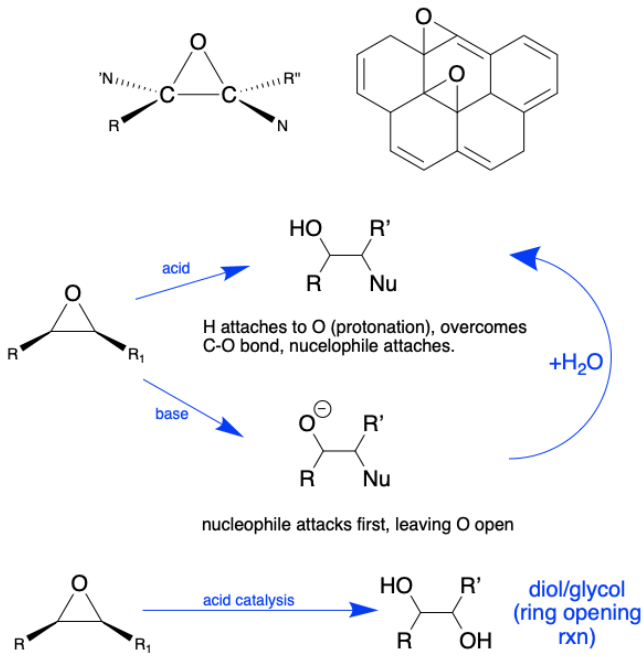

Figure 2.3.12: Illustration of epoxide opening under acid or base addition.

as EDX analysis). Preparation of GO via annealing for Raman or XPS can also alter the nanomaterials, potentially reducing them, however the hydronium layer's sensitivity has not been accounted for in these studies (Rogala et al. 2016). Additionally, Boehm titrations, typically intended to distinguish phenol/carbonyl presence in GO functional groups (Goertzen et al. 2010, Oickle et al. 2010) may also be inaccurate as the hydronium layer would deprotonate first to counter base additions. As a result, NaOH, $NaHCO_3$ and Na_2CO_3, the three Boehm bases will not be able to distinguish functional group composition due to H_3O^+ neutralization interference (Dimiev et al. 2013). GO would also attempt to protonate the remaining water molecules in proximity to reproduce the hydronium ions, which further defeats the intention of performing the Boehm titration in the first place.

By subjecting graphite to ultra-oxidation, the aim is to exaggerate these DSM interactions and infer GO functionalization behaviour by prioritizing the

analysis of the hydronium layer and surface charges produced by HGO, OGO, XGO and LGO. Subsequently, each of the GOs would have varying degrees of oxidation hence it is expected that their respective hydronium layers would vary in terms of surface charge/acidity of their suspensions. However, as GO is self-regulating, there is a preferred equilibrium of H_2O and H_3O^+ molecules surrounding the sheets that facilitates the hydronium layer, and this equilibrium will vary depending on the respective degree of oxidation of GO. In following experiments, OGO is used as control while XGO, being destructively reduced by its post treatments, is a place holder for the worst-case scenario: a defective/reduced GO. Meanwhile, HGO and LGO are two different approaches to ultra-oxidizing graphite, the former being via dilution of the intercalating medium by introducing water molecules.

2.4 Introduction to cement

A basic concrete structure involves mixing cement, aggregates and water. Its preparation is easy and convenient, which lends to versatile mixes depending on strength, workability, durability or other requirements. However, the chemical nature of cement and its hydration are complex and all the intricacies are yet to be fully researched. Cement is manufactured from naturally occurring calcareous and silica/alumina materials, primarily lime (calcium oxide CaO), silica (SiO_2), alumina (Al_2O_3) and oron oxides (Fe_2O_3). These minerals are ground into fine powder and mixed under very high temperatures (1400 °C) via blowing hot coals to form fused clinker. Hence, cement is essentially frozen in a solid-state solution, and kept in dry conditions as exposure to water

will immediately cause an exothermic reaction. To avoid this 'flash setting' of cement, gypsum is usually added in the manufacturing process, which is also highlighted in Figure 2.4.1 (Neville 1996, 2019, Li 2011).

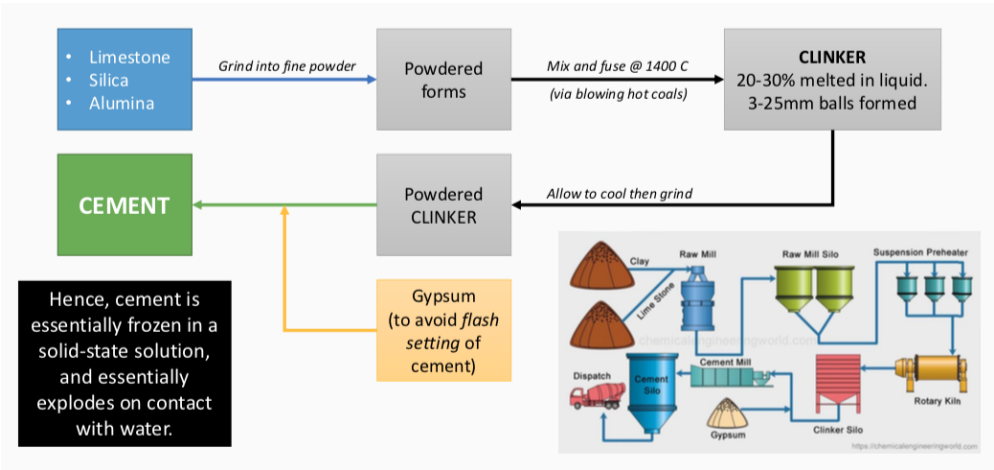

Figure 2.4.1: Outline of cement manufacturing process. Inlet from public domain

The final composition of cement is a mix of 4 fused impure compounds: alite ($3CaO.SiO_2$ or C_3S in chemist notation), belite ($2CaO.SiO/C_2S$), celite (C_3A or ($3CaO.Al_2O_3$) and C_4AF ($4CaO.Al_2O_3.Fe_2O_3$). These are impure compounds as they just exist as oxides in a solid solution due to clinker fusing. Alite and belite, upon contact with water form the main binding agents that hold cementitious materials together (C-S-H). C_3A is an undesirable by-product, which can form ettringite (calcium sulfo-aluminate or AFt) upon hydration and sulfate presence. However, they facilitate silica-lime during the cement manufacturing process hence their inclusion. C_4AF is another compound that does not affect hydration much, instead may accelerate it in the presence of gypsum. Other minor oxides are also present in cement (MgO, TiO_2, Mn_2O_3, K_2O, Na_2O) (Neville 1996, 2019, Li 2011).

$$2C_3S + 6H \rightarrow C_3S_2H_3 + 3CH \tag{4}$$

$$2C_2S + 4H \rightarrow C_3S_2H_3 + CH \tag{5}$$

$$C_3A + 6H \rightarrow C_3AH_6 \tag{6}$$

where $C = CaO$, $S = SiO_2$, $H = H_2O$, $A = Al_2O_3$

Equations 4, 5, and 6 show how alite, belite, and C_3A react with water respectively (approximate, as C-S-H has many varying proportions). The rate of alite hydration is much faster than belite's, and hence is highlighted for contributing to concrete's initial strength. C_3A is faster than both, hence causing flash-setting of cement. To counter this gypsum is added to divert its reactions, which ends up forming the by-product ettringite. Both alite and belite form calcium silicate hydrates, written as C-S-H as it's compound ratios are often variable and hard to determine due to its irregular triclinic crystalline structure (Neville 1996, 2019, Li 2011).

$$\frac{\sigma_{max}}{\sigma} = 2\sqrt{\frac{c}{r}} \tag{7}$$

where σ=tensile stress, c=length of crack, r=equivalent radii at end of crack.

In most cases, concrete with high compressive strength is an industry requirement. To build strong concrete, the mechanics and potential causes of it's failure should be sufficiently understood. Under high compressive strength, the C-S-H microstructure is able to transfer loads effectively to the neighbouring aggregates which can easily support without crushing. However, when any tensile strength is applied to concrete, the C-S-H's weak binding strength

is pulled apart, and cracks start to propagate through the structure. From a fracture mechanics approach, these cracks are often formed perpendicular to the direction of load (see Figure 2.4.2). The failure stress of the C-S-H paste is related to the equivalent radius and length of cracks, shown in Equation 7. It is impossible to not have any cracks exist in a cement structure, as its mixing will often lead to unhydrated cement and air and water voids, from which water can also evaporate over it's lifetime (called shrinkage). Hence our priority from a cementitious materials standpoint is to develop a dense C-S-H structure that can stop or reroute cracks and divert them into branches, reducing change for tensile failure. Even under compressive loads, the mix in concrete can lead to cracks developing at different angles to the applied load. In order to improve the microstructure of hydrated cement, let us understand how the hydration procedure works and where/how nanomaterials can offer mechanical advantages (Neville 1996, 2019, Li 2011).

2.4.1 Mechanism of cement hydration

Bullard et al (2011) outline 6 essential steps of the formation of cement biding paste. These steps are summarized and illustrated in Figures 2.4.3 and 2.4.4 respectively, and are as follows:

1. Dissociation/dissolution: upon contact with water, molecules are detached from the cement/C_3S particle surface.

2. Diffusion: Water molecules diffuse between the detached molecules and adsorb on the cement/C_3S particles themselves

3. Growth (G): New C-S-H molecules are formed on and along the surface

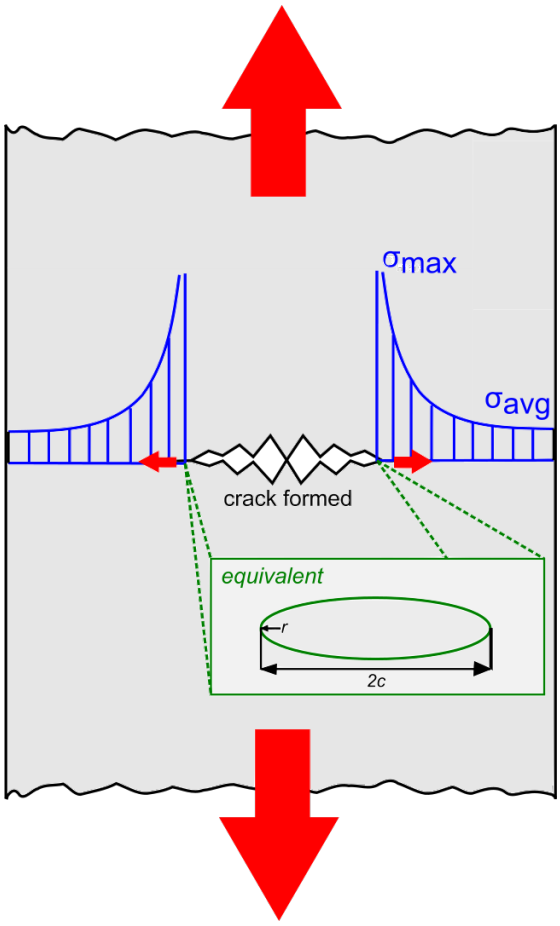

Figure 2.4.2: Illustrating crack development under tensile stress.

of the neighbouring particles.

4. Nucleation (N): Bulk free energy generated from exothermic reaction meets precipitation requirements and C-S-H starts to settle on particle surfaces.

5. Complexation: An ion/molecular complex is formed on the newly created C-S-H molecules, surrounded by gel water molecules.

6. Adsorption: the accumulation of ion/molecules at the interface

It should be noted that these steps are not always sequential but rather interchangeable, e.g. diffusion may also be occurring along with complexation and dissociation. Nucleation and Growth also occur together, and can be seen as one step (N+G). However, we are concerned with determining the limiting

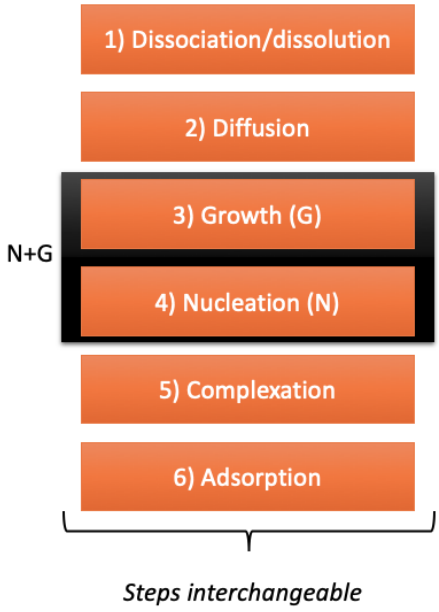

Figure 2.4.3: Interchangeable steps of cement hydration process from Bullard (2011).

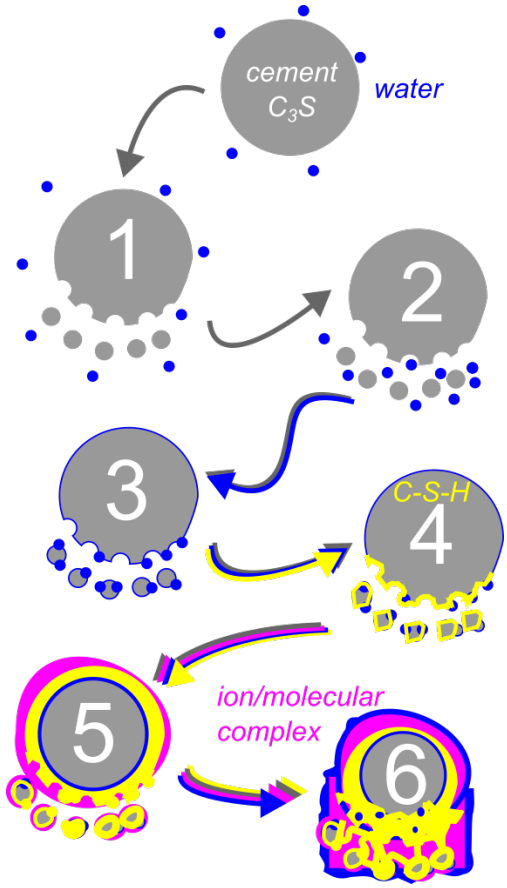

Figure 2.4.4: Illustrating the cement hydrating mechanism steps.

step, in other words the rate-controlling step. The rate of hydration of cement would reach an equilibrium dictated by this limiting step, hence identifying and improving this step is imperative to increase the rate of hydration and produce a denser C-S-H microstructure. Cement/C_3S is also used interchangeably as early hydration of cement is primarily from alite's reactions, and once this early microstructure has hardened, many water and cement particles are locked in place and cannot come in contact. Hence, alite and early hydration is the ideal timeslot to observe the unaffected cementitious system reactions.

$$3CaO.SiO_2 + 3H_2O \rightarrow 3Ca^{2+} + H_2SiO_4^{2+} + 4OH^-,\ \Delta H = -138kJ/mol \quad (8)$$

Equation 8 shows the dissolution of alite and its exothermic energy value. Alite comprises 50-70% of cement, and it's wetting is a catalyst for further dissolution (Parkhurst & Appelo 1999, Hummel et al. 2002). The hydration of cement can be categorized in four phases: 1) initial reaction, 2) period of slow reaction, 3) acceleration period and 4) deceleration period (Gartner et al. 2002). A graph showing the heat flow over these hydration periods is shown in Figure 2.4.5.

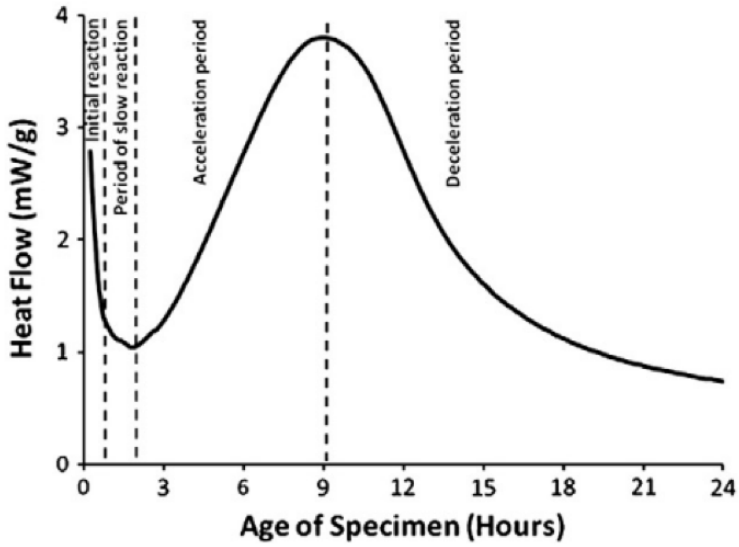

Figure 2.4.5: Heat flow of cement during its early hydration phases. After sharp initial exothermic heat, it slows and accelerates again before slowing in a space of 24 hours. (Bullard et al. 2011).

There are two hypotheses provided for the sudden decrease of heat flow in the the first 2 hours of hydration: the metastable barrier theory proposes that a C-S-H layer forms restricting further access and diffusion of water in to alite particles (Stein & Stevels 2007, Jennings & Pratt 1979). However, no evidence of a continuous C-S-H film have been found via atomic force microscopy (AFM), but rather patches of it (Garrault et al. 2005). Jennings et al (1986) suggested that this C-S-H layer may be semi-permeable filtering out certain ions. Conversely, the slow dissolution step hypothesis states a steady equilibrium

is achieved between C_3S and C-S-H. Barret et al (1980, 1983) suggests the C-S-H is superficially hydroxylated, which increases the concentration of water molecules and hinders further osmosis to allow further dissolution and hence hydration of the covered alite particles. Further experiments that support this hypothesis, where pre-treated alite cause longer induction period and slower decrease in heat flow (Makar & Chan 2008). Other tests show deionized water seeded on alite gave defected surface, while saturated lime water seeding gave a smooth surface, hence higher hydroxyl concentrations seems to allow finer dissolution of cement leading credence to slow barrier hypothesis (Juilland et al. 2010, Damidot et al. 1990). Gartner's recent C-S-H model (2017) shown in Figure 2.4.6 illustrates the surrounding hydroxyls on C-S-H also facilitating the ion/molecular complex adsorption. However, the greater silicon ion dissolution rate relative to alite contradicts the slow dissolution mechanism (Bullard et al. 2011).

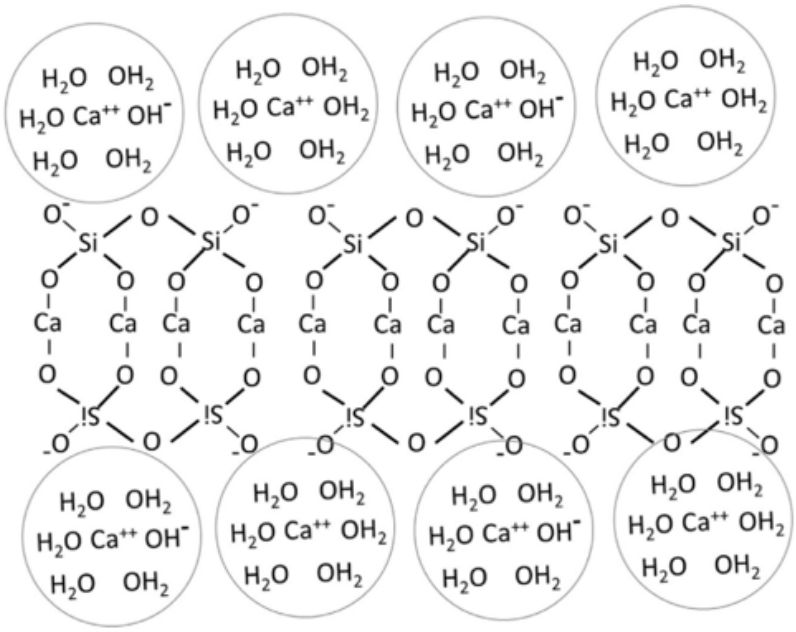

Figure 2.4.6: Gartner's C-S-H model. (Gartner et al. 2017).

From 3 to 9 hours is the accelerating period of C_3S hydration. The N+G

mechanism is the rate controlling step for this period. C-S-H is primarily formed on alite surfaces (Gauffinet et al. 1998, Richardson 2004) and Thomas (2011) found via ^{1}H NMR spectroscopy that C_3S is proportional C-S-H area. It can then be inferred that C-S-H surface area is a good indicator for the rate of hydration. Bullard (2008)and Livingston (2001) proposed the nucleation of C-S-H on C_3S, however experiments show that nucleation occurs in only a short window of a few minutes as the intake of Ca^{2+} and Si^{4+} ions lowers saturation of C-S-H and making growth more energetically favourable than nucleation. Additionally, experiments show that the rate of N+G depend on sufficient growing regions of C-S-H (Wu & Young 1984) and when C-S-H is seeded on alite, there is no induction period (Thomas et al. 2009). Hence, the higher surface area present for C-S-H to grow, the denser the microstructure, but C-S-H prefers growth over further nucleation at least during the accelerating period. Jennings proposed separate low and high packing densities, where over time the lower densities also become highly packed (2000, 2007, 2008).

Thomas (2009) proposed a fractal growth during the acceleration period, where C-S-H nucleates on top of its pre-grown brethren, however this contradicts Bullard's proposition where C-S-H growth is energetically preferred over nucleation (2008). Conversely, Gartner (1997, 2017) proposed 2-dimensional growing silicate chains, where Ca^{2+} and OH^{-} ions are incorporated between the silicate layers, which are approximately 5 nm thick. Hence, it resembles a tobermorite/jennite like structure (Taylor 1992). As the lateral dimensions of C-S-H grow, the strain also increases and inevitably the chains buckle, hence cause divergent, irregular triclinic structure of C-S-H. However, why does the

C-S-H start to regrow after it's initial slow down? Several theories have been presented: the metastable layer from becomes unstable and exposes the unreacted alite, initiating C-S-H N+G. This is unlikely as C-S-H was already forming and it does not explain the acceleration of N+G step. Another theory is that the C-S-H nuclei were already formed, and the acceleration period just illustrate their exponential growth, but this doesn't explain why the growth wouldn't start before nucleation due to discrepant energy requirements. A more likely reason could be that the semi-permeable layer (from the slow dissolution step hypotheses) ruptures due to osmotic pressure. The semi-permeability allows smaller Ca^2 and water ions/molecules, but prevents silicate ions from entry, which pile up against the layer and break it. Conversely, another theory suggests that CH (or calcium hydroxide, portlandite) is rate controlling the hydration. Experiments have shown hydration is retarded in lime water (Odler & Dörr 1979, Brown et al. 1986), and that may be due to increase in production of Ca^{2+} ions, which steal the exothermic energy away from alite dissolution in the portlandite crystallisation process. However, once the portlandite is sufficiently high, nucleation occurs as no more energy is being grabbed by CH any more (de Jong et al. 2007).

The deceleration period can be due to a number of factors: consumption of small alite, leaving only large particles (< 3 μm diameter particles are completely consumed in 10 hours, while 7 μm can take up to 24 hours to consume) (Scrivener et al. 2015). There can also be lack of space or lack of available water for further reactions, which may be locked out of reach due to hydrated cement itself. Peterson and Juenger (2006) discovered that the deceleration period is

dependent on the N+G phase from the acceleration period, which itself was diffuse-controlled. Additionally, Bishnoi & Scrivener (2009) found that particle size distribution can vary this diffusion constant as well. Furthermore, Bullard et al. (2011) and Peterson et al. (2006) state that the available pore space, which could be a limiting factor, is dictated by the volume of water added. Overall, it appears that the limiting factor for the decelerating period cannot be singled out, and may be a combination of lack of space/water/incomplete hydration of larger particles.

2.5 GO's incorporation in cement

Up to now, the mechanisms of cement hydration, the synthesis and structure of GO, and GO's interaction with water have been addressed in sections 2.4.1,2.3.1, and 2.3.2, respectively. Using this knowledge, this particular section now examines existing literature on GO incorporation in cement, providing relevant critique, and detailing key chemical interactions which may have been overlooked in said literature. For instance, it should be noted that most literature does not attempt to explain the nature of GO, specifically the hydronium layer and it's potential role in catalyzing cement hydration, which is the focus of this present study. Hence, it is important to understand prior research into the cement-GO interactions for reference, and critique them based on the extended GOP/cement mechanism information provided above.

In the cement matrix, C-S-H and CH interact with the carboxyl groups in GO, to ensure hydration products are formed among the interlocking GO sheets, while reducing the amount of CH and AFt (and subsequently the for-

mation of ITZ) in the cement paste (Wang, Wang, Yao, Farhan, Zheng & Du 2016, Peyvandi et al. 2013, Li, Lu, Chuah, Li, Liu, Duan & Li 2017, Sharma & Kothiyal 2015*b*). Wang, Wang, Yao, Farhan, Zheng & Du (2016) specifically observed that an increase in GO concentration of cement, going from 0 to 0.05% wt. cement, resulted in a corresponding decrease in calcium hydroxide's (CH or $Ca(OH)_2$) ΔH values (enthalpy change) via TGA/DTG results, from which a decrease in the amount of CH present is inferred (Wang, Wang, Yao, Farhan, Zheng & Du 2016). This was further verified via XPS analysis, where as the GO content was increased, a new product termed $Ca(HCOO)_2$ is being formed (Wang, Wang, Yao, Farhan, Zheng & Du 2016). This is the carboxyl groups linking the free Ca^{2+} ions in the CH solution, a by-product of the cement hydration (see Figure 2.5.1). As CH does not have any mechanical contributions to the hardened cement materials, their bonding with GO platelets allows three dimensional interlinking of different sheets together, occurring at locations of hydration where C-S-H is forming along with CH, ensuring good bondage within the cement matrix and allowing GO to contribute to the strength and crack inhibition of hardened cement paste (Wang, Wang, Yao, Farhan, Zheng & Du 2016). In an earlier research Peyvandi et al. (2013) more so indicated that the carboxyl groups react with C-S-H as well as CH, and their schematic is shown in Figure 2.5.2; however, details were not provided as to how those formulas were ascertained (Peyvandi et al. 2013), but these interfacial bonding reactions have been confirmed in other studies (Sharma & Kothiyal 2015*b*). Furthermore, I believe that measuring the effects of GO reinforced cementitious composites by varying the quantity of carboxyl functional groups in GO (as has been dis-

cussed earlier (Chen et al. 2016)) is essential in furthering our knowledge on these chemical carboxyl-cement matrix interactions and their mechanical results, hence justifying the implementation of XGO in this process.

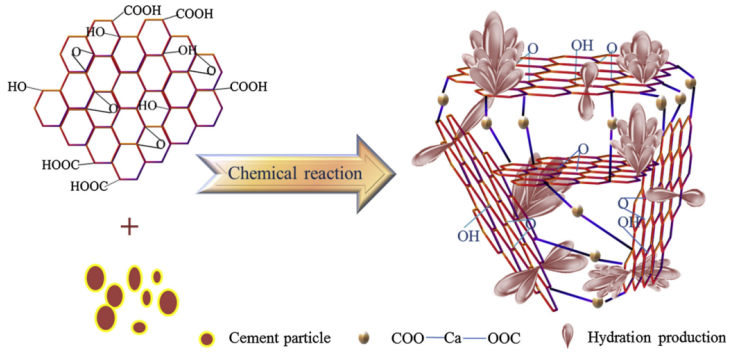

Figure 2.5.1: Functionalized GO and its reactions with cement hydration products. (Wang, Wang, Yao, Farhan, Zheng & Du 2016).

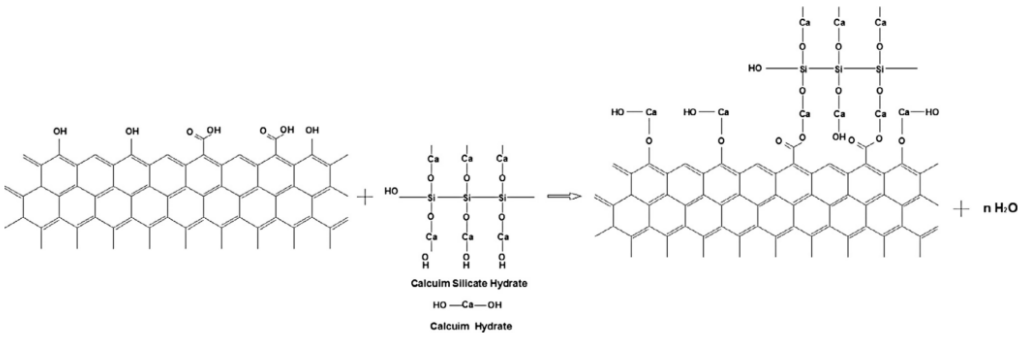

Figure 2.5.2: Chemical reactions between GO carboxyl -COOH groups and hydration products C-S-H and CH. (Peyvandi et al. 2013).

A key issue with prioritizing the carboxyl role in bonding is that there just are not enough carboxyl groups on the GO sheet (due to limited carbon bond availability), and secondly there is no evidence to suggest that these carboxyl bonds will actually strengthen the cementitious matrix by bridging: the amounts of GO in the cement mix is relatively very low, and it is more likely these interlocking GO-CSH-GO structures will only provide localized strength improvements, not throughout the whole structure. Additionally, divalent cations such as Ca^{2+} can cause instant coagulation of GO sheets, further increasing the prob-

ability of small localized interlocks while not densifying the C-S-H cement microstructure (Chowdhury et al. 2015, Szabo et al. 2020). This coagulation effect is explained more in the results section of this thesis.

The oxygen containing hydroxyl and epoxy groups in GO attract water due to their polarity, which contributes to GO's dispersive ability (Medhekar et al. 2010, Gao 2015). As water initiates the cement hydration process, GO provides 'nucleating sites' by collecting the water molecules and encouraging the hydration process to initiate upon itself, serving as a catalyst for hydration (Lin et al. 2016, Lv et al. 2013, Lv, Ting, Liu & Zhou 2014, Li, Lu, Chuah, Li, Liu, Duan & Li 2017). In 2013, via SEM imaging, Lv et al. (2013) discovered that due to the cumulative effects of nucleation, the constraints provided by the additional 3D interlocking of GO, and the hexagonal sheet structure of GO itself, formative C-S-H grows in ordered, flower-like crystals, which ensure better packing and bonding of the cement matrix with the aggregates, hence contributing to the increase in tensile strength of the cement sample (Lv et al. 2013, Qiu et al. 2013, Lv, Liu, Sun, Ma & Zhou 2014). If, however, the amount of GO is increased above 0.04% by wt of cement (bwoc), Lv et al. (2013) found that there were too many nucleating sites to form isolated flower-like crystals, instead the C-S-H compacted together to form polyhedral column like crystals, visually illustrated in Figure 2.5.3 and via SEM imaging in Figure 2.5.4 (Lv et al. 2013). The polyhedral columns better contributed to the compressive strength of concrete, as opposed to the tensile strength improvement from flower like growth; there is better crack propagation redirection and dispelling due to the intricacies of petal and flower like crystals, generating a vast connection of fine

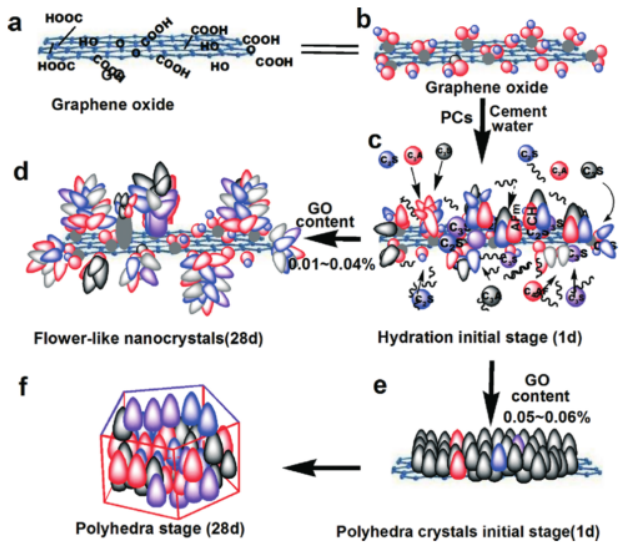

Figure 2.5.3: Regulation and production of hydration crystals arranged due to GO incorporation in concrete. (Lv, Liu, Sun, Ma & Zhou 2014).

holes and cracks that also increase the tortuosity of the nanoreinforced cement matrix, while the bulkier, compact polyhedral structure better withstands compressive strength forces (Lv et al. 2013, Lv, Ting, Liu & Zhou 2014, Lv, Liu, Sun, Ma & Zhou 2014, Qiu et al. 2013, Li, Lu, Chuah, Li, Liu, Duan & Li 2017, Xu et al. 2018). It can be inferred that flexural strength is limited by the tensile abilities rather than the compressive strength of cement mixes: from different test results in separate papers, mostly by Lv et al (Lv et al. 2013, Lv, Ting, Liu & Zhou 2014, Lv, Liu, Sun, Ma & Zhou 2014, Qiu et al. 2013, Li, Lu, Chuah, Li, Liu, Duan & Li 2017), this suggestion seems plausible, with flexural and tensile strengths of GO reinforced concrete steadily increasing until GO reaches 0.03 % bwoc (reaching around 14), after which the compressive strength continues to marginally increase; the results are summarised in Table 2.5.1.

It should also be noted that in a different paper by Lv, Liu, Sun, Ma & Zhou (2014), as the GO concentration was increased from 0 to 0.03% bwoc, porosity decreased at a consistent rate of approximately 8% per 0.01% increase in GO,

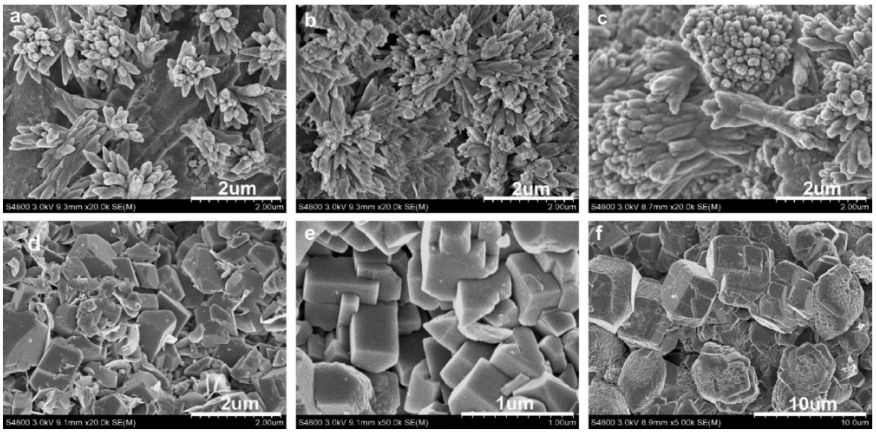

Figure 2.5.4: SEM imaging of the regulation and production of hydration crystals arranged due to (a) 0.01% (b) 0.02% (c) 0.03% (d) 0.04% (e) 0.05% and (f) 0.06% bwoc GO incorporation in concrete (w/c 0.3, 0.2% PC bwoc). (Lv, Liu, Sun, Ma & Zhou 2014).

while from 0.03% to 0.06% GO, rate of reduction in porosity decreased to only 3%; this may lead some credence to the change in formation from flower like crystals to polyhedral columnar growth (Lv, Liu, Sun, Ma & Zhou 2014). Furthermore, early age compressive and flexural strength tests show a more pronounced effect of these crystal growths (see Table 2.5.2), suggesting that GO concentration accelerates hydration for cement paste, reducing the amount of CH and AFt that are produced, but as the crystals continue to grow they will join one another due to confined space of growth, which reduces the impact of the regulatory mechanism of GO somewhat, for both flower like and columnar growth (Skinner et al. 2010, Lv et al. 2013, Lv, Ting, Liu & Zhou 2014, Lv, Liu, Sun, Ma & Zhou 2014). However, attention was not focused on why GO provides the nucleation points in the first place, which we can presume is the effects of the hydronium coating and regeneration. Additionally, SEM testing is qualitative, and correlating the microscopy images with strength performance is viable but not conclusive enough as no chemical reason for the change in C-S-H growth is evident.

Table 2.5.1: Increase rates in 28 day strength for nanoreinforced concrete at different concentrations of added GO.

	Increase in % wrt control of reference					
	(Lv et al. 2013)		(Lv, Ting, Liu & Zhou 2014)		(Lv, Liu, Sun, Ma & Zhou 2014)	
	0.03%	0.06%	0.03%	0.06%	0.03%	0.06%
Tensile Strength	78	35	-	-	-	-
Flexural Strength	60	30	66	42	52	51
Comp. Strength	38	47	46	58	34	38

Table 2.5.2: Increase rates for 3-day and 7-day strength of GO reinforced concrete at different GO% bwoc.

	Increase in % wrt control of reference			
	3-day strength (Lv et al. 2013)		7-day strength (Lv, Ting, Liu & Zhou 2014)	
	0.03%	0.06%	0.03%	0.06%
Tensile Strength	51	24	-	-
Flexural Strength	70	28	76	63
Compressive Strength	45	59	51	72

Qiu et al. (2013) researched the effects of higher oxygen content on the performance of GO in cement/mortar mixes. By keeping graphite flakes submerged in oxidative agent ($KMnO_4$) under progressively long periods (3, 6, 9 and 12 hours) at a set temperature (38°), GO with oxygen contents of approximately 12,18,25 and 29% were obtained (Qiu et al. 2013). It should be noted that the author stated that increasing the oxygen content would make the GO sheets 'thinner': based on previous research discussed in the paper (Gao 2015, Medhekar et al. 2010), O groups exist on basal planes of GO, increasing the sheet thickness; the author may be referring to the increase in hydrophilicity, resulting in better dispersion and lower number of stacked sheets, thus overall reduction of GO agglomerate thickness (Qiu et al. 2013). From their results, incorpo-

ration of 0.02% GO by weight of cement with an oxygen content of 25% resulted in an increase of 97.2% of its tensile strength, 84.5% increase in flexural strength, and 60% increase of its compressive strength compared to control (Qiu et al. 2013). However, as no FTIR or XPS analysis was performed, the particular nature of this oxidation was not ascertained (i.e. how much the oxyl/hydroxyl groups increased, as compared to the carboxyl groups) and the nature of the oxygen bonds that contributed to the increases in the strength. For now, it can be inferred that as the growth of flower like crystals increased with increase in oxygen content, the regulatory mechanism relied primarily on the basal hydroxyl and epoxyl groups (cthe hydronium layer is not employed for this conventional model) (Qiu et al. 2013). Conversely, in a Polish study conducted in 2013, Horszczaruk et al. (2015) found that cement with 3% GO bwoc resulted in no significant difference in hydration (Horszczaruk et al. 2015); since then multitudes of research has found that GO, due to the nucleating sites, significantly accelerates and regulates the cement hydration process (Gong, Asce, Pan, Korayem, Ph, Qiu, Li, Collins, Wang, Duan & Asce 2014, Lv, Liu, Sun, Ma & Zhou 2014, Lin et al. 2016, Wang et al. 2015, Lu et al. 2017, Li, Lu, Chuah, Li, Liu, Duan & Li 2017, Li, Li, Chen, Liu, Duan & Shah 2017, Li, Liu, Li, Li, Sanjayan, Duan & Li 2017, Yang et al. 2017, Chintalapudi & Pannem 2020). A few key differences in Horszczaruk's study are that they used a significantly high amount of GO in their mix (Horszczaruk et al. 2015), which may have cause coagulation of GO sheets from Ca_{2+} bridging and obstructed the hydration growth (GO > 0.08% presents diminishing results via normal mixed incorporation ala (Lv, Liu, Sun, Ma & Zhou 2014)) (Balasubramaniam et al. 2017); they are also

using a higher w/c ratio (0.58) without the addition of plasticizers, as opposed to low w/c ratios with added plasticizers for most present research, hence the seeding effect of GO is diminished. Furthermore, Wang et al. (2015) discovered that as GO amount is increased, exothermic heat produced during hydration decreases; they were not sure as to why and recommended further investigation into the matter; however, it may be due to reduction in produced CH and AFt as observed earlier in (Wang, Wang, Yao, Farhan, Zheng & Du 2016, Lv et al. 2013). It is believed the reduction in produced exothermic heat may also cause a misconstrued approach that the hydration kinetics have not been impacted by GO application. Conversely, Birenboim et al. (2019) measured that the rate of heat flow during hydration for GO-cement has been significantly increased and accelerated wrt control cement only samples. It is believed the reduction in produced exothermic heat may also cause a misinterpretation that the hydration kinetics have not been impacted by GO application.

In a separate study by Lv, Liu, Sun, Ma & Zhou (2014), GO was pre-subjected to varying ultrasonication ('ultrasound') durations of 20, 40 and 60 minutes before being added to the cement mix respectively. As a result, the number of interlocking sheets of GO and the lateral size of these sheets decreased (Lv, Liu, Sun, Ma & Zhou 2014). It should be noted that in this paper the "thickness" of GO may be misleading; the GO sheets themselves are usually 1 nm thick, however the interlinked GO agglomerates end up increasing the width dimensions of the GO particles referred in this paper (Lv, Liu, Sun, Ma & Zhou 2014). The results are summarized and presented in Table 2.5.3. It can be seen that as the lateral size and number of sheets is decreased, the strength of the mixes in-

crease significantly; as the number of sheets per GO agglomerate is decreased, they are better dispersed in the mix and offer increased surface area and more nucleating sites for cement hydration to take place (Lv, Liu, Sun, Ma & Zhou 2014). It can also be observed that at better dispersions and lower number of stacked GO sheets, the 28 day strength improvement between GO concentration of 0.03% and 0.06% bwoc were lower for both flexural and compressive loads respectively, indicating that due to increase in target sites, the beneficial effects of GO on the cement were decreasing due to saturation; this was verified by a recent paper advancing our understanding of hydration, where it was seen that as the time period for hydration progresses, the confined space due to hardening of C-S-H paste indicate how fast hydration will continue, and subsequently the rate of increase of strength and cement matrix continue to increase (Scrivener et al. 2015). Conversely, for larger sheets with more stacking, fewer sites were available for proper hydration nucleation and regulating the growth of C-S-H crystals, resulting in greater disparity between strength results of 0.03% and 0.06% GO (Lv, Liu, Sun, Ma & Zhou 2014). Regardless of this disparity, reducing the sheet stacking (and hence changing classification from graphite oxide to graphene oxide as per Wick et al. (2014)) significantly increases the 28 day strength of the cement mixes, more so for flexural than compressive strength (possibly owing to branching flower like C-S-H crystal growth rather than the thick and straight polyhedral column shapes) (Lv, Liu, Sun, Ma & Zhou 2014). A recent paper by Zhao et al. (2018) proposes a sandwich like structure, where GO sheets have been interspersed into the free floating ion/molecular complex around the Ca-Si-O central C-S-H com-

pound, which makes the most sense as highest amount of water molecules would also be located along the GO sheets. At GO stacked sheet thickness of 3.1 nm, increasing the concentration of GO from 0.03% seemed to have no change in the flexural strength of the whole mix, suggesting saturation level for GO, but mercury intrusion porosimetry (MIP) analysis indicates that the reduction in pore volume continued (14.67% total porosity for 0.03% GO, down to 10.55% for 0.06%GO bwoc), with higher amount of pores with smaller diameters (<100nm, 82% vs 88%), improving crack deflection potential and durability of the cement paste (Lv, Liu, Sun, Ma & Zhou 2014). Hence it can be inferred that better dispersion of thinner GO sheets can increase the strength of nanoreinforced concrete by a greater amount than higher concentrations of thicker sheets. Similarly Sharma & Kothiyal (2015*a*) employed ball milling to reduce the sheet thickness and lateral size of GO sheets, from 900 nm wide and 14 nm thick to 100nm wide and 3nm thick: the results showed a respective 64% to 86% increase in compressive strength for 1% GO bwoc (Sharma & Kothiyal 2015*a*). These results are remarkable for such a high amount of GO in a mix, relative to earlier researches: a possible reasoning for this difference could be the extremely high oxidation ratio of GO for Sharma et al., where EDX analysis show higher O amount than C. However, that may be due to the hydronium oxygen atoms overestimating total O content on the GO sheets. Figure 2.5.5 shows the illustration of this ball-milling process.

From the above research, we see that an increase in the duration of GO ultrasonic/oxidative treatment has uniformly improved the strengths of cement and mortar samples; this goes against the preconceived notions of greater de-

Table 2.5.3: Summary of % increase in mechanical strength wrt control (w/c =0.3, PC = 0.2%) of GO reinforced concrete with varying GO aspect ratios. (Lv, Liu, Sun, Ma & Zhou 2014).

GO sheet size	GO (bwoc)	28-day %-increase in strength wrt control	
		Flexural Strength	Compressive Strength
Length = 430 nm,	0.03%	27	20
thickness = 27.6 nm	0.06%	30	29
Length = 180 nm,	0.03%	43	28
thickness = 9.5 nm	0.06%	39	34
Length = 72 nm,	0.03%	52	34
thickness = 3.1 nm	0.06%	52	38

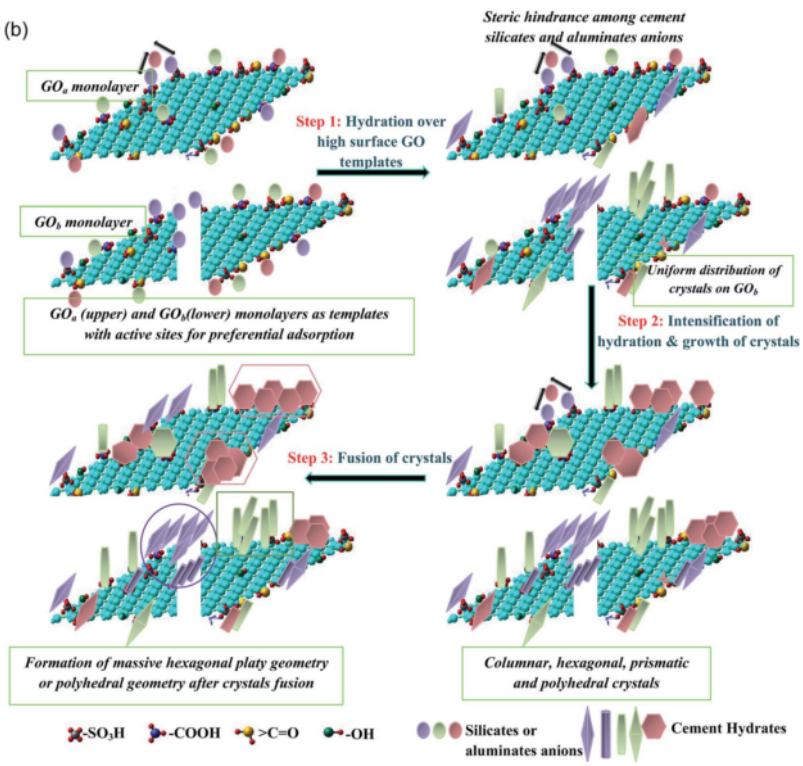

Figure 2.5.5: Effects of thinner and smaller GO sheet on the hydration interlinking of C-S-H cement paste. (Sharma & Kothiyal 2015*a*).

fects and decreased usability of highly oxidized GO (without specific mitigative treatments), which are valid for other fields such as biomedical or electrical engineering (Gao 2015, Posudievsky et al. 2013, Vallés et al. 2015). The nature of GO-cement composite strength and/or durability improvements remain consistent, however the reasoned source of, and the magnitude of these improvements understandably varies throughout other research papers (Babak et al. 2014, Gong, Asce, Pan, Korayem, Ph, Qiu, Li, Collins, Wang, Duan & Asce 2014, Wang, Jiang & Wu 2016, Ahmed Sbia et al. 2015, Chen et al. 2015, Wang et al. 2015, Kang et al. 2017, Li, Li, Chen, Liu, Duan & Shah 2017, Lu & Ouyang 2017, Long et al. 2017, Tong et al. 2016, Lu et al. 2016, Yang et al. 2017, Li, Liu, Li, Li, Sanjayan, Duan & Li 2017, Mokhtar et al. 2017, e Silva et al. 2017). This ensures that GO reinforcement in concrete does not require as stringent measures as in other fields, which increases its economical appeal for large scale use, and focuses our priority on the functionalization degree of GO, a concern shared by GO/epoxy composites as well (Vallés et al. 2015, Zhu et al. 2010, Abdullah & Ansari 2015, Zhang et al. 2016). New novel routes and further functionalization of GO, as well as implementation of rGO have been researched over the years (Zhao et al. 2016, 2017, Murugan et al. 2016, Li et al. 2015, 2016, Liu et al. 2016, Zhou et al. 2017, Qin et al. 2017, Saafi et al. 2014, 2015, Lu et al. 2015, Lv et al. 2016, Bi et al. 2017, Ebrahimizadeh Abrishami & Zahabi 2016, Yan et al. 2016, Lu et al. 2016). Qin et al. (2017) studied the effects of microwave doping GO-cement composite, as opposed to air curing, water curing, and water+microwave curing: it was found that control samples (without GO) reacted negatively to microwave treatment with air curing, although

strength improved for water cured control samples, while with the addition of 1% wt GO (by weight of whole sample) microwave cured samples were the strongest, having >100% compressive strength improvement with respect to air cured control, owing to GO's ability to absorb energy from microwave radiation and contribute positively to the composite (Qin et al. 2017). Qureshi et al. (2019) manufactured GO from a high purity graphite (99.9% carbon) and found synonymous strength and durability improvements

2.5.1 Issues with GO/rGO-cement incorporation and mitigative measures

One issue with the use of GO in cement/mortar is the reduction in workability/fluidity of the mix, as a result of GO's adsorption of water and it's interlinking with the accelerated hydration products, which causes flocculation of cement particles (Wang et al. 2017, Shang et al. 2015). As a mitigative measure Wang et al. (2017) substituted cement with fly ash particles, which proved beneficial with the mortar mixes retaining fluidity; fly ash, being smaller than cement particles (Figure 1.0.2), prevents bunching of cement particles and reduces viscosity while not comprising the strength of the cement/mortar mix significantly (Gong, Chou, Huang & Zhao 2014, Wang et al. 2017). This is illustrated in Figure 2.5.6. Alternatively, Shang et al. (2015) modified silica fume (SF) particles with NH_2 functionalization, followed by electrostatic encapsulation using GO sheets to create graphene oxide coated silica fume particles (GOSF), which were then added to cement mixes (Shang et al. 2015). As expected, GOSF had better fluidity and higher strength than SF only cement mix, however fluidity was still reduced compared to control/plain cement mix; GO only cement was not tested for comparison (Shang et al. 2015). These results

would be later verified by Bai et al. (2018), but it was noted that overdosing silica fume can lead to negative strength performance (Bai et al. 2018). In 2016, Ebrahimizadeh Abrishami & Zahabi (2016) functionalized GO via exposure to ammonia, introducing NH_2 groups to GO:NH_2-GO improved flexural strength by 38.4% relative to control, compared to a 23.4% improvement for pure GO incorporation (Ebrahimizadeh Abrishami & Zahabi 2016). However, these results are for 14 day strength tests, and as such the disparity between pure GO and NH_2-GO maybe owed to the accelerated hydration due to additional functionalization of the graphene oxide; further analytical tests were not performed to verify or ascertain the particular benefits NH_2 groups are providing in the composite microstructure (Ebrahimizadeh Abrishami & Zahabi 2016).

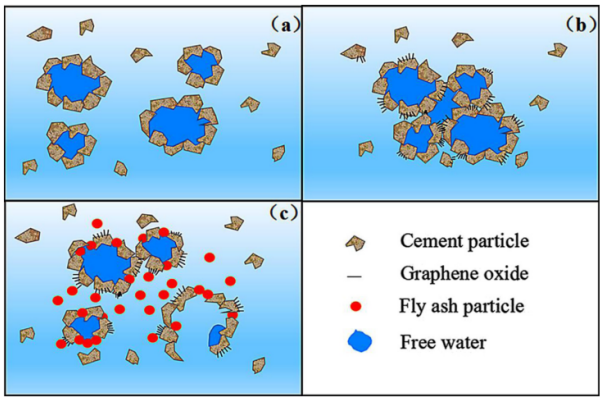

Figure 2.5.6: Flocculation of cement particles due to GO's targeted water adsorption, and role of fly ash as mediator. (Wang et al. 2017).

Converse to preceding studies, Li et al. (2016) discovered that, as opposed to it's excellent dispersion in water, GO has a tendency to quickly agglomerate in saturated CH solution; this raises questions on GO's continued uniform dispersal as cement hydration takes place, gradually introducing CH into the water contained in the cement mix (Li et al. 2016). Li et al. (2016) advised prior shear mixing of GO to break the large agglomerates, in addition to introducing a suf-

ficient amount of silica fume to help disperse the GO into the cement mix before the hydration causes cement flocculation, similar to fly ash's contributions illustrated in Figure 2.5.6 (Li et al. 2016). However, over-dosing silica fume may result in GO not having any open areas to react with the cement, and as such provide no mechanical improvements to the mix at all (Li et al. 2016, Bai et al. 2018). It can be observed that Li et al. (2016) did not use any superplasticizer, unlike earlier studies, which usually assists GO dispersion (as with CNTs) and naturally allows higher workability. Furthermore, these studies strongly indicate the necessity for a standardized nomenclature of GO (Wick et al. 2014), as often varying lengths, C:O ratios and 'thickness' (number of stacked sheets) of GO are used without explanation, while studies have shown how these factors can completely change the performance of the cement mix; rigour and precision is required to ensure future research does not erroneously tread the same mistakes.

Alternatively, an alkaline mix often ends up being a suitable environment for rGO, causing an in-situ reduction of GO itself, as is the case in several geopolymer concrete experiments (Murugan et al. 2016, Yan et al. 2016, Saafi et al. 2015). Unlike regular cement mixes, geopolymer concrete (employing metakaolin and/or fly ash instead of OPC cement) needs the addition of certain chemical activators such as potassium hydroxide (KOH) and/or sodium silicate ($NaNO_3$) to ensure a binding process is initiated; these strong alkaline reactants ensure a pathway for in-situ GO to be reduced to rGO, while continuing to stay dispersed in the mix (Bi et al. 2017, Yan et al. 2016, Saafi et al. 2015). Saafi et al. (2015) recorded a flexural strength increase of 134% with 0.50wt-%

rGO, and 130% for 0.35wt-% (day of measuring not specified, hence it maybe referring to the 7 day strength difference due to accelerated hydration), while noticing a significance increase in the brittleness of the material (Saafi et al. 2015). Yan et al. (2016) discovered that the fracture toughness of rGO geopolymer concrete increased by 61.5%, as well as improvements in flexural strength (45%) for up to 0.3wt-% added rGO, after which performance significantly deteriorated (Yan et al. 2016). There can be multitude of reasons for this variance, as the reduction and amount of alkaline activator (KOH or NaOH) can significantly vary the performance and interactions of fly ash and rGO (Hanjitsuwan et al. 2014). Alternatively, Bi et al. (2017) derived a delivery system by SiO_2 coating CNTs via hydrolysis, improving the flexural strength by 81.2% and compressive strength by 21.2% (Bi et al. 2017), while also increasing it's self-sensing ability for future repair potential without needing external sensors (Bi et al. 2017). Murugan et al. (2016) tested rGO incorporation in OPC cement paste, along with other nanomaterials, and discovered that rGOs resulted in pore refinement, which helped improve the mix's durability, however rGO and GO were not compared (Murugan et al. 2016). Due to better and greater C-S-H crystal growth, cracks can be deflected very early on and do not propagate, also making the matrix much more tortuous and harder for fluid penetration, hence improving durability, simplified in Figure 2.5.7 (Zhao et al. 2017, Du et al. 2016, Pan et al. 2015, Li, Lu, Chuah, Li, Liu, Duan & Li 2017, Mohammed et al. 2015, 2016, Gong, Chou, Huang & Zhao 2014, Gong, Asce, Pan, Korayem, Ph, Qiu, Li, Collins, Wang, Duan & Asce 2014, Lu et al. 2017).

Peyvandi et al. (2013) observed that after 90 days of submersion in a corro-

sive acid, the loss in flexural strength decreased from 70% (control) to only 8% with the addition of 0.2% GO (Peyvandi et al. 2013). Upon addition of 1.5% graphene nanoplatelets (GNP), Du & Pang (2015), Du et al. (2016) found an 80% reduction in water penetration depth, 80% reduction in chloride diffusion, and a 30% reduction in migration coefficient; however the term GNP is used loosely to describe the nanoparticles, as the large lateral size of sheets would only qualify as graphene microplates according to Wick et al. (2014), and additionally the C:O ratio (indicating functionalization) is not known, which previous research have deemed the main factor for accelerating the hydration of cement (Du & Pang 2015, Du et al. 2016). If the GNPs refer to graphitic micro/nano platelets (without any functionalization), greater details as to how these hydrophobic materials were successfully dispersed and their microstructural interactions (apart from being physical filler) need to be provided, given dispersion of non-functionalized graphene nanomaterials has been a primary issue in past research (Gao 2015, Chuah et al. 2014, Parveen et al. 2013, Korayem et al. 2017). A key detriment of hydrophilic GO was illustrated in freeze-thaw cycles resistance test conducted by Tong et al. (2016), where GONPs showed a greater risk of crack failure due to their higher retention of non-evaporable water as a result of their hydrophilicity (Tong et al. 2016). Once again, the confusion in nomenclature can be seen in Liu et al. (2016), where the GO platelets are thinner (approximately 1 nm) relative to GNPs (5 nm). As such it is difficult to ascertain if the compressive strength performance of GONP samples is higher than GNP due to the sheet dimensions, or the functional group parameters (the C:O ratio is not mentioned) (Liu et al. 2016). Liu et al's conclusion is

illuminating, showing the difficulties in setting a w/c ratio: low ratios, while improving the strength benefits greatly, are difficult to maintain due to reduced fluidity from nanomaterials incorporation, while high w/c ratios compromise the nanoreinforcement improvements while also introducing unpredictability due to the hydrophobic/hydrophilic interactions of graphene or GO (Liu et al. 2016). Mokhtar et al. (2017) conversely found a significant reduction in both compressive and flexural strength after >0.03% GONP incorporation, but the thickness of these platelets or C:O ratio is not provided; their cement w/c ratios are also generally low for all samples (0.25-0.30), with no mention of any plasticizer use (Mokhtar et al. 2017). With the addition of GNP, certain measures need to be taken into account: despite the hydrophilicity, because very small amounts of nanoparticles are being added, it is important to successfully disperse them in water via ultrasonication before adding to the cement mix (Korayem et al. 2017), further evidenced in the difference in size distribution shown in Figure 2.5.8.

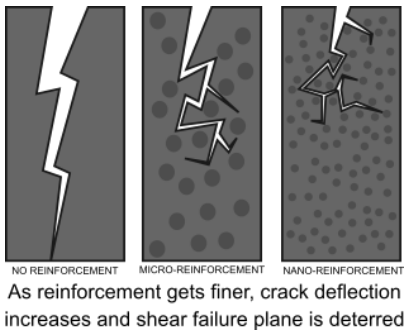

Figure 2.5.7: Illustrating how nano-reinforcement encourages crack deflection and stops crack propagation through structure.

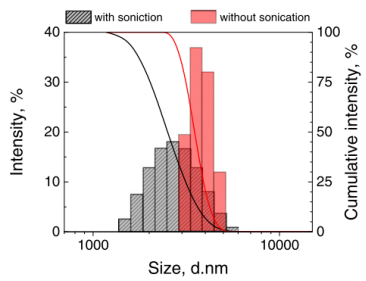

Figure 2.5.8: Difference in size distribution of GNP due to sonication. (Du & Pang 2015).

To summarise, along with not discovering the GO oxygen content or verifying it's sheet dimensions, the majority of research on GO reinforced cement

composites do not have any quantifiable measurements of dispersion (eg via zeta potential or UV-Vis spectroscopy). This leads to a high variability in sample strength/durability results, but also increases the challenge of searching for the underlying causes in such variability, currently estimated to be due to: GO's tenuous interaction with the water in the mix (and prerequisite w/c ratio), as well as the reduction in workability and differences in GO characterization (Korayem et al. 2017, Chuah et al. 2014, Papageorgiou et al. 2017). There is also no guarantee of a good initial dispersion resulting in a good final mix, and further investigation into this hypothesis remains (Korayem et al. 2017, Murugan et al. 2016). The dimensions of GO have also varied widely in research: the thickness of a GO monolayer is approximately 1 nm, however most GO sheets or platelets can have several layers stacked on top of each other, hence the GO platelets/sheets can be 3 to 100 nm thick, and no established nomenclature is currently being employed hence the terms graphene oxide platelets (GOP), graphene nanoplatelets (GnP/GNP) and GO are often used interchangeably; a similar issue persists with the lateral width of the sheets being used, ranging from 100 nm - 1 μm (Gao 2015, Papageorgiou et al. 2017, Wick et al. 2014). Research has shown that thinner GO layers remarkably increase the strength contribution to the samples (Lv, Liu, Sun, Ma & Zhou 2014, Sharma & Kothiyal 2015*b*), while smaller sheets (in terms of lateral width), can provide a greater 3D interlock and surface area for hydration, increasing the samples strength attributes (Sharma & Kothiyal 2015*b*). Alharbi et al. (2018) manufactured a unique edge-only graphene oxide by consistently ball-milling graphite under high temperature. This edge-only graphene oxide was of smaller lateral size

but thicker due to a multi-layer graphene oxide structure, and was dry-mixed into cement before addition of water, showing good strength improvement. Valizadeh Kiamahalleh et al. (2020) further showed rGO improvements were higher with smaller lateral size as well. Once the initial dispersion has taken place, it is important to ensure re-agglomeration does not take place in the alkaline CH saturated cement matrix, while also ensuring that mix fluidity is not severely compromised (Korayem et al. 2017, Parades et al. 2008). GO reinforced cement requires a low water/cement (w/c) ratio to provide any conducive benefits to the mix (Liu et al. 2016), which necessitates the use of superplasticizers. Specifically, polycarboxylate (PC) superplasticizer has shown to be an indispensable part of mixture, providing steric hindrance and temporarily delaying any re-agglomeration (especially for non functionalized graphene nanomaterials), while also increasing the workability of the GO-cement mix, which occurs as a result of the interlocking behaviour of the GO-cement matrix (Zhao et al. 2016, 2017, Lv et al. 2016). Other plasticizers such as polyacrylates or methylcellulose have also shown to help (Lv et al. 2015, Wang, Jiang & Wu 2016, Parveen et al. 2015, Chuah et al. 2018).

The key ingredient of PC superplasticizers are polyethylene oxide (PEO) and polypropylene oxide (PPO) side chains: large polymers with a carboxyl group attached at one end (Parveen et al. 2015). The carboxyl groups are negatively charged and attract (and adsorb) to the cement particles, while the PEO side chains are hydrophilic and spread out as the water molecules fill in the spaces between them. This makes any hydration reaction energetically unfavourable, and is called steric hindrance, delaying the hydration reaction and hence tem-

porarily allowing the cement mix to be less viscous (Neville 2019, Yamada et al. 2000). This hindrance can also be applied to GO and is illustrated in figures 2.5.9 and 2.5.10. However, the bonding shown in Figure 2.5.9 does not make any sense. This mechanism should remain similar for PC-GO incorporation, however not enough research has been done to investigate this claim. Zhao et al. (2016) affirmed that PC incorporation with GO (via stirring at 60 °C followed by ultrasonication) helps retaining fluidity of the mix in saturated CH and KOH solutions, as opposed to agglomeration in no PC inclusion (Zhao et al. 2016).

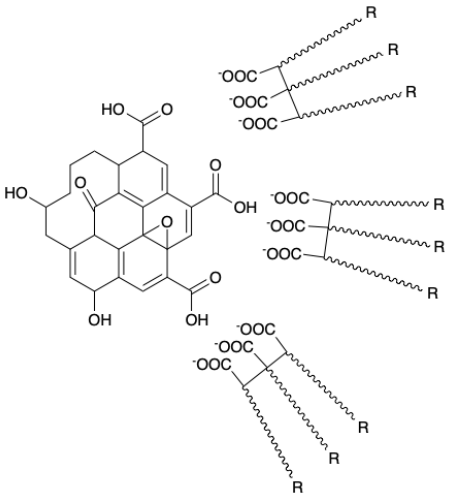

Figure 2.5.9: Large PEO molecules from PC attaching to the GO sheets.

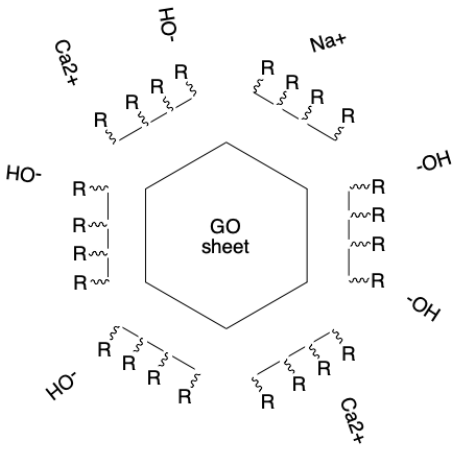

Figure 2.5.10: Large PC molecules providing steric hindrance effect to attached GO sheet.

In a recent paper, Zhao et al. (2017) further tested a fixed PC:GO ratio of 10:1 and report encouraging strength and fluidity improvements, with the ideal combination being 0.022%GO, 0.2%PC (Zhao et al. 2017). Lv et al. (2016) used co-polymerization to develop PC/GON composites, and discovered that PC/GON sheets have smaller sizes (lateral length 20-110 nm, sheet stacked thickness 2-30 nm), hence greater 3D interlock, while the steric effects of PC maintains fluidity of the mix. In 2019, Lv et al intercalated GO with polyacrylic acids (PAA)

and showed a higher monoclinic crystal formation of C-S-H, indicating how the cement hydration was regulated (Lv et al. 2019). This intercalation with the acrylic acid also greatly improved workability, and was further worked on by Wang & Yao (2020) who similar to Lv's earlier work (2016), grafted these PAA on GO and reported improved workability of GO-PAA/cement composites with a very slight reduction in strength, expected as adding the acid groups disrupt water adsorption on GO. Conversely, Zhang et al. (2020) mitigated the rGO dispersibility issue by mixing it extensively with a napthalene water reducer. This facilitated much higher uptake of rGO for strength improvement (2%), but porosity of the hydrated cement material was not significantly finer than control, implying rGO's contribution the cement matrix gel is more physical than chemical (as with GO). Indeed, Jing et al. (2020) highlighted the role of hydroxyl (C-O) groups specifically in attracting water molecules, however not much has been explored as to how that affects GO's performance in cement incorporation (Dimiev et al. 2013).

Recently there have also been attempts of using GO's hydrophilicity to introduce a mix of GO/CNT nanoreinforcement to cement composites (Li et al. 2015, Lu et al. 2015, Zhou et al. 2017). Li et al. introduced GO and SWCNT into a PC suspension, followed by the addition of cement and sand; GO/CNT mix increased the bending strength of mortar significantly more (approximately 72%) than their individual nanoreinforcement (51% from GO, 26% from CNT) (Li et al. 2015). However, they only measured the 7 day strengths, which could indicate accelerated hydration kinetics as opposed to the final 28 day strength improvement; the GO's thickness was not provided, however the sheets seems to

be approximately 80-100 nm in diameter as seen in TEM imaging, and any microstructural SEM/XPS/TGA analysis was not available to examine the bonding microstructure (Li et al. 2015). Lu et al. (2015) also didn't provide any 28 day strength values, instead showing 14 day improvements; they opted not to include PC in the mix, instead illustrating the improved aqueous dispersion of (carboxyl included) fCNT due to GO mixture; however, the characterization provided for GO seem significantly suspect (0.08 nm thickness) (Lu et al. 2015); SEM imaging showed successful linking of CNT and C-S-H paste via GO bridging (Lu et al. 2015). Zhou et al. (2017) discovered that adding PC to a GO/MWCNT suspension in CH solution helps prevent agglomeration; this indicates that, apart from the low w/c ratio, GO with PC inclusion may also result in higher strength improvement due to the steric effects of PEO side chains (Zhou et al. 2017). All three aforementioned studies illustrate that GO's hydrophilicity makes in itself a good disperser for the more hydrophobic materials such as SWCNT or MWCNTS, possibly owing to weak π-π bond interactions (Zhang et al. 2010), and raises questions of whether this behaviour could persist for GNPs, CNFs, rGO, or even non graphene based nanomaterials such as SiO_2, with addition of PC superplasticizer (Meng & Khayat 2016, Zhang et al. 2010, Zhao et al. 2017).

2.6 Summary of Literature Review

The future of nanomaterial incorporation in cement/concrete is very promising, and graphene based nanomaterials have shown to impart tremendous strength and significantly improve durability to cement and mortar mixes. How-

ever, there are several considerations that need to be kept in mind regarding their applications:

1. Graphene is an incredibly strong 2D carbon sheet structure, however non-functionalized derivatives (CNTs, CNFs, MLGs, GNPs) are extremely hydrophobic and have a tendency to agglomerate, necessitating need for chemical/physical treatment such as oxidative functionalization to allow their uniform dispersal in aqueous solution. When dispersal is successful, high strength improvements in the cement/mortar composites have been reported.

2. Despite functionalizing and using admixtures such as MC/Pluronic F-127/PC superplasticizer to improve their dispersion, there is no assurance that after initial dispersion of CNTs/CNFs/GNPs, they will remain dispersed during the cement ingredient mixing and hydration process. Additionally, with the high cost of production and low large scale viability, alternative approach such as using GO is considered more feasible.

3. Due to high oxidative content, different functional groups on GO make it hydrophilic and easily dispersible. It can also be easily and safely made from graphite due to research advances made in the oxidation process (from the dangerous original Brodie and Hummer's methods), with large scale production plausible. GO is seen as an intermediate step towards producing graphene-like pristine rGO, as GO's functional groups render it a bad electric/thermal conductor.

4. While GO is the most versatile and accessible graphene based candidate

for cement nanoreinforcement, even minor changes in its oxidation content, lateral sheet sizes and number of stacked sheets per GO agglomerate can drastically effect their beneficial contributions to the cement nanocomposite. As such, it is strongly advised to establish and strictly follow a general nomenclature. Most researchers interchangeably use terms such as GNP/GO/graphite oxide, while not providing enough characterization information. As a result, their findings cannot be held without ambiguity or be easily replicable, hindering quick progress in the field of concrete nanoreinforcement.

5. While GO has been touted for its hydrophilicity, it has been discovered that, due to the higher water retention of GO reinforced cement, there is a higher risk of crack failure in freeze-thaw conditions. Also, the environment in hydrating cement is slightly alkaline, which causes agglomeration of GO. Particular use of PC superplasticizers is highly recommended as they provide steric hindrance, delaying the agglomeration as cement paste hardens. The dispersion of GO in alkaline solutions, and it's particular interactions with different ratios of PC superplasticizers require additional research, and unlike past experiments, this dispersion needs to be quantified via UV-Vis spectroscopy or XPS analysis among other analytical test methods.

6. Regardless, most nanomaterial use can only be up to a certain limit, as higher quantities cause severe reduction in the workability of cement paste. Once again the use of superplasticizers can mitigate the loss of

fluidity, but only to a certain degree. Higher dosage will result in deteriorating performance due to interference of the hydration process by the nanomaterials..

7. Other unique routes such as: (i) the addition of microparticles (fly ash, silica fume) coated with nanomaterials, (ii) additional modification of GO particles, (iii) *in-situ* reduction of GO in alkali activated fly ash or geopolymer concrete, (iv) using GO as dispersant for functionalized versions of the more hydrophobic nanomaterials (CNT/CNF), or (v) microwave/dry curing of cement have been proposed, with certain success. However, these methods (at the present) do not seem viable in terms of cost and time, and/or large scale productibility.

Ultimately, while strength and/or durability improvements are significant, individual GO performance from past research showed comparable, if not better, strength/durability figures, and with a simpler and more cost-effective pathway for GO production. It is important to keep in mind the logistics and scale of cement/concrete mixing production require perhaps a more pragmatic research approach. GO's complete microstructural interactions are still not sufficiently realized, and may not even be possible without considering the hydronium layer. As cement relies on the availability of water for hydration, the hydronium layer is an ideal location for it to initial hardening, while the potential hydronium regenerative abilities of ultra-oxidized GOs can neutralize hydroxide production (hence increasing saturation limits for C-S-H) and be another source of water molecules for cement hydration, as will be shown in experiments and results.

Chapter 3: Methodology

This chapter of the thesis details all the materials used in the experiments, a brief explanation on which analytical tests were performed, and the methodology for preparation and testing of all nanomaterial and cement samples. The flow of this chapter is illustrated in Figure 3.0.1

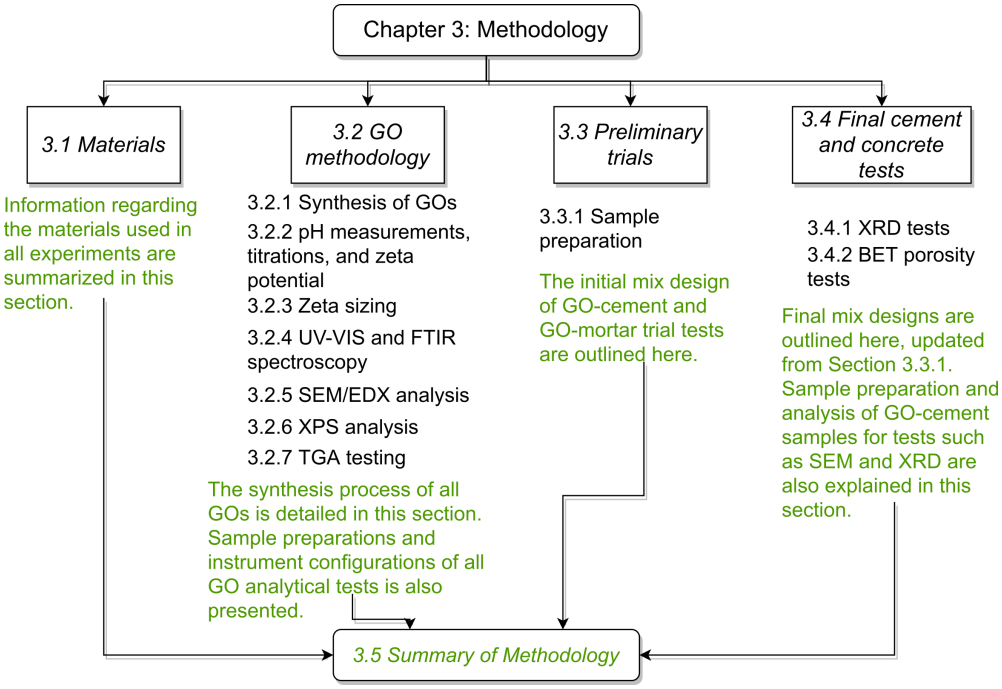

Figure 3.0.1: Flowchart outlining the sections of this chapter.

Figure 3.0.2 illustrates the research framework, relating the methodology to the research objectives. Preliminary trials were performed on mortar samples with and without GO, at varying amounts of plasticizer to find a suitable mix design that can be incorporated with custom tuned GOs. This is in line with research objective 1. Following, preliminary trials, different GOs were synthesized with varying functional groups, and their interactions in water were analyzed, as intended in research objective 2. Once the different GOs are synthesized, they are incorporated in cement and concrete to evaluate their impact on

the hydration of cement, with or without plasticizer treatments. Lastly, based on all the methodology results, an interaction mechanism between GO and cement is proposed, in the Results and Discussions chapter of the thesis. Thus, research objectives 3 and 4 are addressed, respectively.

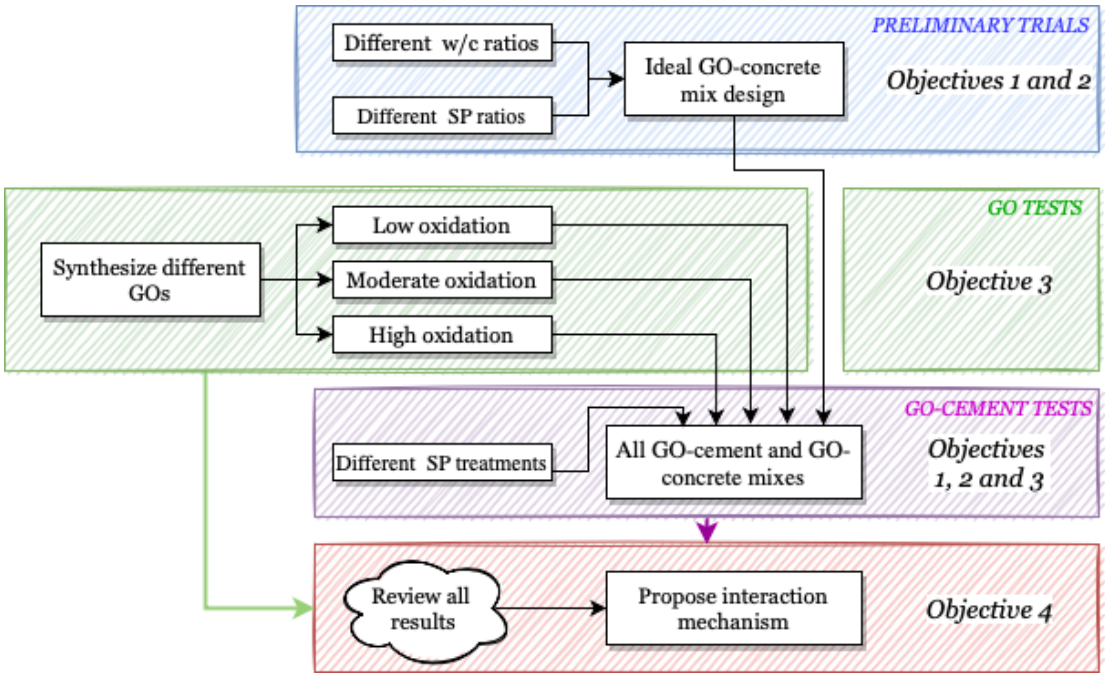

Figure 3.0.2: Research framework for experiments and their relation to the research objectives.

3.1 Materials

Table 3.1.1 shows all the materials used and their grade/company. Table 3.1.2 details the cement type and it's specifications as listed by the manufacturer. It should be noted that the preliminary mortar trials used a different cement composite, which is not included in this table as it was replaced for final experiments. Both the cements used were CEM type II, Portland Cement Composites with additional admixtures. Information on the different cement composites, and reasons for the substitutions can be found in the Methodology Section 3.3.1 and Results Section 4.1.

Table 3.1.1: Materials used in this research.

Material	Formula	Grade	Company	Purpose
		Synthesis of graphene oxides		
Graphite (< 20μm, powder)	C	-	Aldrich	primary material
Sulphuric acid	H_2SO_4	95-97%	Fulltime	intercalant/oxidizer
Phosphoric acid	H_3PO_4	85%	Chemiz	secondary intercalant/oxidizer
Hydrochloric acid	HCl	37%	Fulltime	de-contaminant/washing
Potassium Permanganate	$KMnO_4$	-	Chemiz	Oxidant
Hydrogen Peroxide	H_2O_2	30%	R&M Chemicals	Reaction terminator
		Analytical tests and titration		
Isopropanol alcohol	C_3H_8O	-	R&M Chemicals	organic solvent/analytical preparation
Potassium hydroxide	KOH	-	R&M Chemicals	titration/zeta sizing preparation
		Making cement and concrete		
PCC - Cement - CEM Type II	-		YTL - CASTLE	primary material
fine aggregates	-		(local)	for concrete
coarse aggregates	-		(local)	for concrete
Sika viscocrete 1250NT	-		Sika	polycarboxylate superplasticizer

Table 3.1.2: Specifications of the cement used

Tests		Units	Specifications	Test Results
Type: MS EN 197-1 : 2014 CEM II / B-L 32.5				
Chemical Composition				
Sulphate Content (SO_3)		%	Not more than 3.5	2.1
Chloride (CI)		%	Not more than 0.10	0.01
Physical Properties				
Fineness (According to Blaine)		m^2/kg	-	440
Setting Time : Initial		mins	Not less than 75	155
Soundness		mm	Not more than 10	0.8
Compressive Strength	7 days	MPa	Not less than 16	24
(Mortal Prism)	28 days	MPa	32.5 <X <52.5	35.2

3.2 Graphene oxide methodology

In this thesis, the Hummer's process is modified in three distinct ways, and the three resulting GO variants were compared to one another and to a fourth GO, synthesized using the conventional Hummer's method production (called ordinary GO or OGO). Hydroxyl-rich GO or HGO was obtained by slowly adding water (10mL per 1g of graphite) to the acid-graphite intercalated mixture before introducing $KMnO_4$. This method is based on the research by

Chen et al. (2016), additionally other research has shown that mild dilution of H_2SO_4 can facilitate higher uptake of $KMnO_4$ due to the extra water molecules. Meanwhile, the medium is still sufficiently acidic so as to not cause hydrolysis of the covalent sulfates and interrupt the diffusion of MnO_3^+ between layers of graphite (Li et al. 2020, Dimiev & Tour 2014). Another GO variant is the "Carboxyl-rich" GO (or XGO), as termed by Chen, where after the intercalation and oxidation of GO has occurred, 100 mL of water per 1 g of graphite is added into the mix and the mixture is heated to 95 °C for 15 minutes before termination via H_2O_2. This is a violent thermal reduction process that causes significantly higher vacancies in the GO sheet structure, also reducing their lateral dimensions (Chen et al. 2016). It may also be hypothesized that XGO maintains the C=O double bonds in the sheet, but reduces the C-O single bonds. Lastly, a novel ultra-oxidized GO (LGO) is synthesized, however it's methods of synthesis cannot be disclosed as it is being filed under patent PI2021004199. Hence, LGO synthesis can be added as an addendum to this thesis once the patent is publicly registered.

3.2.1 Synthesis of graphene oxides

Figure 3.2.1 summarizes the chemical oxidation pathways of three of the four graphene oxides (LGO's synthesis is under patent filing).

For ordinary graphene oxide (OGO), 13.4 mL 85% phosphoric acid (H_3PO_4) was added to 120 mL of 95-97% concentrated sulphuric acid (H_2SO_4) (9:1 ratio) and the mixture was allowed to cool to 20 °C. 1 g of graphite powder (<20 μm Sigma-Aldrich) was added and the mixture was stirred at 300 rpm for 10 minutes to allow intercalation. After 10 minutes, 6 g of solid potassium per-

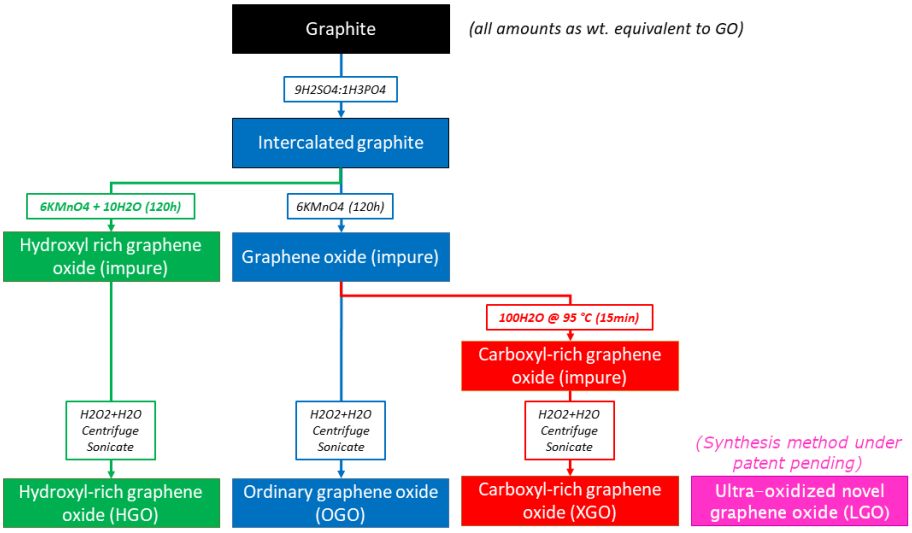

Figure 3.2.1: Summarizing the different oxidation processes for HGO, OGO and XGO. Please note the synthesis of LGO is not being disclosed due to patent filing.

manganate ($KMnO_4$, 6 wt. equivalent) was added slowly to the intercalated graphite mix over a period of 5 minutes. During this period, the mix warmed to approximately 35 °C, after which it was kept under constant stirring in a fume hood at a room temperature of 20 °C for 120 hours. The temperature was not increased as per Chen et al. findings (2016) where keeping a low temperature typically increases the yield of GO. After 120 hours, 30% hydrogen peroxide (H_2O_2) was added dropwise alternating with 135 mL of ice cubes to keep the temperature below 60 °C. The quantity of H_2O_2 varied for each GO type: OGO required 5 mL of H_2O_2 until the colour turned pale yellow and temperature rise subsided, indicating oxidation reaction termination (Figure 3.2.2).

The mix was allowed to cool to room temperature and decontamination process was initiated, first by centrifuging the mix at 7500 rpm for 30 minutes, after which the supernatant was discarded. The filtrate was washed with 1 M HCl and centrifuged at 7500 rpm for thirty minutes (eppendorf 5810R),

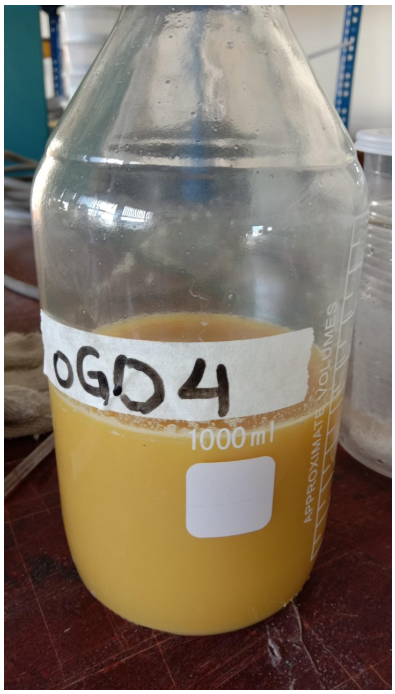

Figure 3.2.2: Pale yellow OGO-acid mix immediately after termination, prior to washing and centrifuging.

after which the filtrate was extracted and subjected to 2 more rounds of washing and centrifugation with 1 M HCl. After 3 repeats, the filtrate was washed with distilled water and centrifuged (7500 rpm) for 30 minutes, and this process was repeated for 7 times. After final centrifugation, the filtrate was added to 100 mL distilled water and stirred manually until all visible particles were mixed evenly. It was then placed in an ultrasonicating bath and sonicated for 20 minutes (Elma Transsonic 35 kHz, 40% intensity). Finally, distilled water was added until total volume reached 500 mL. The initial filtrate was brown in colour and darkened with successive washing. For hydroxyl graphene oxide (HGO), the oxidative treatment is similar to OGO, except that after the intercalation period (10 minutes of stirring of graphite in 9:1 H_2SO_4:H_3PO_4 acid mix), 10 mL of distilled water is added slowly to the mix followed by $KMnO_4$ (6 wt. equivalent) and the remaining procedure is identical to GO oxidation. For ter-

mination, it is found only 3.5 mL of H_2O_2 was required for the mix to turn pale yellow, and subsequent addition of H_2O_2 resulted in no colour change or rise in temperature. The decontamination and sonication of HGO was followed similar to OGO. It was noted that HGO was much lighter brown in colour than OGO (see Figure 3.2.3), however the colour darkened notably over a period of 1-2 weeks, as did all the GO variants.

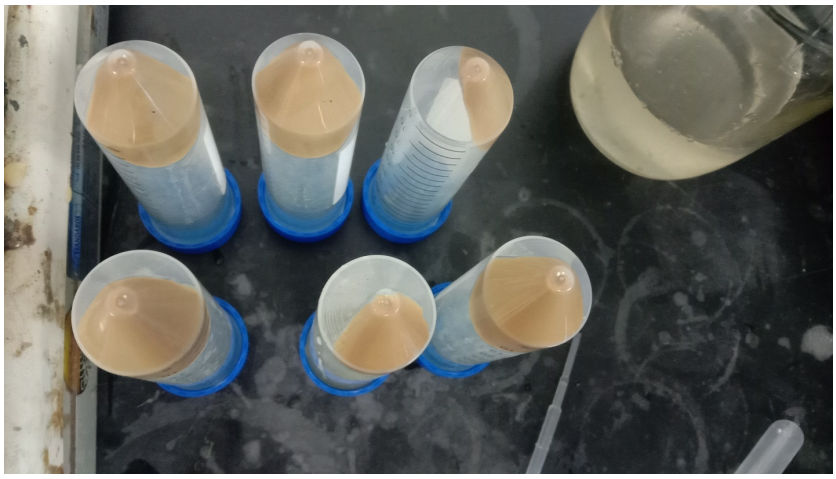

Figure 3.2.3: Appearance of light brown HGO after washing and centrifugation.

For carboxyl graphene oxide (XGO), the intercalation and oxidation processes are similar to OGO, however after 120 hours and prior to termination, 100 ml of water was slowly added and the GO mix was heated to 95 °C and maintained at that temperature for 15 minutes. Visually, the mix changed colour from deep purple to dark mahogany brown, with pale yellow frothing during the heat treatment. After 15 minutes the mix was allowed to cool and any addition of H_2O_2 did not change colour or cause rise temperature of the mix. The decontamination and sonication procedures were identical to OGO, but no colour change was observed (consistently dark mahogany). The GO suspension darkened over weeks. Figure 3.2.4 shows XGO before and after decontamination and sonication process.

Figure 3.2.4: XGO's mahogany appearance (a) immediately after termination and (b) after full decontamination and sonication.

The LGO suspension is also muddy brown, but considerably more viscous than OGO (Figure 3.2.5). Significantly higher yield was obtained for LGO as shown in Figure 3.2.6 where both OGO and LGO suspensions were allowed to settle over several weeks.

Figure 3.2.5: Muddy brown appearance of LGO suspension.

To measure the final concentration of each GO variant, 3 weighed petri dishes were filled with approximately 15-25 mL of the respective GO variant, and their initial weights were recorded. The petri dishes were placed in a furnace at 60 °C for 24 hours, after which their final dry weights were recorded. The remaining mass for each respective volume was calculated and averaged to find the concentration of each HGO, OGO, XGO and LGO suspensions. The colour difference of all four GOs is shown in Figure 3.2.7.

Figure 3.2.6: Yield difference of OGO and LGO.

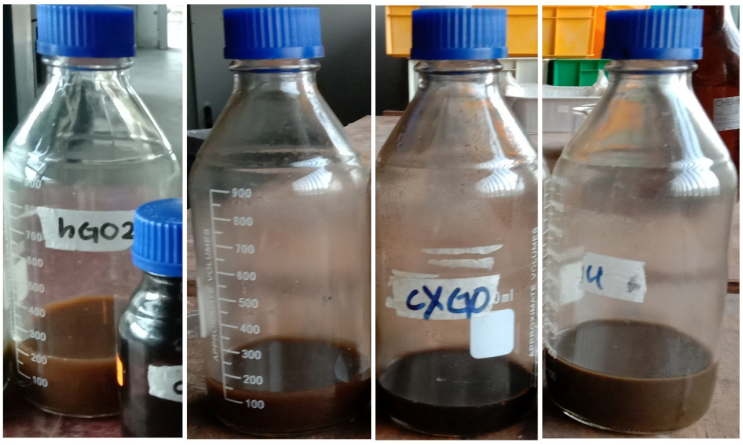

Figure 3.2.7: Suspensions of (left to right) HGO, OGO, XGO and LGO.

3.2.2 pH measurements, titrations, and zeta potential

50 mL of 1.5 mg/mL concentrations of each GO variant were added in a 250 mL beaker and subjected to magnetic stirring at 200 rpm. A Mettler-Toledo FiveEasy pH meter was calibrated and used to measure any pH changes. Nitrogen gas was bubbled through the stirring liquid at a constant rate using a centrifuge tip attached to the end of the gas tube. The beaker was sealed with a parafilm wrapping, while holes were made for the pH meter, the gas tube, and an inlet/outlet tube for addition of base/acid and/or extraction of mix for zeta measurements. This setup is shown in Figure 3.2.8. To facilitate liquid

extraction for zeta, it was not feasible to keep the beaker/container completely airtight, however this setup does allow CO_2 expulsion during titration while keeping the environment free from any unwanted contamination.

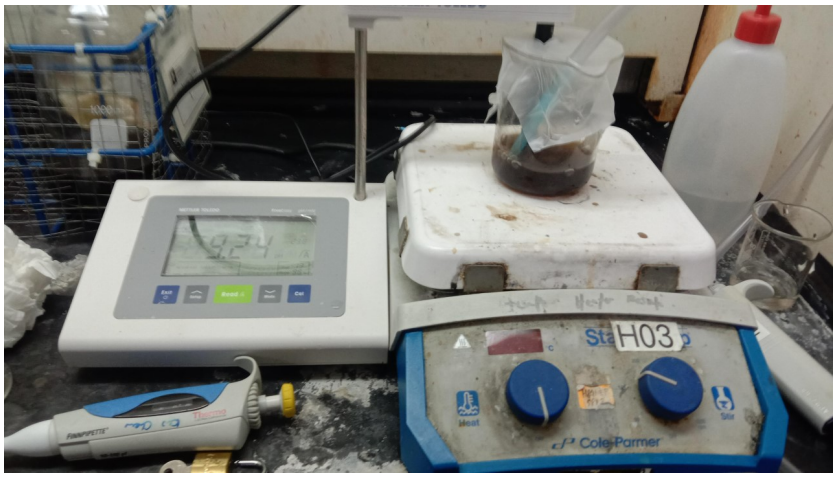

Figure 3.2.8: Setup for titrations of all GOs.

1 M potassium hydroxide (KOH) was prepared by dissolving solid KOH in distilled water and diluting to the appropriate volume. The alkali was added to the mix by pipetting 50 μL, each time allowing the pH to stabilize before taking measurements and extracting 0.50 mL using a dropper for zeta potential measurements. To better observe the regenerative ability of the GO-hydronium layer, two separate pH readings were recorded, one after 10 seconds of reading stabilization, another after 20 seconds. The pH reading is considered stable when after 10 or 20 seconds, the pH stays within ±0.01 respectively. As expected, if 20 seconds are allowed between base additions the pH continues to decrease for ultra-oxidized GOs (HGO and LGO), and this is explained in great detail in the discussions section of this paper.

Once the pH measurements reach 9 or subsequent additions of each alkali cause little change in pH, the mixes were subjected to back-titration by pipetting 50 μL of 1 M HCl and allowing the pH to stabilize for 10 seconds before

recording. The addition of acid was stopped when pH level reaches close to initial pH of the GO suspensions. For zeta potential measurements, 0.5 mL of each liquid was pipetted into a DTS1070 folded capillary cell which was inserted into a Malvern-Panalytical zetasizer nanoZS machine. The cell was equilibrated for 30 seconds at 25 °C and 3 runs were taken, each for at least 10 measurements (more measurements are taken automatically by the zetasizer if needed). The average zeta potential for each of 3 runs is obtained from the zetasizer software, and the two nearest zeta potentials are given as average results. The Smoluchowski equation was used for calculation of zeta potential.

3.2.3 Zeta sizing

Initially, size fractionation via extensive filtration and centrifuging was performed, following Szabo's methodology (Szabo et al. 2020). However, to equilibrate the samples required the addition of hydroxide ions, which cause instant coagulation of ultra-oxidized GOs (described in section 4.2.2). As size estimation of GO in suspension was required to investigate it's interaction during cement hydration, once the pH of all GO variants (4mg/mL) were equilibrated to 10 (once again, accounting for higher neutralization due to ultra-oxidation), the suspensions were subjected to pulse sonication for 5 minutes (Cole Parmer ultrasonic processor, 17% amplitude, 30 seconds on, 30 seconds off) to disperse coagulation, and instantly tested via a Malvern Panalytical Zetasizer NanoZS. Calibration time was set to 30 seconds (as suspensions would coagulate again), 3 runs were taken and final results ewre taken as averages.

3.2.4 Ultra-violet/Visible (UV-VIS) and Fourier-Transform Infrared (FTIR) Spectroscopy

Both UV-VIS and FTIR analysis are spectra absorption tests that subject samples to electromagnetic waves (at visible light, ultraviolet or infrared wavelengths), and measure how much of those transmitted rays were absorbed (UV-VIS) or reflected (FTIR) by the sample. Both procedures follow the Beer-Lambert law, which states that absorption of light by the sample is proportional to the concentration of the attenuating species in the sample and/or the thickness of the sample (if solids are used in FTIR) (Beer 1852). This is summed in Equation 9 below:

$$T = \frac{\Phi_e^t}{\Phi_e^i} = e^{-\tau} = 10^{-A} \tag{9}$$

where for a transmittance T, optical depth τ and absorbance A,

Φ_e^t is the light transmitted by the sample,

Φ_e^i is the light received by the sample.

This can be weighted and added if multiple attenuating species exist in the sample, provided the sample is undisturbed and clean (Beer 1852)

Both FTIR and UV-VIS are often used for determining which functional bonds exist in a organic solutions, as opposed to XRD which can only work for crystalline solids in most cases. UV-VIS can also determine the presence of metal ions, as it uses visible light or ultraviolet wavelengths to excite electrons in the sample solution. At certain wavelengths, these electrons will absorb enough energy from the passing light to jump between molecular orbitals.

Four of these transitions can be recorded by UV-VIS, in order of energy required to transition, σ–σ^* > n–σ^* > π–π^* > n–π^*. For the scope of this research, UV-VIS is being used to determine quantitatively the concentration of nanoparticles (with or without the addition of plasticizers) and to correlate any change, if at all, in the dispersal of nanoparticles in water and an alkaline environment (found in cement hydration and curing pools) over 28 days.

FTIR spectroscopy works differently from UV-VIS, where instead of firing a monochromatic beam that sequentially goes through a range of preselected wavelengths, infrared light with multiple wavelengths is transmitted to the sample. Different functional bonds that exist in the sample will 'stretch' and 'wag' at certain resonating frequencies of the infrared light (the behaviour is also called rovibrionic movements). Once these these frequencies align, the IR waves will be respectively absorbed. Hence following Beer-Lambert's law, the frequencies that were not absorbed can be plotted with respect to a range of wavelengths. The higher wavelengths (lower frequency) region of 4000-1800 cm^{-1} can then be used to determine which functional groups are present, and the higher frequencies can fine tune the identification process (similar to a fingerprint identification) using matching existing spectra data. This is shown in Figure 3.2.9.

For UV-VIS, all GO samples were diluted to a concentration of 0.05 mg/mL with distilled water. PerkinElmer Lambda 35 UV-VIS for used to conduct the experiments, with wavelengths from 100 nm to 900 nm at a rate of 450 nm/min, slit size 2 nm and UV-Visible lamp change at 380 nm.

In FTIR a range of materials: for aqueous solvents, 1 mg/mL concentrations

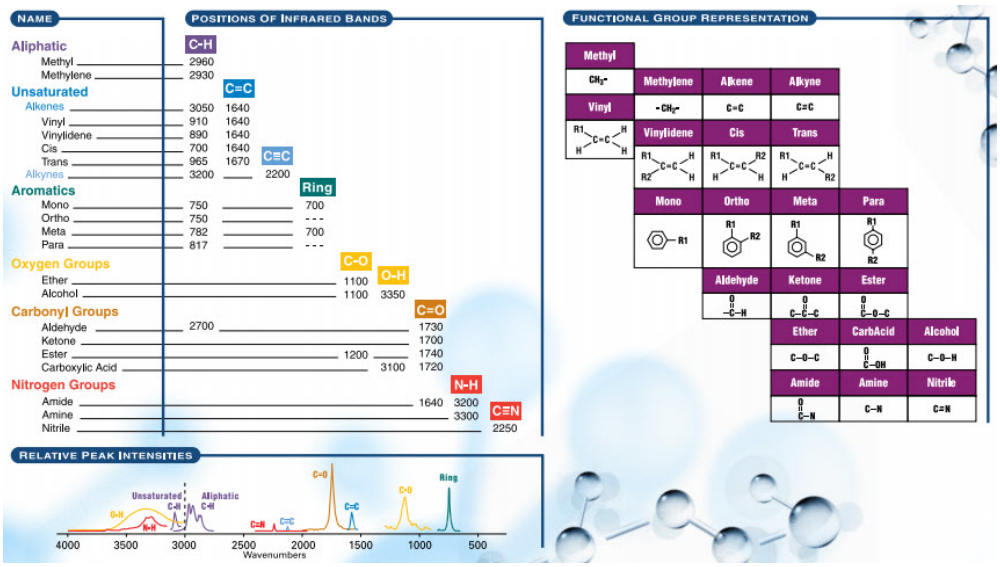

Figure 3.2.9: Range classification for IR/FTIR absorption spectra. Source: Thermo-Fisher (https://tinyurl.com/ftirtTF)

of all GO (in distilled water) were used. For organic solvents, 300 μL of each 1 mg/mL GO was pipetted into 2.5 mL isopropanol alcohol respectively, and both solvent variants were bath sonicated for 5 minutes (40% intensity at 35 kHz) before testing. For oven dried, all GO samples were heated to 65 °C for 48 hours prior to testing. Lastly, GO samples were freeze dried for 72 hours and stored in a desiccator with silica gel until FTIR was conducted. Perkin Elmer Frontier was used and 10 scans from 4000 to 400 cm^{-1} wavelength were performed for HGO, OGO, XGO and LGO for each organic solvent, inorganic solvent, oven dried and freeze-dried samples respectively, and the spectra were base corrected using the Perkin Elmer Spectrum 10 software. The graphs were normalized (maximum and minimum transmission set to a scale of 0 to 1 and transmission % ratioed appropriately) to better compare peaks between the GO nanomaterials. For cement samples (of various degrees of hydration), the freeze-dried powder was tested for FTIR at 400 cm^{-1} to 4000 cm^{-1}, with 4 runs for each sample. The graphs were also normalized for testing to better compare

peak shift between hydration. The cement preparation procedure is explained in Section 3.4.

3.2.5 Scanning Electron Microscopy/Energy Dispersive X-ray Analysis (SEM/EDX)

Scanning Electron Microscopy (SEM) is a qualitative analysis where electrons are fired from a gun/emitter and accelerated towards any surface on the sample. The electron beam is controlled using magnets and scanning coils which allow proper focusing of the beams on a sample. If the energy of the electrons is sufficient they will replace the electrons on the sample themselves, while the replaced electrons will be detected using electron detectors located close to the samples. Deep, rough surfaces will not be able to reflect a smooth stream of electrons, and hence will not be captured by the detector, while smooth surfaces will be shown as white (or rather grayscale, depending on amount of reflected electrons), and hence an image can be drawn which accurately captures 3D surface topography to an extent. This process is outlined in Figure 3.2.10.

Aluminium SEM stubs were used, with double sided carbon tape as an adhesive, on which the freeze-dried cement and/or nanomaterial powder were placed carefully using forceps and/or spatula. The samples were then platinum coated to enhance reflectivity and improve image capture, and mounted on the SEM stub holders, in high vacuum environment.

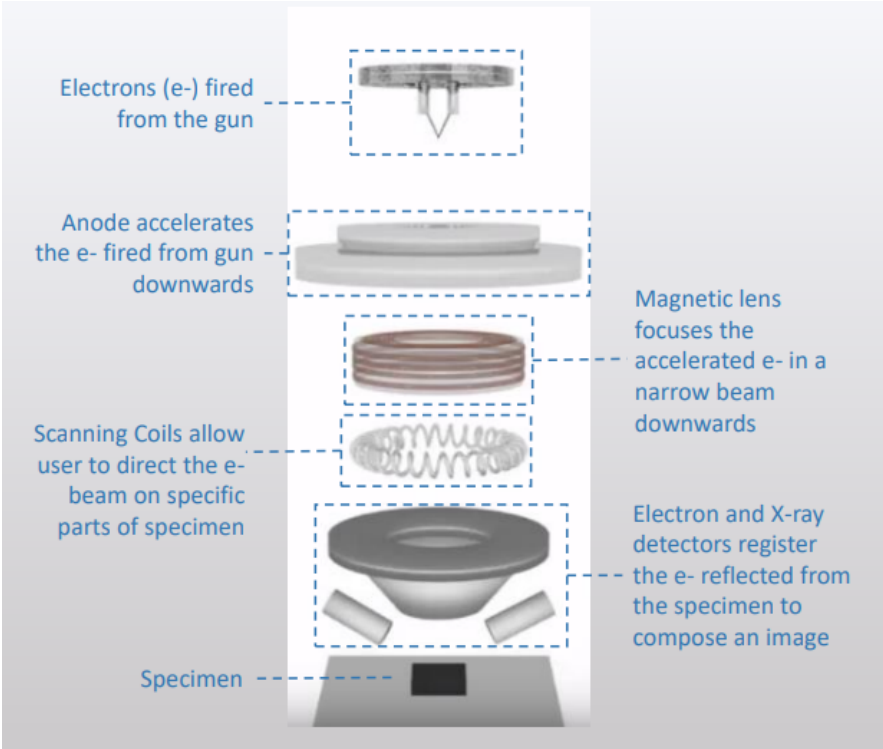

Figure 3.2.10: Simplified explanation of the SEM machine operation.

3.2.6 X-Ray Photoelectron Spectroscopy (XPS)

The GO samples were outsourced to Malaysian Institute of Microelectronic Systems (MIMOS) for far and near spectra scan (C1s and O1s, including peak fitting analysis). The Quantera II, ULVAC-PHI XPS was used with an Al Ka X ray source (25 W, voltage source 15 kV) with beam size 100 μm at tilt angle of 45°. Pass energy was kept at 112 eV, with a dwell time of 20 ms per step. Sample preparation was identical to FTIR testing.

3.2.7 Thermogravimetric Analysis (TGA)

The Perkin Elmer STA6000 was used to conduct TGA tests on GO samples oven dried at 65 °C for 48 hours. The temperature range was set from 30 °C to 950 °C at a rate of 10 °C/min, with inert N_2 gas chosen to purge the sample at flow rate 20 mg/mL.

3.3 Preliminary trials - Mortar cube preparation

3.3.1 Sample Preparation

The graphene oxide used in all preliminary trials is OGO, and 50 mm x 50 mm x 50 mm cube samples were prepared. Mortar samples were chosen as opposed to cement or concrete to limit amount of nanomaterial used for economical reasons. However, there does not exist any mix design manual for mortar as opposed to the BS standard for concrete design. As such, trial and error experiments had to be undertaken until a suitable water/cement/aggregate ratio was found capable for testing. Initially the ASTM C1329 Standards was used to establish a mix design of 1 : 2.75 cement to fine aggregate ratio, by adding water until a suitable ratio was established (in this case, approximately 0.5). Finally a 0.5 : 1 : 3 ratio of water : cement: fine aggregates was reached which provided enough workability at the expense of some compressive strength and GO's contribution.

It should be noted that conditions for mix design can vary wildly based on ambient temperatures and humidity (the climate of Malaysia versus Great Britain, for instance), the shape and properties of aggregates used, vibration and mixing style, etc. However, in most mix designs the water in water/cement ratio refers to the free-water, or alternatively the water that is available for cement to react with and not adsorbed by any other constituents of the mix (Teychenné et al. 1975). This is relevant as the fine aggregates for the experiments were locally sourced, porous and extremely dry (contrary to the presumed saturated surface dry condition for most mix design), hence would 'steal' the wa-

ter added in the mix for their own moisture absorption. Naturally this resulted in being unable to use a sufficiently low w/c ratio to exaggerate the strengths of the cube samples (as plasticizer use was being controlled according to the amount of nanomaterials added). In addition to the moisture condition of the aggregate, the particle size distribution showed a greater amount of fines (10% or higher < 150 μm diameter), which results in increased surface area of the sample which subsequently also increases the demand for cement, water and ultimately GO nanomaterials to effectively reinforce the expanded cement matrix. This is shown in Figure 3.3.1, where early trials gave failed mixes.

Figure 3.3.1: Failed mortar trial mixes.

The particle size distribution for the fine aggregates is tabulated and graphed in Figure 3.3.3 (over 3 trial runs). Further characteristics of fine aggregates were obtained using the Standard Proctor Test (ASTM D854): the fineness modulus was 2.35, Bulk Density 1350 kg/m^3, Specific Gravity 2.6, and the mortar mix density was found to be approximately 2250 kg/m^3. Figure 3.3.2 shows how the aggregate was placed under various conditions (fully soaked, saturated surface dry or SSD and oven dry or OD) to obtain these characteristics.

Figure 3.3.2: Testing aggregate for moisture conditions.

Sieve type			agg.	cum.	%retained	%passing
2	mm	2000	150	0	0%	100%
1.18		1180	94	94	16%	84%
600		600	162	256	45%	55%
425		425	166	422	74%	26%
300		300	26	448	78%	22%
212	µm	212	58	506	89%	11%
150		150	20	526	92%	8%
75		75	26	552	97%	3%
63		63	3	555	97%	3%
pan		10	16	571	100%	0%
			721	571		

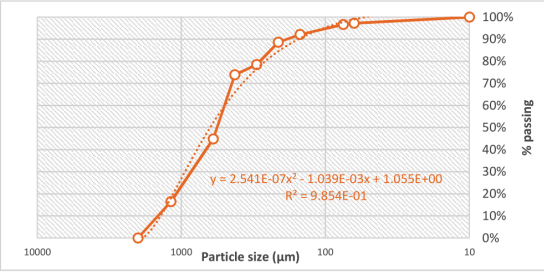

Sieve type			agg.	cum.	%retained	%passing
2	mm	2000	151	0	0%	100%
1.18		1180	91	91	16%	84%
600		600	150	241	42%	58%
425		425	173	414	72%	28%
300		300	26	440	77%	23%
212	µm	212	61	501	87%	13%
150		150	22	523	91%	9%
75		75	29	552	96%	4%
63		63	3	555	97%	3%
pan		10	19	574	100%	0%
			725	574		

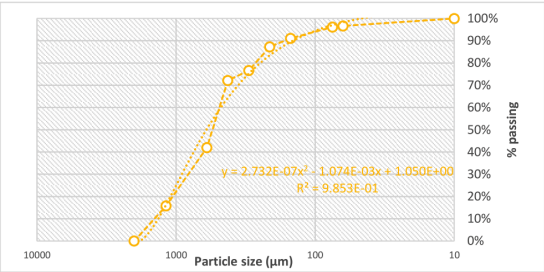

Sieve type			agg.	cum.	%retained	%passing
2	mm	2000	134	0	0%	100%
1.18		1180	93	93	16%	84%
600		600	172	265	45%	55%
425		425	183	448	76%	24%
300		300	28	476	81%	19%
212	µm	212	58	534	90%	10%
150		150	19	553	94%	6%
75		75	24	577	98%	2%
63		63	0	577	98%	2%
pan		10	14	591	100%	0%
			725	591		

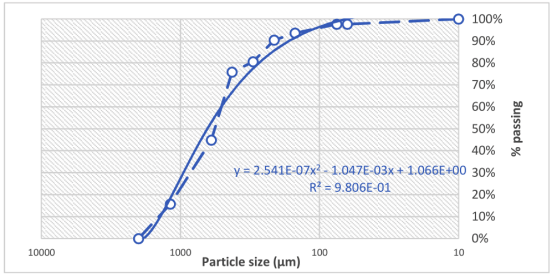

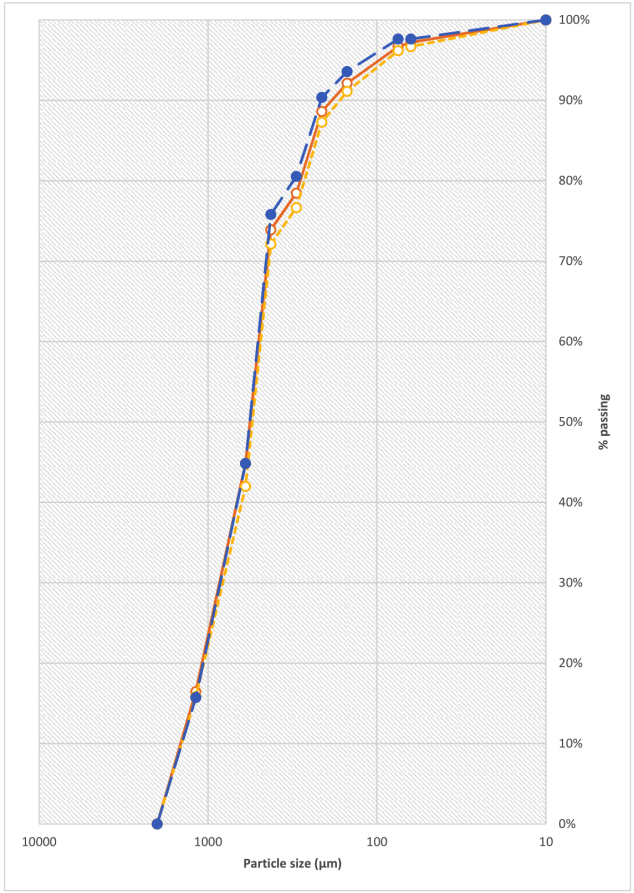

Figure 3.3.3: Particle size distribution for fine aggregates.

Panda Green PCC (Portland Composite Cement) was used for all mortar samples in the preliminary tests. It complies to MS EN 197-1:2014 CEM II/B-M(S-L) 32.5R requirements, however its ingredients are not listed other than 'portland cement clinker with other cementitious materials'. The cement and fine aggregates were dry mixed in a pre-wetted stainless steel container for a couple of minutes to ensure uniform dispersal. A Hobart mixer was used for mixing mortar. Slowly, over a period of approximately 5 minutes, water with diluted GO or GO-p solution was poured using a dropper bottle. Once all the ingredients had been mixed in, the sludge was transferred to pre-oiled iron moulds where it was poured in 3 successive layers, each with 30 seconds of vibrating time on the vibrating table, until the moulds were completely filled. They were left overnight in the moulds, after which the samples were demoulded and placed in a water container for 28 days. 5 cube samples were prepared for each different mix. The process is illustrated in Figure 3.3.4.

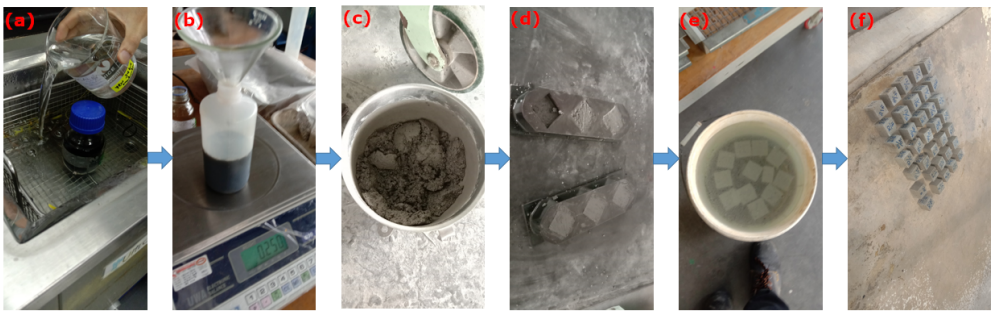

Figure 3.3.4: Illustration of the mortar sample preparation for compressive strength tests. After (a) GO-superplasticizer-water sonication, the (b) mix was poured and (c) mixed with the cement/fine aggregates. After mortar was mixed, it was (d) poured into mould and vibrated, then (e) demoulded after 24 hours and water cured until (f) 28 days.

3.4 Final mix cement and concrete tests

PCC cement (YTL Castle, CEM II/B-L 32.5N, certified MS EN 197-1:2014) was used in all final cement and concrete samples. CEM Type II cement was chosen as it is more environmentally friendly than Ordinary Portland Cement (OPC), and is also the most widely used type of cement in Malaysia. All cement was sourced from a single bag of YTL Castle, to ensure the same cement composition was analyzed and tested for strength, durability, and microstructure. Fine and coarse aggregates were locally sourced from the Negeri-Sembilan quarry (river sand), and their size distribution was measured via sieve analysis and is shown in Figure 3.4.1 and tabulated in Table 3.4.1.

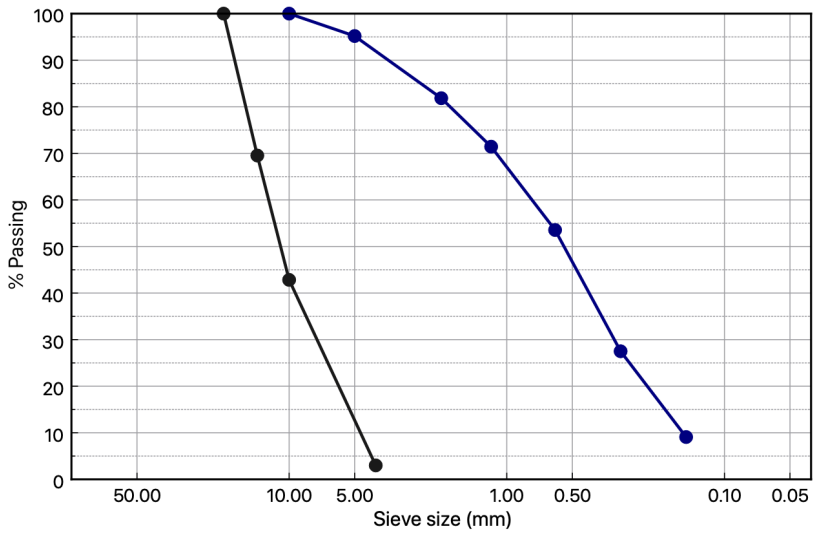

Figure 3.4.1: Particle size distribution of aggregates.

All GO-incorporated cement and concrete samples are labelled GCs respectively (i.e., OGO in cement becomes OGC, HGO becomes HGC and so on). For compressive and flexural concrete strength testing, the BRE concrete mix design manual (Teychenné et al. 1997) was employed and the mix design process is included in Appendix 1 (section 6). A target strength of 40 MPa with

Table 3.4.1: Coarse and fine particle size distributions.

Sieve size (mm)	Average weight retained (g)	Cumulative weight retained (g)	Cumulative % retained	Cumulative % passing
20	0	0	0.00%	100.00%
14	822	822	30.47%	69.53%
10	734	1556	57.67%	42.33%
4	1064	2620	97.11%	2.89%
pan	78	2698	100.00%	0.00%
10	0	0	0.00%	100.00%
5	36	36	4.81%	95.19%
2	100	136	18.16%	81.84%
1.18	78	214	28.57%	71.43%
0.6	134	348	46.46%	53.54%
0.3	195	543	72.50%	27.50%
0.15	138	681	90.92%	9.08%
pan	68	749	100.00%	0.00%

slump 20 mm was set, however superplasticizer had to be added to ensure sufficient workability. Through trial and error 0.8% superplasticizer was found to be appropriate for the concrete samples, however it was raised to 1% to accommodate for reduction in flow by GO addition. Coarse aggregates were sieved to obtain maximum aggregate size of 20 mm. Three 100 x 100 x 100 mm concrete cubes and one 500 x 100 x 100 mm concrete prism were designed for each variable types. The variable types include one control, four pre-treated GO-PC samples, and four GO-PC samples without pre-treatment. These samples were water cured for 28 days and tested for average compressive strength and flexural strength via three-point bending tests. Due to insufficient quantity of prepared nanomaterials for multiple prisms (for all 8 sample types), multiple 500 x 100 x 100 mm concrete beams could not be cured. As such, separate smaller cement beams were designed, and subjected to flexural stress at 28 days to obtain additional cement flexural strength results.

The concrete, nanomaterial and superplasticizer mix proportions for each

Table 3.4.2: Concrete mix design proportions.

	mix design (kg/m3)	ratio wrt cement	per batch - g
water	160	0.44	576
cement	365	1	1314
fine aggregates	715	1.96	2574
coarse aggregates	1160	3.18	4176
superplasticizer	-	0.01	13.14
GO (solid)	-	0.0004	0.526

sample are tabulated in Table 3.4.2. For pre-treated GCs, a concentrated suspension of the respective GO (4 mg/mL) was heated to 60 °C under constant stirring and superplasticizer was added in a 10:1 ratio wrt the weight of the GO material. The mix was kept under 60 °C with stirring for 15 minutes, and then allowed to cool before being placed in an ultrasonicating bath for 15 minutes at 40% intensity (35 kHz). Meanwhile, the required amounts of cement and aggregates were weighed and dry mixed in a pan mixer. After sonication, the pre-treated GO-superplasticizer was poured into water for the concrete mix, and remaining superplasticizer was added to the GO-superplasticizer water. It should be noted that in pre-treatment the superplasticizer were added to all GO variants in a 10:1 ratio, however the remaining plasticizer was added to the final water-GO-superplasticizer suspension to make sure total quantities were controlled for in all batches. A 10:1 pre-treatment ratio was employed from preliminary trials that confirmed its efficacy, with the leftover plasticizer is added as cement for its intended target. For the non pre-treated GO-concrete samples, only the 4 mg/mL GO suspensions were subjected to ultrasonication before pouring into water, with all superplasticizer added separately. Figures 3.4.2 and 3.4.3 summarize the divergent mix design procedures for GCp and GC+p concrete samples respectively. The final quantities for each batch are outlined

Table 3.4.3: Final mix quantities for each batch.

	cement (kg)	water (mL)	fine aggregates (kg)	coarse aggregates (kg)	super-plasticizer (pre-treatment) (mL)	concentrated GO (4mg/mL)	super-plasticizer (no treatment) (mL)
control	1.314	565.57	2.574	4.176	0		12.17
HGCp	1.314	434.17	2.574	4.176	4.87	131.4	7.30
OGCp	1.314	434.17	2.574	4.176	4.87	131.4	7.30
XGCp	1.314	434.17	2.574	4.176	4.87	131.4	7.30
LGCp	1.314	434.17	2.574	4.176	4.87	131.4	7.30
HGC+p	1.314	434.17	2.574	4.176	0	131.4	12.17
OGC+p	1.314	434.17	2.574	4.176	0	131.4	12.17
XGC+p	1.314	434.17	2.574	4.176	0	131.4	12.17
LGC+p	1.314	434.17	2.574	4.176	0	131.4	12.17

in Table 3.4.3. This water was mixed for a few seconds, and then poured slowly into the dry mix while the mixer was switched on. Total wet mixing time was controlled to maximum 10 minutes for each sample, after which the machine was switched off and the mix was allowed to sit. After 10 minutes the mix was poured (in 3 batches) into a slump cone (305 mm height, 100 mm top diameter and 200 mm bottom diameter) and tamped 25 times with a metal rod for each poured batch, before lifting the cone and measuring slump. The final slump value was recorded when consecutive slump tests for each type did not vary by more than 1 mm: most sample mixes gave the same consecutive slump after 3 tests, with the XGO based concrete mixes took 4 slump measurements to show similar consecutive slump. The mix was then poured, again, in 3 runs into the respective cube and prism moulds, and subjected to 10 second vibrations via vibrating table. Once the moulds were fully filled and vibrated, they were left to harden for 24 hours, after which they were demoulded and placed in a pond (with pH 11) and water cured for 28 days. The process is illustrated in Figure 3.4.4.

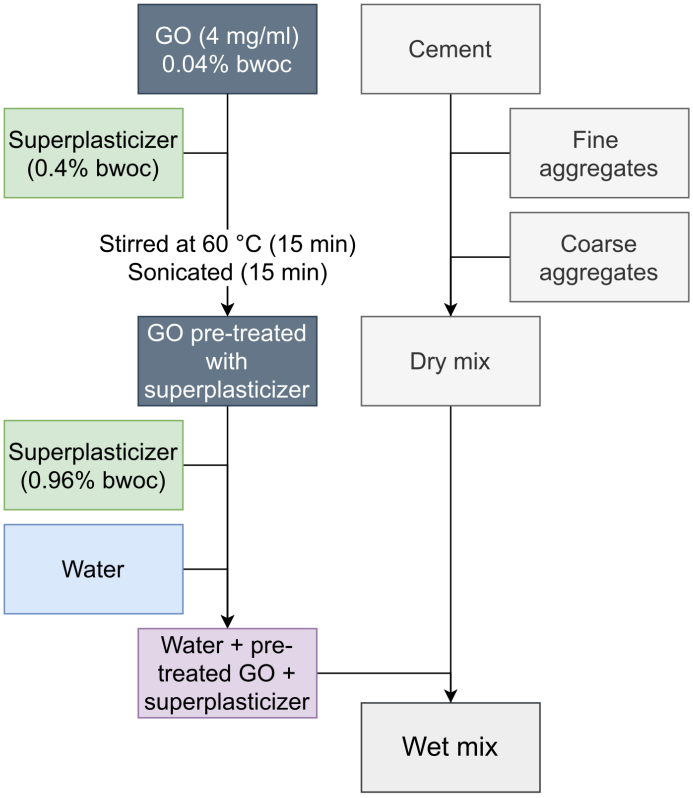

Figure 3.4.2: Mix design for all GCp samples. GO applies to all four variants.

For flexural cement samples, moulds were prepared using a wood panel as base and styrofoam as the walls of the moulds. The styrofoam was attached to the wood using silicon epoxy, which was also poured along the corners on the inside of the moulds to ensure no leakage. The moulds were allowed to dry for 24 hours, and were oiled to reduce friction when demoulding. the mould sizes were approximately 400 mm x 20 mm x 15 mm. The nanomaterials were not pre-treated as the cement quantity is small, hence the prerequisite amount of sonicated GO (0.04% bwoc) and polycarboxylate superplasticizer (reduced to 0.5% bwoc) were added separately to water (w/c ratio is 0.40). The water mix was added slowly to the cement in a Hobart mixer (speed 2) over 30 seconds, and the mix was stirred for a further 45 seconds at the same speed, and 15 seconds at speed 3. Immediately the machine was switched off, al-

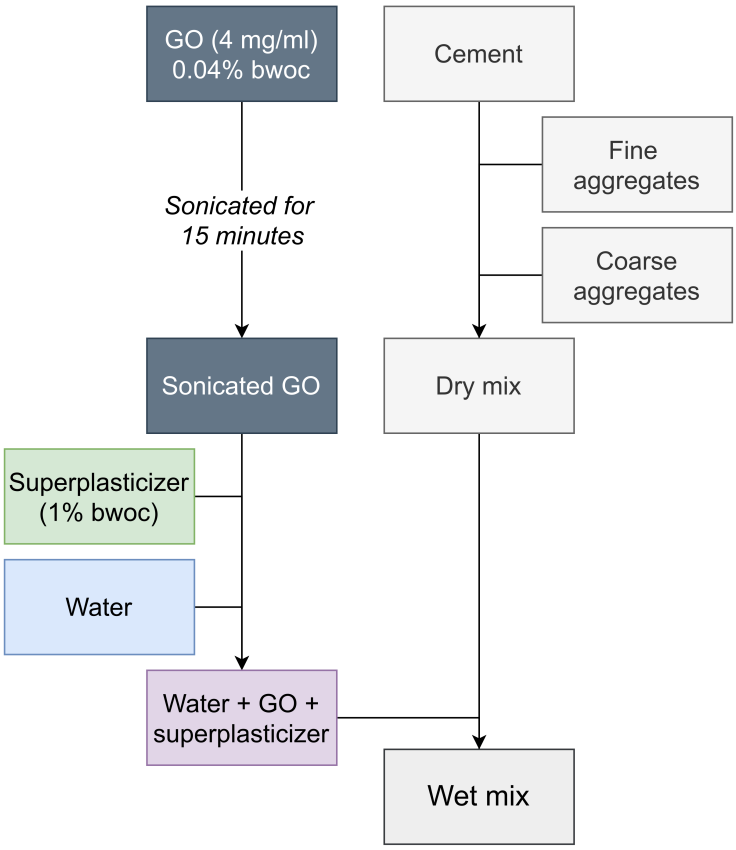

Figure 3.4.3: Mix design for all GC+p samples. GO applies to all four variants.

lowed to settle for 30 seconds, then gradually poured with constant manual stirring (using a glass rod) to ensure no cement particles settle at the bottom of the mixer container. While initially planned to be water cured for 28 days, due to the unexpected Covid-19 lock-down the lab was closed for three weeks (month of October 2020). Therefore the samples were allowed to air-cure instead. However, after 3 weeks of air curing, it was observed that the samples were brittle. As the beams were also slender, it was suspected that the samples would break upon demoulding. As a mitigative measure, the samples were submerged and allowed to water cure for the final week before testing for 28 day flexural strength. To summarize, the cement samples were subjected to 3 weeks of air curing and 1 week of water curing before demoulding and test-

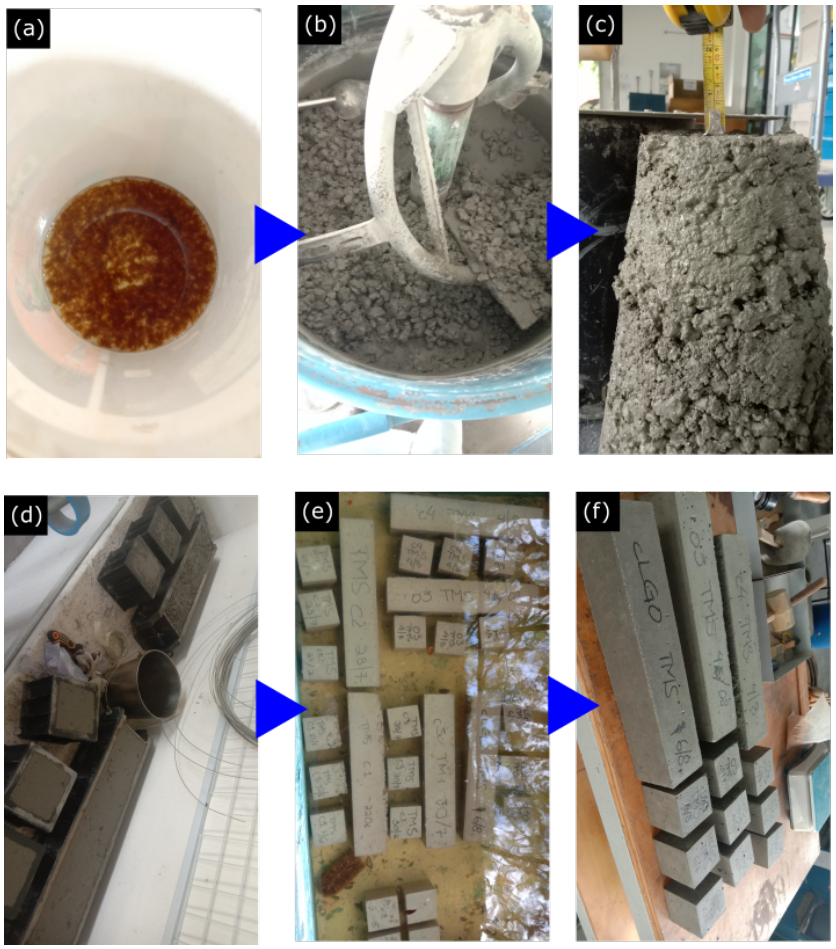

Figure 3.4.4: (a) The GO-water-superplasticizer mix was added to the (b) dry cement/aggregates and thoroughly mixed, and (c) slump tests were performed to check workability. Then the concrete was vibrated and poured into (d) moulds, then (e) de-moulded after 24 hours and placed in a water pond for 28 days (e) prior to compressive and flexural testing.

ing. This preparation is highlighted in Figure 3.4.5. Upon demoulding, most samples broke at the middle, however as their initial length was quite long, flexural tests could still be carried, with the new different lengths accounted for in their flexural stress calculations. It should be noted that while all cement samples were cured in the same manner, their mix of water and air curing consequently disallows 28 day flexural strength result comparison to any existing literature. The Lloyd LRK50-plus universal testing machine was used to perform the experiments (see Figure 3.4.6). After fracturing, the failure plane was scraped and cement powder was obtained for further 28-day analytical and

microscopic characterization.

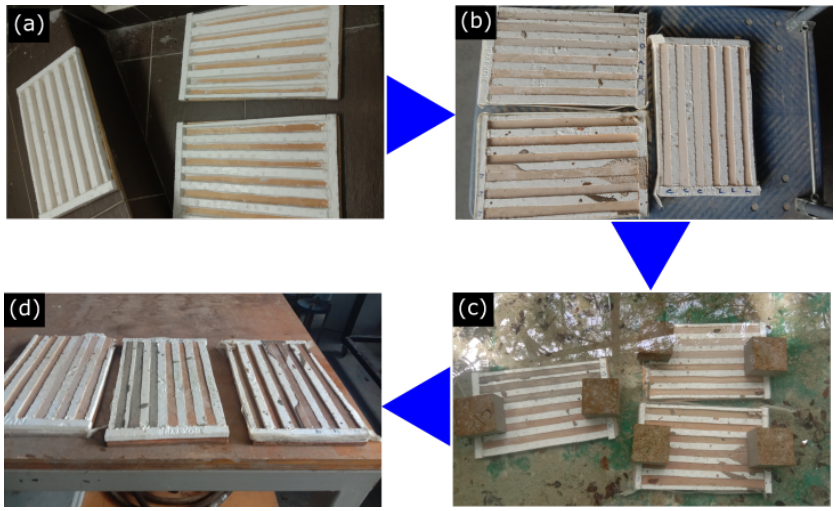

Figure 3.4.5: (a) The moulds for cement beams (b) after pouring of cement, left for air curing for 3 weeks (c) water cured in the final week (d) 28-day beams just before demoulding and testing for flexural strength.

Figure 3.4.6: Illustration of set-up for flexural testing of small cement beams.

For the flow tests, cement control, GO (without superplasticizer) and GO samples with superplasticizer were mixed similar to the flexural cement samples. After mixing, they were poured in a mini aluminium slump cone (74 mm height, top diameter 35.8 mm and bottom diameter 82.8 mm), which was then lightly tapped three times with the rod and then lifted. The resulting spread di-

ameter of the cement mix was recorded at three different angles and averaged (figures 3.4.7, 3.4.8, 3.4.9) highlight the flow variabilities between the cement samples). For remaining hydration analytical tests (3 hours, 6 hours, 12 hours, 24 hours and 72 hours), the GO-cement with superplasticizer (0.5% bwoc) was prepared similar to above, but poured in plastic cups until demoulding at their respective time. Immediately after demoulding, the top surface of each sample was removed by a blade, as that is where most of the water and superplasticizer has risen due to bleeding. After surface removal, the samples were crushed manually and freeze-dried (Martin Christ machine) for 72 hours to remove all water and cease hydration. After freeze drying, the samples were further ground using the Retsch ZM200 ultracentrifugal mill (0. 2 mm sieve), and the ground samples were placed in a desiccator filled with silica gels to keep them as dry as possible, until analytical tests (FTIR, SEM, TGA, XRD) were performed. The preparation is shown in Figure 3.4.10.

Figure 3.4.7: Reduced flow for GC sample without superplasticizer.

Figure 3.4.8: Flow for a control sample without superplasticizer.

Figure 3.4.9: Flow of a GC sample with superplasticizer.

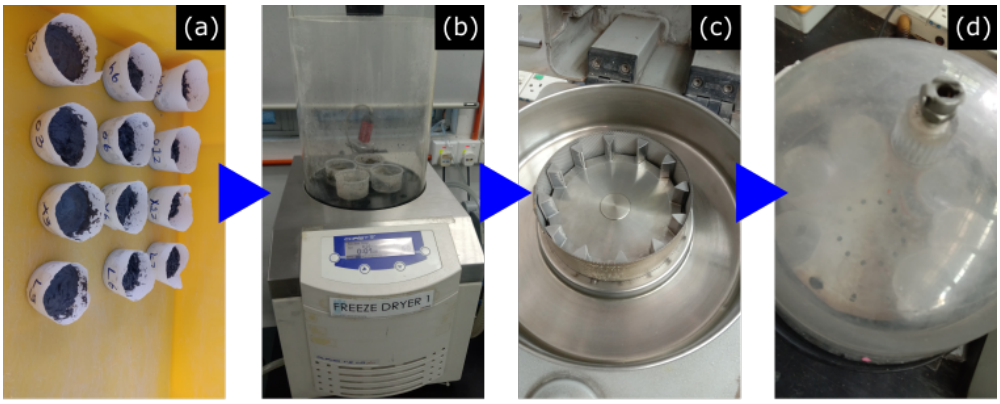

Figure 3.4.10: (a) Cement cups after prerequisite hours of hydrations were (b) freeze-dried for 72 hours and (c) grounded into fine powder, after which they were (d) placed in a desiccator with silica gel to remove any moisture.

3.4.1 X-Ray Diffraction (XRD) tests

The X-Ray Diffraction (XRD) test is essential in determining the compound composition of any crystalline solid. Unlike the Energy Dispersive X-Ray Analysis (EDX) test, which is conducted in conjunction with Scanning Electron Microscopy (SEM), the XRD obtains diffractograms that can be used to identify which compounds are significantly present in the sample being tested. Meanwhile SEM-EDX is used to discover the presence of elements and not compounds, a rather inefficient way to characterize hydrated cement as most by-products are comprised of the same handful of elements (i.e. Calcium, Silicon, Aluminium, Oxygen).

In essence, XRD involves firing x-rays from an emitter onto the sample, while a detector is situated on the opposite to catch any clearly diffracted beams from the sample (see Figure 3.4.11). The sample is then slowly rotated over an angle θ while the x-rays continue to bombard it, and the counts of x-rays received by the detector over the angle 2θ is plotted on a graph called the diffractogram. The premise follows that any crystalline solid with a distinct crystal

structure would reflect significantly higher x-rays at specific angles of θ and none at others. The alignment must follow Bragg's Law, a simple trigonometric rule that states:

$$n\lambda = 2dsin\theta \tag{10}$$

Where d is the interplanar spacing between a given crystal lattice in the sample, θ is the angle of rotation from which the x-rays are being fired onto the sample, and λ is the wavelength of the incident x-rays, for any integer n.

Hence using previously gathered diffractogram patterns of certain compounds, it is possible to identify which compounds are present in the tested sample, and in certain cases estimate their quantity. However, this analytical technique only works on samples with a defined structural shape (i.e. crystalline lattice). Both hydrated and unhydrated portland cement have been shown to have a defined, albeit complex tobermorite structure (see Figure 3.4.12) (Neville 2019, Li 2011).

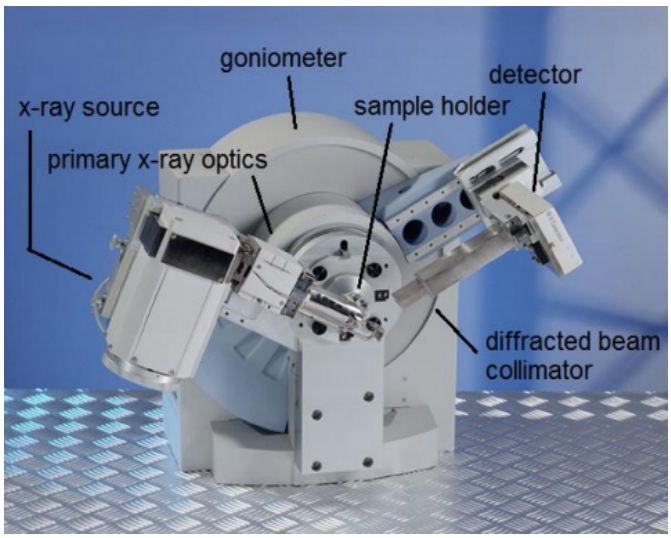

Figure 3.4.11: Basic operation of an XRD machine.
https://docplayer.org/docs-images/67/57819458/images/5-0.jpg.

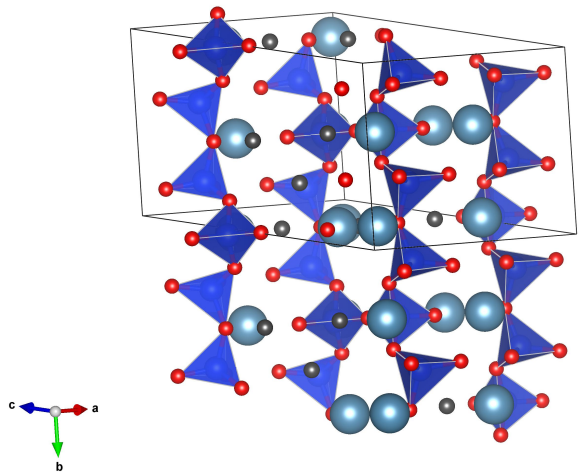

Figure 3.4.12: Generated C-S-H Tobermorite Structure.

With the hydration process, the key ingredient C-S-H is produced from alite's (C_3S) and belite's (C_2S) reaction with water, which also forms other by-products such as portlandite (CH). Other compounds are also present such as gypsum, celite (C_3A) and C_4AF which form ettringite and other sulphate compounds. All of the above mentioned compounds have their own crystalline lattice structure, or multiple in the case of alite and belite, which have their own sub-phases with different crystalline geometry (orthorombic, triclinic, monoclinic). These compounds, along with other minor metal oxides mostly comprise the final hydrated cement. Therefore, it can be seen that the XRD diffractogram is very complex and contains multitudes of stoichiometric overlap between these sub-phases and different compounds. In addition, C-S-H itself has variable stoichiometry due to complex formations of it's own building blocks (CaO, SiO_2 and H_2O), which adds to the complexity. Hence to successfully quantitatively analyze cement samples, the Rietveld Refinement procedure is performed (Renaudin et al. 2009, Jadhav & Debnath 2011, Elena & Lucia 2012, Stutzman et al. 2016).

Rietveld Refinement uses the nonlinear least squares method to iteratively fit the data via convergence (Rietveld 1969). Once the observed diffractogram is 'cleaned' by subtracting unnecessary background data, iterations are performed on pre-known phases of crystals in the sample (e.g. in our case C-S-H, C_3S monoclinic, C_3S triclinic etc) where the diffractogram's various peak locations, shape and intensities are taken into consideration, and a calculated peak profile is drawn that converges on the original observed data. If the calculated profile falls statistically convergent with the observant data, the refinement procedure is successful and hence the quantitative amounts of the entered phases can be determined. It can be argued that this process is semi-quantitative, and may lead to false positives as the phases are entered by the user, however the iterative procedure is exhaustive and it is statistically quite improbable to have a high chance of converging false positives (Rietveld 1969). The Rietveld Refinement equation is stated as follows:

$$\Phi = \sum_{i=1}^{n} w_i (Y_i^{obs} - (b_i + \sum_{l=1}^{p} K_l \sum_{j=1}^{m} I_{l,j} y_{l,j}(x_{l,j})))^2 \tag{11}$$

where, for all data points n, w_i is the weight, Y_i^{obs} is the observed intensity of a point i in the XRD pattern, b_i is the background function (observed minus calculated values) at the ith data point., K is the phase scale factor, m is the number of Bragg reflections contributing to the intensity of the ith point, $I_{l,j}$ is the integrated intensity of the lth and j^{th} Bragg peaks, $y_{l,j}(x_{l,j})$ is the peak shape function for the multiple phases p (Rietveld 1969).

Due to recent advancements in computational technology, the iteration procedure does not take nearly as long as before. Following is an outline of XRD's

instrument configuration.

Figure 3.4.13: The PANalytical x'pert PRO XRD machine.

The PANalytical X'Pert pro XRD machine (see Figure 3.4.13) was used for analyzing the respective samples, over a rotation of 10° to 80° with a step size of 0.02° and scan time of 0.15 seconds, using Cu anode with K-Alpha1 setting at 1.54060. Further configuration settings are summarized in Table 3.4.4. Profex BGMN software was used to analyze the output XRD files, with the above instrument configuration imported for refinement, and Table 3.4.5 shows the selected phases used in running the refinement procedure. All of the phases were pre-included in the software package, and as can be seen, multiple phases are also present for the same compounds due to their different crystalline formations on hydration. Despite multiple phases, only C_2S β was used for identification due to it's higher reactivity. For alite, the monoclinic Mumme and triclinic Belov structures were used, while the two cubic and orthorhombic C_3A forms are both used in the XRD analysis. C_4AF only has one crystalline structure and as the cement used in my experiments has high limestone amounts, calcite also had to be included to form an appropriate statistical fit. All phase

Table 3.4.4: XRD instrument configuration details.

XRD Parameter	Specification
Scan Axis	Gonio
Start Position [$2\theta°$]	10.01
End Position [$2\theta°$]	79.99
Step Size [$2\theta°$]	0.02
Scan Step Time [s]	0.15
Scan Type	Continuous
Offset [$2\theta°$]	0
Divergence Slit Type	Fixed
Divergence Slit Size [°]	0.957
Specimen Length [mm]	10
Receiving Slit Size [mm]	0.1
Measurement Temperature [°C]	25
Anode Material	Cu
K-Alpha1 [Å]	1.5406
K-Alpha2 [Å]	1.54443
K-Beta [Å]	1.39225
K-A2 / K-A1 Ratio	0.5
Generator Settings	40 mA, 45 kV
Diffractometer Type	11067808
Goniometer Radius [mm]	240
Dist. Focus-Diverg. Slit [mm]	91
Incident Beam Monochromator	No

Table 3.4.5: Selected phases for Rietveld Refinement.

Parameter Name	Compound	Name
QCSH	C-S-H	calcium-silicate-hydrate
QCSH0625	C-S-H	
QbetaC2S	C_2S	belite
QC3ACubic	C_3A	celite
QC3AOrt	C_3A	
Qc3smumme	C_3S	alite
Qc3stbel	C_3S	
Qc4af	C_4AF	C_4AF
Qcalcite	$CaCO_3$	limestone
Qportlandite	CH	calcium hydroxide

inclusions were decided as per Thermo fisher scientific's XRD cement manual (2008). However, it should be noted that C-S-H does not show up prominently in most XRD measurements, not aided by it's irregular triclinc structure, and AFt's XRD peak falls below 10° not measured in this machine, hence most inferences from XRD can only be performed on measuring alite and CH changes.

3.4.2 Brunaur-Emmett-Teller (BET) porosity tests

BET porosity tests are performed to determine the total surface area of particles. As a consequence of it's material make-up, it is inevitable that cement mixtures will have pores in them of various sizes (from air voids or evaporated water or unreacted water locked out by hydrated cement). A denser hydrated cement microstructure should logically then have finer pores and higher total surface area (illustrated in Figure 3.4.14). For BET tests, initially the particles are degassed completely to remove moisture and any other air molecules that are inhabiting the material. Once degassed, N_2 gas is introduced at specific relative pressures, and the N_2 molecules are attracted and adsorb to the surface of the degassed samples. At a certain relative pressure, the N_2 molecules completely coat the surface area of the sample (monolayer adsorption), and hence for a known quantity of the N_2 gas volume provided at that pressure, the surface area of the sample can be calculated (Figure 3.4.15).

Moreover, as the relative pressure is further increased to 1 (complete saturation), the N_2 molecules then proceed to fill up pores of the sample, and relative pressure is maintained to achieve an equilibrium of N_2 gas adsorption. Once full volume adsorption is reached, the relative pressure is gradually subsided until 0. Hence, adsorption and desorption isotherms can be plotted. The inter-

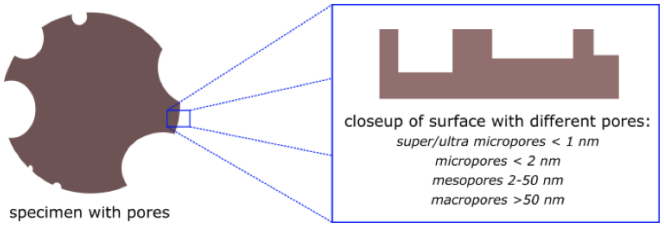

Figure 3.4.14: Pore classification of a sample subjected to BET tests.

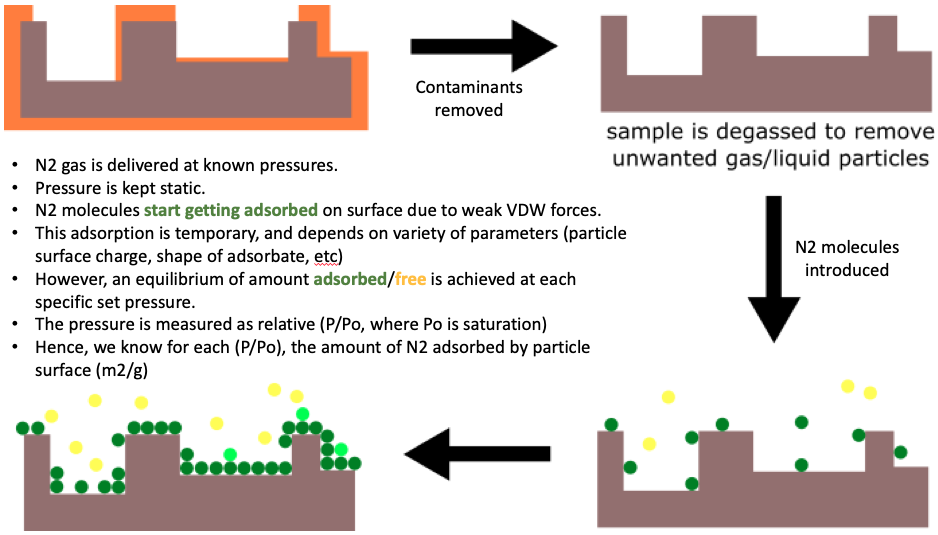

Figure 3.4.15: Explaining the BET porosity test procedure.

val between the adsorption and desorption isotherm plots further indicate the size of these pores (micro, nano or macro pores). This process is highlighted in Figure 3.4.16. The micrometrics ASAP 2020 surface area and porosity analyzer was used to conduct BET tests (Figure 3.4.17). The sample (weighing around 0.3g) is first degassed for approximately 60 minutes. After degassing, helium is introduced to remove any other gas or unwanted molecules, after which purified N_2 is introduced and the adsorption process is initiated. The whole adsorption/desorption process takes around 12 hours for each sample.

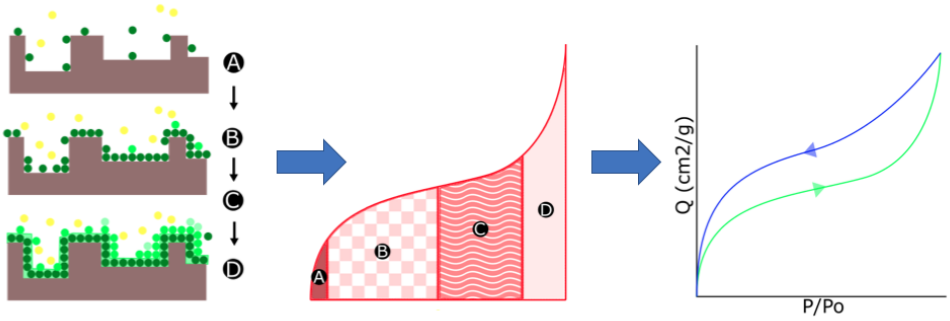

Figure 3.4.16: Illustrating how the isotherm curve regions A to D are plotted as relative pressure is increasing for a BET sample.

Figure 3.4.17: The ASAP 2020 porosity analyzer machine.

3.5 Summary of Methodology

This chapter details the materials and methodology behind GO and cement research experiments. The materials and chemicals used for GO synthesis and by cement/concrete mix design were tabulated, followed by an explanation of synthesis process of the different GOs. There were noticeable visual differences between the GO chemical oxidation processes, expounded in Section 3.2.1. To verify the changes in chemical compositions between the GOs, several analytical characterizations and pH/titration tests are undertaken, for which the sam-

ples' preparations and instrument configurations are outlined in sections 3.2.2 - 3.2.7. Following GO synthesis and testing methods, the mix design for preliminary trial samples are outlined in section 3.3.1. Lastly, the final mix design details are included in section 3.4. This section also outlines the particle size distribution of the aggregates, and the preparations undergone to make GO-cement samples for analytical characterization tests such as XRD and BET. A brief overview of the cement analytical characterization tests is also provided.

Chapter 4: Results and Discussion

This chapter provides all the results obtained from the GO and cement analytical, workability and strength tests. The results are discussed in detail, and a hypothetical model explaining GO-cement hydration interactions is presented. The outline of this chapter is illustrated in Figure 4.0.1.

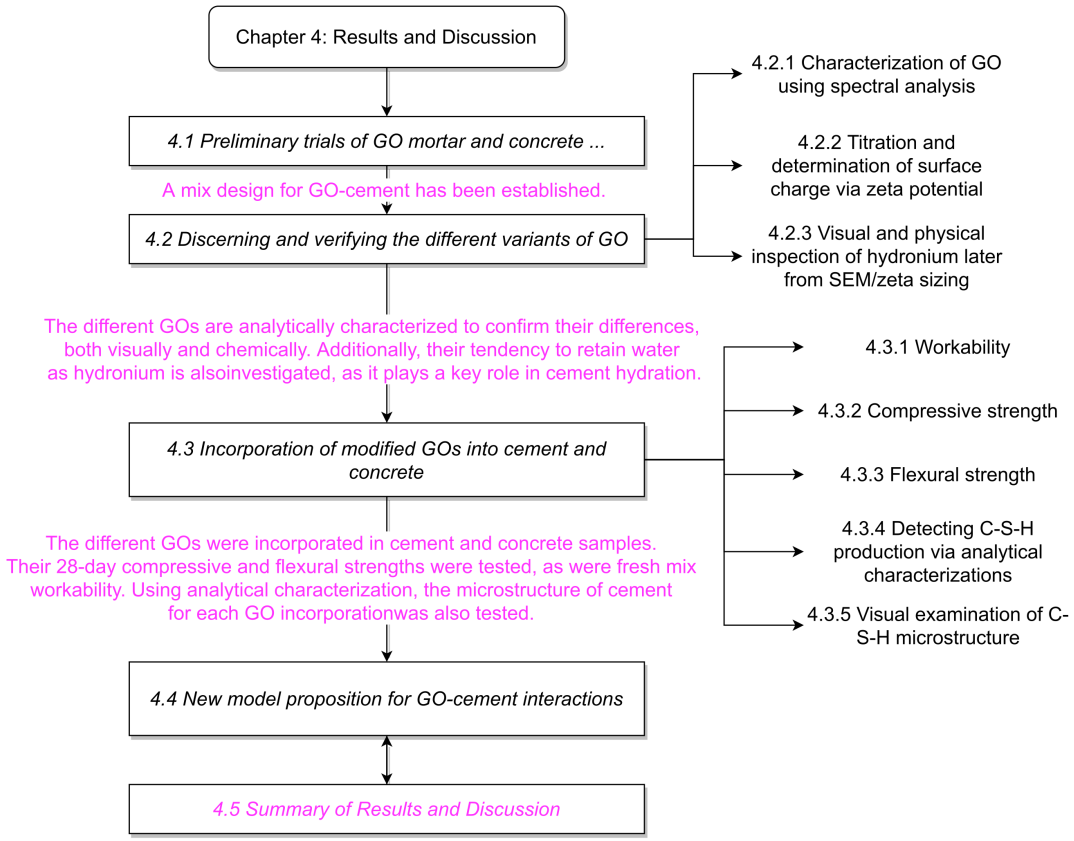

Figure 4.0.1: Flowchart outlining all the sections in this chapter.

4.1 Preliminary trials of GO mortar and concrete cubes

To prepare samples for preliminary trials, it is important to reiterate some presumptions regarding GO behaviour with PC, as following:

1. If the goal is to provide steric hindrance for GO to disperse uniformly

before reacting with cement, only minute amounts of PC are required.

2. GO and superplasticizer may react chemically and cause unpredictable stress behaviour.

3. GO will only be effective as C-S-H seeders if the water in the cement mix is a limiting factor.

To confirm the first hypothesis, preliminary compressive strengths trials were carried out with mortar cubes and the results are summarized in Table 4.1.1 and Figure 4.1.1. Control samples (cont, 5P, 10P) with none or different amount of superplasticizers (5x and 10x the equivalent weight of GO respectively, hence present in very small amounts) were tested against GO mortar samples with none or respective amount of superplasticizers to the the above (1G, 5P1G, 10P1G). Additionally, a separate mortar cube type was prepared with same proportions as 10P1G, however the GO-superplasticizer mix was not sonicated prior to dispersal (10P1G0S).

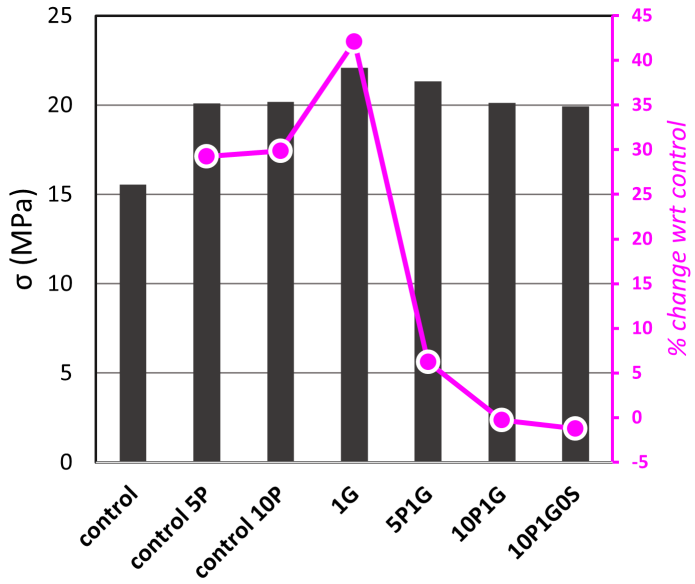

Figure 4.1.1: 28 day compressive strength values for GO and control mortar cubes.

Table 4.1.1: 28 day compressive strength results for preliminary mortar cubes.

	Peak stress σ (MPa)						
	sample 1	sample 2	sample 3	sample 4	sample 5	average	%Δ wrt control
control	13.71	11.65	16.67	19.58	16.09	15.5	
control 5P	20.37	20.91	19.33	19.36	20.43	20.1	29.22
control 10P	18.31	19.38	26.26	18.33	18.61	20.2	29.85
1G	24.73	23.73	23.29	18.96	19.69	22.1	42.09
5P1G	24.53	21.08	18.91	22.12	20.02	21.3	6.24
10P1G	18.48	21.96	19.78	22.62	17.75	20.1	-0.30
10P1G0S	19.88	17.57	22.44	19.18	20.57	19.9	-1.23

Both control samples with superplasticizers performed significantly better than their control counterpart, increased in strength by approximately 29%. The GO mortar with no superplasticizer was the strongest at 22 MPa, a 42% increase in peak stress. However, the effects of GO were not pronounced when superplasticizer was added, with all GO mortar counterparts exhibiting 20-22 MPa in compressive strength. The reason for 1G's high increase in stress stems from the control sample being exceptionally weak, possible due to reduced workability hindering it's strength gains. Additionally, not sonicating the sample did not change final stress significantly, possibly due to GO's already excellent hydrophilicity in water. Slump tests were not performed at this stage due to limited amount of nanomaterials, however in final mix design the workability was tested.

Several variables could be the contributing factor for the subpar compressive strength performance of GO mortar samples: the amount of plasticizer and the water/cement ratio. The cement used was a Portland Cement Composite (PCC), with high fly ash content. Fly ash is a pozzolanic material. It is suspected that high fly ash presence, coupled with GO, are not allowing for uniform strength development throughout the mortar samples. Thus, a PCC

with low fly ash content was chosen for the remaining preliminary and final experiments. For the amount of plasticizer, the additional concerns in hypothesis 2 prompted more tests. Woo Chee Zheng, an M.Eng student, graciously decided to undertake this project for his full year project, and while extended analytical tests could not be performed due to the Covid-19 lockdown earlier in 2020, Figure 4.1.2 summarizes stress strain curves for different concrete samples with same amount of GO (0.02% bwoc) pre-treated with different, minute amounts of superplasticizer (0.05%, 0.1%, 0.15%) before it's incorporation in concrete. As observed, the change in superplasticizer amount did not change compressive strength significantly. However the w/c ratio was considerably high (0.6), which brings us to hypothesis 3.

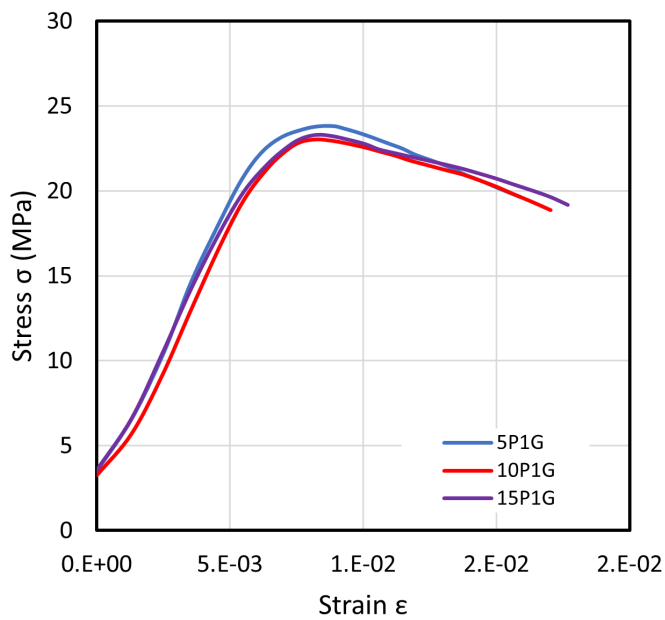

Figure 4.1.2: Stress-strain curves of GO-concrete pre-treated with varying superplasticizer amounts.

Khoo Seng Him, another M.Eng student, pursued the effects of GO incorporation in (0.02% bwoc) concrete with varying w/c ratios. The cement content was kept constant for all mix designs, while the water content was altered from

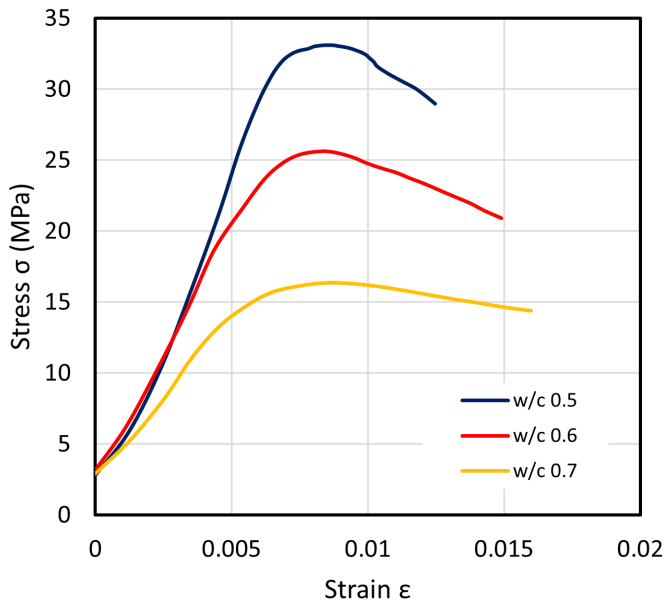

Figure 4.1.3: Stress-strain curves of GO-concrete with varying w/c ratios.

a w/c ratio of 0.5 to 0.7. To keep the overall mix density constant, the aggregate weights were reduced to adjust for the increased water content. The results are summarized in Figure 4.1.3. They definitively show that a lower w/c ratio is essential for GO to exhibit any improvements in the concrete microstructure. This is because if water molecules are available in abundance, there is no reason for cement to nucleate on the GO sheets themselves, whereas in water-scarce conditions, GO's persistent hydronium coating prompts C-S-H nucleation and growth in denser more regulated sheet surfaces. Additionally, it is suspected that GO re-protonates water molecules constantly around it, which can be a catalyst for C-S-H growth. Hence, the following conclusions were made for the above hypotheses:

1. Providing steric hindrance to GO reduces it's potential positive influence to the C-S-H gel matrix. Priority should be providing steric hindrance primarily to cement, and potentially secondary to GO.

2. GO-superplasticizer interactions do not cause any change in stress-strain of concrete at high w/c ratios

3. A low w/c ratio would be essential for GO incorporation. A trade-off for strength may be workability, hence superplasticizer is also necessary

From the above inferences, it was decided that both pre-treated and untreated GO-superplasticizer design mixes are tested for compressive strength. As different types of GO are being incorporated, their reactions to pre-treatment (or not) may vary. Hence, while the amount of superplasticizer for pre-treatment was kept minute (10x wt. equivalent of GO), extra superplasticizer was also added to water after the pre-treated GO-superplasticizer mix to keep the total amount of superplasticizer at 1% bwoc in final mix. This was necessary to keep w/c ratio low and allot some superplasticizer for cement as well. Conversely, for untreated GO-superplasticizer batches, the 1% bwoc superplasticizer was added in full to the water and GO mix which was then slowly added to the dry cement and aggregates under constant mixing.

4.2 Discerning and verifying the different variants of graphene oxide

Multiple batches of each GO were produced, and LGO showed a staggeringly high yield of approximately 4 times the weight of initial graphite. Meanwhile HGO showed a 1.5-fold increase in weight from graphite, XGO 1.5 and OGO approximately 1.3x the wt. equivalent of graphite.

4.2.1 Characterization of graphene oxides using spectral analysis

Figure 4.2.1 shows the UV-VIS spectra absorbance of all four graphene oxides. All the graphene oxides exhibit the typical 235 nm $\pi \rightarrow \pi^*$ peak commonly attributed to C=C bonding and the shoulder 305 nm $n \rightarrow \pi^*$ peak attributed to C=O bonding. XGO's thermal reduction is not as effective at removing carbonyl groups relative to phenol groups (Li et al. 2008).

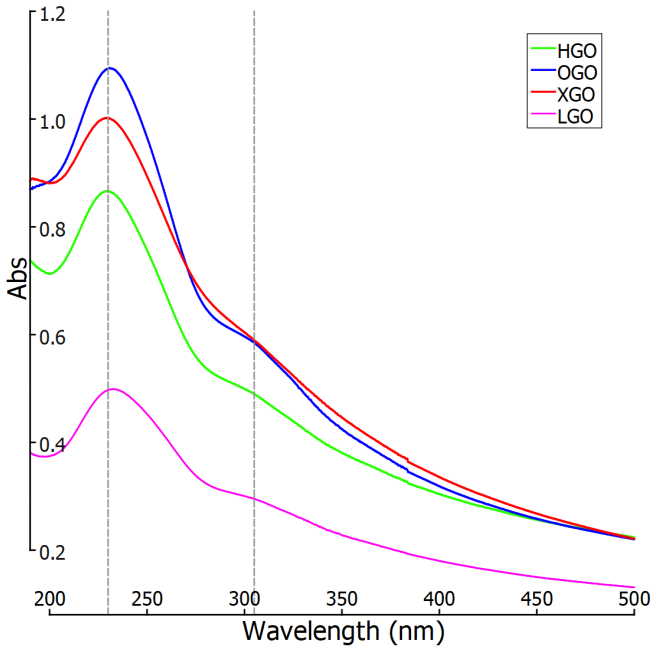

Figure 4.2.1: UV-VIS spectra of HGO, OGO, XGO and LGO.

FTIR was performed on different conditions of GO: 1 mg/mL aqueous suspension, 300 μL of 1mg/mL GO in 2.5 mL isopropanol alcohol, oven dried GO solids and freeze dried GOs solids. For both organic and aqueous solvents, the bonds in the solvents overpowered the IR spectra and no significant comparison could be made between the samples. Slow heating ensured the GO sheet's hydronium layers do not get destroyed in the process and Figure 4.2.2 shows the FTIR spectra for each GO nanomaterial, normalized and combined for better comparison in Figure 4.2.3. The graphs are shown from 500 to 3500 cm^{-1}

wavelengths for better clarity.

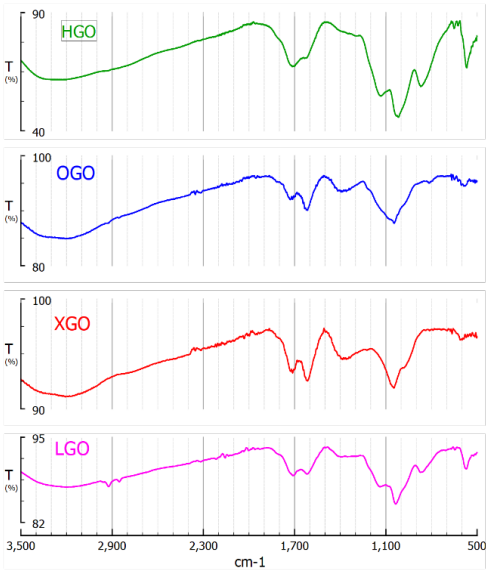

Figure 4.2.2: FTIR spectra for oven dried GO samples.

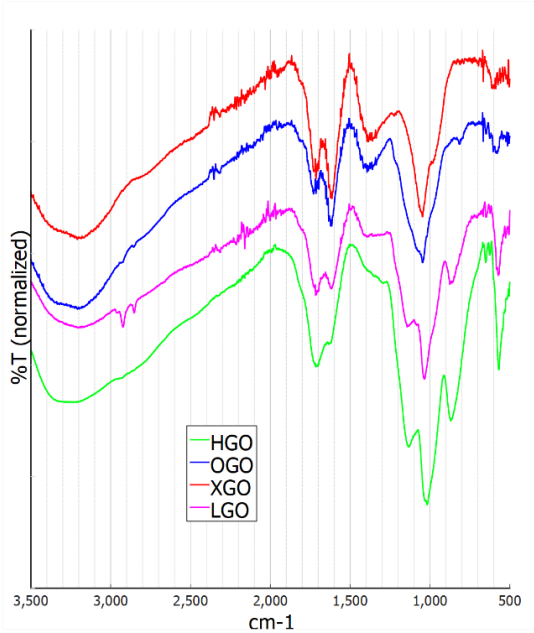

Figure 4.2.3: Normalized FTIR spectra of oven dried GO samples.

All bond attribution was made using the comprehensive Sigma-Aldrich website for reference (Sigma-Aldrich 2021). The 3200-3300 cm^{-1} broad strong peak is due to alcoholic O-H stretching, prominent in all GO variants. However, only LGO registers two weak peaks at 2950 and 2850 cm^{-1}. This is mostly likely unsaturated C-H stretching as a consequence of it's synthesis procedure.

There are several sets of peaks overlapping from 1620-1720 cm^{-1}, with variable absorptions for each HGO, OGO, XGO, and LGO. At 1720 cm^{-1} HGO and XGO show high relative spectra absorption, followed by OGO and LGO respectively. This peak indicates carbonyl presence due to C=O stretching. It is inferred that the thermal reduction treatment of XGO would lead to high structural defects and open carbon chains, allowing greater carbonyl bonding. The higher oxidation of HGO is also reflected in this peak, but not LGO. The 1620 cm^{-1} peak, typically attributed to carboxyl groups, has been shown by previ-

ous research (Rourke et al. 2011, Oickle et al. 2010, Li et al. 2008) to also indicate water absorption via solvent exchange of H_2O to it's heavier counterpart, deuterium oxide (D_2O). In addition, they discovered a higher pH of the solution increased the absorption of this peak, which also coincides with our own findings (XGO > OGO > HGO > LGO in pH value, while XGO > OGO > HGO > LGO for 1620 cm^{-1} spectra absorption). The 1620 cm^{-1} peak is additionally attributed to the C=C diene stretching, which was also highest for thermally reduced XGO. It is also noted that there is an overlapped peak between 1620 and 1720 cm^{-1} (1680 cm^{-1}) peak, highest for the ultra-oxidized GOs (HGO and LGO). This is attributed to the C=O conjugated ketone stretching and is present in all four nanomaterials. A 1400 cm^{-1} bending O-H peak is registered in all GO's as well, notably smaller for HGO and LGO.

C-O stretching is evident in all GO's from 1000-1300 $^{-1}$, yet the shape and position of peaks vary in between. A 1280 cm^{-1} aromatic ester C-O stretching shoulder peak is registered highest for XGO then OGO, respectively; this peak is severely diminished for HGO and LGO. XGO's defects and open chains would result in higher aromatic ester presence. The 1130 cm^{-1} peak can be an overlap of several alcohol groups, and spectra absorption is greatest for HGO and LGO, while non-existent (or possibly shifted) for OGO and XGO, hence indicating greater hydroxyl functionalization. Epoxides may also be represented in this spectral range, however distinguishing them in presence of other C-O bonds is impossible in FTIR. All GO's exhibit strong peaks at 1020 cm^{-1}, which belongs to vinyl/alkyl ether C-O stretch indicating their oxidation, with HGO and LGO showing greater number of peaks and absorption in this range, but

no further deductions can be made at this stage.

HGO and LGO both exhibit a prominent peak at 820 cm^{-1}, conspicuously absent for OGO and XGO. This is registering a C=C alkene bond stretch. When compared to the 1620 cm^{-1} peak (which also overlaps with O-H water bending spectra as discussed earlier), we can see both HGO and LGO show greater alkene presence, while OGO and XGO show higher diene bonds. It can be inferred that due to higher oxidation of HGO and LGO, they are more inclined to form alkene bonds (if any) from limited carbon bond availability. Meanwhile, the less oxidized OGO and reduced XGO display greater inclination towards successive diene C=C bonding. Lastly, there is a sharp peak for both HGO and LGO at 580 cm^{-1}. It may be possible this is due to the intact benzene ring structure of GO (but in that case it should be evident for OGO as well).

Figure 4.2.4 compares FTIR spectra differences between oven dried and freeze-dried GO. The broad peak at 3200-3300 cm^{-1} has reduced significantly, but is still present in freeze-dried samples, indicating that some of the hydroxyl and protonated layer remains on GO. Peaks at 1720, 1620 and 1280 cm^{-1} in both sample types, with the slight reduction of absorption at 1620 cm^{-1} indicates some water bending signals were reduced upon freeze drying. The 1130 cm^{-1} and 1020 cm^{-1} peaks are significantly high for LGO, followed by HGO and small in OGO and XGO. C-O-C epoxide bonds were formed in neighbouring C atoms for HGO and LGO as they attempted to stabilize, following the forceful removal of the hydronium layer resulting in C-O^{-1} open bonds. As HGO, OGO, and XGO do not have any significant C-H presence, their respective peaks remain close to their oven dried counterparts. The remaining peaks do not show

any significant change relative to oven dried samples.

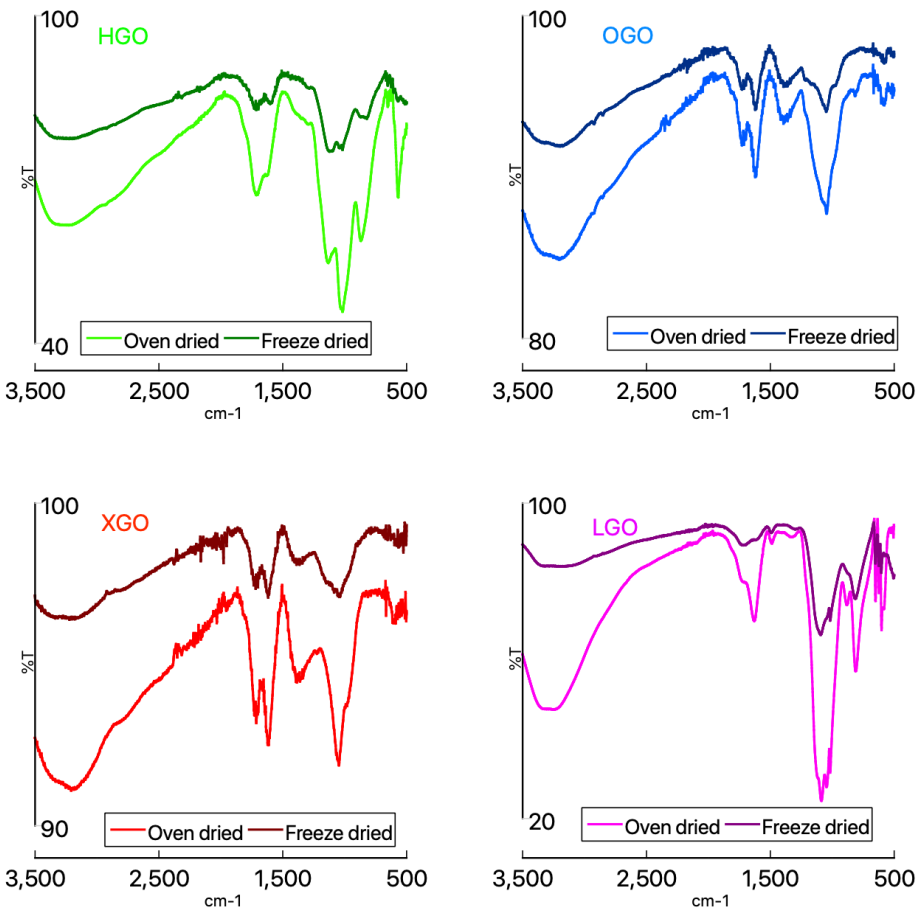

Figure 4.2.4: Comparison of oven dried vs freeze dried GO samples.

To verify our conclusions for FTIR, XPS was performed to confirm the carbon oxygen bonding in HGO, OGO, XGO, and LGO. However, it should be emphasized that while XPS can uncover the compositional bonding for GO, it cannot discern the actual quantities of oxygen bonding in GO sheets between each nanomaterial. Many papers use XPS to discern the C/O ratio, but the H_3O^+ in the hydronium layer can significantly increase the quantity of oxygen molecules in the spectra. It is very difficult to extract the protonated H_3O^+ film around the GO sheets, as forcibly removing the hydronium layer could adversely affect the GO sheet itself and may not represent the *in-situ* behaviour of the nanoparticles in suspensions. For ultra-oxidized GO's, the concentration of

hydronium is much higher and significant amounts of base needs to be added for neutralization, which can interfere with most analytical tests.

Figures 4.2.5 and 4.2.6 display the C1s and O1s spectra for all four GO nanomaterials collectively. The thermal reduction of XGO is evident with much smaller C1s peaks, however both HGO and XGO display much higher background spectra for C1s. Additionally, it was found that both HGO and XGO showed higher impurities and residue Mn/S content (full XPS spectra is included in Appendix 2, section 6). Despite the ultraoxidation, LGO displays smaller O1s than both XGO and HGO. However the HGO's high absorption for O1s may be attributed to the H_3O^+ layer but it is in unclear why XGO would also possess it. Figure 4.2.7 illustrates the C1s spectra of each nanomaterials respectively, with peak energies summarized in Table 4.2.1.

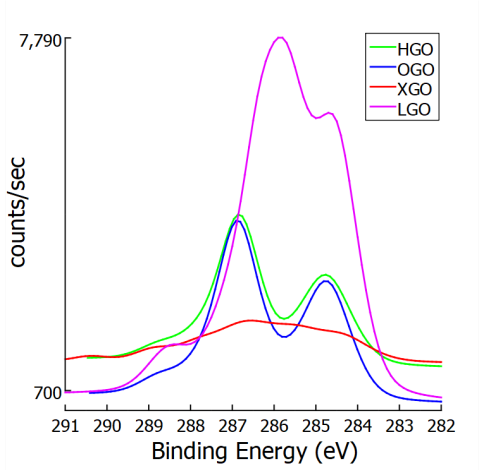

Figure 4.2.5: C1s XPS of all GO.

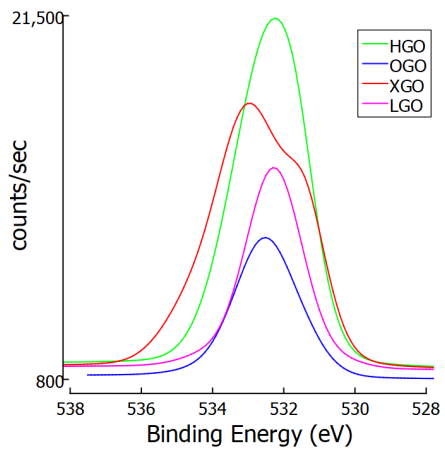

Figure 4.2.6: O1s XPS of all GO.

Despite the significant difference in degree of oxidation, HGO and OGO have very similar binding energies. HGO, OGO, and XGO have higher peaks for C-O than C-C bonding, indicating they are all well oxidized. For LGO, a surprisingly large amount of C sp^3 bond ratios are observed, most likely from

Table 4.2.1: XPS Binding energies (eV) and atomic concentrations (%) of all GO.

		HGO		OGO		XGO		LGO	
		Binding Energy (eV)	(%)	Binding Energy (eV)	(%)	Binding Energy (eV)	(%)	Binding Energy (eV)	(%)
C1s	C-C	284.74	37.55	284.73	37.83	284.32	22.64	284.51	33.34
	sp^3	285.58	2.09	285.88	5.85	285.46	23.22	285.7	35.6
	C-O	286.83	49.49	286.87	46.42	286.69	35.89	286.39	19.2
	C=O	287.82	7.37	287.8	6.4	287.86	12.43	287.18	7.24
	C(O)O	288.78	3.5	288.77	3.51	288.91/290.39	5.82	288.52	4.62
O1s	C=O	531.66	26.87	531.28	8.3	531.37	27.66	530.2	1.87
	C-O	532.53	65.83	532.54	89.67	532.98	63.76	532.27	94.27
	C(O)O	533.81	7.3	534.45	2.04	534.79	8.59	534.34	3.86

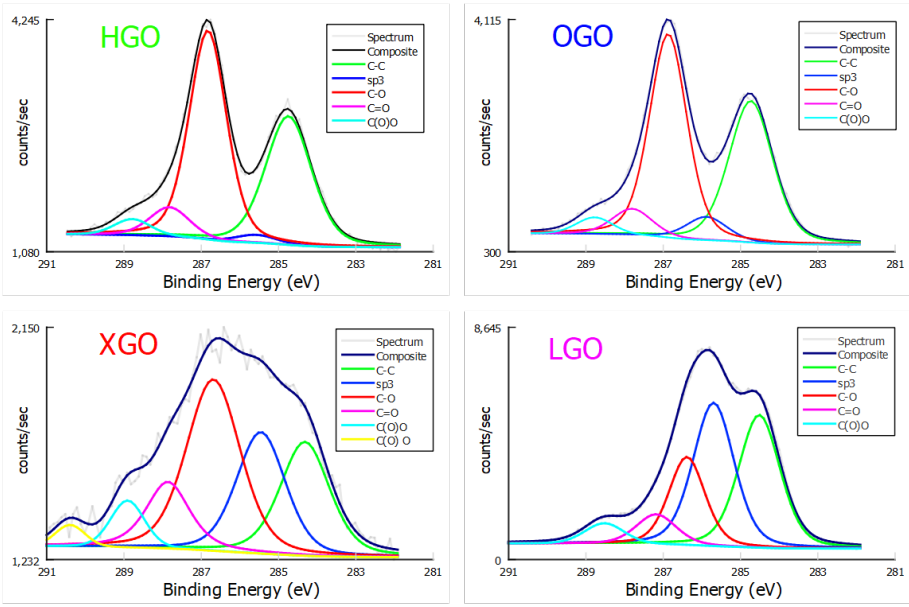

Figure 4.2.7: C1s XPS peak fitting of HGO, OGO, XGO and LGO.

its synthesis. XGO showed the worst peak fitting out of all GO's due to its reduced structure, possessing a much wider and flatter C1s spectra with higher C(O)O peak shifts. Chen et al (2016) stated XGO as carboxyl-rich, which is clearly visible in XPS, however the carboxyl groups may also be more evident due to XGO's reduction and removal of C-O bonds rather than a significant quantitative increase of overall C=O. As XPS cannot distinguish C-C and C=C bonding, the diene/alkene spread between the nanomaterial variants cannot be determined. The O1s XPS of all GOs are shown in Figure 4.2.8 and tabulated in

Table 4.2.1, respectively.

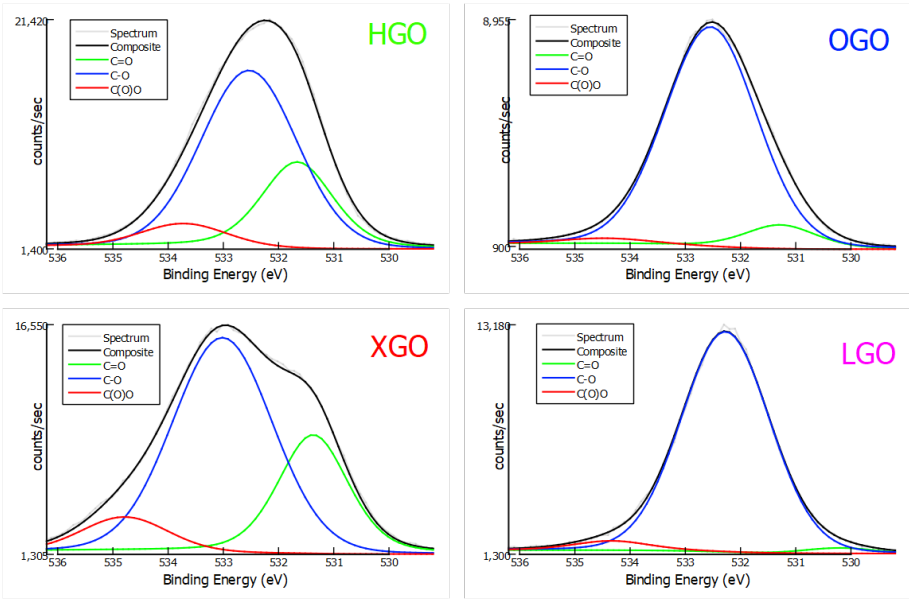

Figure 4.2.8: O1s XPS peak fitting of HGO, OGO, XGO and LGO.

The O1s results further expound on the C1s spectra fitting, with LGO and OGO showing little C=O binding energy by composition, while markedly higher in HGO and XGO. XGO once again has higher shifted bond energies with greater C(O)O presence, made possible by its defective sheet structure. Figures 4.2.9 and 4.2.10 summarize the atomic concentrations (%) of all GO bond energies registered in C1s and O1s XPS, respectively.

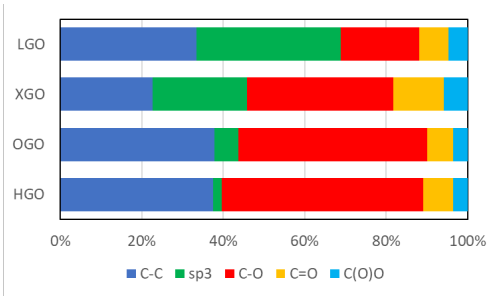

Figure 4.2.9: C1s XPS atomic composition.

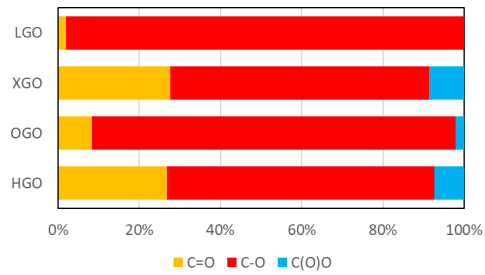

Figure 4.2.10: O1s XPS atomic composition.

HGO's significantly higher IR absorption throughout the FTIR spectra indicates higher oxidation, but from XPS we can further infer that the bond com-

position remains like OGO. The slight proportionate increase of C-O and C=O comes at the expense ofsp^3 bonding. Conversely, LGO's oxidation seems to be more targeted to C-O bonding with freeze dried LGO IR spectra showing immensely high C-O bonding. XPS confirms higher C-O bonding, but also shows significantly highersp^3 bonding, and via FTIR we believe it is unsaturated alkane C-H bonding in LGO. LGO shows least proportionate concentration of carbonyl groups. XGO, due to its violent thermal reduction, has poor, indistinct C1s spectra, although O1s shows similar peak fitting to OGO. Ultimately, despite the modification in treatments, it should be noted that HGO, OGO and LGO exhibit similar C-C bond compositions in XPS, surprisingly lower for XGO despite its reduction.

Figure 4.2.11 shows the TGA and DTG for each GO sample, where the high oxidation of each material is evident (even for XGO).

The curves are offset to better distinguish the nature of thermal deterioration for each nanomaterial. All materials lost approximately 80% of their mass under heating to 950 °C (±5%). The deterioration of ultra-oxidized HGO and LGO are clearly different from OGO, with HGO showing highest water retained, dipping at 50 °C and 170 °C. Although all water retained is lost when heated to 200 °C, the temperature range where the water is lost is different for each GO, where the more oxidized GO's lose water at earlier temperatures compared to OGO and XGO (which show drops in masses at ≥200 °C). The remaining curves follow OGO's trend except for a pronounced drop in mass for LGO at approximately 700 °C. This can be attributed to a shift in C sp^2 to sp^3 bond configurations (Botas et al. 2013). OGO and HGO also have very minor

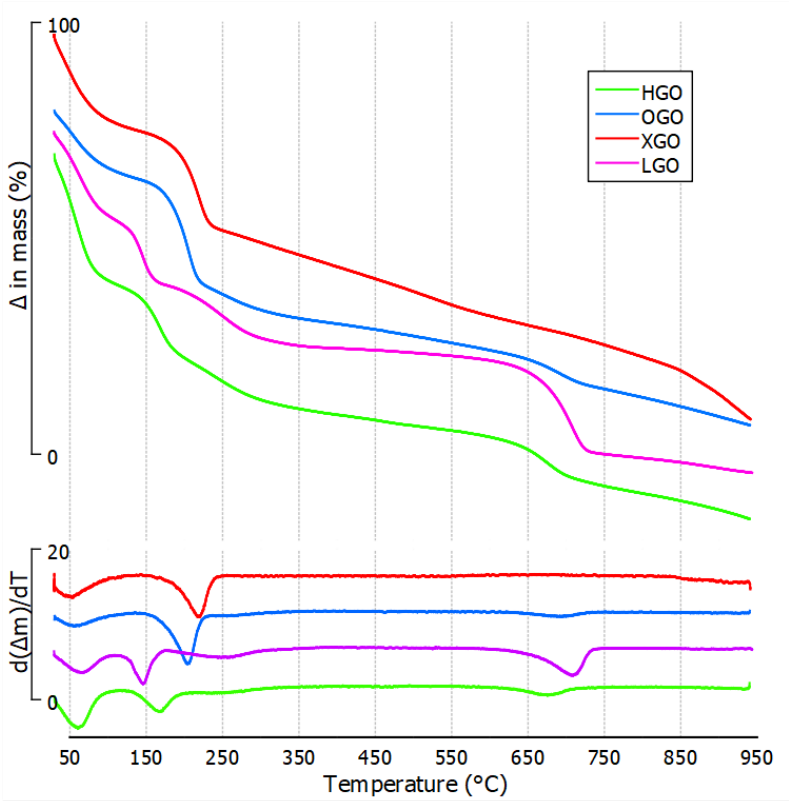

Figure 4.2.11: TGA and DTG curves for each GO nanomaterial.

dips in the 650-700 °C range, also due to the $sp^2 \rightarrow sp^3$ configuration. The 400 to 1000 °C degeneration is typically associated with loss in epoxy and carboxyl groups (Botas et al. 2013), and as thermal reduction mainly removes hydroxyl groups, the drop in mass can be attributed to high epoxy or carbonyl presence. Of all the GOs, LGO is expected to have high hydroxyl presence (which is not removed at temperatures < 1000 °C) and high sp^3 presence, hence apart from its significant loss in mass at 700 °C, it shows the mildest gradient in the carbonyl loss region. Conversely, HGO mimics OGO with a slightly higher gradual loss than LGO, owing to greater oxidation with similar bond ratios to OGO. XGO, possibly due to high carbonyl presence (not altered via thermal reduction) possesses a steep gradual loss in mass from 400 °C onwards. Figure 4.2.12 shows the XRD analysis for all GO variants.

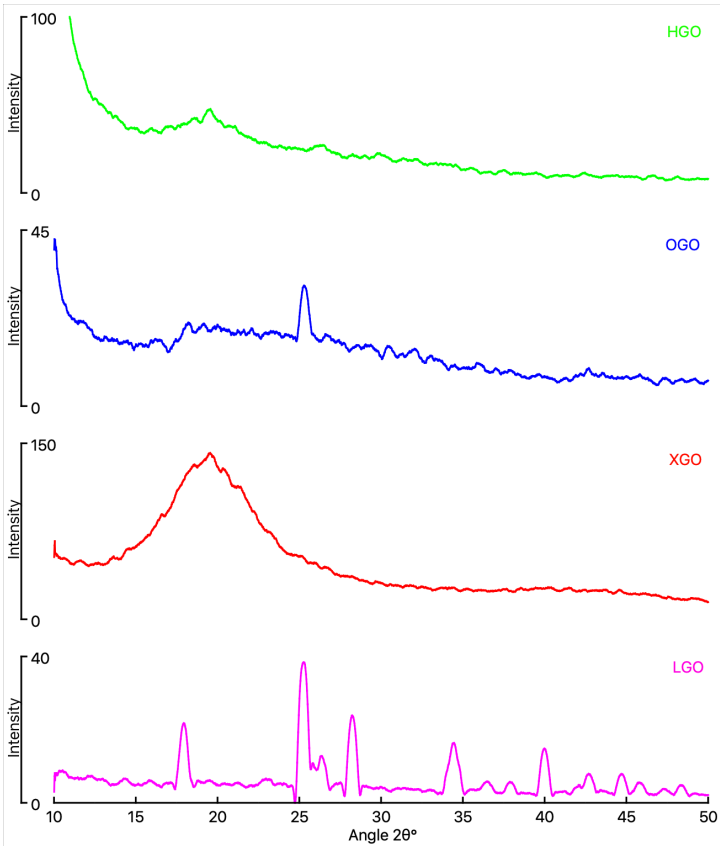

Figure 4.2.12: XRD graphs of all GO variants from 10° to 50°.

As discussed in the Methodology (section 3.4.1), the Bragg's law that defines the diffraction angle can be used to calculate the interlayer spacing of the GO samples. The figure shows typical angle values for the HGO and OGO, despite ultra-oxidation of the former, and XGO's angle is also reflective of the reduced graphene oxide's lower interplanar spacing. However LGO expresses a vast number of fine peaks, implying a range of spacings between it's layers. It should be noted these GO samples were oven dried to keep their hydronium layer intact, hence their interplanar spacings are reflective of the GO suspensions. Table 4.2.2 lists all d spacing values for the GOs.

As both HGO and OGO's peak intensity falls below a 2θ of 10°, which cannot be captured by this machine, their precise d value cannot be measured. However they both exhibit the highest d spacings of all GOs. It is possible

Table 4.2.2: $2\theta^{\circ}$ values and respective interplanar d spacings of GO samples measured with XRD.

	θ	d (nm)	interplanar spacing range (nm)
HGO	10	8.83	mostly 8.83
	19.57	4.53	
	26.49	3.36	
OGO	10	8.83	3.51- (mostly) 8.83
	25.365	3.51	
XGO	19.57	4.53	4.53
LGO	18.01	4.92	2.25-4.92
	25.28	3.52	
	28.22	3.16	
	34.45	2.60	
	39.99	2.25	

that HGO may possess higher interplanar spacing as a result of it's ultraoxidation, but that cannot be ascertained from this XRD machine. OGO also shows a clear secondary peak for d = 3.51 nm (faintly visible in HGO) which hints at the aromatic non-functionalized regions in the nanomaterial not producing enough hydronium to cause interplanar repulsion. Logically HGO with it's ultra-oxidation and initial high stacking of hydronium shows the highest interplanar spacing. XGO exhibits a reduced d of 4.53 nm, with no multiple spacing values. However, LGO shows multiple clear peaks of varying intensities, possessing an interplanar spacing of only 2.25-4.92 nm, which is remarkably low for the ultraoxidized GO. LGO also has finer spacing than XGO, which goes against the logic of ultra-oxidation as the higher hydronium and/or functional group presence should lead to greater water intrusion and repulsion between the LGO sheets. This is explained in greater detail in the following section where to further expound on the effect of these different oxidations, surface charge of the graphene oxide is measured via titration and zeta potential.

4.2.2 Titration and determination of surface charge via zeta potential

Assuming the dynamic structural GO model is valid, this raises a lot questions: primarily, how do we measure the density of the hydronium layer, and more so how do we differentiate GO's particular traits being imparted by the hydronium layer and functional groups categorically? As previously discussed, the Boehm titration does not take base neutralization by protonated water molecules into account. Furthermore, as the oxidations of the GO samples vary, it follows that their hydronium layer should also be protonated differently, either via (i) higher initial density of H_3O^+ molecules, (ii) greater ability to regenerate H_3O^+ molecules or both. To test this hypothesis, potentiometric titrations were performed, and Figure 4.2.13 shows the results for each of the nanomaterials tested. The millimolars of acid or alkalis added were divided by the weight of solid GO in each suspension for standardization.

Despite the higher oxidation of HGO observed from FTIR and XPS, LGO displays the highest initial acidity at pH 1.8, followed by HGO (2.1), OGO (2.5) and XGO (2.6). LGO also requires the highest addition of OH^- (0.006 mM/mg of GO), before its pH level starts to steadily increase, indicating either a (i) high density of H_3O^+ ions or (ii) high regeneration of hydronium that counter any base addition. The latter is more likely as XRD indicated smaller interlayer spacing for LGO, implying less hydroniums present initially. HGO required approximately 0.002 mM/mg GO before its pH started to neutralize, followed by OGO (< 0.001) and XGO (< 0.001). Conversely, the HGO titration had the least steep rising curve, requiring 0.003 mM/mg GO for an increase in pH of 3 to 8, while LGO's pH jumps from 3 to 7 with 0.001 mM/mg GO (0.006 to

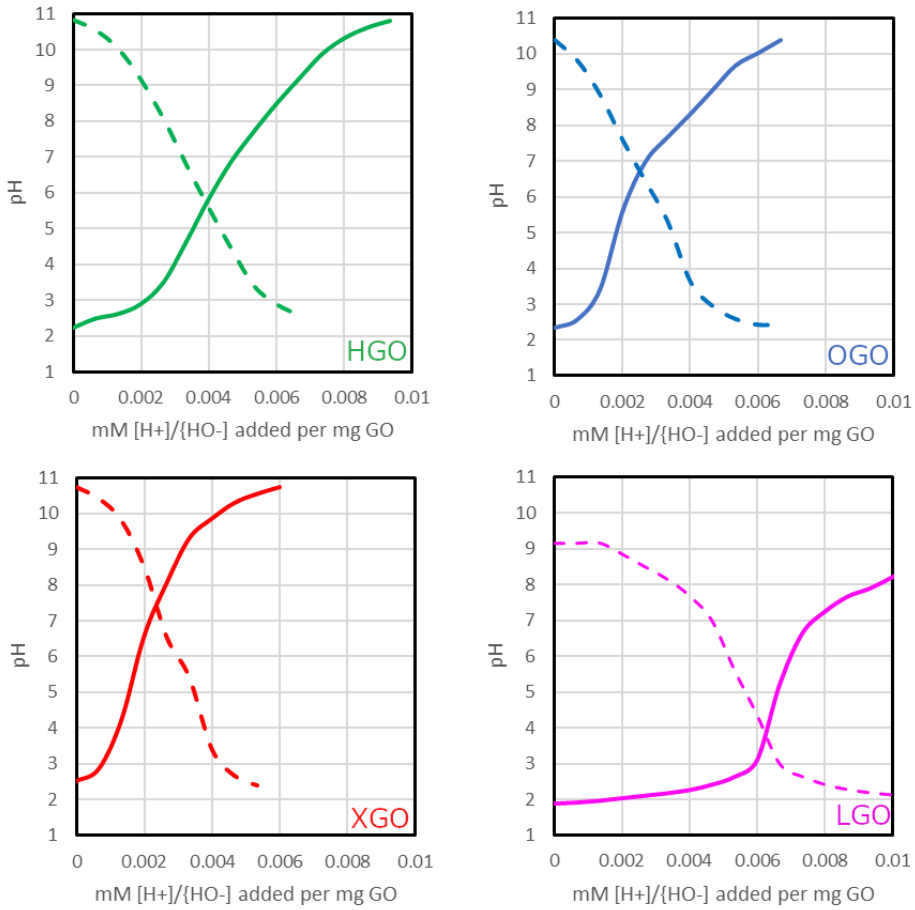

Figure 4.2.13: Titration of all GO variants. Dotted lines indicate back titration of 1 M HCl after 1 M KOH was sufficiently added.

0.007 mM OH^- total). OGO and XGO show similar jumps in pH albeit at lower base concentrations. The steeper pH curves for base addition indicate lower regeneration ability for OGO, XGO and LGO relative to HGO, despite LGO's higher initial resistance to neutralization. It should also be noted that once the pH reaches approximately 7, all pH curves' rate of increase drops, most prominent in LGO, followed by OGO, XGO and HGO. Although, HGO's drop in the rate of pH increase may be shadowed by its overall low rate of increase of pH. Lastly, LGO's overall increase in pH was much lower than the other GO nanomaterials, flat-lining between pH 8 and 9 relative to 10 and 11 for the rest. Back titration with 1 M HCl was performed to obtain the pH equilibration points

(pH_{eq}) for all GO, and logically LGO had the lowest pH_{eq} at 3.8, followed by HGO (5.7), OGO (6.8) and XGO (7.3), respectively. To better understand the regenerative ability of the GO hydronium layer, separate base additions were performed with different waiting intervals (10 seconds and 20 seconds) for the pH reading to stabilize. Longer waiting periods allowed the GOs to counter to the pH increase by protonating surrounding water molecules, hence regeneration. The curves were plotted for each nanomaterial and the ranges were shaded and illustrated in Figure 4.2.14.

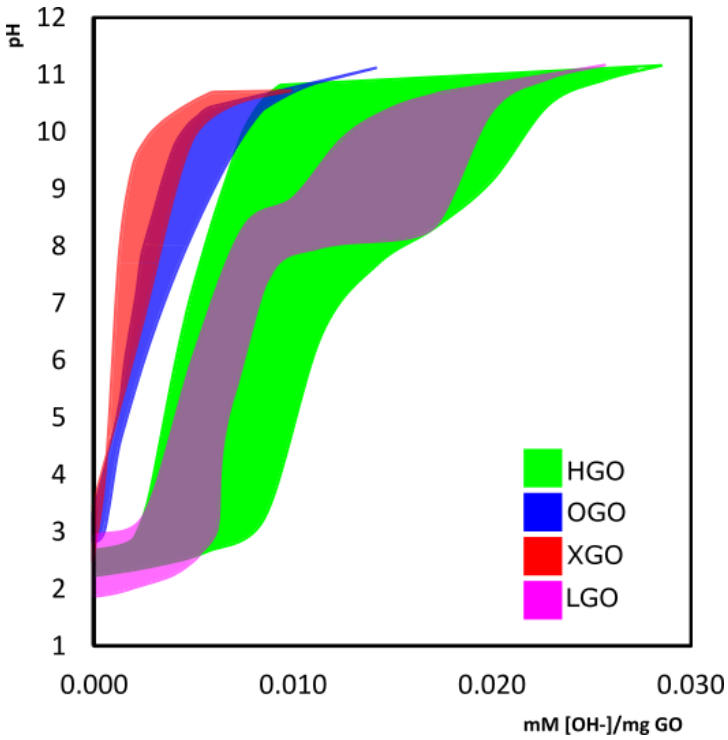

Figure 4.2.14: Range of pH values during base addition with different reading interval times.

Due to its thermal reduction, XGO is neutralized the quickest, followed by OGO. Both GOs exhibit similar range of pH resistance when subjected to higher waiting periods. The broadening of the resistance area after pH 7 is clearly visible. For both ultra-oxidized GOs (HGO and LGO) the resistance area is significantly greater. HGO shows broad resistance area throughout the

pH ranges 3 to 10: the 10 second interval reaching pH 10 at approximately 0.008 mM $[OH]^-$/mg of GO, but when 20 seconds were given for the reading to stabilize, it took more than twice the amount of OH^- (0.020 mM) to reach the same pH. This greatly illustrates how the H_3O^+ layer continues to regenerate and slowly react with the OH^- ions to form water, hence lowering the pH and increasing water molecules in the vicinity for further protonation. However, once the pH crosses 10, it seems the hydroxide concentration is too high and all GOs are unable to provide any resistance to the alkalinity. For LGO, despite greater and higher pH resistance than OGO and XGO, its pH resistance range is completely different from the other GO. Unlike HGO, it's resistance area is not uniformly broad, but rather narrow until pH 8 is reached, where for the 20 second reading interval the pH change is almost flat-lined, indicating much higher H_3O^+ regeneration resisting pH changes (from 0.008 to 0.018 mM [OH-]/mg GO). The initial pH of LGO is also varying, that may be due to dilution of GO into 1.5 mg/mL and waiting for 20 seconds as opposed to 10 for consistent pH value (which drops from 3 to 1.8). To better illustrate the regeneration of H_3O^+, zeta potential tests were carried out for each addition of 50 μL 1 M KOH addition to OGO and XGO, and for each 100 μL addition for HGO and LGO (as they require greater amount of hydroxide ions to neutralize).

During testing, it was observed that even minute additions of KOH caused aggregation of HGO and LGO almost instantly, despite no change in pH. This could be due to the initial removal of GO-hydronium layer: The positively charged GO-DSM sheets are stable in suspension due to the electrochemical double layer repulsion, well known in colloidal studies (Everett 2007), but co-

agulated almost immediately once the layer was base washed, despite the regenerative abilities of HGO and LGO. This is not observed in OGO or XGO. It is plausible that some HGO and LGO sheets get de-protonated before others, leading to GO sheets with opposite charges (GO hydronium have positive charge and stripped GO sheets have negative charge) that attract and aggregate. Chowdhury (Chowdhury et al. 2013, 2015) and Szabo (Szabo et al. 2020) found that even slight presence of metal ions (typically divalent such as Ca^{2+}) caused aggregation of GO. Hence it is surmised that K^+, while not divalent, obstructs the formation of a hydronium layer long enough for GO sheets with opposite net charges to exist, leading to coagulation of sheets before the H_3O^+ layer is regenerated. OGO and XGO did not possess such a dense hydronium layer in the first place and are not oxidized enough to regenerate the hydronium rapidly, so despite the protonation there was no opposite charge attraction and hence no coagulation. Typically, zeta potential is used to approximate the colloidal stability, but we found through our results that despite colloidal instability of HGO and LGO, zeta potential's falling trend correlated with OGO at pH 11 or greater. We believe zeta potential is a much better indicator of net surface charge of GO particles rather than dispersion. Figures 4.2.15 and 4.2.16 illustrate the zeta potentials with respect to both pH and hydroxide concentrations, respectively.

As succinctly outlined by Lowry et al. (2016), zeta potential (via electrophoresis) is typically intended for spherical particles having a diameter of approximately 300 nm or greater. As such, there is an expected error of ±2 mV for each reading, as shown in both above figures. Assuming the GO-DSM model,

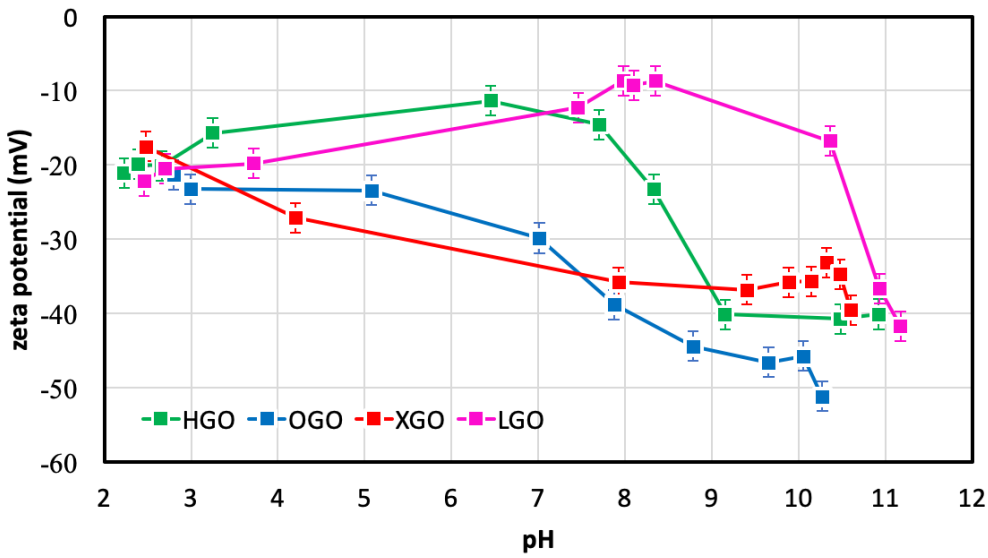

Figure 4.2.15: pH vs. zeta potential for all GO.

the surface net charge of the particles results from opposing negative charges from the C-O functional group, and the positive charges from the H_3O^+ in the surrounding hydronium layer. As shown in both XPS (where sample is subjected to high vacuum) and freeze dried FTIR spectroscopy, the hydronium layer cannot be easily removed, hence its contributions to the overall zeta potential must be accounted for. At no addition of KOH, all GOs exhibit a zeta potential between -17 to -22 mV. As more OH^- are introduced in the suspensions, they strip away the H_3O^+ from the GO layer. Additionally, in more basic conditions there are less water molecules present for GO to protonate and regenerate without the resistance of the hydroxide ions. However, surprisingly both ultra-oxidized GOs display an increase in zeta potential before decreasing sharply to the -40 mV range at high pH values (9 or greater). For LGO, zeta increases to -10 mV at pH 8, coinciding with its flat-lining of pH during base addition shown in Figure 4.2.14. One explanation is as GO is self-regulating in aqueous suspension, there is an equilibrium of H_2O and H_3O^+ molecules

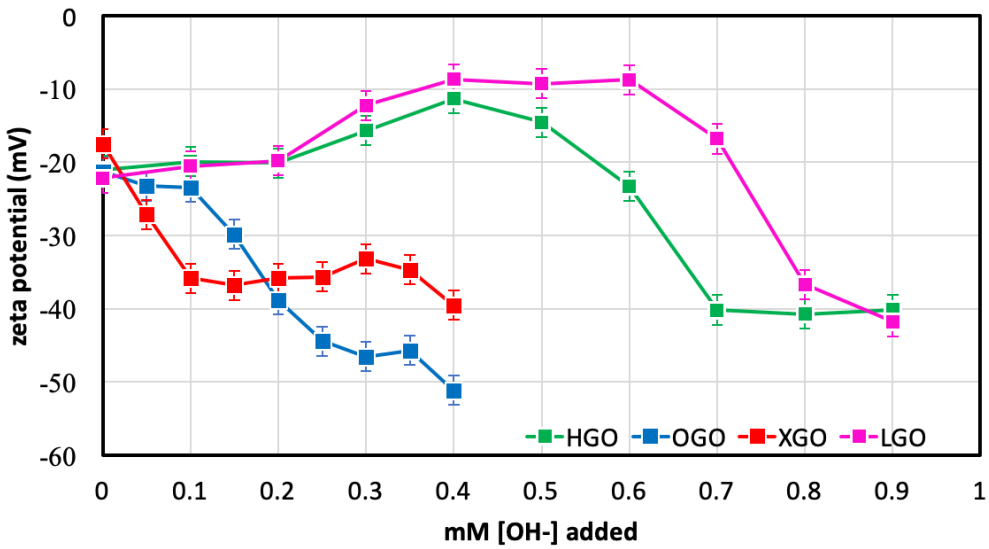

Figure 4.2.16: mM $[OH]^-$ added vs. zeta potential for all GO.

surrounding the GO sheets. For ultra-oxidized GOs such as HGO and LGO, this equilibrium is shifted towards more H_3O^+ which also lends to the higher acidities of their suspensions. As hydroxide ions are flooded into the system, however, this equilibrium is once again shifted, as the H_3O^+ react with OH^- to make H_2O, hence a third variable is introduced into the system (OH^-). To resist the siphoning of hydronium molecules, the GOs then further protonate the new water molecules and in the new three species system (OH^-, H_3O^+ and H_2O) attempt to re-establish the same H_3O^+ density, creating more H_3O^+ in the process. This temporary increase in H_3O^+ increases the positive charge of the system, and with the static negative charges on the GO sheets, shift the net surface charge positively, hence increasing the zeta potential which is exhibited in HGO and LGO. Additionally, as Figure 4.2.14 showed how the resistance ranges for both HGO and LGO are different, this echoes in their increase of zeta potentials as well: HGO shows a slight but uniform increase in zeta for pH 3 to 8 (-20 to -15 mV), while LGO shows a much sharper increase from pH

6 to 8 (-15 mV to -8 mv). HGO's zeta potential reaches -40 mV after pH 8, while LGO takes much higher alkalinity and registers -40 mV zeta potential at pH 11. The drop in zeta potential occurs once the hydroxide influx is too high for the GOs to counteract, and/or when all the hydroxyl groups on the GO sheet have already donated their hydrogen ions for previous protonations. It is hypothesized this behaviour would also exist for OGO but is not prominent enough to fall outside the error ranges or may only occur at low hydroxide concentrations. As XGO is thermally reduced, it has almost no hydronium regeneration ability and hence it's zeta drops sharply with hydroxide addition, with the final zeta potential lying at approximately -38 mV to -40 mV, less negative than OGO's (which reaches -50 mV). This may be it's actual GO sheet charge, but the same cannot be ascertained for HGO and LGO, which require too high OH^- amounts to strip their hydronium production ability, and the high ion concentration in those solutions disrupts the zeta potential measuring ability of the tests. This ultra-oxidized behaviour is illustrated in Figure 4.2.17.

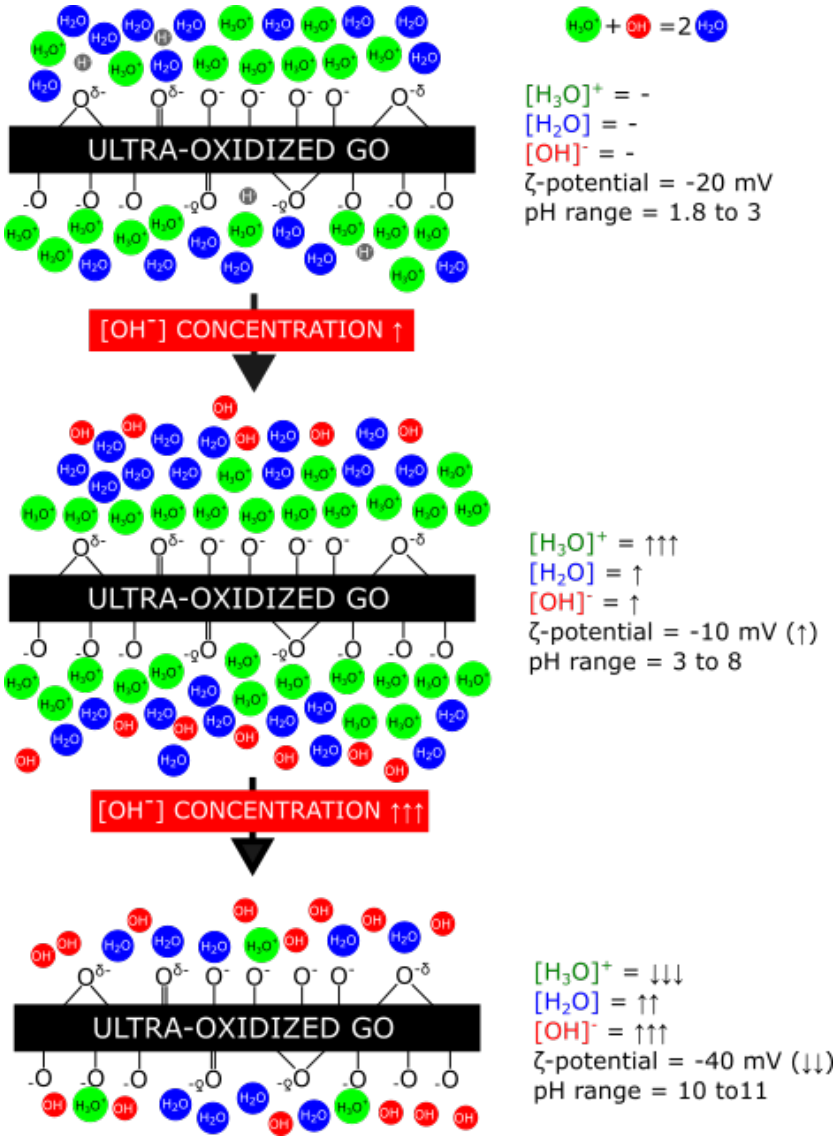

Figure 4.2.17: Illustration of ultra-oxidized GO's hydronium regeneration upon base addition.

4.2.3 Visual and Physical inspection of hydronium layer from SEM/zeta sizing

Figure 4.2.18 shows SEM images of all four freeze-dried GOs. The higher water coating of both ultra-oxidized GO's is evident, as is the bulging of the sheets due to the freeze-drying regimen. Conversely, OGO and XGO have much flatter sheets, with streaks of water coating which may also conceal sheet tearing because of its treatment. XGO, despite being thermally reduced, continues to be water coated, indicating its functionalized groups have not been completely eliminated. Figure 4.2.19 takes a deeper look at the water coating on HGO/LGO before and after freeze drying.

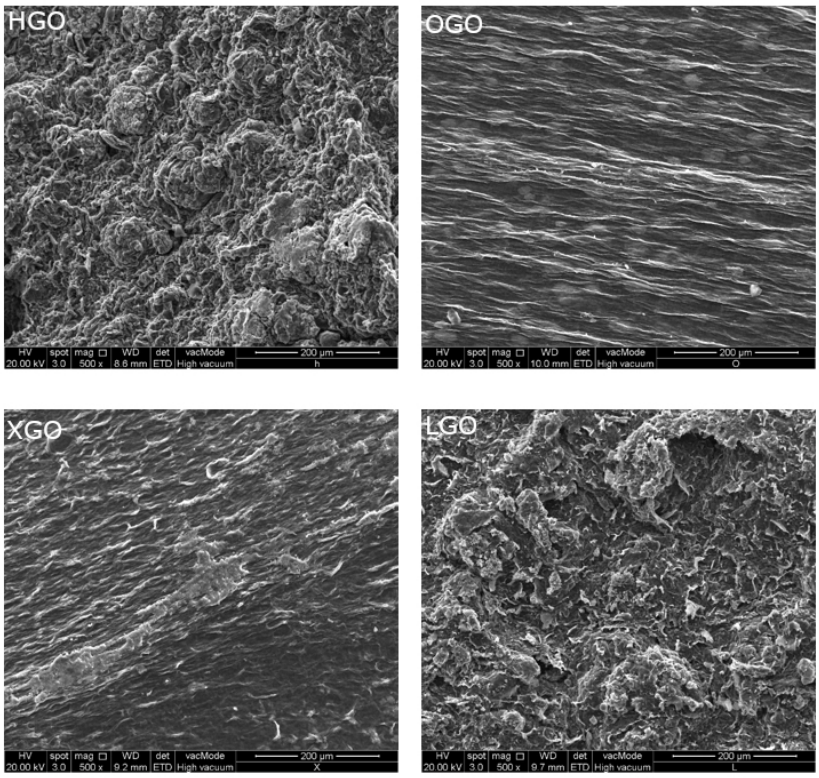

Figure 4.2.18: SEM of all freeze-dried GO samples.

Surprisingly, HGO shows a greater stacking and coating of water/H_3O^+ molecules than LGO before freeze drying. After freeze drying, both GOs ex-

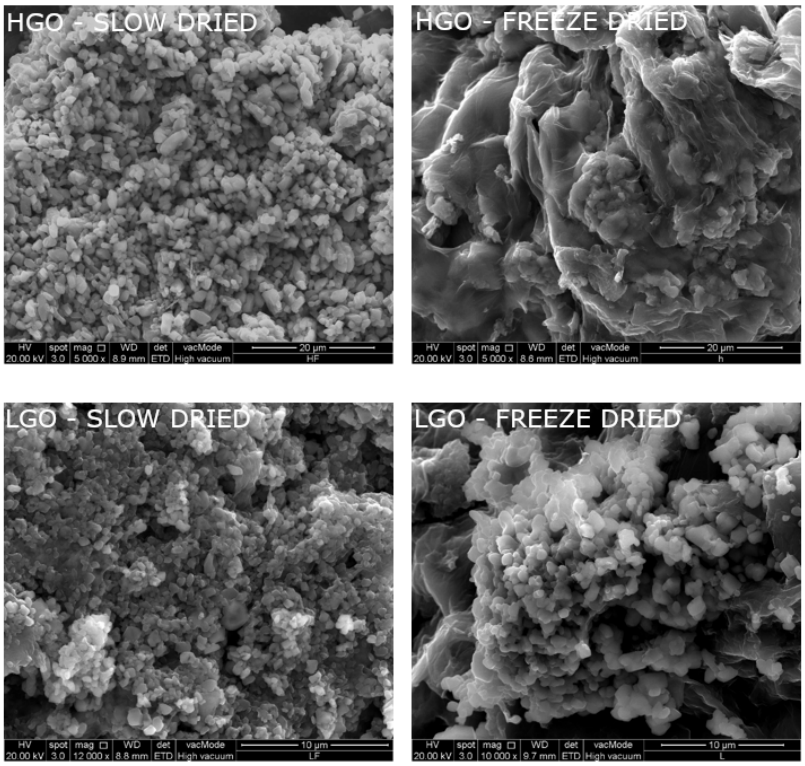

Figure 4.2.19: Comparison of oven dried and freeze dried HGO and LGO.

hibit bulging of sheets: this may be due to suction from freeze drying, attempting to pull away the hydronium layer unsuccessfully, causing distortion and tearing of sheets.

It is inferred that while ultra-oxidation provides excess hydronium ions and serve as seeders for cement particles to initiate hydration, once hydration has begun, the GO sheets themselves regulate the growth of C-S-H along its lateral dimensions, with the protonated H_3O^+ substituting the role of hydrates. The $Ca(OH)_2$ by-product from the cement hydration neutralizes the initial H_3O^+, present in all GOs, but ultra-oxidized HGO and LGO contain an extraordinary capacity to regenerate the H_3O^+ ions and continue to use up the hydroxide ions, as was shown in titration tests on the nanomaterial themselves. Additionally, while LGO does not possess the high initial stacking of water and H_3O^+ molecules (seen in SEM), it develops far more H_3O^+ ions upon base-washing,

especially at pH 7-9 (determined via titration). Zeta sizing also showed LGO having much better sheet integrity upon forced filtration. The longer sheets of LGO provide better regulation for C-S-H growth, which leads to finer pore distribution relative to HGO. However, HGO's high initial H_3O^+ layer provides more nucleating points for C-S-H to grow. Ultimately, they may both improve the cement microstructure, albeit differently. However, an issue lies with the dispersive ability of GOs in divalent ion solutions (Ca^{2+}). Chowdhury (2013, 2015) and Szabo (2020) both showed that even slight quantities of divalent ion presence in GO suspensions can cause coagulation of the nanomaterial, and quantified it using the critical coagulation coefficient (CCC). Divalent ions cause bridging between different GO sheets, hence obstructing proper dispersion. It is believed this may be the reason for reduced workability of GO-cement mixes, and while previous research has lauded this bridging as a source of cement strength improvement, I believe it is the primary deterrent, agglomerating GOs and creating localized strength improvements which do not translate to the overall samples. For the ultra-oxidized GOs, the dense H_3O^+ and it's constant regeneration even under base conditions allows the sheets to remain sufficiently dispersed and reduce chances of Ca^{2+} bridging, while also being a 'canvas' for C-S-H crystals to densely propagate. Conversely, XGO and OGO do not possess this hydronium regeneration layer hence they may be more susceptible to inter-bridging of GO sheets, leading to strength deterioration and/or unpredictable results.

Figure 4.2.20 shows the sizing of GO sheets via zetasizer. It should be noted that this method is quite imprecise, as it is intended for spherical, uniformly

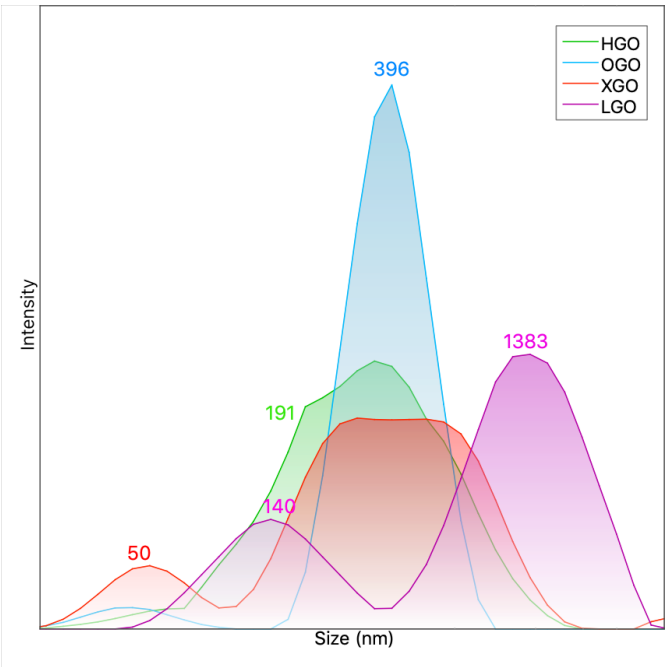

Figure 4.2.20: Zeta sizing of all GO samples after pulse sonication.

sized particles, not polydispersed, sheet-like GO. However, an estimate of the size of GO sheets in suspensions was preferred over drying methods (such as SEM/AFM) to conserve it's nature as it is being incorporated into the cement/concrete mixes. Perhaps unsurprisingly, LGO showed the largest size at approximately 1380 nm, while the remaining GOs fell in the 100-500 nm range. However, any further conclusions cannot be made on zeta sizing. The small lateral sheet sizes should allow greater C-S-H development in the GO-cement mix, as indicated in previous literature research.

4.3 Incorporation of modified GOs into cement and concrete

4.3.1 Workability

Having a low w/c ratio in wet mix creates stronger concrete at the expense of reduced workability, which hinders proper uniform application of concrete in structures before hardening. To increase the flow of concrete, polycarboxylate

superplasticizers are used. They are comb shaped, with a negatively charged backbone that latches on the positively charged cement particles. Meanwhile, the combs themselves have polyethylene oxide groups, which attract water molecules, and 'fan out'. Due to the fanned out branches of the superplasticizer, it is energetically unfavourable for other molecules to come in contact with the wrapped cement molecule, hence steric hindrance is produced (see Figure 4.3.1). This stericity allows the cement and water in the wet mix to fully disperse before initiating any hydration, hence increasing the fluidity and workability of the mix. However, all GO nanoparticles possess a net negative surface charge, due to negative oxygen groups on the sheets, and positive H_3O^+ molecules surrounding the sheet themselves. Hence, their inclusion in wet cement mixes greatly complicates things, as now they may have their own superplasticizer interactions, apart from the cement-GO and cement-superplasticizer interactions themselves. The positive charge of the hydronium layer would be attracted to the backbone of the superplasticizers, however the GO functional groups would repel the same backbone of the molecule. It is hypothesized that ultra-oxidized HGO should co-operate with the polycarboxylate molecules, but LGO not possessing a dense initial hydronium layer may repel the superplasticizer and cause some unwanted chemical effects in the GO-cement interface.

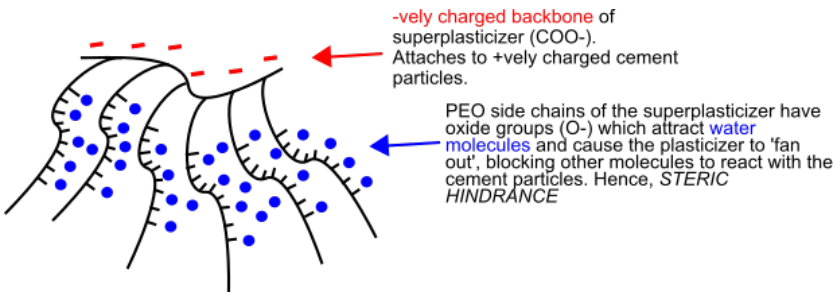

Figure 4.3.1: The make-up of a polycarboxylate superplasticizer molecule.

It is presumed that for the same w/c ratio, all GO based cements (GCs) would have decreased workability wrt control, due to their role in accelerating cement hydration by providing seeding points. To confirm this belief, mini flow tests were carried out and the resulting diameter of the cement spread was measured thrice and averaged. Full slump tests with concrete/mortar were not as beneficial because no slump is registered without the addition of superplasticizer, and w/c ratio had to be kept low to ensure the GOs could perform as seeders. Figure 4.3.2 shows the change in flow diameter wrt control sample for all of the GO-cements with and without superplasticizer. Error bars of ±5% are presumed due to the imprecise nature of flow test (flow table friction, cement quality, flow cone material, cone removal angle etc.) and implementing greater quality control was not logistically feasible.

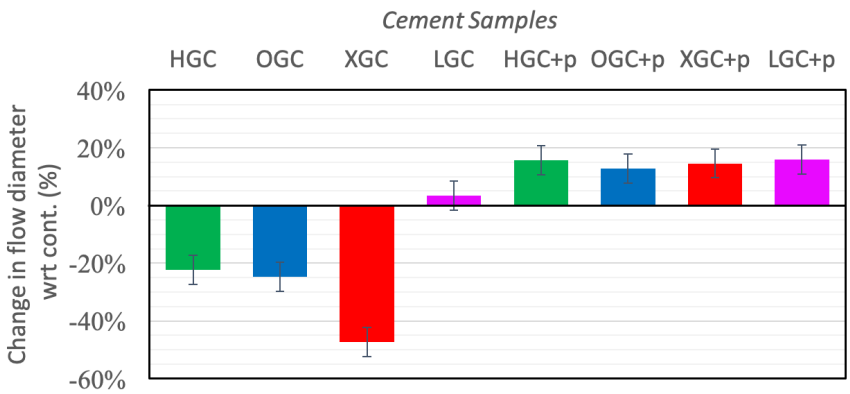

Figure 4.3.2: Flow values for control, GC and GC+p (GC with superplasticizer) samples.

As can be seen in Figure 4.3.2, HGO and OGO based cements showed a 20% decrease in flow, while XGO showed >40% decrease. Surprisingly LGO showed no significant change in workability. Upon addition of 0.5% bwoc superplasticizer all GO based cements showed 10-15% increase in flow wrt control, which is sufficient workability. Next, slump tests were carried out for

control and all GO-concrete batches, with two methods of superplasticizer incorporation. All GCp samples were mixed by adding superplasticizer to a 4 mg/mL concentrated GO suspensions, and maintained at 60 °C for 15 minutes under constant stirring. Meanwhile, all GC+p batches did not undergo any special GO/superplasticizer combination, but both the nanomaterials suspension and superplasticizer was mixed into the water which was then added to the dry mix as usual. The results of the slump test are shown in Figure 4.3.3, with ±10% error anticipated as the test is not precise.

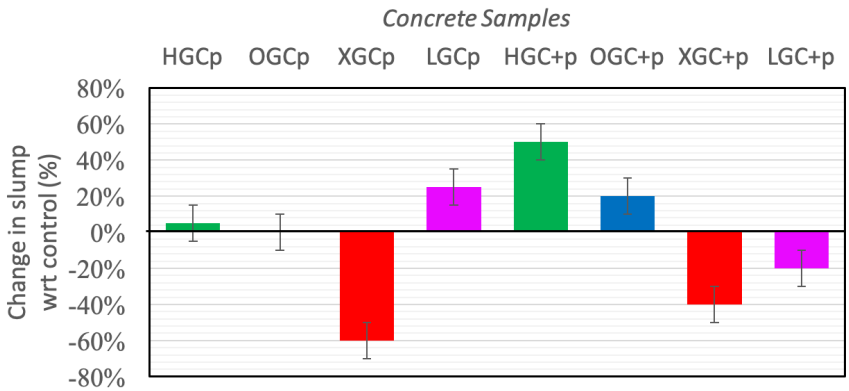

Figure 4.3.3: Slump values for control, GCp and GC+p samples.

Among all GCp samples, XGCp exhibits 60% reduced slump (8 mm) wrt control (20 mm), while HGCp and OGCp show no significant change (approx. 20 mm). LGCp has 20% higher workability at 25 mm. Meanwhile HGC+p showed an approximately 50% higher workability (40 mm slump vs. control at 20 mm), OGC+p at 24 mm, and both XGC+p and LGC+p showed reduced workability as 12 mm and 16 mm, respectively. Due to XGO's thermal reduction and removal of C-O bonds, its ability to produce hydronium is much more limited, hence its surface charge would be relatively negative compared to the remaining GO nanomaterials, attracting less superplasticizers to it while also

interacting with alite and bridging with calcium divalent ions, hence reducing workability.

Adding superplasticizer to cement samples show expected results, with superplasticizers increasing flow uniformly (it should be noted that the control sample does not contain GO but does include superplasticizer). However, LGC showing no change in flow rate without adding superplasticizer is significant. A possible reason for this behaviour could be due to LGO's high regenerating hydroniums under alkaline conditions. This hydronium layer increases the positive charges on the nanomaterials, and may act as a lubricating layer that provides hydronium for cement interactions while regenerating the H_3O^+ layer on the sheet itself which acts as a lubricant, lessening friction and maintaining workability comparable to control. Conversely, HGO has a denser initial H_3O^+ layer that is stripped in the alkaline wet mix, and its lower hydronium regeneration does not offer the same lubrication as LGO, hence it's reduction in workability. For concrete samples, the slump results are harder to infer from due to added variabilities of the fine and coarse aggregates. Pre-treatment of superplasticizer with HGO, OGO and XGO is not as effective at increasing workability as no pre-treatment (HGC+p, OGC+p, XGC+p), but the opposite holds true for LGCp and LGC+p.

Out of all the GO, LGO showed the most negative surface charge from zeta potential tests, arising from it's low initial hydronium counting and highly oxidized negative C-O^- bonds on it's sheet. However, even a slight increase in OH^- ions instantly decreased the surface charge (considerably more than HGO) due to it's high generation/regeneration potential of hydronium. Hence, upon con-

tact with cement in flow tests (in absence of PC superplasticizer), this generated hydronium was able to repel the positively charged dissociated cement particles and workability remained unaffected/increased. When pre-treated with superplasticizer (LGCp), the negative surface charges on both the plasticizer and LGO successfully repelled each other, hence when finally poured in the cement/concrete mix the superplasticizers are able to completely interact with cement and workability is higher than control. However, when no pre-treatment is performed (LGC+p), LGO immediately starts generating hydronium which diverts the superplasticizers and makes them cap the GO instead of the cement, decreasing the workability relative to LGCp. Conversely, HGO has a dense initial hydronium layer, which regardless of superplasticizer treatment, is dense enough to fulfil the capping of superplasticizer (making them drift away instead of surrounding the nanomaterial) and regenerating hydronium to allow for C-S-H planting, nucleation and growth. XGO's reduced nature is once again highlighted as it shows decreased workability with or without pre-treatment, made worse in concrete due to added friction of the aggregates. The effects of these different plasticizer-GO interactions are also discussed in Sections 4.3.2 and 4.3.3, when comparing 28 day compressive and flexural strengths, respectively.

4.3.2 Compressive strength

The average 28-day compressive strength of 3 concrete cubes for each GO with and without superplasticizer pre-treatment were measured and the respective stress-strain curves were calculated. Figure 4.3.4 compares the stress-strain for each GCp and GC+p sample, while Figures 4.3.5 and 4.3.7 compare all GCp and

GC+P samples, respectively. The ultimate compressive strength of all GCp and GC+p samples (along with their % change in stress compared to control) are also plotted in Figures 4.3.6 and 4.3.8 . Ultra-oxidized GOs clearly improved the compressive strength of concrete with or without superplasticizer treatment, however HGO and LGO reacted differently to the treatment itself. HGO improved concrete's ultimate compressive strength similarly regardless of pre-treatment with superplasticizer, increasing it by 28% wrt control (52 MPa vs 40 MPa control).

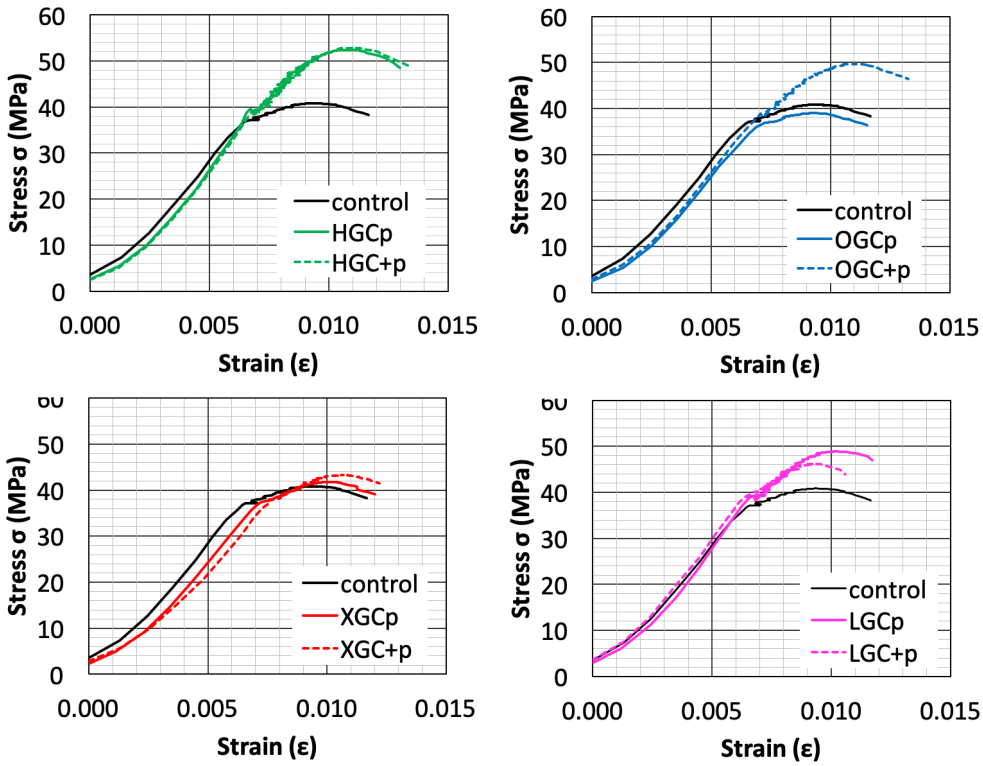

Figure 4.3.4: Comparison of compressive strength curves for GCp and GC+p samples.

What may be more beneficial is the added ductility to concrete, as at fracture the strain borne by HGCp is 11% higher than control (0.013 vs 0.011) and HGC+p is 16% greater (0.0135), shown in Figures 4.3.9 and 4.3.10. While LGO has also significantly improved concrete's strength, there is no ductility improvement for LGCp, and 9% reduced fracture strain for LGC+p (0.0106).

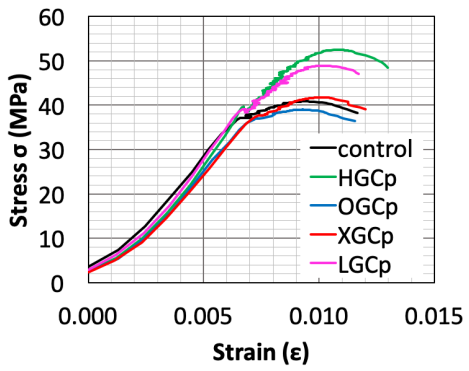

Figure 4.3.5: Compressive strength curves for all GCp samples.

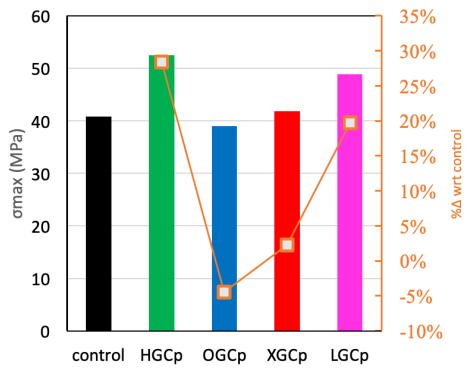

Figure 4.3.6: Ultimate stress comparison for all GCp samples.

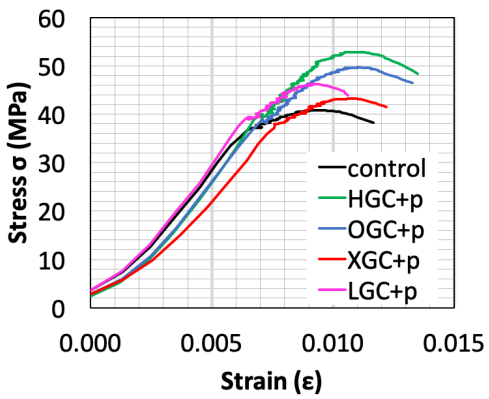

Figure 4.3.7: 28-day compressive strength curves for all GC+p samples.

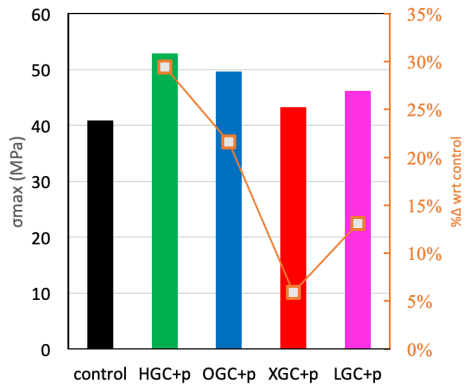

Figure 4.3.8: 28-day compressive strength comparison for all GC+p samples.

LGCp's ultimate compressive strength was 48 MPa (20% > control), while LGC+p only showed a 13% improvement (46 MPa). LGO appears to not mix well with superplasticizer without heating or stirring, greatly reducing the already low ductility of concrete if not pre-treated. OGO seems to follow the opposite trend, with OGCp actually being only slightly weaker than the control (39 vs 40 MPa). OGC+p however, has maximum compressive strength of 49 MPa, higher than LGCp and second only to HGO based concrete. OGC+p also significantly improves concrete's durability, however not applicable for OGCp. This again reinforces how hydronium regeneration which is not significant in OGO, does not allow high strength improvements relative to LGCp. Finally, as expected

the thermally reduced XGO showed the worst GO performance, with XGCp < control in compressive strength (39 vs 40 MPa), and XGC+p only slightly improved at 43 MPa.

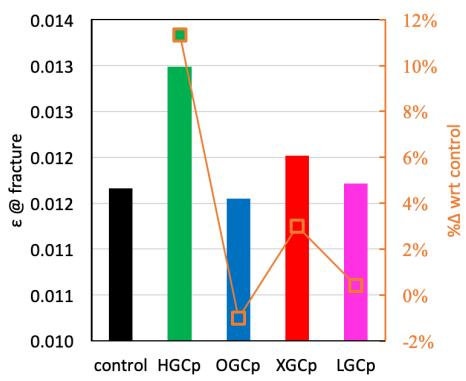

Figure 4.3.9: Fracture strain for all GCp samples.

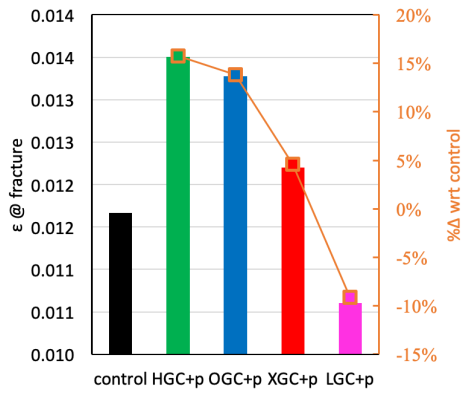

Figure 4.3.10: Fracture strain for all GC+p samples.

The Young Moduli difference (the slope for the linear portion of the stress-strain curves) between all GC samples are shown in Figures 4.3.11 and 4.3.12. Finally, all of the above results are tabulated in Tables 4.3.1, 4.3.2 and 4.3.3.

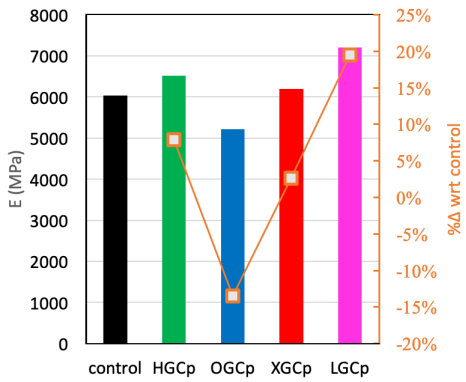

Figure 4.3.11: Young Moduli for all GCp samples.

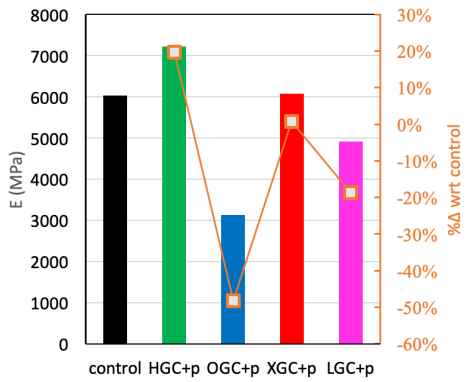

Figure 4.3.12: Young Moduli for all GC+p samples.

Table 4.3.1: Ultimate compressive strength and respective strain values for all GC samples wrt. to control.

	σ_{max}(MPa)	%Δ wrt control	ϵ@ σ_{max}	%Δ wrt control
control	40.85		9.31E-03	
HGCp	52.45	28%	1.08E-02	16%
OGCp	39.02	-4%	9.29E-03	0%
XGCp	41.79	2%	1.03E-02	11%
LGCp	48.89	20%	1.02E-02	10%
HGC+p	52.86	29%	1.11E-02	19%
OGC+p	49.68	22%	1.10E-02	18%
XGC+p	43.27	6%	1.06E-02	14%
LGC+p	46.20	13%	9.24E-03	-1%

(Table is colour-coded green to red highlighting best to worst performing samples, respectively.)

Table 4.3.2: Fracture strain and corresponding strength values for all GC wrt to control.

	ϵ_{max}	%Δ wrt control	σ @ fracture	%Δ wrt control
cont	1.17E-02		38.30	
hGCp	1.30E-02	11%	48.42	26%
oGCp	1.15E-02	-1%	36.41	-5%
XGCp	1.20E-02	3%	39.12	2%
LGCp	1.17E-02	0%	47.04	23%
hGC+p	1.35E-02	16%	48.42	26%
oGC+p	1.33E-02	14%	46.43	21%
XGC+p	1.22E-02	5%	41.44	8%
LGC+p	1.06E-02	-9%	43.97	15%

(Table is colour-coded green to red highlighting best to worst performing samples, respectively.)

Table 4.3.3: Young Moduli and %Δ wrt control for all GC samples.

	E (MPa)	%Δ wrt control.
control	6033.5	
hGCp	6510.0	8%
oGCp	5218.8	-14%
XGCp	6193.5	3%
LGCp	7207.1	19%
hGC+p	7222.0	20%
oGC+p	3125.9	-48%
XGC+p	6074.7	1%
LGC+p	4910.3	-19%

(Table is colour-coded green to red highlighting best to worst performing samples, respectively.)

4.3.3 Flexural Strength

As GO improves the C-S-H microstructure, it is expected that not only the compressive strength, but flexural strength and resistances of concrete would also improve significantly. Figures 4.3.13 and 4.3.14 show the 28-day peak bending strength and % improvement for all GCp and GC+p samples, which are also presented in Table 4.3.4. Almost all samples exhibited >20% improvement in flexural strength, with LGCp showing a 40% higher peak flexural strength vs. control (23 vs 16.4 MPa). LGC+p by comparison, had lower bending strength at 20.4 MPa. XGC+p is the singular exception, only showing a 1 MPa increase wrt control. However, the benefits for each GO incorporation cannot be fully discerned due to imprecision of the three-point bending testing machine, and also strength variabilities due to quasi-brittle effects in large concrete samples (Bažant & Planas 2019). Additionally due to scheduling delays from Covid-19 pandemic and logistic issues, only 1 prism was created for flexural strength measurement. As such, small cement beams were created to further conduct bending strength examinations. Their results are summarized in Figure 4.3.15 and Table 4.3.5.

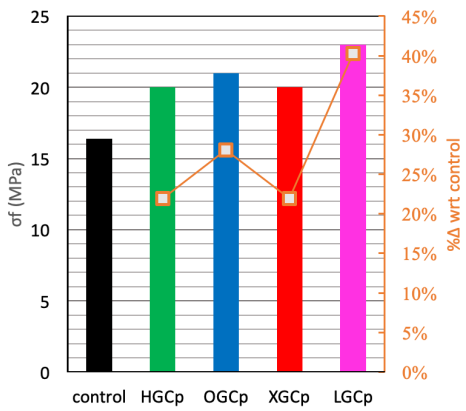

Figure 4.3.13: 28-day flexural strength for all GCp concrete samples.

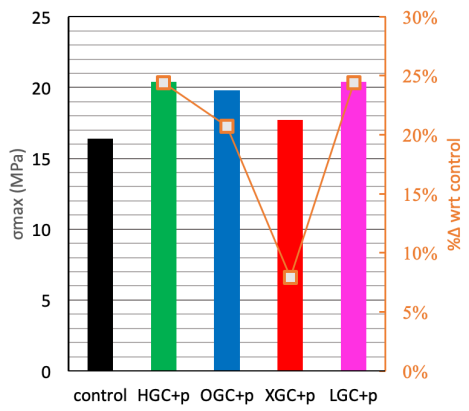

Figure 4.3.14: 28-day flexural strength for all GC+p concrete samples.

Table 4.3.4: 28-day flexural strength and %Δ change wrt control for all GC concrete samples.

	σ_f (MPa)	%Δ wrt control
control	16.4	
hGCp	20	22%
oGCp	21	28%
xGCp	20	22%
LGCp	23	40%
hGC+p	20.4	24%
oGC+p	19.8	21%
XGC+p	17.7	8%
LGC+p	20.4	24%

(Table is colour-coded green to red highlighting best to worst performing samples, respectively.)

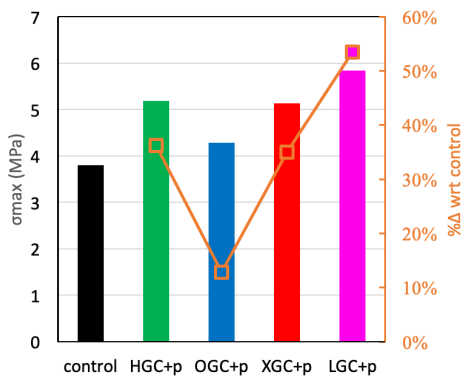

Figure 4.3.15: 28-day flexural strength for all GCp cement samples.

Table 4.3.5: 28-day flexural strength for all GC+p cement samples.

	σ_f (Mpa)	%Δ wrt control
control	3.80	
HGC+p	5.18	36%
OGC+p	4.29	13%
XGC+p	5.14	35%
LGC+p	5.84	54%

(Table is colour-coded green to red highlighting best to worst performing samples, respectively.)

Only GC+p samples were tested, as the samples were so small the quantity of GO and superplasticizer was already minute, and it was feared any heating pre-treatment would raise the mix temperature of the water, or affect the GO concentrations by evaporation. All samples showed an increase in bending strength, with LGC+p registering 5.84 MPs vs control's 3.81 MPa. As the samples are very small, such low values are typically expected as cement is generally very weak in tensile and flexural strength if not reinforced. To summarize the strength and workability findings, Table 4.3.6 lists all improvements (or reductions) for each GC sample. HGC is the best performer, regard-

Table 4.3.6: Summary of strength and workability results for all GC samples.

		%Δ wrt control						Comments			
		σ_c ult	E	ϵ_{max}	σ_f cement	σ_f concrete	slump	comp. strength	ductility	flex. strength	workability
HGC	p	28	8	11		22	5	↑	↑	↑	↑
	"+p"	29	20	16	36	24	50				
OGC	p	-4	-14	-1		28	0	±	±	↑	-
	"+p"	22	-48	14	13	21	20				
XGC	p	2	3	3		22	-60	-	-	↑	↓
	"+p"	6	1	5	35	8	-40				
LGC	p	20	19	0		40	25	↑	↓	↑	±
	"+p"	13	-19	-9	53	24	-20				

↑ = improved − = no change ↓ = deteriorated ± = variable

less of pre-treatment strength, ductility and workability have all shown improvement. LGC shows highest flexural strength improvement, and with pre-treatment also shows higher compressive strength and more workability. Conversely, OGC's performance is unpredictable, but significantly worse with pre-treatment. XGC ultimately shows worst workability and only slight strength improvements. Appendix 3 (section 6) shows the compressive and flexural strengths for each sample that were averaged.

4.3.4 Detecting C-S-H production via analytical characterizations

Typically, FTIR is used to detect compound molecule vibrations and stretching, suited for organic materials. However, cement possesses silica and carbonate bonds, not to mention water, which can be used to indicate hydration (Hughes et al. 1995, Fernández-Carrasco et al. 2012, Ylmén & Jäglid 2013). A lot of carbonate, silica, oxygen and sulphate bonds can overlap in their molecular stretching/bending vibrational frequencies, making pinpointing quantities very difficult. Nevertheless, to gain a better understanding of cement hy-

dration, Figure 4.3.16 shows the development (or reduction) of certain wavelengths in control sample that will illustrate their molecular components.

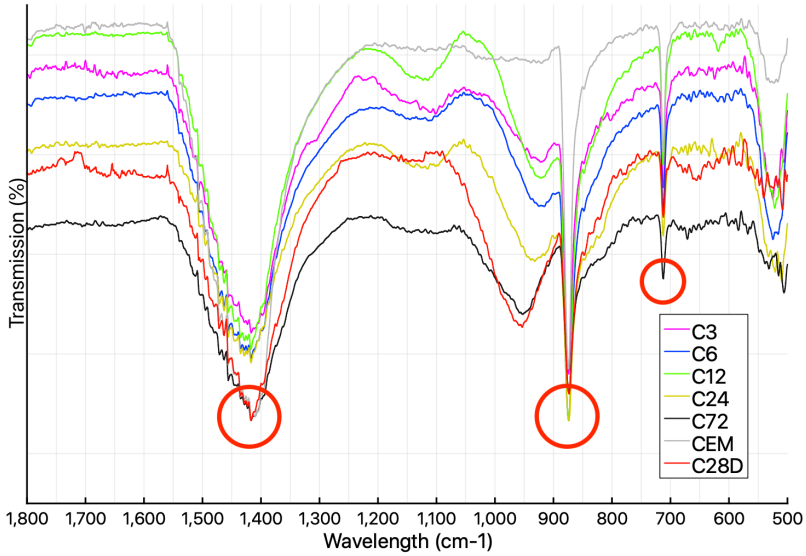

Figure 4.3.16: FTIR spectra of control over 28 days of hydration.

C in their acronym refers to the control, while the number refers to respective hours of hydration. 28D is the 28 day hydrated sample. CEM is unhydrated cement.

From Figure 4.3.16 certain wavelengths can be seen, that are present in unhydrated cement and continue to persist even after 28 days of hydration. These peaks lie at approximately 1410 cm^{-1}, 870 cm^{-1} and 710 cm^{-1}, and all can be attributed to calcium carbonate in calcite (Fernández-Carrasco et al. 2012). As all these samples were excessively freeze dried (72 hours at 0.1 mbar), most of the O-H and water bending/stretching mode vibrations have been removed, hence leaving only 2-3 peaks of concern (in the 1500 cm^{-1} to 500 cm^{-1} range). From zero hours (cement) to 12 hours, a peak develops at 1120 cm^{-1}, and this is attributed to sulphate bonds from ettringite build-up (Ylmén & Jäglid 2013). After 12 hours, the growth of this peak stagnates and subsides from 24 hours until full 28-day hydration. The peak of most concern is at 900-1000 cm^{-1}, the C-S-H peak (Ylmén et al. 2009). While unhydrated cement understandably has no

such peak, even from 3 hours of hydration the peak is clearly evident, and continues to grow at 28 days. Most interestingly, as it grows, it also shifts higher, as at 3 to 24 hours the peak stands close to 930 cm^{-1}, while after 72 hours to 28 days the peak has shifted and stays around 950-1000 cm^{-1}. Due to variabilities in IR spectra capture, it is hard to quantify how much C-S-H is produced from these peaks, but the rate of shift of this peak over hours or hydration is identifiable and can be used to gauge how nanomaterial incorporation has affected C-S-H growth rate and form. Figures 4.3.17, 4.3.18, 4.3.19 and 4.3.20 show the FTIR spectra of each HGC+p, OGC+p, XGC+p and LGC+p over different periods of hydration. Figure 4.3.21 shows the isolated 900-1150 cm^{-1} peaks to better see the shift in each GC+p sample.

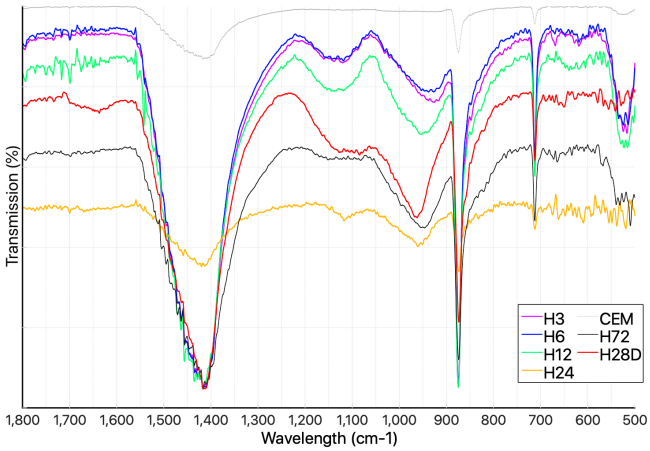

Figure 4.3.17: FTIR spectra of HGC+p over 28 days of hydration.

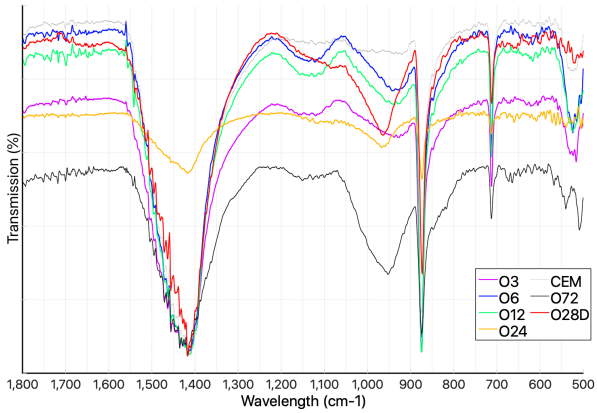

Figure 4.3.18: FTIR spectra of OGC+p over 28 days of hydration.

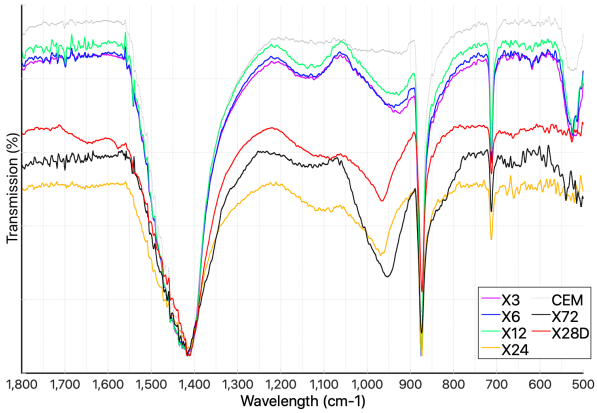

Figure 4.3.19: FTIR spectra of XGC+p over 28 days of hydration.

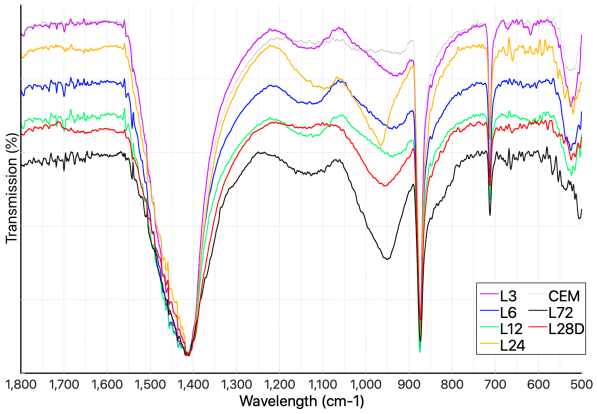

Figure 4.3.20: FTIR spectra of LGC+p over 28 days of hydration.

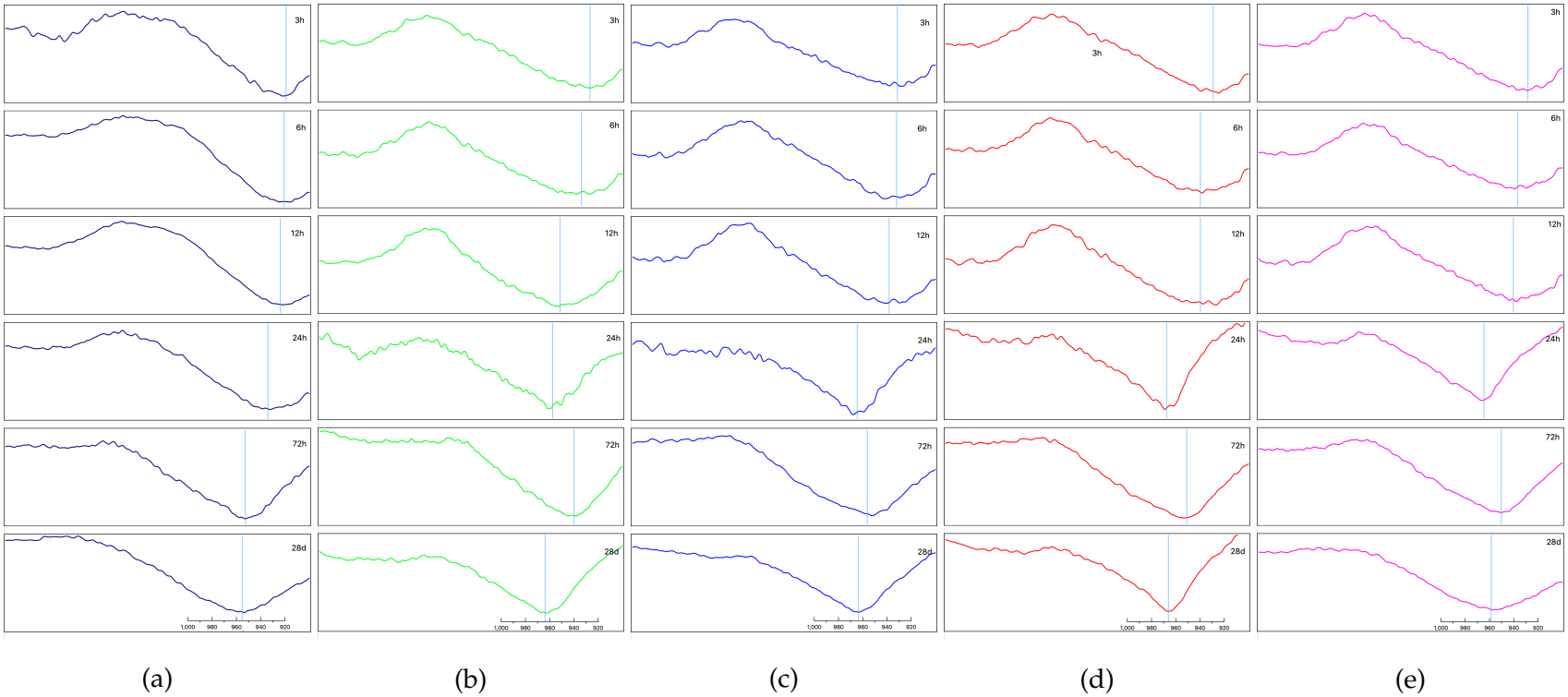

Figure 4.3.21: IR spectra shift of (a) control, (b) HGC+p, (c)OGC+p, (d) XGC+p, and (e) LGC+p samples.

The number refers to the hours of hydration of the respective sample, while 28D refers to 28 day hydrated sample.

As can be clearly seen, all GCp samples show early shifting of the peaks. The peak shift amount vs. hours of hydration (up to 72 hours) as plotted in Figure 4.3.22 and tabulated in Table 4.3.7. The control sample shows a very gradual shift over hours of hydration, rising from 920 to 950 cm^{-1} over 3 days. Conversely, all GCp samples peak shifted to the 955-965 cm^{-1} range in the first 24 hours, and decreased over time. This implies an acceleration of C-S-H growth, followed by regulation back to the same peak as control, regardless of the oxidation degree of GO. Additionally, there is a small rise in FTIR shift for 6-h hydrated XGC+p and LGC+P, indicating these nanomaterials have also affected the second stage of early hydration (section 2.4.1) but more hours of hydration measurements need to be performed to verify its accuracy. HGC+p shows the earliest uniform rise in peak shift, but it's actual peak shift at 24 hours is much less than the remaining GC+p samples (958 vs 965 cm^{-1}). Typically, a higher shift of wavelength signifies reduction in bond length of the molecular vibrations being measured. It can be then hypothesized that a denser microstructure may in fact cause compaction of molecules and reduction in bond lengths, but the shift is not drastic enough to confirm this. However, there is no denying that C-S-H growth rate and density have been altered by the addition of nanomaterials.

Table 4.3.7: FTIR shift of C-S-H peak during hydration.

hydration (h)	control (cm^{-1})	HGC+p (cm^{-1})	OGC+p (cm^{-1})	XGC+p (cm^{-1})	LGC+p (cm^{-1})
3	919	927	931	929	928
6	920	934	932	940	936
12	923	951	938	940	940
24	934	958	965	967	965
72	952	948	956	951	950
672	955	964	964	966	959

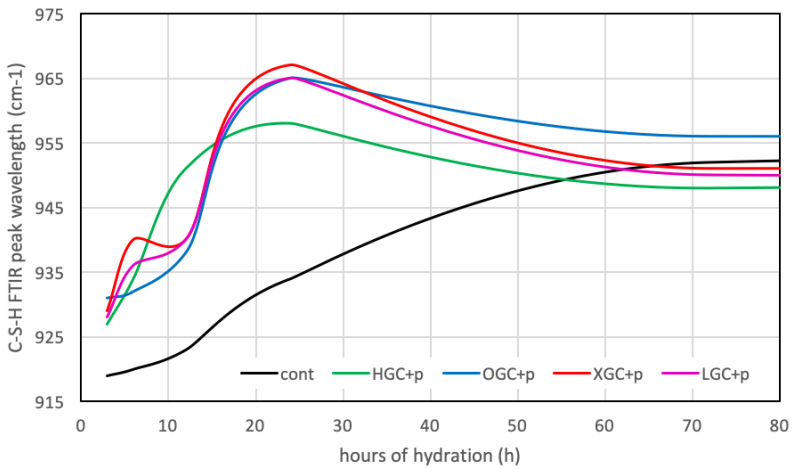

Figure 4.3.22: FTIR shift of C-S-H peak over hydration.

To confirm a change C-S-H density, the 24-hour samples were subjected to porosity tests. Table 4.3.8 outlines the BET porosity results showing the surface area estimates via Langmuir, single point and BET plot calculations. In addition, the pore volume and width are also calculated.

Table 4.3.8: Summary of results from BET porosity tests.

	HGCO	OGC	XGC	LGC	CONT
Surface Area (m^2/g)					
Single point surface area @ $P/P_o \approx 0.200$:	9.9152	7.5165	8.9045	9.5611	6.9426
BET Surface Area	10.0062	7.5631	8.9391	9.7133	7.1077
Langmuir Surface Area	13.6617	10.303	12.1681	13.324	9.7846
BJH Adsorption cumulative surface area of pores (17 - 3000 Å)	6.832	5.305	6.546	6.775	6.759
BJH Desorption cumulative surface area of pores (17 - 3000 Å)	14.1139	10.296	12.7983	11.2602	11.5817
Pore Volume (cm^3/g) - lower is better					
BJH Adsorption cumulative volume of pores (17 - 3000 Å)	0.058915	0.051263	0.079149	0.043513	0.052973
BJH Desorption cumulative volume of pores (17 - 3000 Å)	0.060087	0.052032	0.079908	0.044817	0.05288
Pore Size (Å) - lower is better					
Adsorption average pore width (4V/A by BET):	160.333	194.0097	212.4599	132.1839	229.3798
Desorption average pore width (4V/A by BET):	182.4244	225.9315	245.2477	127.9074	259.2231
BJH Adsorption average pore width (4V/A):	344.92	386.5	483.679	256.908	313.504
BJH Desorption average pore width (4V/A):	170.29	202.143	249.746	159.206	182.66

(Table is colour-coded green to red highlighting best to worst performing samples, respectively.)

From the summary of results, it is observed that despite three different measurements of surface area, the ultra-oxidized HGCp and LGCp consistently show the highest cumulative surface area, with HGCp $\geq$ 40% relative to control, and LGCp at $\geq$ 36%. Surprisingly, OGCp performed worse than XGCp, at 5 - 8% improvement vs. 24 - 28% improvement, respectively. As previously established, C-S-H nucleation and microstructure depends primarily on amount of surface area available to facilitate said growth (Neville 2019), and employing ultra-oxidized GOs significantly increased the surface area of the samples. This increase signifies a more regulated, denser C-S-H microstructure. Conversely, the pore size results indicate LGCp has the finest pore distributions, with an average width of 127-132 Å (at least 42% smaller than control's 229-259 Å pore width), followed by HGCp (30% smaller), OGCp (13%) and XGCp (5%). Additionally, from the isotherm adsorption and desorption curves (Figures 4.3.23 and 4.3.24), we can see that pore distribution is considerably different between LGCp and HGCp. Adsorption isotherms indicate HGCp, XGCp and LGCp all had greater N_2 adsorption than the control (for relative pressures up to 0.5), hence it can be inferred they possess finer pores that are filled up quicker than both control and OGCp based cement samples. After P/P_0 of 0.6 the control sample's adsorption rate greatly increases, leaving behind OGCp and trailing HGCp and XGCp. LGCp's adsorption rate falls (relative to other samples) until P/P_0 0.9, indicating it does not have as many macropores that facilitate multilayer adsorption unlike HGCp or XGCp. OGCp, despite being more oxidative than XGCp, shows considerably lower adsorption throughout the isotherm, which raises concern about its *in-situ* efficacy.

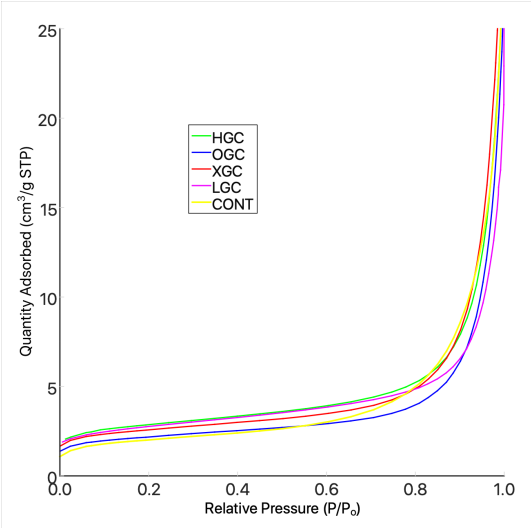

Figure 4.3.23: Adsorption isotherms of all 24 hour cured cement samples.

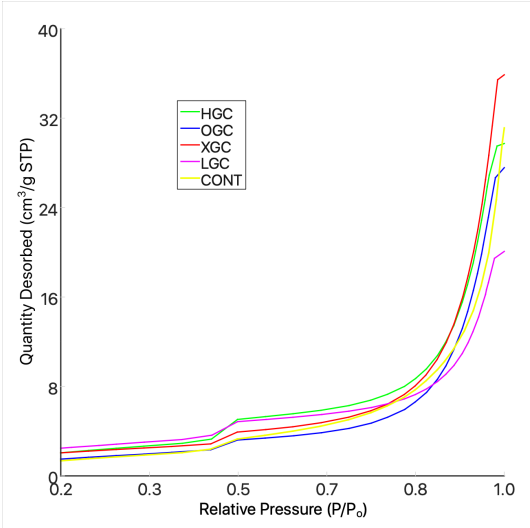

Figure 4.3.24: Desorption isotherms of all 24 hour cured cement samples.

Desorption curves (Figure 4.3.24) show highest initial retainment of N_2 gas for XGCp, followed by control, HGCp, OGCp and LGCp, respectively. These results indicate macropores being emptied, with higher amounts indicating bigger pores filled with N_2 gas. At lower relative pressures (0 to 0.8), both ultra-oxidized GCps exhibit similar high desorptions, indicating their finer pore distributions. XGCp trails behind, followed by control and OGCp, respectively.

Figure 4.3.25 shows the BET plots for control and each of the GCp samples. All samples show excellent correlation with positive interpolated y intercept values reassuring data meets quality criteria. Control has the highest BET line, followed by OGCp, XGCp, LGCp and HGCp, which indicate the specific surface area (lower the y-intercept, higher surface area), which was validated in BET summary Table 4.3.8.

Hence, from the above results, we gather that the higher the oxidation of GO, the denser the C-S-H microstructure and better overall strength. Furthermore, higher oxidation shows consistently improved results in both mi-

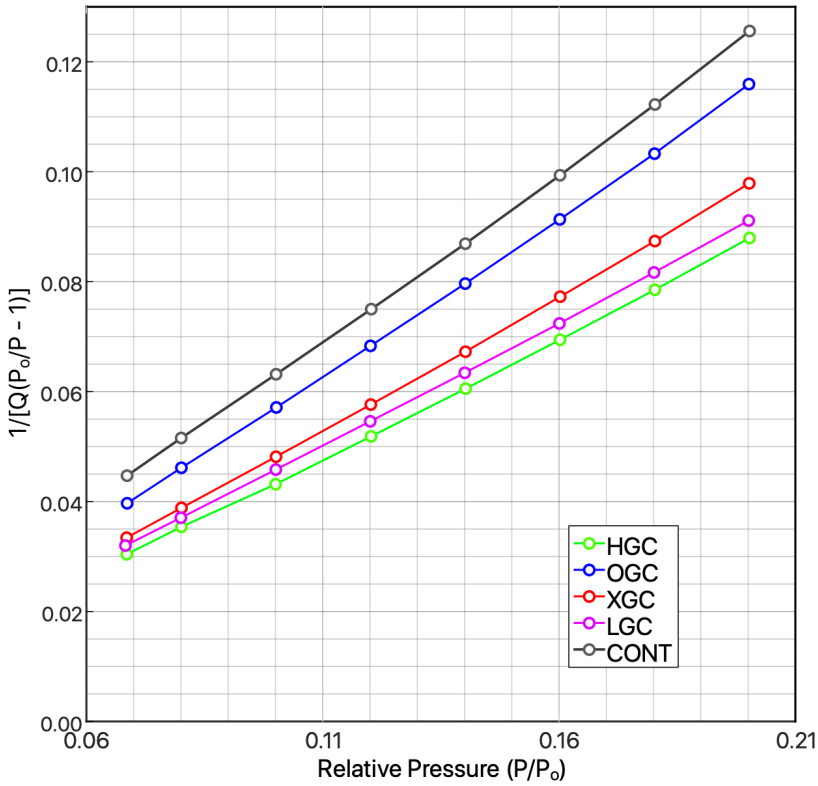

Figure 4.3.25: BET plots for all 24 hour cement samples.

crostructure and concrete strength, with no major reduction in workability. Conversely, reduced GO (XGO) showed least improvement in strength and significantly reduced workability. HGCp, despite being ultra-oxidized, still showed high workability once polycarboxylate superplasticizer was employed. As shown in GO characterization tests, the total amount of functional groups do not rise greatly upon higher oxidation, rather their contributions to the surrounding hydronium layer and its regeneration is highly improved. This suggests that the hydroniums on the GO sheets may be the primary component contribution to the development of such a dense microstructure. Once the C-S-H structure has nucleated (most likely on the GO sheets themselves), the sheet's integrity conforms the growth of the C-S-H crystals, possibly by affecting the ion/molecular complex surrounding the silicon/calcium inner skeleton. To

verify that the C-S-H microstructure has not been altered, rather only it's rate and/or density of growth has, TGA/DTG results were performed to see how the cement microstructure decomposes upon heat. The results for 12 hours, 24 hour and 28 day freeze-dried samples are shown in Figures 4.3.26, 4.3.27 and 4.3.28.

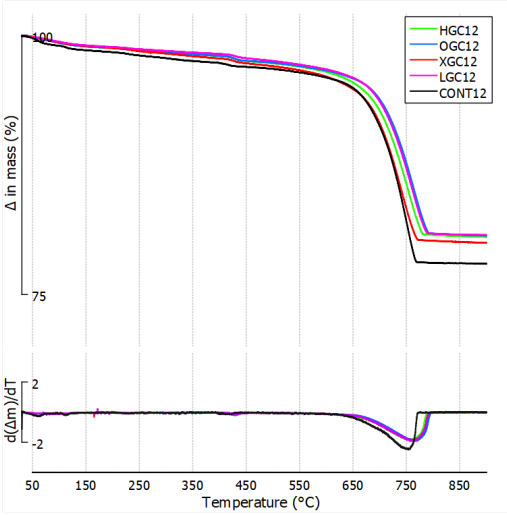

Figure 4.3.26: TGA/DTG curves of 12-hour hydrated freeze-dried samples.

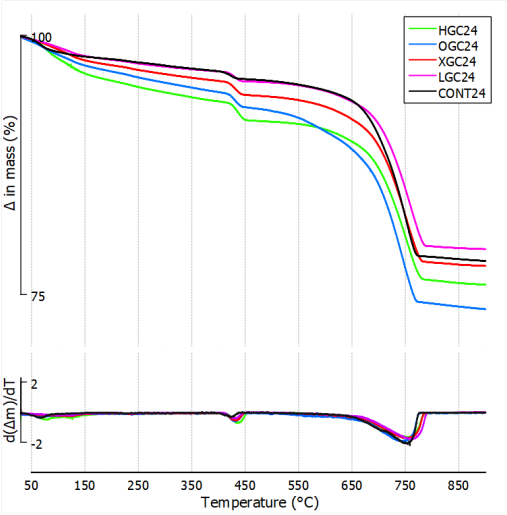

Figure 4.3.27: TGA/DTG curves of 24-hour hydrated freeze-dried samples.

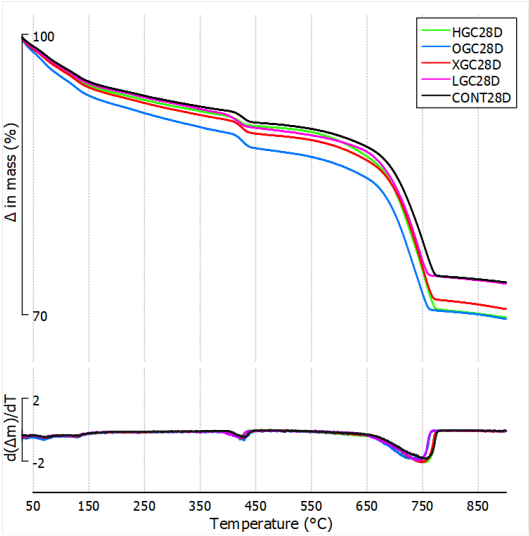

Figure 4.3.28: TGA/DTG curves of 28-day hydrated freeze-dried samples.

As can be seen, despite the early hydration peak shift of all GC samples, their TGA/DTG results do not differ significantly from control. The samples

were freeze-dried to remove any trapped water, as the GO sheets also retain water as part of their hydronium layer and thus amount of gel water cannot be discerned from mere decomposition curves. Hence, the samples microstructure is similar to control, even at 24 hours where the rate of hydration is suspected to be the most altered. As microstructure decomposition is similar to control, we look to XRD testing to better discern which cement hydration materials have been affected by GO incorporation. From the XRD results, we are primarily concerned with only alite (C_3S) and portlandite (CH):

1. Alite gets consumed first to form C-S-H during hydration. Hence, a faster decrease of alite signifies hydration reaction is accelerated.

2. Portlandite is a by-product of cement hydration. However, as discussed earlier, HGO/LGO's hydronium regeneration can significantly use up the hydroxide ions and promote higher amounts of C-S-H production.

Figure 4.3.29 shows the amounts of alite proportion in cement samples hydrated for 12 hours, 24 hours and 28 days respectively. From FTIR we know that peak changes in hydration development arise in the 12-24 hour range, hence the 12 hour samples are used as a baseline to measure changes in alite/CH amounts. After 24 hours, alite use has increased significantly for XGC (44% decrease), followed by OGC (40%), HGC (39%) and lastly LGC (17%) compared to only 8% reduction for control. For 28 days, control had a 44% reduction in alite amount, while XGC had the highest reduction of 81%, followed by OGC (62%), HGC (46%) and LGC with only 20%. The trend from 24 hours followed up till 28 days, however the results are the inverse of strength or porosity improvements: OGC and XGC were the worst performing GO nanoreinforced samples,

but according to XRD they had the highest and fastest reduction of alite. This implies that faster use of alite may not correlate with better strength and porosity development. Indeed, it is possible faster alite use may lead to localized C-S-H formation that hindered overall uniform cement matrix development. As both ultraoxidized GO incorporations ultimately resulted in relatively lower alite use (compared or below control alite reduction), it indicates that their hydronium layer regeneration does not accelerate alite use. However the rate of hydration is still increased with respect to control. Hence Figure 4.3.30 shows the respective CH amounts which are discussed below.

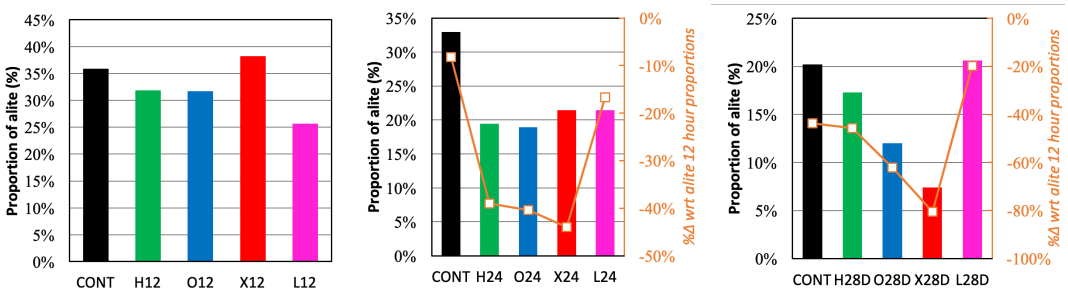

Figure 4.3.29: Alite proportions in 12-hour, 24-hour and 28-day control and GC samples.

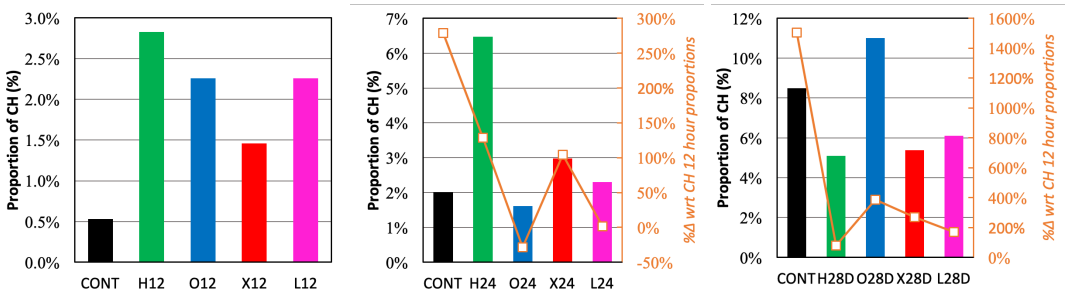

Figure 4.3.30: CH proportions in 12-hour, 24-hour and 28-day control and GC samples.

At 12 hours, all GC samples have higher CH amounts than control, indicating their seeding of water molecules has initiated hydration early. As expected, the ultraoxidized HGC and LGC have the highest CH, followed by OGC and XGC. At 24 hours, control has the highest increase in CH production (279%),

although CH total amount is still quite low (2%). Conversely, we can see the regeneration ability of ultraoxidized GO's: HGC, despite it's highest CH amount in the 24 hour sample, has a lower rate of increase in the last 12 hours of hydration than control (129%). Conversely, LGC has shown almost no increase in CH production, indicating it's remarkable ability to regenerate hydronium and neutralize hydroxide ions consistently (as explained in section 4.2.2). Surprisingly, OGC has also not increased it's CH significantly, while XGC has shown some increase. For the 28 day samples, we can see control has much higher increased CH amounts (0.5% to 8% proportion). In 28 days, OGC now has the highest CH proportion out of all samples. It can be inferred that this caused it's sub-par compressive strength performance in concrete samples. Other than OGC, all remaining GC types have lower 28-day CH amount than control, providing proof of the neutralization of hydroxide by the hydronium of GO. Conversely, XGC did not increase the hydration rate relative to other GCs in the first 12 hours (inferred from it's 12-hour CH amounts), as it did not have a dense hydronium layer due to it's thermal reduction. However, the production of CH during hydration may have prompted some water protonation for XGC as well, as it's final CH amount is also quite low. Figures 4.3.31 and 4.3.32 summarize the change in alite and CH proportions over the hydration periods of all samples, respectively. Appendix 4 (section 6) lists all the Rietveld refinement reports for further perusal.

In order to visually illustrate these changes in the crystal growth amounts of hydrated cement, the following section shows SEM images captured from control and GC samples at various stages of their cement hydrations.

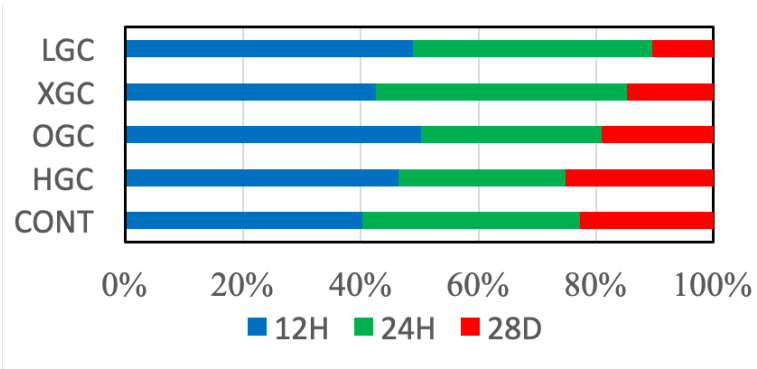

Figure 4.3.31: Change in alite for control and GC samples during hydration.

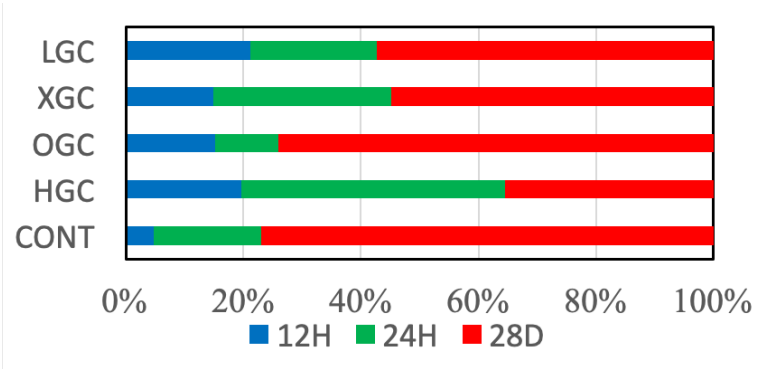

Figure 4.3.32: Change in CH for control and GC samples during hydration.

4.3.5 Visual examination of cement microstructure

Figure 4.3.33 shows all GC and control samples after 12 hours of hydration. In control sample, some isolated hydrated samples (floating white spherical globules) can be seen floating outside, not connected to the matrix. Large CH sheets are also visible in the control sample, not present in the other samples.

As previously found in XRD, there is a higher amount of CH in all the GC samples rather than control due to their seeding of hydration reactions, however their constant GO protonotion of water in early stages does not facilitate the continued growth of these large portlandite sheets. Unlike control, all the GC samples are interconnected in the cement matrix, with HGC showing the most dense microstructure. XGC also shows a dense microstructure, however they do not seem to be as well connected as the former. Figure 4.3.34 magnifies

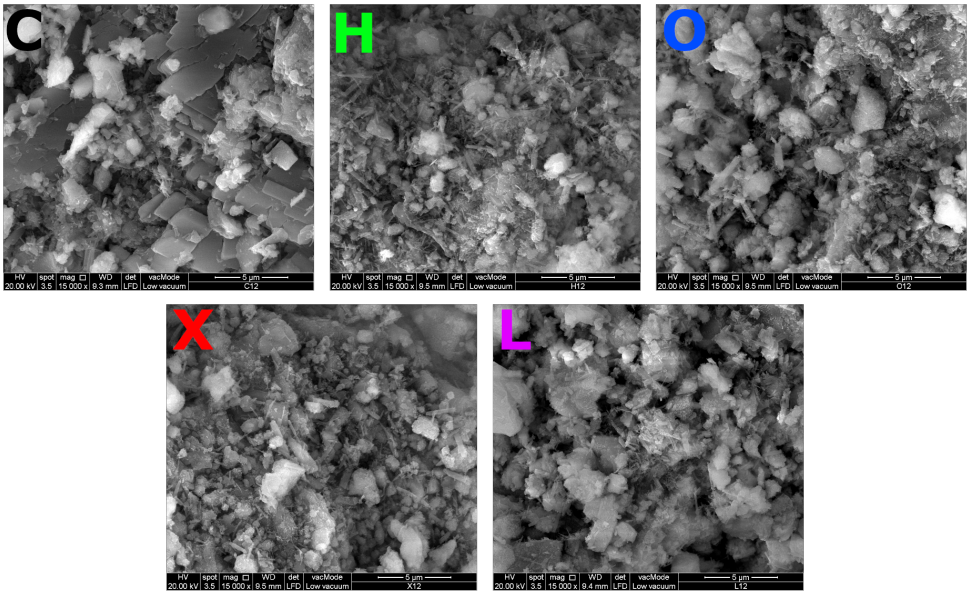

Figure 4.3.33: SEM images of 12 hour hydrated control and GC samples at 15k magnification.

these differences.

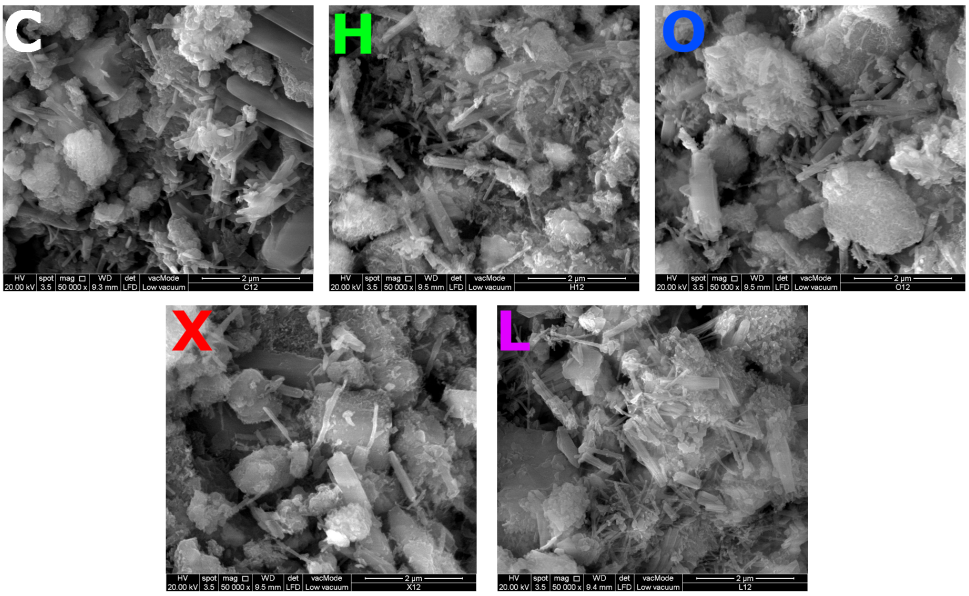

Figure 4.3.34: SEM images of 12 hour hydrated control and GC samples at 50k magnification.

At 24 hours of hydration, we can see (Figure 4.3.35) a much higher amount of white floating C-S-H coated cement particles in all samples. However, control's hydrated cement particles are much larger in size and not as well connected to the cement matrix compared to LGC and OGC. At a higher mag-

nification (Figure 4.3.36), the finer microstructures of all GC can be seen, and development of CH plates is also observed in OGC, indicating that perhaps OGO's regenerative ability has been extinguished.

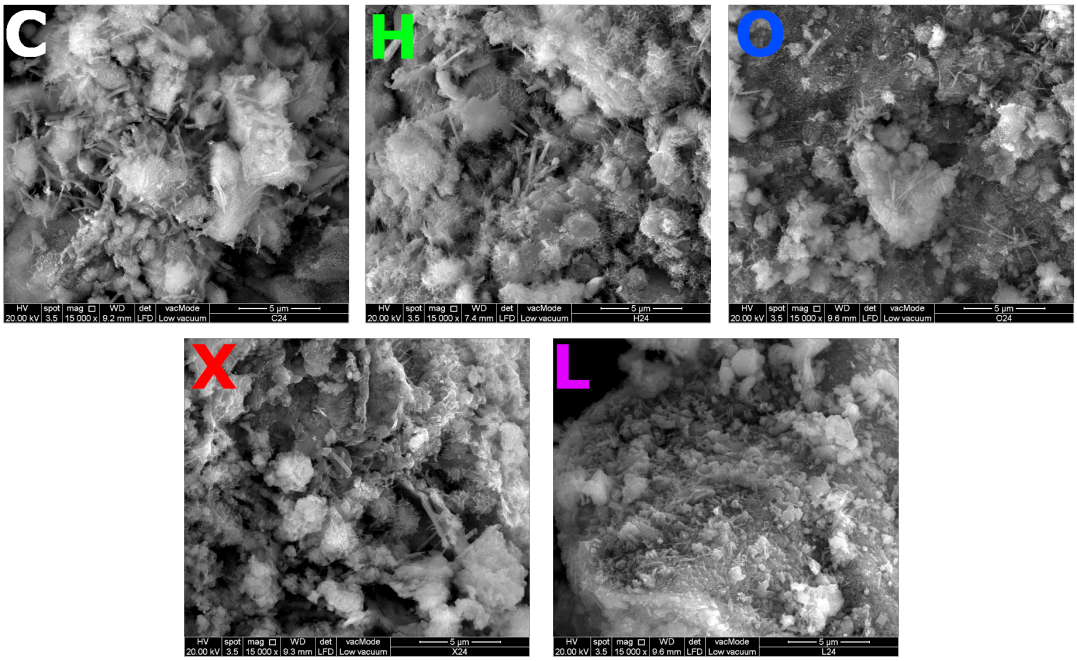

Figure 4.3.35: SEM images of 24 hour hydrated control and GC samples at 15k magnification.

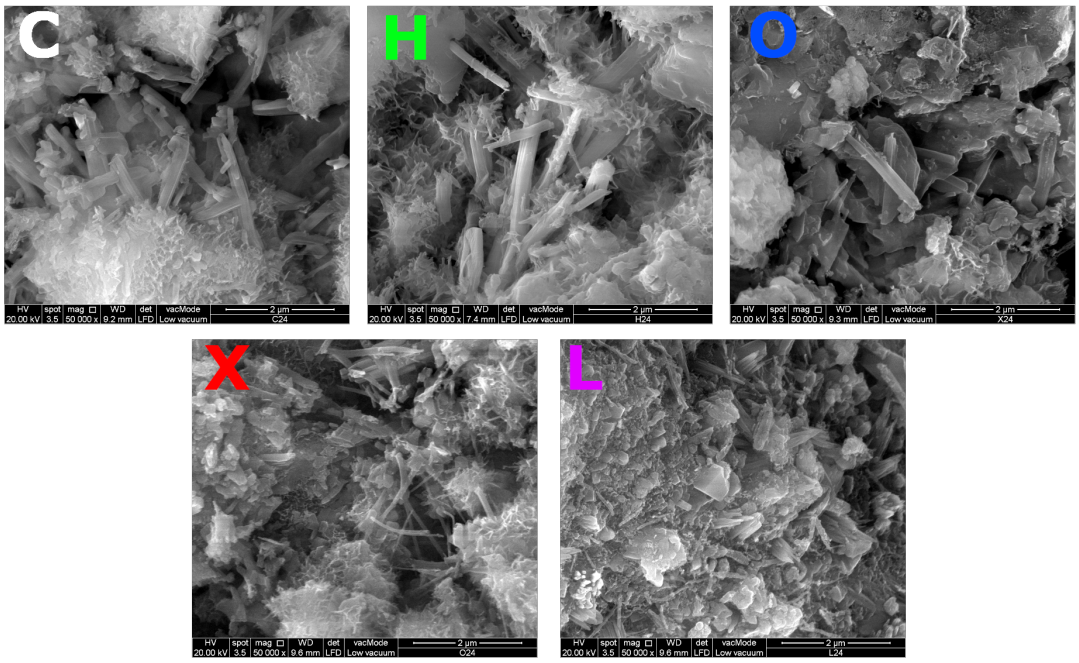

Figure 4.3.36: SEM images of 24 hour hydrated control and GC samples at 50k magnification.

At 72 hours (Figure 4.3.37) the lack of an interconnected cement gel matrix is clearly evident in the control sample. However, after the full 28 days, all samples show similar cement microstructure (Figure 4.3.38), indicating that most of GO's improvements to cement microstructure only occur in the first few days of curing.

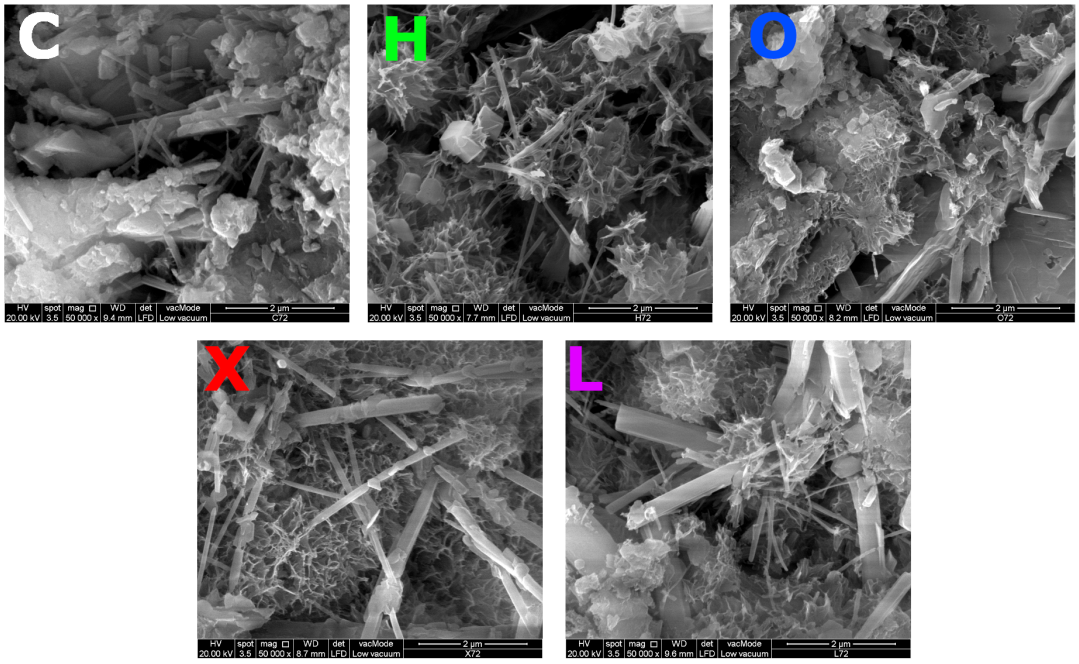

Figure 4.3.37: SEM images of 72 hour hydrated control and GC samples at 50k magnification.

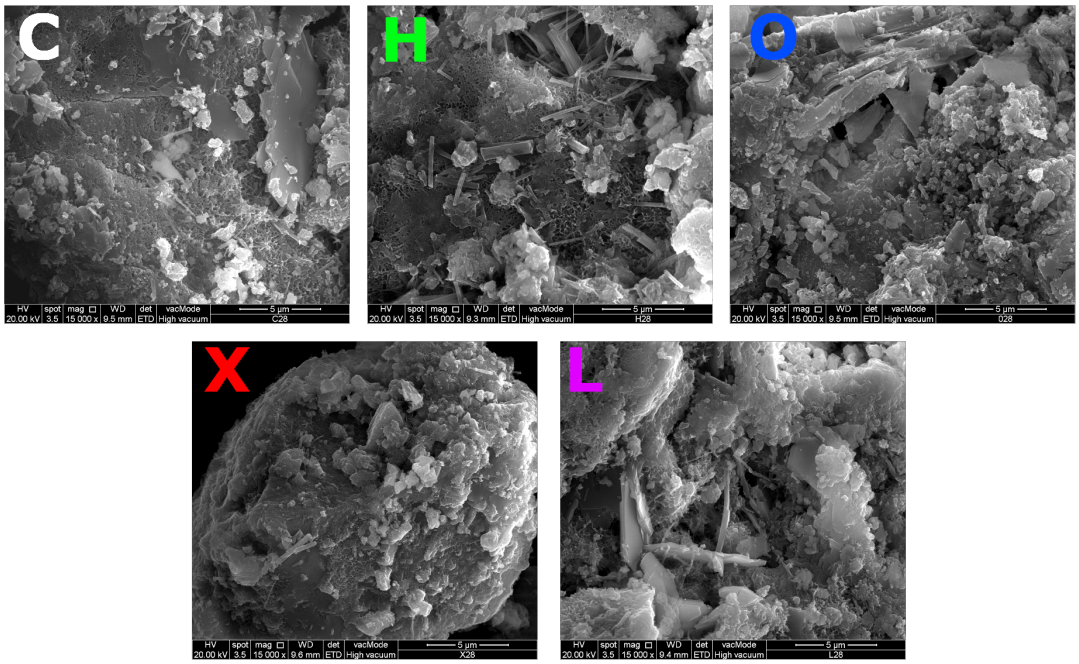

Figure 4.3.38: SEM images of 28 day hydrated control and GC samples at 15k magnification.

4.4 New model proposition for GO-cement interactions

To illustrate how GO is affecting the cement microstructure development, Figure 4.4.1 shows both hypothetical mechanisms of GO regulation on the C-S-H microstructure growth, either assuming the GO-DSM model or the conventional GO model. This model depicts a unit calcium-silicate oxide cell that branches two dimensionally (in the directions shown by the black arrows on left and right of the unit cell). This unit cell is surrounded by water molecules, hydroxides and free calcium ions. When GO is incorporated, this unit cell is forced to grow along the basal planes of the GO sheets, attracted by the hydronium/water layer on the GO sheets, hence crystal growth regulation.

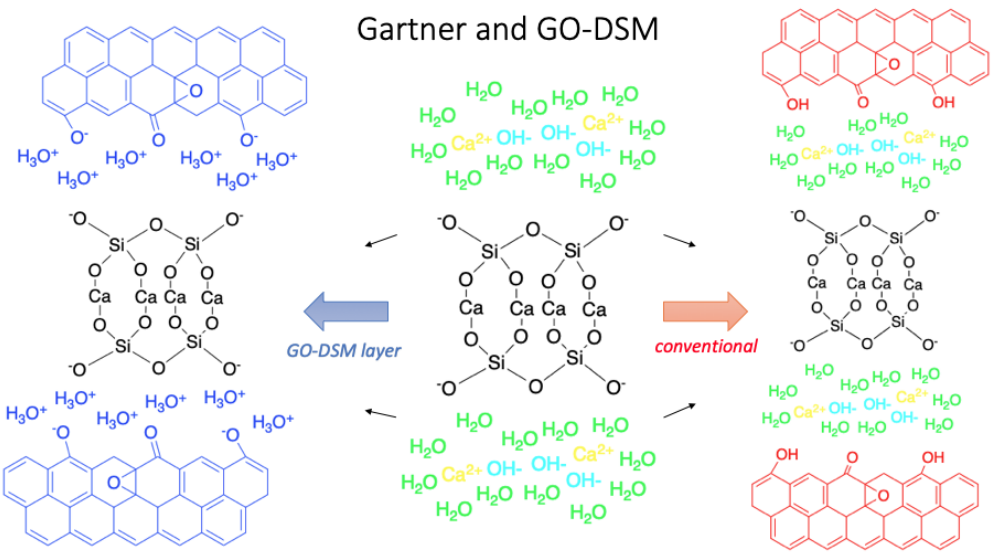

Figure 4.4.1: Applying the conventional GO and GO-DSM model to Gartner's C-S-H crystal growth.

The size of C-S-H crystals (approximately 60 x 20 x 40 nm^3 found by Gauffinet (1998)) are much smaller than GO sheets (shown in Figure 4.2.20) Furthermore, despite LGO's sheet size being > HGO's, HGO has performed much better in terms of overall strength and microstructure. This shows that hydronium layer

may be playing a much more significant role than the sheet size in regulating the C-S-H crystals. As the GO sheets are strongly attached to the hydronium and can regenerate them by protonating surrounding water molecules, it will impose itself in the C-S-H ion molecular complex, hence dictating crystal formations. The regenerating hydronium would also affect the ion charges in the hydration reactions, shifting the solubility rates by occupying the portlandite by-products which in turn dictate the hydration rate of cement which are outlined in section 2.4.1. The hydroxide ions from portlandite react with hydronium to produce more water molecules, extending alite hydration periods while the GO regenerates more hydronium and this cycle persists. Ultra-oxidized GOs have higher hydronium regeneration ability (shown in section 4.2.2), neutralizing more hydroxides for longer periods and thus improving the C-S-H gel matrix in terms of both density and overall concrete strength. This mechanism would not exist in the conventional GO model. This intrusion in the reactions can also be seen in the FTIR peak shifts, where C-S-H peak appeared earlier for both HGO and LGO based cements. Conversely, the conventional GO model does not explain this tendency to affix onto the C-S-H microstructure, as there are no regenerating hydroniums to shift the solubility rate of ions in the hydration environment. Furthermore, the conventional GO model has exposed negative functional groups (phenol and carbonyl), which would simply react with the Ca^{2+} ions and hinder the C-S-H structure formation instead of encouraging it's growth, while GO-DSM model does not have exposed negative functional groups due to continuously regenerating high amounts of hydronium in it's vicinity, which are extremely hard

to remove as shown in GO titration experiments in section 4.2.2. The strong attraction of the hydronium layer to the GO sheets also force the C-S-H to latch on the sheets for nucleation and growth, unlike for the conventional GO model where both the calcium-silicate oxide and the functional groups of GO are negative charged, and would just strip away the water and metal ions away from each other, having no reason to latch on to each other for growth. Furthermore, if the GO functional groups were to directly react with the C-S-H gel matrix, it would significantly alter the de-compositional ability of the material, which is debunked by TGA/DTG tests showing similar mass decomposition of control and GC samples.

To summarize the whole mechanism, the following figures show the step by step impact of ultra-oxidized GO-cement hydration. In Figure 4.4.2, the dissociated alite particles (shown in grey) from the cement powder float and land on the GO sheets (black), attracted by the high volume of water particles on the ultra-oxidized GO surface. However, unlike other research hypotheses, the cement and subsequent C-S-H particles will not contact or react with the phenol/carbonyl functional groups on the GO itself. Rather, the C-S-H affix onto the hydronium layer (in green, surrounding the GO), and stay 'attached' to it due to the hydronium positive charge attracting the negative open ended calcium silicate oxide unit of C-S-H, portrayed clearly in Gartner's model from Figure 4.4.1. Once the alite seats on the hydronium layer, the abundance of H_3O^+ and H_2O molecules prompt the N+G (cement nucleation + growth mechanism from section 2.4.1) cement hydration process. This C-S-H will grow along the surface of GO sheets due to easily available water molecules.

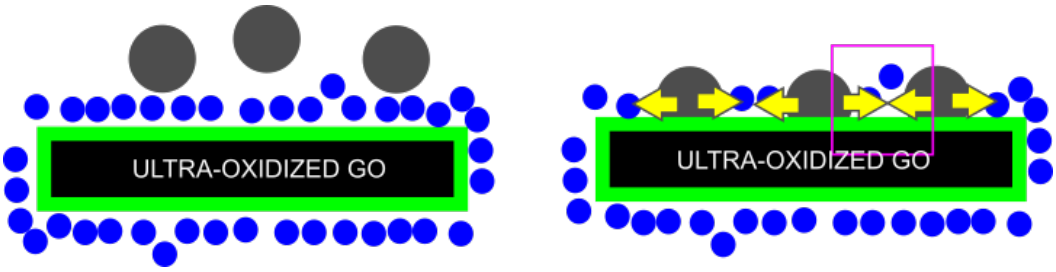

Figure 4.4.2: Illustrating alite/cement landing on the GO's hydronium/water stacked surface.

GO is shown as the black sheet in the middle of the diagram, coated by the light green layer of hydronium. The blue particles are water molecules, while the larger grey circles represent dissociated alite particles. The pink square highlights a smaller area which is described in detail in subsequent figures.

Figure 4.4.3 shows a close-up of the GO hydronium surface (blue-green pattern) and two neighbouring hydrating grey cement particles. In initial N+G stages, flower like growth of C-S-H crystals is observed (from current GO-cement research literature), however a by-product of C-S-H formation is portlandite or calcium hydroxide, and hydroxide ions are seen as red circles in the figure. Due to ultra-oxidation, there is a higher amount of hydronium (green circles) in the environment, which neutralizes this hydroxide to form more water molecules (blue), which get re-protonated on the GO surface, and this exchange of ions is shown by the inflow and outflow green and blue arrows in the figure. Meanwhile, more water molecules continue to provide fuel for further C-S-H growth.

Finally, we can see in Figure 4.4.4 that the C-S-H grows in polyhedral column shapes, as the previous flower like crystals have thickened, and the two dimensional nature of C-S-H growth plus the limited growth space prompts the newer design form. This GO facilitated spur of denser C-S-H growth may be short lived unfortunately, as C-S-H will preferentially spread along GO sheets first, and potentially sandwich the hydroniums ions between the GO sheet and

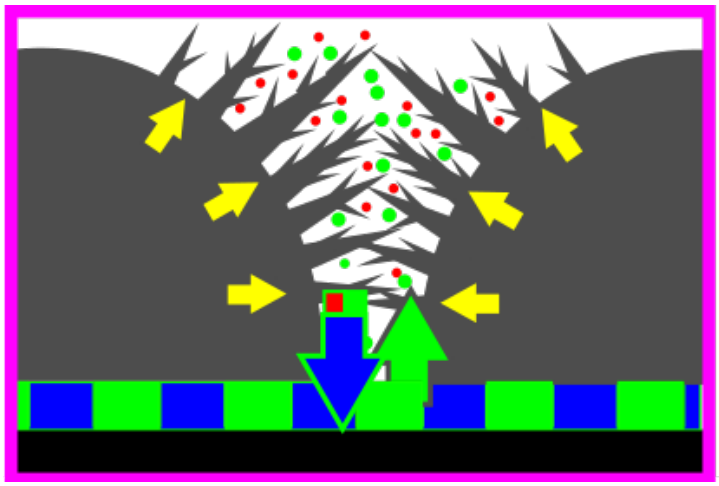

Figure 4.4.3: Close-up of C-S-H growth on the basal plane of GO sheet.

itself, hence the benefits of GO are completely terminated, verified by the relapse of the FTIR C-S-H peaks back to control's wavelengths over subsequent days of hydration (until 28 days, as shown in Figure 4.3.22 earlier). From SEM of the current report as well as other findings, the GO sheets are never seen bare in any cement incorporations, rather they are all coated with C-S-H or other by-products.

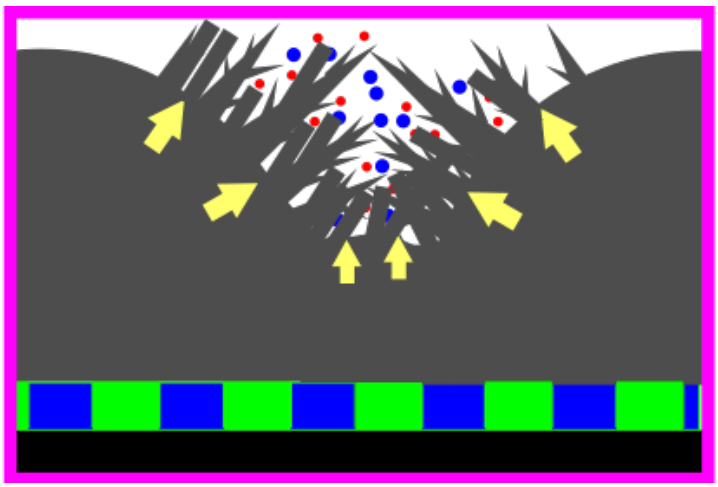

Figure 4.4.4: C-S-H growth completely seals the hydronium from remaining alite/C-S-H, terminating any further GO benefits.

Interestingly, if C-S-H will always coat the GO sheets first, then that also indicates that larger sheet size may not be as beneficial for cement nano-reinforcement,

as the C-S-H growth will be focused only on the sheets themselves, leaving less cement to successfully coat the aggregates and make a uniformly dense, interconnected cement matrix. Conversely, smaller sized sheets can lead to greater spread of C-S-H coated sheets (smaller but higher in quantity) in the whole cement microstructure, which statistically would lead to higher inter-bridging of C-S-H throughout the sample. Indeed, this may also be an alternative answer to why smaller GO sheets improved cement's strength considerably for Sharma et. al (2015*a*), and may be the reason for HGO's better incorporation than LGO's in cement (smaller sheet size).

Finally, several researchers have proposed of calcium bridging between GO functional groups and the C-S-H gel matrix (and were discussed in literature review, e.g. see Figure 2.5.2). This is unlikely due to heavy hydronium presence in the GO DSM model, but free calcium divalent ions (in the ion/molecular complex discussed in cement hydration mechanisms section 2.4.1, or from calcium hydroxide as cement hydration's by-products) have been notorious for causing GO in suspension to coagulate immediately, as was discussed in section 4.2.2. While calcium bridging is possible between GO sheets themselves, it would not improve the strength of cement in any significant manner, as these attractions would be localized. Furthermore, this bridging does not explain the increased rate of cement hydration or the identical FTIR/TGA results for GC vs control samples, as such bridging would drastically change the structure of C-S-H, unlike the Gartner GO DSM model where the nanoreinforcement is a a secondary result of higher nucleation and growth (N+G mechanism from section 2.4.1) due to persistent water availability.

4.5 Summary of Results and Discussion

This chapter details the results of analytical, chemical and mechanical tests performed on the different GOs and their respective cement/concrete incorporation. Preliminary trials in Section 4.1 confirmed that PC chemically interferes with GO, and greater amount of PC would be needed to add separately to the concrete during mixing. A lower w/c ratio is also essential to maximize GO's mechanical improvements in concrete. Section 4.2 distinguishes the chemical differences between the GOs, while also verifying their physical similarities. Furthermore, their ability to seed water is also determined via titration and surface charge analysis, whereby GOs with higher single C-O bond groups (the ultra-oxidized GOs, HGO and LGO) showed greater acidity and hydronium regeneration potential. In Section 4.3, it was shown that both HGO and LGO improved cement hydration development, leading to denser microstructure and consistently stronger yet more workable concretes. Conversely, XGO performed inconsistently, with greatly reduced workability and small strength improvements. As XGO had the lowest amount of C-O bonds, it was inferred that GO improvements in cement and concrete lie with their hydronium regeneration potential. Furthermore, high hydronium also resulted in improved workability, however the different GOs also interact differently with the PC, resulting in different GO-concrete strengths based on their treatment with PC. Lastly, a chemical interaction model based on all the tests results was presented and discussed in Section 4.4.

Chapter 5: Conclusions and Recommendations

In preliminary mortar trials, it was shown that GO unequivocally improves concrete's compressive strength (up to 42%), However the nature as to how is hypothesized. The oxidation of normal GO (OGO) was instrumental and chemical interactions were primarily involved in cement's improvement, rather than any physical contributions. To prove this hypothesis, GO was custom tuned and different types of GO were synthesized to incorporate in concrete. However, it was found that research on behaviour of oxidized graphene is scarce, hence an in depth fundamental study of GO was decided.

By adding a small amount of water to the intercalant's pre-oxidation of graphite, ultra-oxidized HGO was synthesized which shows similar compositional ratios to OGO (via XPS), but higher quantities of both carbonyl and hydroxyl (and potentially epoxide) groups (determined via FTIR). It's higher functionalization contributes to a stronger hydronium layer that resists base addition as observed in titration. Conversely, ultra-oxidized LGO exhibits significantly different properties: FTIR registered a significant C-O single bond presence (epoxide/phenol) with lower carbonyl presence, confirmed by XPS. XPS also showed significant sp^3 bonds in LGO, resulting in much higher hydronium regenerative ability than OGO and even HGO, determined via titration and zeta potential. SEM shows that for HGO there is a greater stacking of water/hydronium molecules on the layer, but forcibly removing the hydronium layer via freeze drying cause bulging and tearing on sheets. LGO additionally showed more localized water stacking in SEM images, while HGO sheets were

uniformly coated. Zeta potential revealed GO's tendency to resist and rise in pH by overproducing H_3O^+ ions to re-establish equilibria and cause a net increase in surface charge for the ultra-oxidized GOs.

By ultra-oxidizing GOs, it's protonation behavior and acidic traits are more evident, and should be kept in mind when attempting to use GO suspensions in any chemical capacity. Additionally, by ultra-oxidation the flaws in current deductions of analytical tests are highlighted: discounting H_3O^+ presence on GO suspension (and oven dried GOs) leads to incorrect interpretations due to overestimation of O-H bonds and oxygen atoms to the GO sheets themselves. Freeze drying does not remove this layer entirely and causes building and tearing of sheets consequently.

When incorporated into concrete and cement, both ultra-oxidized GOs improved strength and microstructure density significantly, while OGO gave unpredictable results. The least oxidized XGO did not significantly improve compressive strength and caused high reduction in workability. As such, it was proven that oxidation of GO is key in it's best application to concrete. Additionally, with polycarboxylate superplasticizer HGO showed an increase in workability, indicating some beneficial steric reaction that could not be replicated in LGO or OGO. Hence, the nature of how GO is manufactured is also important when predicting it's effects in cement/concrete application. Porosity tests indicate that even at 24 hours, all GOs improve the surface area and reduce pore sizes compared to control, verified by FTIR tests which indicated early shifting and development of the C-S-H peak, more so for the ultra-oxidized GOs. However, HGO and LGO had different reactions to superplasticizer treatments, and

offered varying strengths in compressive and flexural (LGO improved flexural strength the most, while HGO improved more compressive strength). Additionally, HGO also improved the ductility of concrete significantly, which greatly helps the safety of the brittle material. These differing results indicate that both ultra-oxidized GOs have aided the development of C-S-H crystals in their own way, however if we are to keep GO-DSM model in mind, identifying particularly how they have contributed to cement microstructure precisely is still complex and out of reach. Two models were proposed of the nucleation and growth regulation of C-S-H by GO, one using conventional behavioural traits of the nanomaterials, while the other presents the hydronium based GO-DSM layers interactions.

5.1 Answers to Research Questions

Ultimately, the hypotheses presented in section 1.4 were proven true and the respective research aims can be answered as follows:

1. The hydration process of cement is affected by GO inclusion, primarily due to the unique water re-generation ability of GO.

2. Higher oxidation of GO results in stronger, more durable, and, when mixed with a PC superplasticizer, more workable concrete. Additionally, higher oxidation shows more consistent overall improvements than typical GO-concrete mix. Conversely, lower oxidation of GO results in a weaker, less workable concrete with inferior microstructural development.

3. Highly oxidized GO neutralizes alkaline CH (a by-product of cement hydration), and provides more water molecules to facilitate further cement hydra-

tion. This results in a denser cement matrix contributing to higher strength and durability of concrete.

4. Functional groups on the GO sheets do not appear to provide any direct bondage with the cement. Instead, these groups (specifically C-O phenol group) are responsible for creating a dynamic hydronium layer around GO, which is primarily responsible for neutralizing cement hydration by-products and forming water molecules facilitating the hydration process.

5.2 Attainment of Research Objectives

Following are the conclusions of the research Aims and Objectives as presented in Section 1.3.

1. Strength of ultra-oxidized GO-concrete is not significantly affected by superplasticizer, while retaining high concrete mix workability. Meanwhile, low hydroxyl GOs show reduced workability and inconsistent strength development when treated with superplasticizer. At high w/c ratios with low GO amounts (0.02% bwoc), all GOs are not affected by superplasticizer addition.

2. Ultra-oxidized GOs are more acidic in water, and create a dense, regenerating hydronium layer which is the primary interactor with the hydrated cement microstructure.

3. Ultra-oxidized GOs show consistently improved strength, workability of concrete, with smaller pore size and increased cement hydration during the first 24 hours after mixing.

4. Ultra-oxidized GOs are able to generate a hydronium layer around their proximity, which provides seeding points for hydrated cement nucleation, while also neutralizing alkaline by-product development, retaining heat energy for increased and accelerated cement hydration in the 24 hours of mixing.

Hence, the overall aim of this research has been addressed, in that there is a definitive chemical interaction between GO and cement, which is due to the hydronium layer, itself generated by a chemical interaction between GO hydroxyl groups and water. GOs with sufficiently high hydroxyl presence (eg ultra-oxidized GOs) can overcome interference by the superplasticizers, providing a stronger and denser concrete, but with more workability.

Ultimately, it has been shown without a doubt that the primary contributor of strength in GO based cements and concrete are hydronium ions which are a by-product of the oxidative phenol and carbonyl groups of GO. This is a much more economical and easier application of GO relative to other engineering applications (such as lubricants or conductive materials) where clean, large, unoxidized/reduced GO or graphene sheet sizes are typically preferred, which are more expensive and require intensive manufacturing processes.

5.3 Recommendations for future work

It is recommended that the GO hydronium layer must be further investigated if a clearer picture of cement hydration is to be gleaned. The new GO/C-S-H hydronium model also raises a lot more complex questions: how is the hydration reaction altered? How much does sheet size play a role in this mechanism?

Most importantly, how specifically do both ultra-oxidized GOs used in this research differ in creating this microstructure, and how does that explain their differing improvements in compressive and flexural strengths? It can be intuited that if the C-S-H microstructure has been improved, the durability and resistance of concrete would also have been improved, however due to Covid-19 pandemic interruptions in the last year of this research, no long term concrete durability tests could be planned or performed. The alkaline neutralization ability of GO-cement and it's denser microstructure also implies higher resistance to the alkali-silica reaction. The presence of hydronium from GO may also neutralize chloride ions and prevent rebar corrosion, and further experiments must be performed to prove this hypothesis. The unique properties of GO and it's contributions to cement are multifold, and further research of the GO-cement composite can help address a vast array of cement and concrete industry woes.

Chapter 6: References

Abdullah, S. I. & Ansari, M. (2015), 'Mechanical properties of graphene oxide (GO)/epoxy composites', *HBRC Journal* **11**(2), 151–156.

URL: *https://www.sciencedirect.com/science/article/pii/S168740481400042X*

Abu Al-Rub, R. K., Ashour, A. I. & Tyson, B. M. (2012), 'On the aspect ratio effect of multi-walled carbon nanotube reinforcements on the mechanical properties of cementitious nanocomposites', *Construction and Building Materials* **35**, 647–655.

URL: *http://dx.doi.org/10.1016/j.conbuildmat.2012.04.086*

Ahmed Sbia, L., Peyvandi, A., Soroushian, P., Balachandra, A. M. & Sobolev, K. (2015), 'Evaluation of modified-graphite nanomaterials in concrete nanocomposite based on packing density principles', *Construction and Building Materials* **76**(1), 413–422.

URL: *http://dx.doi.org/10.1016/j.conbuildmat.2014.12.019*

Alharbi, Y., An, J., Cho, B. H., Khawaji, M., Chung, W. & Nam, B. H. (2018), 'Mechanical and sorptivity characteristics of edge-oxidized graphene oxide (EOGO)-cement composites: Dry-and wet-mix design methods', *Nanomaterials* **8**(9).

Aliyev, E., Filiz, V., Khan, M. M., Lee, Y. J., Abetz, C. & Abetz, V. (2019), 'Structural characterization of graphene oxide: Surface functional groups and fractionated oxidative debris', *Nanomaterials* **9**(8).

Babak, F., Abolfazl, H., Alimorad, R. & Parviz, G. (2014), 'Preparation and me-

chanical properties of graphene oxide: Cement nanocomposites', *The Scientific World Journal* **2014**.

Bai, S., Jiang, L., Xu, N., Jin, M. & Jiang, S. (2018), 'Enhancement of mechanical and electrical properties of graphene/cement composite due to improved dispersion of graphene by addition of silica fume', *Construction and Building Materials* **164**.

Balasubramaniam, B., Mondal, K., Ramasamy, K., Palani, G. S. & Iyer, N. R. (2017), 'Hydration Phenomena of Functionalized Carbon Nanotubes (CNT)/Cement Composites', *Fibers* **5**(4), 39.
URL: *http://www.mdpi.com/2079-6439/5/4/39*

Barret, P. & Ménétrier, D. (1980), 'Filter dissolution of C3S as a function of the lime concentration in a limited amount of lime water', *Cement and Concrete Research* **10**(4), 521–534.

Barret, P., Ménétrier, D. & Bertrandie, D. (1983), 'Mechanism of C3S dissolution and problem of the congruency in the very initial period and later on', *Cement and Concrete Research* **13**(5), 728–738.

Bažant, Z. P. & Planas, J. (2019), *Fracture and Size Effect in Concrete and Other Quasibrittle Materials*, Vol. 44, Routledge.
URL: *https://www.taylorfrancis.com/books/9781351447294*

Beer (1852), 'Bestimmung der absorption des rothen lichts in farbigen flüssigkeiten', *Annalen der Physik* **162**(5), 78–88.
URL: *https://onlinelibrary.wiley.com/doi/abs/10.1002/andp.18521620505*

Bi, S., Liu, M., Shen, J., Hu, X. M. & Zhang, L. (2017), 'Ultrahigh Self-Sensing Performance of Geopolymer Nanocomposites via Unique Interface Engineering', *ACS Applied Materials and Interfaces* **9**(14), 12851–12858.

Birenboim, M., Nadiv, R., Alatawna, A., Buzaglo, M., Schahar, G., Lee, J., Kim, G., Peled, A. & Regev, O. (2019), 'Reinforcement and workability aspects of graphene-oxide-reinforced cement nanocomposites', *Composites Part B: Engineering* **161**(October 2018), 68–76.
URL: *https://doi.org/10.1016/j.compositesb.2018.10.030*

Bishnoi, S. & Scrivener, K. L. (2009), 'Studying nucleation and growth kinetics of alite hydration using μic', *Cement and Concrete Research* **39**(10), 849–860.
URL: *http://dx.doi.org/10.1016/j.cemconres.2009.07.004*

Botas, C., Álvarez, P., Blanco, C., Santamaría, R., Granda, M., Gutiérrez, M. D., Rodríguez-Reinoso, F. & Menéndez, R. (2013), 'Critical temperatures in the synthesis of graphene-like materials by thermal exfoliation-reduction of graphite oxide', *Carbon* **52**, 476–485.

Brown, P. W., Harner, C. L. & Prosen, E. J. (1986), 'The effect of inorganic salts on tricalcium silicate hydration', *Cement and Concrete Research* **16**(1), 17–22.

Buchsteiner, A., Lerf, A. & Pieper, J. (2006), 'Water dynamics in graphite oxide investigated with neutron scattering', *Journal of Physical Chemistry B* **110**(45), 22328–22338.

Bullard, J. W. (2008), 'A determination of hydration mechanisms for tricalcium silicate using a kinetic cellular automaton model', *Journal of the American Ce-*

ramic Society **91**(7), 2088–2097.

URL: *https://doi.org/10.1111/j.1551-2916.2008.02419.x*

Bullard, J. W., Jennings, H. M., Livingston, R. A., Nonat, A., Scherer, G. W., Schweitzer, J. S., Scrivener, K. L. & Thomas, J. J. (2011), 'Mechanisms of cement hydration', *Cement and Concrete Research* **41**(12), 1208–1223.

URL: *http://dx.doi.org/10.1016/j.cemconres.2010.09.011*

Chen, J., Zhang, Y., Zhang, M., Yao, B., Li, Y., Huang, L., Li, C. & Shi, G. (2016), 'Water-enhanced oxidation of graphite to graphene oxide with controlled species of oxygenated groups', *Chem. Sci.* **7**(3), 1874–1881.

URL: *http://xlink.rsc.org/?DOI=C5SC03828F*

Chen, J., Zhao, D., Ge, H. & Wang, J. (2015), 'Graphene oxide-deposited carbon fiber/cement composites for electromagnetic interference shielding application', *Construction and Building Materials* **84**, 66–72.

Chintalapudi, K. & Pannem, R. M. R. (2020), 'The effects of Graphene Oxide addition on hydration process, crystal shapes, and microstructural transformation of Ordinary Portland Cement', *Journal of Building Engineering* **32**(May), 101551.

URL: *https://doi.org/10.1016/j.jobe.2020.101551*

Chowdhury, I., Duch, M. C., Mansukhani, N. D., Hersam, M. C. & Bouchard, D. (2013), 'Colloidal properties and stability of graphene oxide nanomaterials in the aquatic environment', *Environmental Science and Technology* **47**(12), 6288–6296.

Chowdhury, I., Mansukhani, N. D., Guiney, L. M., Hersam, M. C. & Bouchard, D. (2015), 'Aggregation and Stability of Reduced Graphene Oxide: Complex Roles of Divalent Cations, pH, and Natural Organic Matter', *Environmental Science and Technology* **49**(18), 10886–10893.

Chuah, S., Li, W., Chen, S. J., Sanjayan, J. G. & Duan, W. H. (2018), 'Investigation on dispersion of graphene oxide in cement composite using different surfactant treatments', *Construction and Building Materials* **161**.

Chuah, S., Pan, Z., Sanjayan, J. G., Wang, C. M. & Duan, W. H. (2014), 'Nano reinforced cement and concrete composites and new perspective from graphene oxide', *Construction and Building Materials* **73**, 113–124.
URL: *http://dx.doi.org/10.1016/j.conbuildmat.2014.09.040*

Ciofani, G., Raffa, V., Pensabene, V., Menciassi, A. & Dario, P. (2009), 'Dispersion of multi-walled carbon nanotubes in aqueous pluronic F127 solutions for biological applications', *Fullerenes Nanotubes and Carbon Nanostructures* **17**(1), 11–25.

Cwirzen, A., Habermehl-Cwirzen, K. & Penttala, V. (2008), 'Surface decoration of carbon nanotubes and mechanical properties of cement/carbon nanotube composites', *Advances in Cement Research* **20**(2), 65–73.
URL: *https://doi.org/10.1680/adcr.2008.20.2.65*

Damidot, D., Nonat, A. & Barret, P. (1990), 'Kinetics of Tricalcium Silicate Hydration in Diluted Suspensions by Microcalorimetric Measurements', *Journal of the American Ceramic Society* **73**(11), 3319–3322.
URL: *https://doi.org/10.1111/j.1151-2916.1990.tb06455.x*

de Jong, J. G. M., Stein, H. N. & Stevels, J. M. (2007), 'Hydration of tricalcium silicate', *Journal of Applied Chemistry* **17**(9), 246–250.
URL: *https://doi.org/10.1002/jctb.5010170902*

Dimiev, A., Kosynkin, D. V., Alemany, L. B., Chaguine, P. & Tour, J. M. (2012), 'Pristine graphite oxide', *Journal of the American Chemical Society* **134**(5), 2815–2822.

Dimiev, A. M., Alemany, L. B. & Tour, J. M. (2013), 'Graphene oxide. Origin of acidity, its instability in water, and a new dynamic structural model', *ACS Nano* **7**(1), 576–588.

Dimiev, A. M., Bachilo, S. M., Saito, R. & Tour, J. M. (2012), 'Reversible formation of ammonium persulfate/sulfuric acid graphite intercalation compounds and their peculiar Raman spectra', *ACS Nano* **6**(9), 7842–7849.

Dimiev, A. M. & Tour, J. M. (2014), 'Mechanism of graphene oxide formation', *ACS Nano* **8**(3), 3060–3068.

Du, H., Gao, H. J. & Pang, S. D. (2016), 'Improvement in concrete resistance against water and chloride ingress by adding graphene nanoplatelet', *Cement and Concrete Research* **83**, 114–123.

Du, H. & Pang, S. D. (2015), 'Enhancement of barrier properties of cement mortar with graphene nanoplatelet', *Cement and Concrete Research* **76**, 10–19.
URL: *http://dx.doi.org/10.1016/j.cemconres.2015.05.007*

e Silva, R. A., de Castro Guetti, P., da Luz, M. S., Rouxinol, F. & Gelamo, R. V.

(2017), 'Enhanced properties of cement mortars with multilayer graphene nanoparticles', *Construction and Building Materials* **149**, 378–385.

Ebrahimizadeh Abrishami, M. & Zahabi, V. (2016), 'Reinforcing graphene oxide/cement composite with NH2 functionalizing group', *Bulletin of Materials Science* **39**(4), 1073–1078.

Elena, J. & Lucia, M. D. (2012), 'Application of X-Ray Diffraction (XRD) and Scanning Electron Microscopy (SEM) Methods to the Portland Cement Hydration Processes', *Journal of Applied Engineering Sciences* **2(15)**, 35–42.

Emiru, T. F. & Ayele, D. W. (2017), 'Controlled synthesis, characterization and reduction of graphene oxide: A convenient method for large scale production', *Egyptian Journal of Basic and Applied Sciences* **4**(1), 74–79.
URL: *http://linkinghub.elsevier.com/retrieve/pii/S2314808X16301762*

Everett, D. H. (2007), *Basic Principles of Colloid Science*, Vol. 4 of *RSC Paperbacks*, Royal Society of Chemistry, Cambridge.
URL: *http://ebook.rsc.org/?DOI=10.1039/9781847550200*

Fasolino, A., Los, J. H. & Katsnelson, M. I. (2007), 'Intrinsic ripples in graphene', *Nature Materials* **6**(11), 858–861.

Fernández-Carrasco, L., Torrens-Martín, D., Morales, L. & Martínez-Ramírez, S. (2012), 'Infrared Spectroscopy in the Analysis of Building and Construction Materials', *Infrared Spectroscopy - Materials Science, Engineering and Technology* .

Gao, W. (2015), 'The chemistry of graphene oxide', *Graphene Oxide: Reduction Recipes, Spectroscopy, and Applications* pp. 61–95.

Garrault, S., Finot, E., Lesniewska, E. & Nonat, A. (2005), 'Study of C-S-H growth on C3S surface during its early hydration', *Materials and Structures* **38**(4), 435–442.
URL: *https://doi.org/10.1007/BF02482139*

Gartner, E. M. (1997), 'A proposed mechanism for the growth of C-S-H during the hydration of tricalcium silicate', *Cement and Concrete Research* **27**(5), 665–672.

Gartner, E., Maruyama, I. & Chen, J. (2017), 'A new model for the C-S-H phase formed during the hydration of Portland cements', *Cement and Concrete Research* **97**(c), 95–106.
URL: *https://linkinghub.elsevier.com/retrieve/pii/S0008884616303921*

Gartner, Young, Damidot & Jawed (2002), 'Hydration of Portland cement, Structure and Performance of cement', *Industrial and Engineering Chemistry* **13**(8), 978–0.

Gauffinet, S., Finot, É., Lesniewska, E. & Nonat, A. (1998), 'Observation directe de la croissance d'hydrosilicate de calcium sur des surfaces d'alite et de silice par microscopie a force atomique', *Comptes Rendus de l'Academie de Sciences - Serie IIa: Sciences de la Terre et des Planetes* **327**(4), 231–236.

Ghorbani, M., Abdizadeh, H. & Golobostanfard, M. (2015), 'Reduction of Graphene Oxide via Modified Hydrothermal Method', *Procedia Materials Sci-*

ence **11**(2009), 326–330.

URL: *http://linkinghub.elsevier.com/retrieve/pii/S2211812815004460*

Goertzen, S. L., Thériault, K. D., Oickle, A. M., Tarasuk, A. C. & Andreas, H. A. (2010), 'Standardization of the Boehm titration. Part I. CO2 expulsion and endpoint determination', *Carbon* **48**(4), 1252–1261.

Gong, J., Chou, K., Huang, Z. Y. & Zhao, M. (2014), 'A quantitative study on packing density and pozzolanic activity of cementitious materials based on the compaction packing model', *IOP Conference Series: Materials Science and Engineering* **62**(1).

Gong, K., Asce, S. M., Pan, Z., Korayem, A. H., Ph, D., Qiu, L., Li, D., Collins, F., Wang, C. M., Duan, W. H. & Asce, a. M. (2014), 'Reinforcing Effects of Graphene Oxide on Portland Cement Paste', *Journal of Materials in Civil Engineering* **vol 27**(2), 1–6.

Hanjitsuwan, S., Hunpratub, S., Thongbai, P., Maensiri, S., Sata, V. & Chindaprasirt, P. (2014), 'Effects of NaOH concentrations on physical and electrical properties of high calcium fly ash geopolymer paste', *Cement and Concrete Composites* **45**, 9–14.

URL: *http://dx.doi.org/10.1016/j.cemconcomp.2013.09.012*

Higginbotham, A. L., Kosynkin, D. V., Sinitskii, A., Sun, Z. & Tour, J. M. (2010), 'Lower-defect graphene oxide nanoribbons from multiwalled carbon nanotubes', *ACS Nano* **4**(4), 2059–2069.

Hofmann, B. Y. U. & Structure, C. (1938), 'T H E FORMATION OF S A L T S FROM GRAPHITE'.

Horszczaruk, E., Mijowska, E., Kalenczuk, R. J., Aleksandrzak, M. & Mijowska, S. (2015), 'Nanocomposite of cement/graphene oxide - Impact on hydration kinetics and Young's modulus', *Construction and Building Materials* **78**, 234–242.

Hughes, T. L., Methven, C. M., Jones, T. G., Pelham, S. E., Fletcher, P. & Hall, C. (1995), 'Determining cement composition by Fourier transform infrared spectroscopy', *Advanced Cement Based Materials* **2**(3), 91–104.

Hummel, W., Berner, U., Curti, E., Pearson, F. J. & Thoenen, T. (2002), 'Nagra / PSI Chemical Thermodynamic Data Base 01/01; Nagra technical report 02-16', **813**, 805–813.

Identification and Quantification of Cement Phases by X-Ray Diffraction (2008), Technical report.

Jadhav, R. & Debnath, N. C. (2011), 'Computation of X-ray powder diffractograms of cement components and its application to phase analysis and hydration performance of OPC cement', *Bulletin of Materials Science* **34**(5), 1137–1150.

JENNINGS, H. M. (1986), 'Aqueous Solubility Relationships for Two Types of Calcium Silicate Hydrate', *Journal of the American Ceramic Society* **69**(8), 614–618.

URL: *https://doi.org/10.1111/j.1151-2916.1986.tb04818.x*

Jennings, H. M. (2000), 'Model for the microstructure of calcium silicate hydrate in cement paste', *Cement and Concrete Research* **30**(1), 101–116.

Jennings, H. M., Bullard, J. W., Thomas, J. J., Andrade, J. E., Chen, J. J. & Scherer, G. W. (2008), '113037917 5-29 Characterization and modeling of pores and surfaces in cement paste: Correlations to processing and properties', *Journal of Advanced Concrete Technology* **6**(1), 5–29.

Jennings, H. M. & Pratt, P. L. (1979), 'An experimental argument for the existence of a protective membrane surrounding portland cement during the induction period', *Cement and Concrete Research* **9**(4), 501–506.

Jennings, H. M., Thomas, J. J., Gevrenov, J. S., Constantinides, G. & Ulm, F. J. (2007), 'A multi-technique investigation of the nanoporosity of cement paste', *Cement and Concrete Research* **37**(3), 329–336.

Jing, G., Wu, J., Lei, T., Wang, S., Strokova, V., Nelyubova, V., Wang, M. & Ye, Z. (2020), 'From graphene oxide to reduced graphene oxide: Enhanced hydration and compressive strength of cement composites', *Construction and Building Materials* **248**, 118699.

URL: *https://doi.org/10.1016/j.conbuildmat.2020.118699*

Juilland, P., Gallucci, E., Flatt, R. & Scrivener, K. (2010), 'Dissolution theory applied to the induction period in alite hydration', *Cement and Concrete Research* **40**(6), 831–844.

URL: *http://dx.doi.org/10.1016/j.cemconres.2010.01.012*

Kang, D., Seo, K. S., Lee, H. & Chung, W. (2017), 'Experimental study on mechanical strength of GO-cement composites', *Construction and Building Materials* **131**, 303–308.

URL: *http://linkinghub.elsevier.com/retrieve/pii/S0950061816318438*

Konsta-Gdoutos, M. S., Metaxa, Z. S. & Shah, S. P. (2010), 'Highly dispersed carbon nanotube reinforced cement based materials', *Cement and Concrete Research* **40**(7), 1052–1059.

URL: *http://dx.doi.org/10.1016/j.cemconres.2010.02.015*

Korayem, A. H., Tourani, N., Zakertabrizi, M., Sabziparvar, A. M. & Duan, W. H. (2017), 'A review of dispersion of nanoparticles in cementitious matrices: Nanoparticle geometry perspective'.

Kovtyukhova, N. I., Wang, Y., Berkdemir, A., Cruz-Silva, R., Terrones, M., Crespi, V. H. & Mallouk, T. E. (2014), 'Non-oxidative intercalation and exfoliation of graphite by Brønsted acids', *Nature Chemistry* **6**(11), 957–963.

Lee, C., Wei, X., Kysar, J. W. & Hone, J. (2008), 'Measurement of the elastic properties and intrinsic strength of monolayer graphene', *Science* **321**(5887), 385–388.

URL: *http://science.sciencemag.org/content/321/5887/385*

Li, C., Chen, X., Shen, L. & Bao, N. (2020), 'Revisiting the Oxidation of Graphite: Reaction Mechanism, Chemical Stability, and Structure Self-Regulation', *ACS Omega* **5**(7), 3397–3404.

Li, D., Müller, M. B., Gilje, S., Kaner, R. B. & Wallace, G. G. (2008), 'Processable aqueous dispersions of graphene nanosheets', *Nature Nanotechnology* **3**(2), 101–105.

Li, W., Li, X., Chen, S. J., Liu, Y. M., Duan, W. H. & Shah, S. P. (2017), 'Effects of graphene oxide on early-age hydration and electrical resistivity of Portland cement paste', *Construction and Building Materials* **136**, 506–514.

Li, X., Korayem, A. H., Li, C., Liu, Y., He, H., Sanjayan, J. G. & Duan, W. H. (2016), 'Incorporation of graphene oxide and silica fume into cement paste: A study of dispersion and compressive strength', *Construction and Building Materials* **123**, 327–335.

Li, X., Liu, Y. M., Li, W. G., Li, C. Y., Sanjayan, J. G., Duan, W. H. & Li, Z. (2017), 'Effects of graphene oxide agglomerates on workability, hydration, microstructure and compressive strength of cement paste', *Construction and Building Materials* **145**, 402–410.

Li, X., Lu, Z., Chuah, S., Li, W., Liu, Y., Duan, W. H. & Li, Z. (2017), 'Effects of graphene oxide aggregates on hydration degree, sorptivity, and tensile splitting strength of cement paste', *Composites Part A: Applied Science and Manufacturing* **100**, 1–8.
URL: *http://dx.doi.org/10.1016/j.compositesa.2017.05.002*

Li, X., Wei, W., Qin, H. & Hang Hu, Y. (2015), 'Co-effects of graphene oxide sheets and single wall carbon nanotubes on mechanical properties of cement', *Journal of Physics and Chemistry of Solids* **85**, 39–43.

Li, Z. (2011), Advanced cementitious composites, *in* 'Advanced Concrete Technology', pp. 251–325.

Lin, C., Wei, W. & Hu, Y. H. (2016), 'Catalytic behavior of graphene oxide for cement hydration process', *Journal of Physics and Chemistry of Solids* **89**, 128–133.

Liu, Q., Xu, Q., Yu, Q., Gao, R. & Tong, T. (2016), 'Experimental investigation on mechanical and piezoresistive properties of cementitious materials contain-

ing graphene and graphene oxide nanoplatelets', *Construction and Building Materials* **127**, 565–576.

Livingston, R. A., Schweitzer, J. S., Rolfs, C., Becker, H. W. & Kubsky, S. (2001), 'Characterization of the induction period in tricalcium silicate hydration by nuclear resonance reaction analysis', *Journal of Materials Research* **16**(3), 687–693.

URL: *https://www.cambridge.org/core/article/characterization-of-the-induction-period-in-tricalcium-silicate-hydration-by-nuclear-resonance-reaction-analysis/0C1776D452BEC5207CFFDE1672543966*

Long, W.-J., Wei, J.-J., Ma, H. & Xing, F. (2017), 'Dynamic Mechanical Properties and Microstructure of Graphene Oxide Nanosheets Reinforced Cement Composites', *Nanomaterials* **7**(12), 407.

URL: *http://www.mdpi.com/2079-4991/7/12/407*

Lowe, S. E. & Zhong, Y. L. (2016), 'Challenges of Industrial-Scale Graphene Oxide Production', *Graphene Oxide: Fundamentals and Applications* (November 2017), 410–431.

Lowry, G. V., Hill, R. J., Harper, S., Rawle, A. F., Hendren, C. O., Klaessig, F., Nobbmann, U., Sayre, P. & Rumble, J. (2016), 'Guidance to improve the scientific value of zeta-potential measurements in nanoEHS', *Environmental Science: Nano* **3**(5), 953–965.

Lu, C., Lu, Z., Li, Z. & Leung, C. K. (2016), 'Effect of graphene oxide on the mechanical behavior of strain hardening cementitious composites', *Construction*

and Building Materials **120**, 457–464.

URL: *http://dx.doi.org/10.1016/j.conbuildmat.2016.05.122*

Lu, L. & Ouyang, D. (2017), 'Properties of Cement Mortar and Ultra-High Strength Concrete Incorporating Graphene Oxide Nanosheets', *Nanomaterials* **7**(7), 187.

URL: *http://www.mdpi.com/2079-4991/7/7/187*

Lu, Z., Hou, D., Meng, L., Sun, G., Lu, C. & Li, Z. (2015), 'Mechanism of cement paste reinforced by graphene oxide/carbon nanotubes composites with enhanced mechanical properties', *RSC Adv.* **5**(122), 100598–100605.

URL: *http://xlink.rsc.org/?DOI=C5RA18602A*

Lu, Z., Li, X., Hanif, A., Chen, B., Parthasarathy, P., Yu, J. & Li, Z. (2017), 'Early-age interaction mechanism between the graphene oxide and cement hydrates', *Construction and Building Materials* **152**, 232–239.

Lv, S., Cui, Y., Zhou, Q., Yang, W. & Zhao, H. (2015), 'Effect of polyacrylate/go nanocomposites on properties of cement paste', **68**, 1–10.

Lv, S. H., Deng, L. J., Yang, W. Q., Zhou, Q. F. & Cui, Y. Y. (2016), 'Fabrication of polycarboxylate/graphene oxide nanosheet composites by copolymerization for reinforcing and toughening cement composites', *Cement and Concrete Composites* **66**, 1–9.

Lv, S., Hu, H., Zhang, J., Lei, Y., Sun, L. & Hou, Y. (2019), 'Structure, performances, and formation mechanism of cement composites with large-scale regular microstructure by distributing uniformly few-layered graphene oxide in cement matrix', *Structural Concrete* **20**(1), 471–482.

Lv, S., Liu, J., Sun, T., Ma, Y. & Zhou, Q. (2014), 'Effect of GO nanosheets on shapes of cement hydration crystals and their formation process', *Construction and Building Materials* **64**, 231–239.
URL: *http://linkinghub.elsevier.com/retrieve/pii/S095006181400378X*

Lv, S., Ma, Y., Qiu, C., Sun, T., Liu, J. & Zhou, Q. (2013), 'Effect of graphene oxide nanosheets of microstructure and mechanical properties of cement composites', *Construction and Building Materials* **49**, 121–127.

Lv, S., Ting, S., Liu, J. & Zhou, Q. (2014), 'Use of graphene oxide nanosheets to regulate the microstructure of hardened cement paste to increase its strength and toughness', *CrystEngComm* **16**(36), 8508.
URL: *http://xlink.rsc.org/?DOI=C4CE00684D*

Makar, J. M. & Chan, G. W. (2008), 'End of the induction period in ordinary portland cement as examined by high-resolution scanning electron microscopy', *Journal of the American Ceramic Society* **91**(4), 1292–1299.
URL: *https://doi.org/10.1111/j.1551-2916.2008.02304.x*

Marcano, D. C., Kosynkin, D. V., Berlin, J. M., Sinitskii, A., Sun, Z. Z., Slesarev, A., Alemany, L. B., Lu, W. & Tour, J. M. (2010), 'Improved Synthesis of Graphene Oxide', *Acs Nano* **4**(8), 4806–4814.

Medhekar, N. V., Ramasubramaniam, A., Ruoff, R. S. & Shenoy, V. B. (2010), 'Hydrogen bond networks in graphene oxide composite paper: Structure and mechanical properties', *ACS Nano* **4**(4), 2300–2306.

Meng, W. & Khayat, K. H. (2016), 'Mechanical properties of ultra-high-

performance concrete enhanced with graphite nanoplatelets and carbon nanofibers', *Composites Part B: Engineering* **107**.

Metaxa, Z. S., Konsta-Gdoutos, M. S. & Shah, S. P. (2013), 'Carbon nanofiber cementitious composites: Effect of debulking procedure on dispersion and reinforcing efficiency', *Cement and Concrete Composites* **36**(1), 25–32.
URL: *http://dx.doi.org/10.1016/j.cemconcomp.2012.10.009*

Mohammed, A., Sanjayan, J. G., Duan, W. H. & Nazari, A. (2015), 'Incorporating graphene oxide in cement composites: A study of transport properties', *Construction and Building Materials* **84**, 341–347.
URL: *http://dx.doi.org/10.1016/j.conbuildmat.2015.01.083*

Mohammed, A., Sanjayan, J. G., Duan, W. H. & Nazari, A. (2016), 'Graphene Oxide Impact on Hardened Cement Expressed in Enhanced Freeze – Thaw Resistance', *Journal of Materials in Civil Engineering* **28**(9), 04016072–1 – 04016072–6.

Mokhtar, M. M., Abo-El-Enein, S. A., Hassaan, M. Y., Morsy, M. S. & Khalil, M. H. (2017), 'Mechanical performance, pore structure and micro-structural characteristics of graphene oxide nano platelets reinforced cement', *Construction and Building Materials* **138**, 333–339.

Moriwake, H., Kuwabara, A., Fisher, C. A. & Ikuhara, Y. (2017), 'Why is sodium-intercalated graphite unstable?', *RSC Advances* **7**(58), 36550–36554.
URL: *http://dx.doi.org/10.1039/C7RA06777A*

Mouhat, F., Coudert, F. X. & Bocquet, M. L. (2020), 'Structure and chemistry of graphene oxide in liquid water from first principles', *Nature Communications*

11(1), 1–9.

URL: *http://dx.doi.org/10.1038/s41467-020-15381-y*

Murugan, M., Santhanam, M., Sen Gupta, S., Pradeep, T. & Shah, S. P. (2016), 'Influence of 2D rGO nanosheets on the properties of OPC paste', *Cement and Concrete Composites* **70**, 48–59.

URL: *http://www.sciencedirect.com/science/article/pii/S0958946516300464?via%3Dihub*

Musso, S., Tulliani, J.-M., Ferro, G. & Tagliaferro, A. (2009), 'Influence of carbon nanotubes structure on the mechanical behavior of cement composites', **69**, 1985–1990.

Nasibulin, A. G., Shandakov, S. D., Nasibulina, L. I., Cwirzen, A., Mudimela, P. R., Habermehl-Cwirzen, K., Grishin, D. A., Gavrilov, Y. V., Malm, J. E., Tapper, U., Tian, Y., Penttala, V., Karppinen, M. J. & Kauppinen, E. I. (2009), 'A novel cement-based hybrid material', *New Journal of Physics* **11**.

Neville, A. M. (1996), *Properties of Concrete*, Vol. Fourth.

Neville, A. M. (2019), 'Concrete Technology by A M Neville', (June), 1–443.

Norhasri, M. S., Hamidah, M. S. & Fadzil, A. M. (2017), 'Applications of using nano material in concrete: A review', *Construction and Building Materials* **133**, 91–97.

URL: *https://www.sciencedirect.com/science/article/pii/S0950061816319110?via%3Dihub*

http://linkinghub.elsevier.com/retrieve/pii/S0950061816319110

Odler, I. & Dörr, H. (1979), 'Early hydration of tricalcium silicate II. The induc-

tion period', *Cement and Concrete Research* **9**(3), 277–284.

URL: *https://linkinghub.elsevier.com/retrieve/pii/0008884679901194*

Oickle, A. M., Goertzen, S. L., Hopper, K. R., Abdalla, Y. O. & Andreas, H. A. (2010), 'Standardization of the Boehm titration: Part II. Method of agitation, effect of filtering and dilute titrant', *Carbon* **48**(12), 3313–3322.

URL: *http://dx.doi.org/10.1016/j.carbon.2010.05.004*

Ollivier, J. P., Maso, J. C. & Bourdette, B. (1995), 'Interfacial transition zone in concrete'.

Pan, Z., He, L., Qiu, L., Korayem, A. H., Li, G., Zhu, J. W., Collins, F., Li, D., Duan, W. H. & Wang, M. C. (2015), 'Mechanical properties and microstructure of a graphene oxide-cement composite', *Cement and Concrete Composites* **58**, 140–147.

Papageorgiou, D. G., Kinloch, I. A. & Young, R. J. (2017), 'Mechanical properties of graphene and graphene-based nanocomposites'.

URL: *https://www.sciencedirect.com/science/article/pii/S0079642517300968*

Parades, J. I., Villar-Rodil, S., Martínez-Alonso, A. & Tascón, J. M. (2008), 'Graphene oxide dispersions in organic solvents', *Langmuir* **24**(19), 10560–10564.

Parkhurst, D. L. & Appelo, C. A. J. (1999), User's Guide to PHREEQC (Version 2): A Computer Program for Speciation, Batch-Reaction, One-Dimensional Transport, and Inverse Geochemical Calculations, Technical Report Water-Resources Investigations Report 99-4259.

URL: *http://www.acamedia.info/sciences/J_G/references/PHREEQC_Manual.pdf*

Parveen, S., Rana, S. & Fangueiro, R. (2013), 'A review on nanomaterial dispersion, microstructure, and mechanical properties of carbon nanotube and nanofiber reinforced cementitious composites', *Journal of Nanomaterials* **2013**.

Parveen, S., Rana, S., Fangueiro, R. & Paiva, M. C. (2015), 'Microstructure and mechanical properties of carbon nanotube reinforced cementitious composites developed using a novel dispersion technique', *Cement and Concrete Research* **73**, 215–227.
URL: *http://dx.doi.org/10.1016/j.cemconres.2015.03.006*

Peterson, V. K., Brown, C. M. & Livingston, R. A. (2006), 'Quasielastic and inelastic neutron scattering study of the hydration of monoclinic and triclinic tricalcium silicate', *Chemical Physics* **326**(2), 381–389.
URL: *https://www.sciencedirect.com/science/article/pii/S0301010406001273*

Peyvandi, A., Soroushian, P., Balachandra, A. M. & Sobolev, K. (2013), 'Enhancement of the durability characteristics of concrete nanocomposite pipes with modified graphite nanoplatelets', *Construction and Building Materials* **47**, 111–117.

Posudievsky, O. Y., Kozarenko, O. A., Khazieieva, O. A., Koshechko, V. G. & Pokhodenko, V. D. (2013), 'Ultrasound-free preparation of graphene oxide from mechanochemically oxidized graphite', *J. Mater. Chem. A* **1**, 6658–6663.
URL: *http://dx.doi.org/10.1039/C3TA10542C*

Qin, H., Wei, W. & Hang Hu, Y. (2017), 'Synergistic effect of graphene-oxide-doping and microwave-curing on mechanical strength of cement', *Journal of Physics and Chemistry of Solids* **103**, 67–72.

Qiu, C., Zhou, Q., Lv, S. & Ma, Y. (2013), 'Regulation of GO on cement hydration crystals and its toughening effect', *Magazine of Concrete Research* **65**(20), 1246–1254.

URL: *http://www.scopus.com/inward/record.url?eid=2-s2.0-84884524234&partnerID=tZOtx3y1*

Qiu, Y., Guo, F., Hurt, R. & Külaots, I. (2014), 'Explosive thermal reduction of graphene oxide-based materials: mechanism and safety implications', *Carbon* **72**, 215–223.

URL: *http://www.ncbi.nlm.nih.gov/pmc/articles/PMC4088991/*

Qureshi, T. S., Panesar, D. K., Sidhureddy, B., Chen, A. & Wood, P. C. (2019), 'Nano-cement composite with graphene oxide produced from epigenetic graphite deposit', *Composites Part B: Engineering* **159**, 248–258.

URL: *https://doi.org/10.1016/j.compositesb.2018.09.095*

Rattana, T., Chaiyakun, S., Witit-Anun, N., Nuntawong, N., Chindaudom, P., Oaew, S., Kedkeaw, C. & Limsuwan, P. (2012), 'Preparation and characterization of graphene oxide nanosheets', *Procedia Engineering* **32**, 759–764.

URL: *http://dx.doi.org/10.1016/j.proeng.2012.02.009*

Renaudin, G., Russias, J., Leroux, F., Frizon, F. & Cau-dit Coumes, C. (2009), 'Structural characterization of C-S-H and C-A-S-H samples-Part I: Long-range order investigated by Rietveld analyses', *Journal of Solid State Chemistry* **182**(12), 3312–3319.

Richardson, I. G. (2004), 'Tobermorite/jennite- and tobermorite/calcium hydroxide-based models for the structure of C-S-H: Applicability to hard-

ened pastes of tricalcium silicate, β-dicalcium silicate, Portland cement, and blends of Portland cement with blast-furnace slag, metakaolin, or silica fume', *Cement and Concrete Research* **34**(9), 1733–1777.

Rietveld, H. M. (1969), 'A profile refinement method for nuclear and magnetic structures', *Journal of Applied Crystallography* **2**(2), 65–71.

Rogala, M., Dabrowski, P., Kowalczyk, P. J., Wlasny, I., Kozlowski, W., Busiakiewicz, A., Karaduman, I., Lipinska, L., Baranowski, J. M. & Klusek, Z. (2016), 'The observer effect in graphene oxide - How the standard measurements affect the chemical and electronic structure', *Carbon* **103**, 235–241.
URL: *http://dx.doi.org/10.1016/j.carbon.2016.03.015*

Rourke, J. P., Pandey, P. A., Moore, J. J., Bates, M., Kinloch, I. A., Young, R. J. & Wilson, N. R. (2011), 'The Real Graphene Oxide Revealed: Stripping the Oxidative Debris from the Graphene-like Sheets', *Angewandte Chemie* **123**(14), 3231–3235.

Saafi, M., Tang, L., Fung, J., Rahman, M. & Liggat, J. (2015), 'Enhanced properties of graphene/fly ash geopolymeric composite cement', *Cement and Concrete Research* **67**, 292–299.

Saafi, M., Tang, L., Fung, J., Rahman, M., Sillars, F., Liggat, J. & Zhou, X. (2014), 'Graphene/fly ash geopolymeric composites as self-sensing structural materials', *Smart Materials and Structures* **23**(6).

Sanchez, F. & Sobolev, K. (2010), 'Nanotechnology in concrete – a review', *Construction and Building Materials* **24**(11), 2060–2071.
URL: *https://www.sciencedirect.com/science/article/pii/S0950061810001625*

Scrivener, K. L., Juilland, P. & Monteiro, P. J. (2015), 'Advances in understanding hydration of Portland cement', *Cement and Concrete Research* **78**.

Shahriary, L. & Athawale, A. a. (2014), 'Graphene Oxide Synthesized by using Modified Hummers Approach', *International Journal of Renewable Energy and Environmental Engineering* **02**(01), 58–63.

Shang, Y., Zhang, D., Yang, C., Liu, Y. & Liu, Y. (2015), 'Effect of graphene oxide on the rheological properties of cement pastes', *Construction and Building Materials* **96**, 20–28.

Sharma, S. & Kothiyal, N. C. (2015*a*), 'Influence of graphene oxide as dispersed phase in cement mortar matrix in defining the crystal patterns of cement hydrates and its effect on mechanical, microstructural and crystallization properties', *RSC Adv.* **5**(65), 52642–52657.
URL: *http://xlink.rsc.org/?DOI=C5RA08078A*

Sharma, S. & Kothiyal, N. C. (2015*b*), 'Influence of graphene oxide as dispersed phase in cement mortar matrix in defining the crystal patterns of cement hydrates and its effect on mechanical, microstructural and crystallization properties', *RSC Adv.* **5**(65), 52642–52657.
URL: *http://xlink.rsc.org/?DOI=C5RA08078A*

Sharon, M. & Sharon, M. (2015*a*), *Applications of Graphene*, John Wiley & Sons, Inc., pp. 145–165.
URL: *http://dx.doi.org/10.1002/9781118842577.ch6*

Sharon, M. & Sharon, M. (2015*b*), *Graphene in Industry, Commercialization Chal-*

lenges and Economics, John Wiley & Sons, Inc., pp. 217–255.

URL: *http://dx.doi.org/10.1002/9781118842577.ch9*

Sharon, M., Sharon, M., Shinohara, H., Tiwari, A. & Tiwari, A. (2015), *Graphene : An Introduction to the Fundamentals and Industrial Applications*, John Wiley & Sons, Incorporated, Hoboken, UNITED STATES, chapter 3.

URL: *http://ebookcentral.proquest.com/lib/unmc-ebooks/detail.action?docID=4039170*

Sigma-Aldrich (2021), 'IR Spectrum Chart'.

URL: *https://www.sigmaaldrich.com/technical-documents/articles/biology/ir-spectrum-table.html*

Silvestre, J., Silvestre, N. & De Brito, J. (2016), 'Review on concrete nanotechnology', *European Journal of Environmental and Civil Engineering* **20**(4), 455–485.

URL: *http://dx.doi.org/10.1080/19648189.2015.1042070*

Sindu, B., Sasmal, S. & Gopinath, S. (2014), 'A multi-scale approach for evaluating the mechanical characteristics of carbon nanotube incorporated cementitious composites', *Construction and Building Materials* **50**, 317 – 327.

URL: *http://www.sciencedirect.com/science/article/pii/S0950061813008933*

Skinner, L. B., Chae, S. R., Benmore, C. J., Wenk, H. R. & Monteiro, P. J. M. (2010), 'Nanostructure of Calcium Silicate Hydrates in Cements', *Phys. Rev. Lett.* **104**(19), 195502.

URL: *https://link.aps.org/doi/10.1103/PhysRevLett.104.195502*

Stein, H. N. & Stevels, J. M. (2007), 'Influence of silica on the hydration of 3 CaO,SiO2', *Journal of Applied Chemistry* **14**(8), 338–346.

Stutzman, P. E., Feng, P. & Bullard, J. W. (2016), 'Phase Analysis of Portland Cement by Combined Quantitative X-Ray Powder Diffraction and Scanning Electron Microscopy', *Journal of Research of the National Institute of Standards and Technology* **121**, 47.

Szabó, T., Berkesi, O., Forgó, P., Josepovits, K., Sanakis, Y., Petridis, D. & Dékány, I. (2006), 'Evolution of Surface Functional Groups in a Series of Progressively Oxidized Graphite Oxides Evolution of Surface Functional Groups in a Series of Progressively Oxidized Graphite Oxides', *Chemistry of Materials* **18**(11), 2740–2749.

URL: *http://pubs.acs.org/doi/abs/10.1021/cm060258%2B*

Szabo, T., Maroni, P. & Szilagyi, I. (2020), 'Size-dependent aggregation of graphene oxide', *Carbon* **160**, 145–155.

URL: *https://doi.org/10.1016/j.carbon.2020.01.022*

Taylor, H. F. (1992), 'Tobermorite, jennite, and cement gel', *Zeitschrift fur Kristallographie - New Crystal Structures* **202**(1-2), 41–50.

Teychenné, D. C., Franklin, R. E. & Erntroy, H. C. (1997), 'Design of normal concrete mixes', *Building Research Establishment Ltd* **331**(1), 46.

URL: *https://epdf.pub/design-of-normal-concrete-mixes-br-331-ci-sfb.html*

Teychenné, D., Franklin, R., Erntroy, H., Transport & Laboratory, R. R. (1975), *Design of normal concrete mixes*, H.M.S.O. [for the] Building Research Establishment [and the] Transport and Road Research Laboratory.

URL: *https://books.google.com.my/books?id=R-IhAQAAIAAJ*

Thomas, J. J., Biernacki, J. J., Bullard, J. W., Bishnoi, S., Dolado, J. S., Scherer, G. W. & Luttge, A. (2011), 'Modeling and simulation of cement hydration kinetics and microstructure development'.

Thomas, J. J., Jennings, H. M. & Chen, J. J. (2009), 'Influence of nucleation seeding on the hydration mechanisms of tricalcium silicate and cement', *Journal of Physical Chemistry C* **113**(11), 4327–4334.

Tong, T., Fan, Z., Liu, Q., Wang, S., Tan, S. & Yu, Q. (2016), 'Investigation of the effects of graphene and graphene oxide nanoplatelets on the micro- and macro-properties of cementitious materials', *Construction and Building Materials* **106**, 102–114.

URL: *http://dx.doi.org/10.1016/j.conbuildmat.2015.12.092*

Valizadeh Kiamahalleh, M., Gholampour, A., Tran, D. N., Ozbakkaloglu, T. & Losic, D. (2020), 'Physiochemical and mechanical properties of reduced graphene oxide–cement mortar composites: Effect of reduced graphene oxide particle size', *Construction and Building Materials* **250**, 118832.

URL: *https://doi.org/10.1016/j.conbuildmat.2020.118832*

Vallés, C., Beckert, F., Burk, L., Mülhaupt, R., Young, R. J. & A., K. I. (2015), 'Effect of the c/o ratio in graphene oxide materials on the reinforcement of epoxy-based nanocomposites', *Journal of Polymer Science Part B: Polymer Physics* **54**(2), 281–291.

URL: *https://onlinelibrary.wiley.com/doi/abs/10.1002/polb.23925*

Vorobiev, A., Dennison, A., Chernyshov, D., Skrypnychuk, V., Barbero, D. & Talyzin, A. V. (2014), 'Graphene oxide hydration and solvation: an in situ

neutron reflectivity study', *Nanoscale* **6**(20), 12151–12156.

URL: *http://xlink.rsc.org/?DOI=C4NR03621B*

Wang, B., Jiang, R. & Wu, Z. (2016), 'Investigation of the Mechanical Properties and Microstructure of Graphene Nanoplatelet-Cement Composite', *Nanomaterials* **6**(11), 200.

URL: *http://www.mdpi.com/2079-4991/6/11/200*

Wang, M., Wang, R., Yao, H., Farhan, S., Zheng, S. & Du, C. (2016), 'Study on the three dimensional mechanism of graphene oxide nanosheets modified cement', *Construction and Building Materials* **126**, 730–739.

URL: *http://www.sciencedirect.com/science/article/pii/S0950061816315410?via%3Dihub*

Wang, M. & Yao, H. (2020), 'Comparison study on the adsorption behavior of chemically functionalized graphene oxide and graphene oxide on cement', *Materials* **13**(15).

Wang, Q., Cui, X., Wang, J., Li, S., Lv, C. & Dong, Y. (2017), 'Effect of fly ash on rheological properties of graphene oxide cement paste', *Construction and Building Materials* **138**, 35–44.

URL: *http://dx.doi.org/10.1016/j.conbuildmat.2017.01.126*

Wang, Q., Wang, J., Lu, C.-X., Liu, B.-w., Zhang, K. & Li, C.-Z. (2015), 'Influence of graphene oxide additions on the microstructure and mechanical strength of cement', *New Carbon Materials* **30**(4), 349–356.

URL: *http://dx.doi.org/10.1016/S1872-5805(15)60194-9*

http://linkinghub.elsevier.com/retrieve/pii/S1872580515601949

Wick, P., Louw-Gaume, A. E., Kucki, M., Krug, H. F., Kostarelos, K., Fadeel, B., Dawson, K. A., Salvati, A., Vázquez, E., Ballerini, L., Tretiach, M., Benfenati, F., Flahaut, E., Gauthier, L., Prato, M. & Bianco, A. (2014), 'Classification framework for graphene-based materials', *Angewandte Chemie - International Edition* **53**(30), 7714–7718.

Wu, Z. Q. & Young, J. F. (1984), 'The hydration of tricalcium silicate in the presence of colloidal silica', *Journal of Materials Science* **19**(11), 3477–3486.

Xu, Y., Zeng, J., Chen, W., Jin, R., Li, B. & Pan, Z. (2018), 'A holistic review of cement composites reinforced with graphene oxide', *Construction and Building Materials* **171**, 291–302.
URL: *http://www.sciencedirect.com/science/article/pii/S0950061818306469*

Yamada, K., Takahashi, T., Hanehara, S. & Matsuhisa, M. (2000), 'Effects of the chemical structure on the properties of polycarboxylate-type superplasticizer', *Cement and Concrete Research* **30**(2), 197–207.

Yan, S., He, P., Jia, D., Yang, Z., Duan, X., Wang, S. & Zhou, Y. (2016), 'Effect of reduced graphene oxide content on the microstructure and mechanical properties of graphene–geopolymer nanocomposites', *Ceramics International* **42**(1), 752–758.
URL: *http://linkinghub.elsevier.com/retrieve/pii/S0272884215017022*

Yang, H., Monasterio, M., Cui, H. & Han, N. (2017), 'Experimental study of the effects of graphene oxide on microstructure and properties of cement paste composite', *Composites Part A: Applied Science and Manufacturing* **102**, 263–272.
URL: *http://dx.doi.org/10.1016/j.compositesa.2017.07.022*

Yazdanbakhsh, A., Grasley, Z., Tyson, B. & Abu Al-Rub, R. (2012), 'Challenges and benefits of utilizing carbon nanofilaments in cementitious materials', *Journal of Nanomaterials* **2012**.

Ylmén, R. & Jäglid, U. (2013), 'Carbonation of Portland Cement Studied by Diffuse Reflection Fourier Transform Infrared Spectroscopy', *International Journal of Concrete Structures and Materials* **7**(2), 119–125.

Ylmén, R., Jäglid, U., Steenari, B.-M. & Panas, I. (2009), 'Early hydration and setting of Portland cement monitored by IR, SEM and Vicat techniques', *Cement and Concrete Research* **39**(5), 433–439.

URL: *http://www.sciencedirect.com/science/article/pii/S0008884609000465*

You, S., Luzan, S. M., Szab??, T. & Talyzin, A. V. (2013), 'Effect of synthesis method on solvation and exfoliation of graphite oxide', *Carbon* **52**, 171–180.

Yu, H., Zhang, B., Bulin, C., Li, R. & Xing, R. (2016), 'High-efficient Synthesis of Graphene Oxide Based on Improved Hummers Method', *Scientific Reports* **6**(October), 1–7.

Zaaba, N. I., Foo, K. L., Hashim, U., Tan, S. J., Liu, W. W. & Voon, C. H. (2017), Synthesis of Graphene Oxide using Modified Hummers Method: Solvent Influence, *in* 'Procedia Engineering', Vol. 184, Elsevier, pp. 469–477.

URL: *http://www.sciencedirect.com/science/article/pii/S1877705817316235*

Zhang, C., Ren, L., Wang, X. & Liu, T. (2010), 'Graphene Oxide-Assisted Dispersion of Pristine Multiwalled Carbon Nanotubes in Aqueous Media', *The Journal of Physical Chemistry C* **114**(26), 11435–11440.

URL: *https://doi.org/10.1021/jp103745g*

Zhang, N., She, W., Du, F. & Xu, K. (2020), 'Experimental study on mechanical and functional properties of reduced graphene oxide/cement composites', *Materials* **13**(13).

Zhang, R. L., Gao, B., Du, W. T., Zhang, J., Cui, H. Z., Liu, L., Ma, Q. H., Wang, C. G. & Li, F. H. (2016), 'Enhanced mechanical properties of multiscale carbon fiber/epoxy composites by fiber surface treatment with graphene oxide/polyhedral oligomeric silsesquioxane', *Composites Part A: Applied Science and Manufacturing* **84**, 455–463.

Zhao, J., Wang, Z., White, J. C. & Xing, B. (2014), 'Graphene in the aquatic environment: Adsorption, dispersion, toxicity and transformation', *Environmental Science and Technology* **48**(17), 9995–10009.

Zhao, L., Guo, X., Ge, C., Li, Q., Guo, L., Shu, X. & Liu, J. (2016), 'Investigation of the effectiveness of PC@GO on the reinforcement for cement composites', *Construction and Building Materials* **113**, 470–478.

Zhao, L., Guo, X., Liu, Y., Ge, C., Guo, L., Shu, X. & Liu, J. (2017), 'Synergistic effects of silica nanoparticles/polycarboxylate superplasticizer modified graphene oxide on mechanical behavior and hydration process of cement composites', *RSC Adv.* **7**(27).

Zhao, L., Guo, X., Liu, Y., Zhao, Y., Chen, Z., Zhang, Y., Guo, L., Shu, X. & Liu, J. (2018), 'Hydration kinetics, pore structure, 3D network calcium silicate hydrate, and mechanical behavior of graphene oxide reinforced cement composites', *Construction and Building Materials* **190**, 150–163.
URL: *https://doi.org/10.1016/j.conbuildmat.2018.09.105*

Zhou, C., Li, F., Hu, J., Ren, M., Wei, J. & Yu, Q. (2017), 'Enhanced mechanical properties of cement paste by hybrid graphene oxide/carbon nanotubes', *Construction and Building Materials* **134**, 336–345.

Zhu, Y., Murali, S., Cai, W., Li, X., Suk, J. W., Potts, J. R. & Ruoff, R. S. (2010), 'Graphene and graphene oxide: Synthesis, properties, and applications', *Advanced Materials* **22**(35), 3906–3924.

Appendix 1: Concrete BRE mix design

Table 1 Concrete mix design form

Job title Mix design – Thesis.

Stage	Item		Reference or calculation	Values
1	1.1	Characteristic strength	Specified	35 N/mm² at 28 days; Proportion defective 5 %
	1.2	Standard deviation	Fig 3	8 N/mm² or no data ____ N/mm²
	1.3	Margin	C1 or Specified	(k = 1·64) ____ × ____ = ____ N/mm²; ____ N/mm²
	1.4	Target mean strength	C2	____ + ____ = 48·12 N/mm²
	1.5	Cement type	Specified	OPC/SRPC/RHPC
	1.6	Aggregate type: coarse Aggregate type: fine		Crushed/uncrushed Crushed/uncrushed
	1.7	Free-water/cement ratio	Table 2, Fig 4	0·44
	1.8	*Maximum free-water/cement ratio*	*Specified*	0·44 — Use the lower value 0·44
2	2.1	Slump or Vebe time	Specified	Slump 20 mm or Vebe time ____ s
	2.2	Maximum aggregate size	Specified	20 mm
	2.3	Free-water content	Table 3	160 kg/m³
3	3.1	Cement content	C3	160 ÷ 0·44 = 363·6 kg/m³
	3.2	*Maximum cement content*	*Specified*	— kg/m³
	3.3	*Minimum cement content*	*Specified*	— kg/m³
				use 3.1 if ≤ 3.2 use 3.3 if > 3.1 — 363·6 kg/m³
	3.4	Modified free-water/cement ratio		
4	4.1	Relative density of aggregate (SSD)		2·6 known/assumed
	4.2	Concrete density	Fig 5	2400 kg/m³
	4.3	Total aggregate content	C4	2400 − 160 − 363·6 = 1876·3 kg/m³
5	5.1	Grading of fine aggregate	Percentage passing 600 μm sieve	55 %
	5.2	Proportion of fine aggregate	Fig 6	38 %
	5.3	Fine aggregate content	C5	____ × ____ = 713·02 kg/m³
	5.4	Coarse aggregate content	C5	____ − ____ = 1163·35 kg/m³

Quantities	Cement (kg)	Water (kg or L)	Fine aggregate (kg)	Coarse aggregate (kg) 10 mm	20 mm	40 mm
per m³ (to nearest 5 kg)	365	160	715		1160	
per trial mix of ____ m³						

Items in italics are optional limiting values that may be specified (see Section 7)

1 N/mm² = 1 MN/m² = 1 MPa (see footnote to Section 3).
OPC = ordinary Portland cement; SRPC = sulphate-resisting Portland cement; RHPC = rapid-hardening Portland cement.
Relative density = specific gravity (see footnote to Para 5.4). SSD = based on a saturated surface-dry basis.

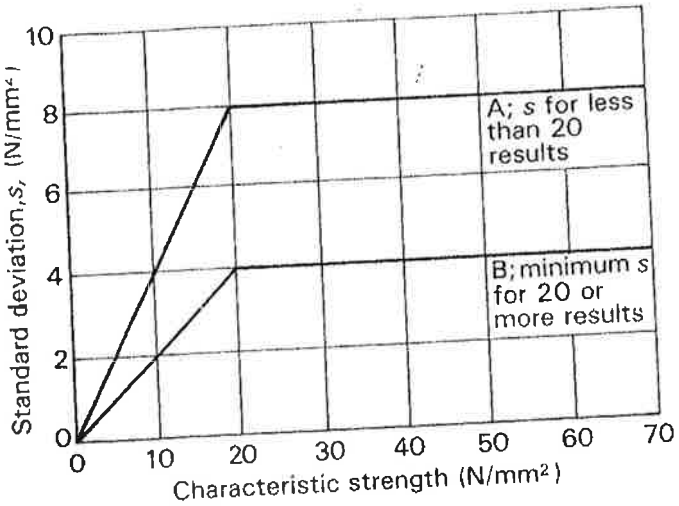

Figure 3 Relationship between standard deviation and characteristic strength

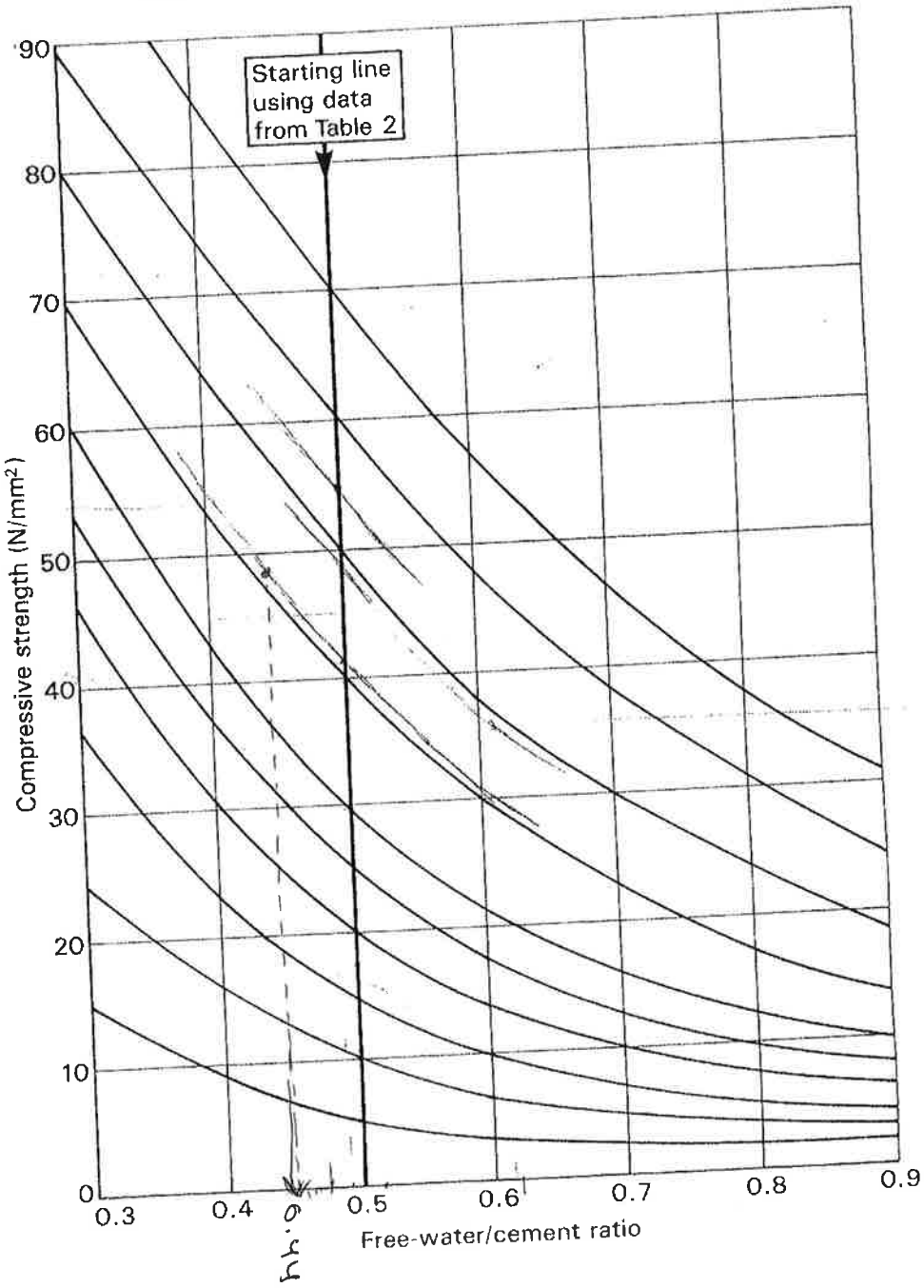

Figure 4 Relationship between compressive strength and free-water/cement ratio

Table 2 Approximate compressive strengths (N/mm²) of concrete mixes made with a free-water/cement ratio of 0.5

Type of cement	Type of coarse aggregate	Compressive strengths (N/mm²) Age (days) 3	7	28	91
Ordinary Portland (OPC) or sulphate-resisting Portland (SRPC)	Uncrushed	22	30	42	49
	Crushed	27	36	49	56
Rapid-hardening Portland (RHPC)	Uncrushed	29	37	48	54
	Crushed	34	43	55	61

1 N/mm² = 1 MN/m² = 1 MPa (see footnote on earlier page).

Table 3 Approximate free-water contents (kg/m³) required to give various levels of workability

Slump (mm) Vebe time(s)		0-10 >12	10-30 6-12	30-60 3-6	60-180 0-3
Maximum size aggregate (mm)	**Type of aggregate**				
10	Uncrushed	150	180	205	225
	Crushed	180	205	230	250
20	Uncrushed	135	160	180	195
	Crushed	170	190	210	225
40	Uncrushed	115	140	160	175
	Crushed	155	175	190	205

Note: When coarse and fine aggregates of different types are used, the free-water content is estimated by the expression

$$\tfrac{2}{3} W_f + \tfrac{1}{3} W_c$$

where W_f = free-water content appropriate to type of fine aggregate
and W_c = free-water content appropriate to type of coarse aggregate.

5.3 Determination of cement content (Stage 3)

The cement content is determined from calculation C3:

$$\text{Cement content} = \frac{\text{free-water content}}{\text{free-water/cement ratio}} \quad \ldots C3$$

The resulting value should be checked against any maximum or minimum value that may be specified. If the calculated cement content from C3 is below a specified minimum, this minimum value must be adopted and a modified free-water/cement ratio calculated which will be less than that determined in Stage 1. This will result in a concrete that has a mean strength somewhat higher than the target mean strength. Alternatively, the free-water/cement ratio from Stage 1 is used resulting in a higher free-water content and increased workability.

On the other hand, if the design method indicates a cement content that is higher than a specified maximum then it is probable that the specification cannot be met simultaneously on strength and workability requirements with the selected materials. Consideration should then be given to changing the type of cement, the type and maximum size of aggregate or the level of workability of the concrete, or to the use of a water reducing admixture.

5.4 Determination of total aggregate content (Stage 4)

Stage 4 requires an estimate of the density of the fully compacted concrete which is obtained from Figure 5 depending upon the free-water content and the relative density* of the combined aggregate in the saturated surface-dry condition (SSD). If no information is available regarding the relative density of the aggregate an approximation can be made by assuming a value of 2.6 for uncrushed aggregate and 2.7 for crushed aggregate. From this estimated density of the concrete the total aggregate content is determined from calculation C4:

$$\text{Total aggregate content} = D - C - W \quad \ldots C4$$
(saturated and surface-dry)

where D = the wet density of concrete (kg/m³)
C = the cement content (kg/m³)
W = the free-water content (kg/m³).

*The internationally known term 'relative density' used in this publication is synonymous with 'specific gravity' and is the ratio of the mass of a given volume of substance to the mass of an equal volume of water.

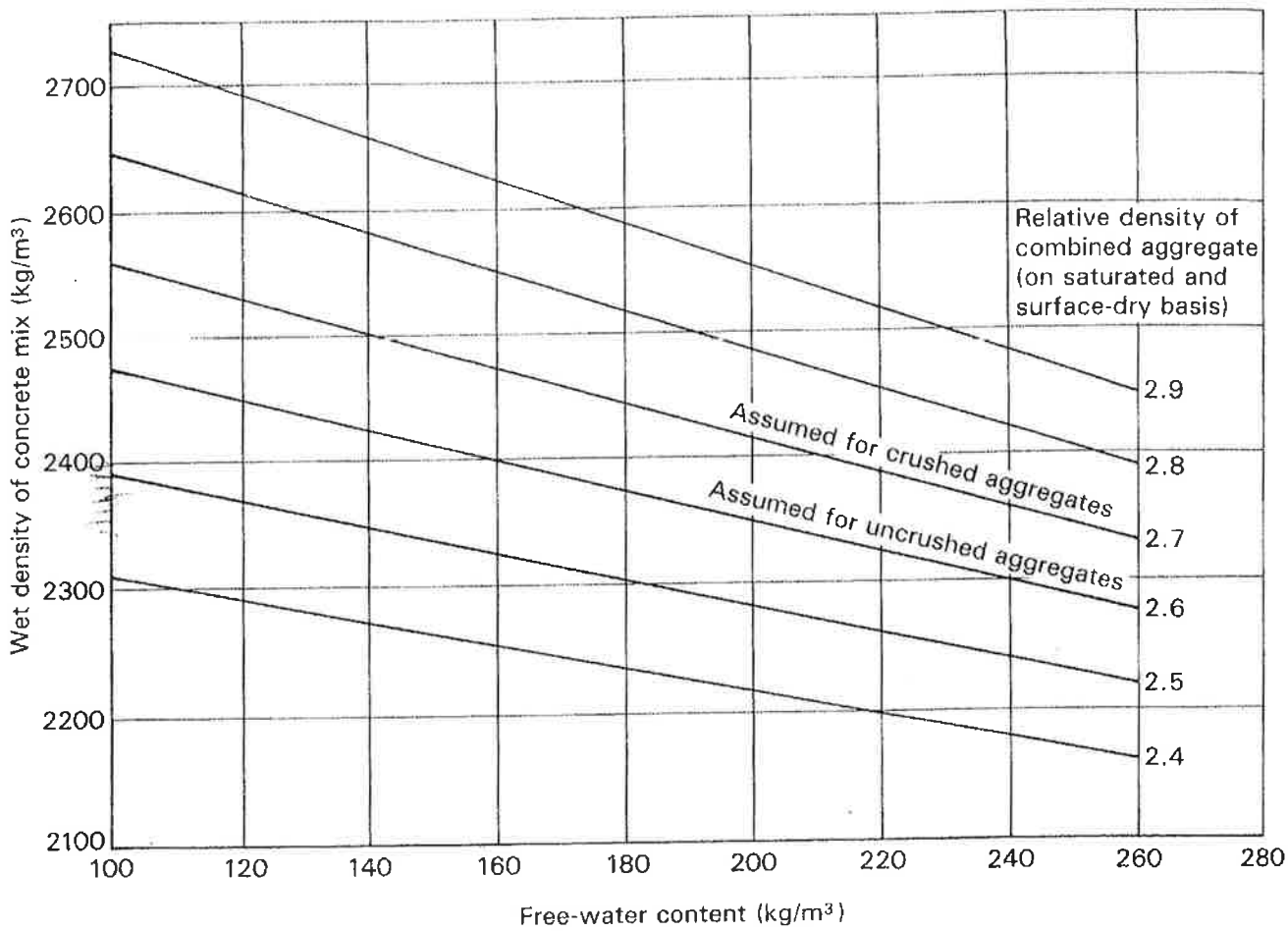

Figure 5 Estimated wet density of fully compacted concrete

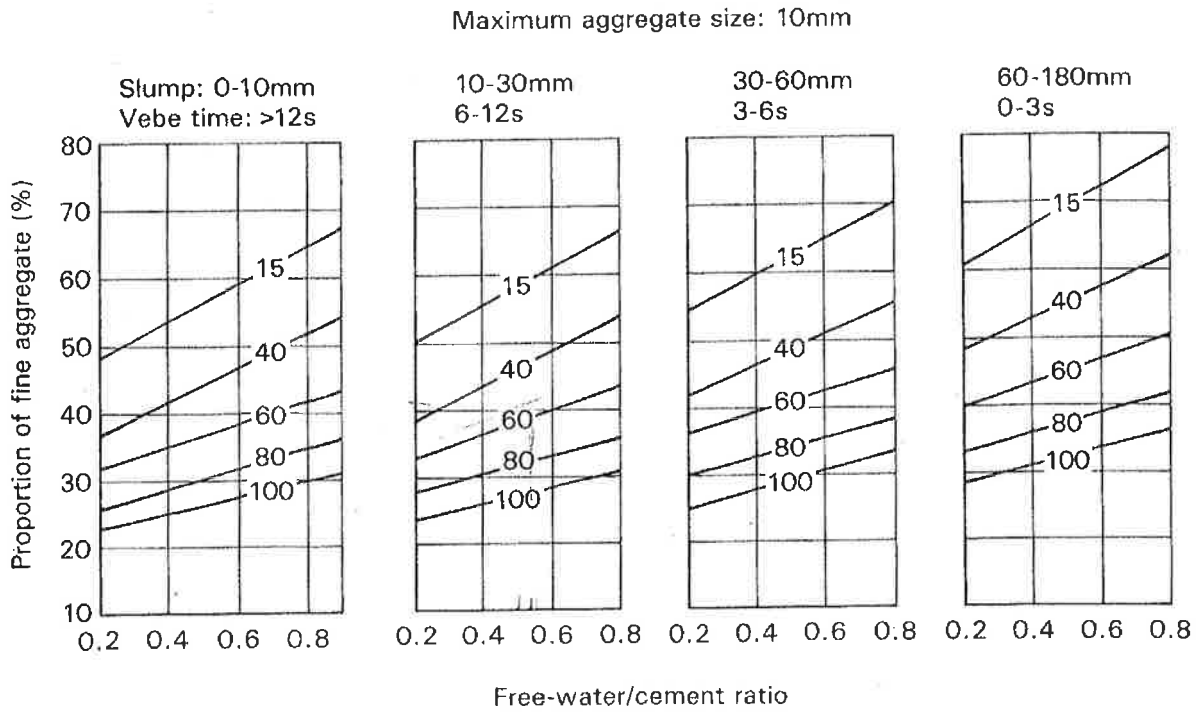

Figure 6 Recommended proportions of fine aggregate according to percentage passing a 600 μm sieve

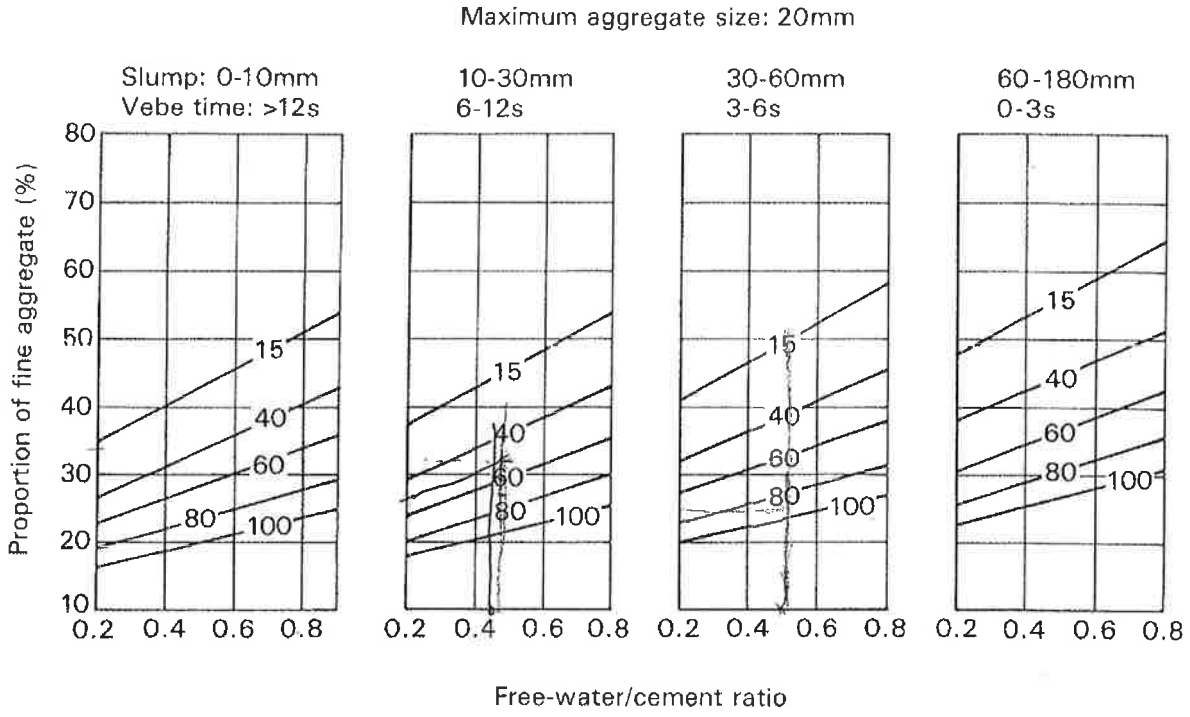

Figure 6 *(continued)*

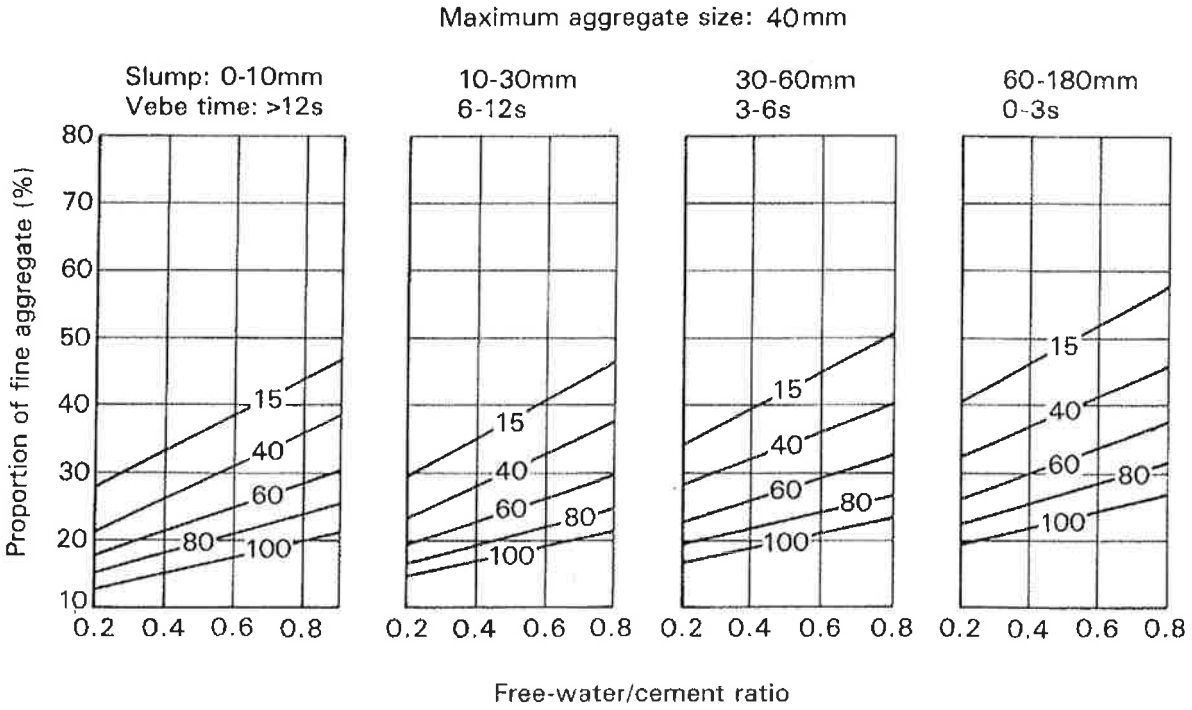

Figure 6 *(continued)*

Appendix 2: XPS Reports

MFA20200694

Nottingham University – Dr Kasturi

2020-11-11.106.spe: 2020-11-11 Company Name

2020 Nov 11 Al mono 24.3 W 100.0 µ 45.0° 280.00 eV 2.1958e+004 max 8.01 min

Su1s/Point2: LGO/1

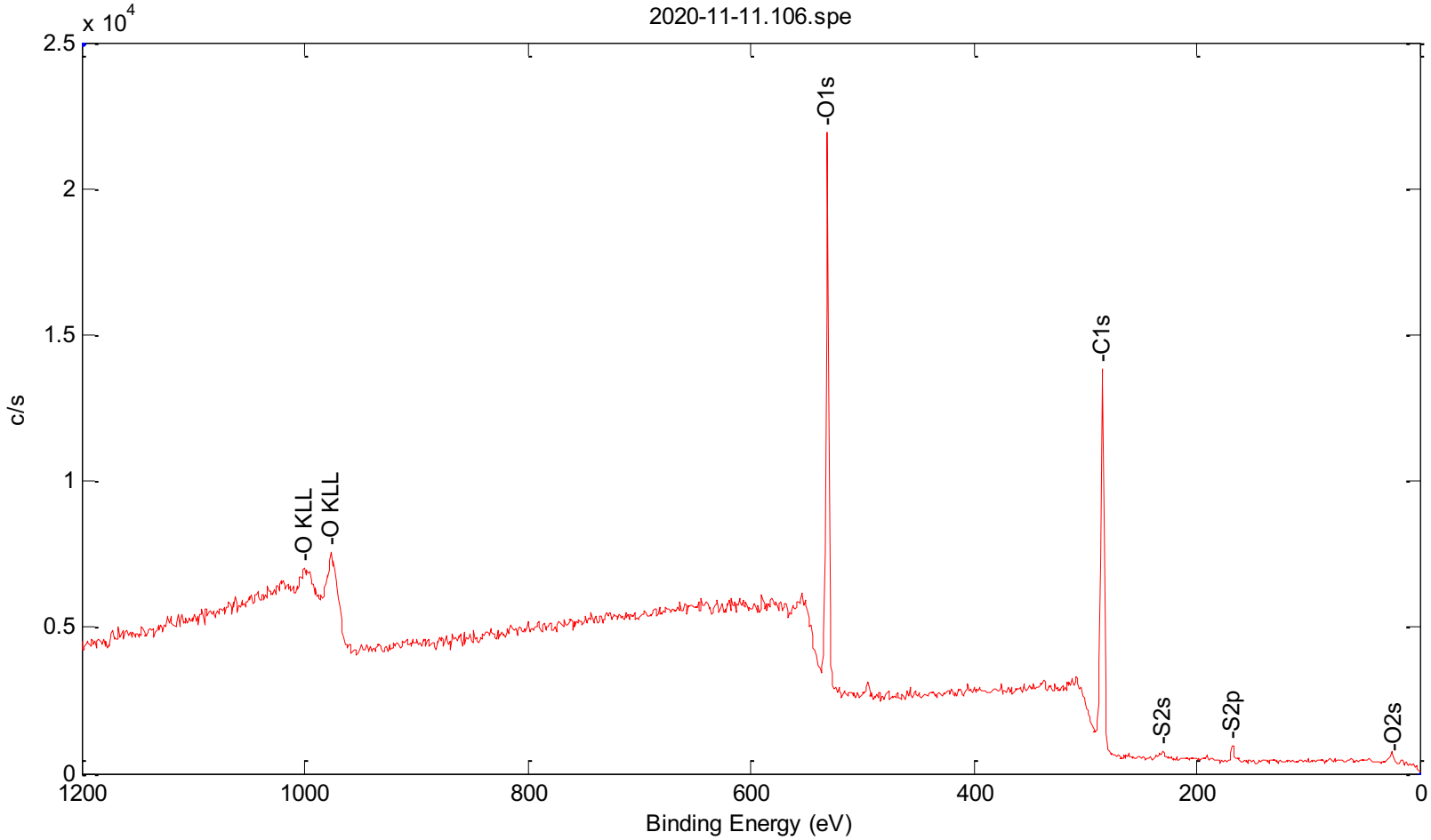

Atomic Concentration Table

C1s	O1s	S2p
67.23	32.05	0.72

Weight % Table

C1s	O1s	S2p
60.11	38.16	1.73

2020-11-11.110.spe: 2020-11-11 Company Name

2020 Nov 11 Al mono 24.3 W 100.0 µ 45.0° 112.00 eV 7.8950e+003 max 3.98 min

C1s/Point2: LGO/1 (Shft)

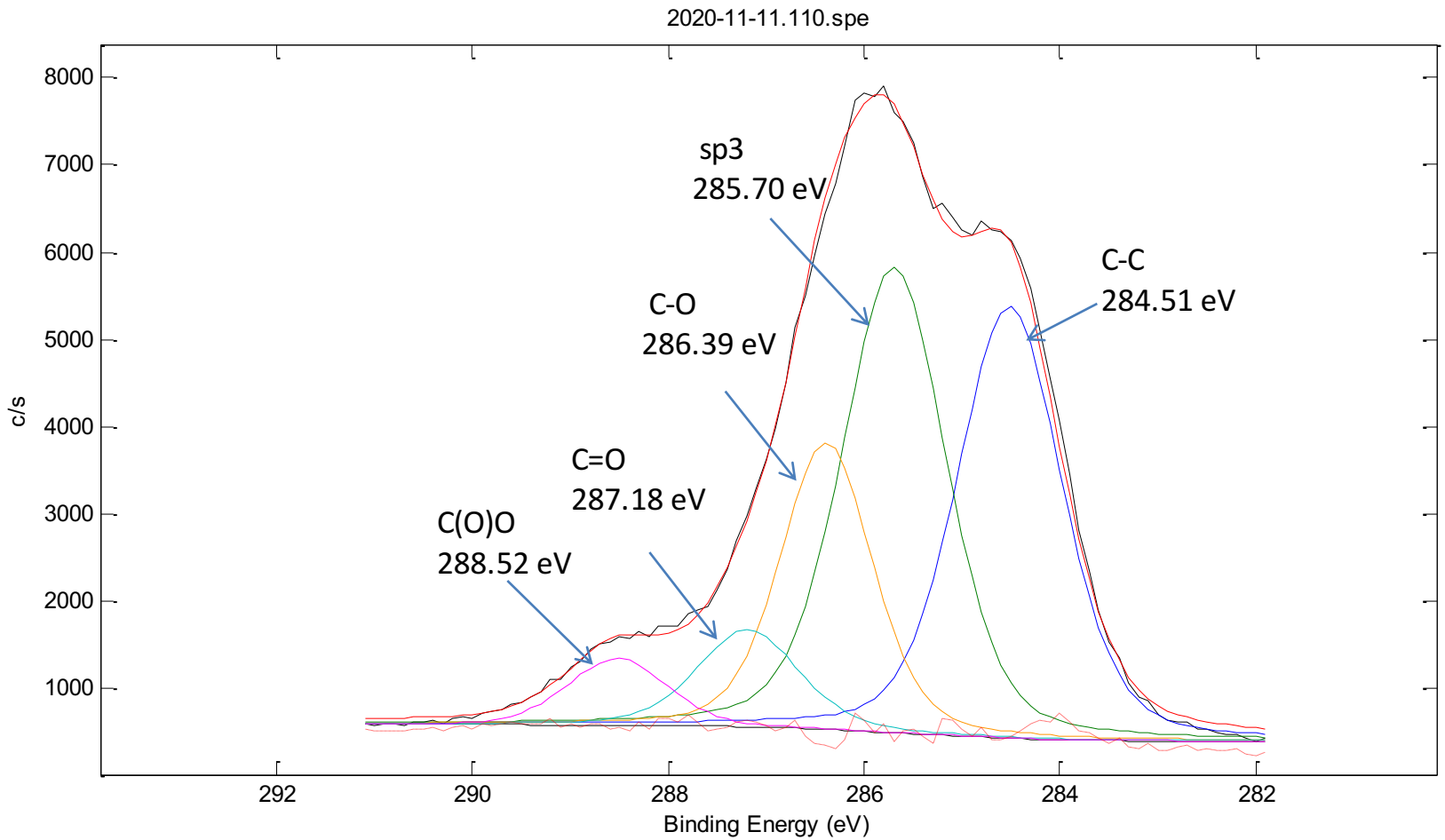

Atomic Concentration Table

C-C	sp3	C-O	C=O	C(O)O
33.34	35.60	19.20	7.24	4.62

2020-11-11.110.spe: 2020-11-11 Company Name

2020 Nov 11 Al mono 24.3 W 100.0 µ 45.0° 112.00 eV 1.3188e+004 max 3.98 min

O1s/Point2: LGO/1 (Shft)

	Ban...	Ba...	Ba...
Chem State	C=O	C-O	C(O)O
Area	469	23689	971
Position	530.20	532.27	534.34
Height	290	11409	485
FWHM	1.47	1.88	1.63
% Gauss	93	93	68

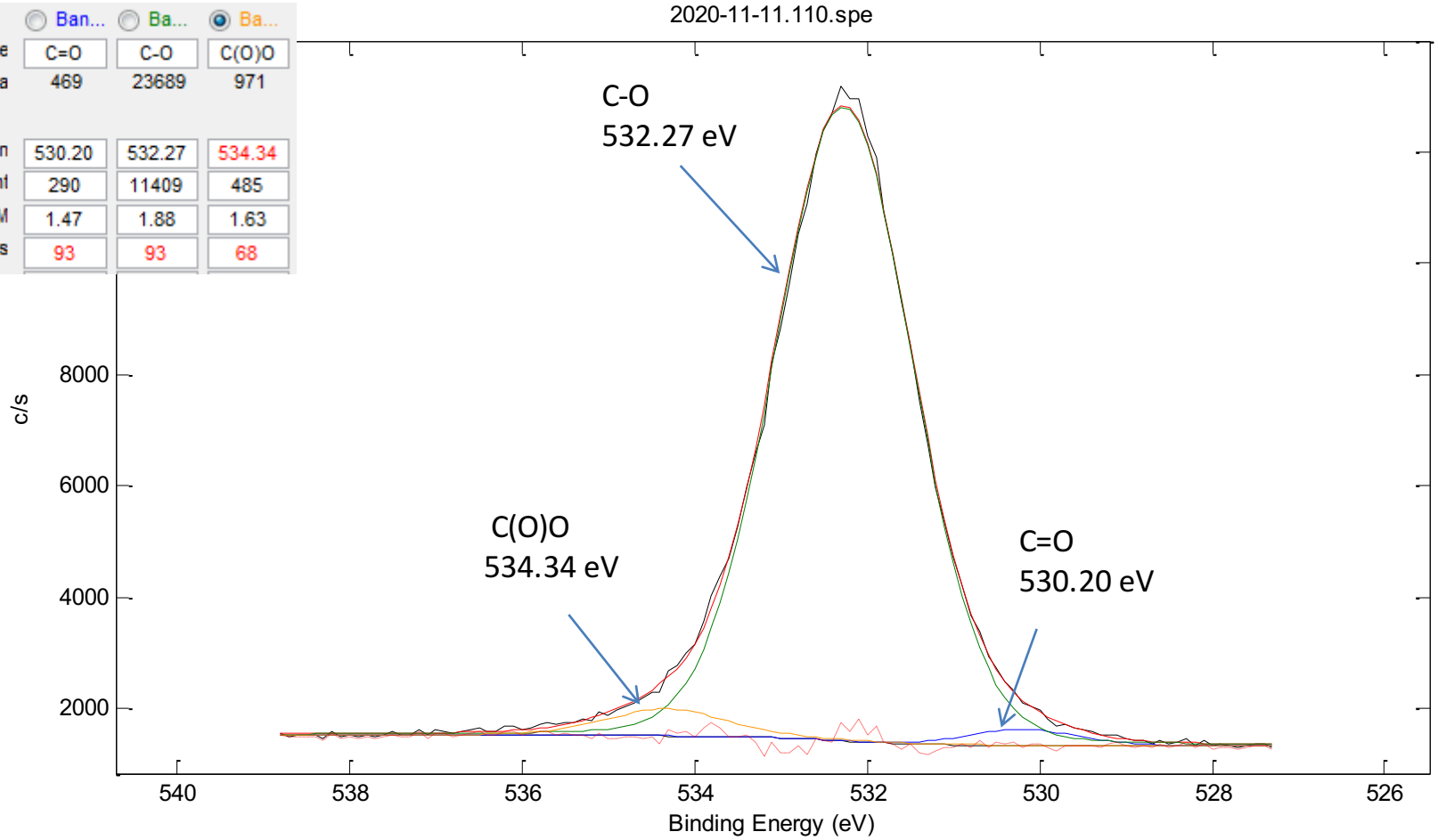

Atomic Concentration Table

C=O	C-O	C(O)O
1.87	94.27	3.86

2020-11-11.107.spe: 2020-11-11 Company Name

2020 Nov 11 Al mono 24.3 W 100.0 µ 45.0° 280.00 eV 3.9960e+004 max 8.01 min

Su1s/Point4: HGO/1

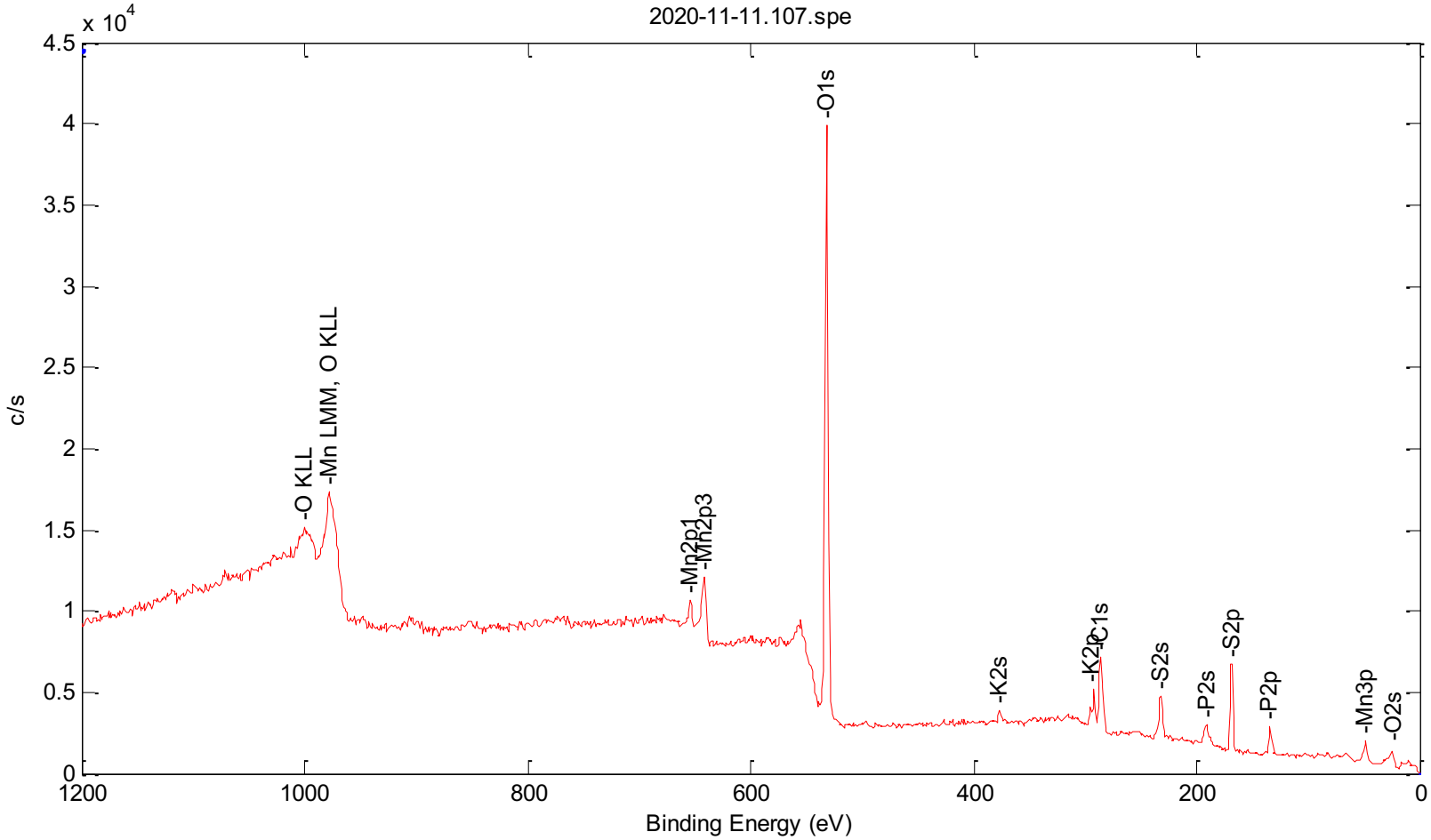

Atomic Concentration Table

C1s	O1s	P2p	S2p	Mn2p3
20.50	65.09	3.17	8.18	3.06

Weight % Table

C1s	O1s	P2p	S2p	Mn2p3
13.55	57.34	5.40	14.44	9.27

2020-11-11.111.spe: 2020-11-11 Company Name

2020 Nov 11 Al mono 24.3 W 100.0 µ 45.0° 112.00 eV 4.2450e+003 max 4.02 min

C1s/Point4: HGO/1 (Shft)

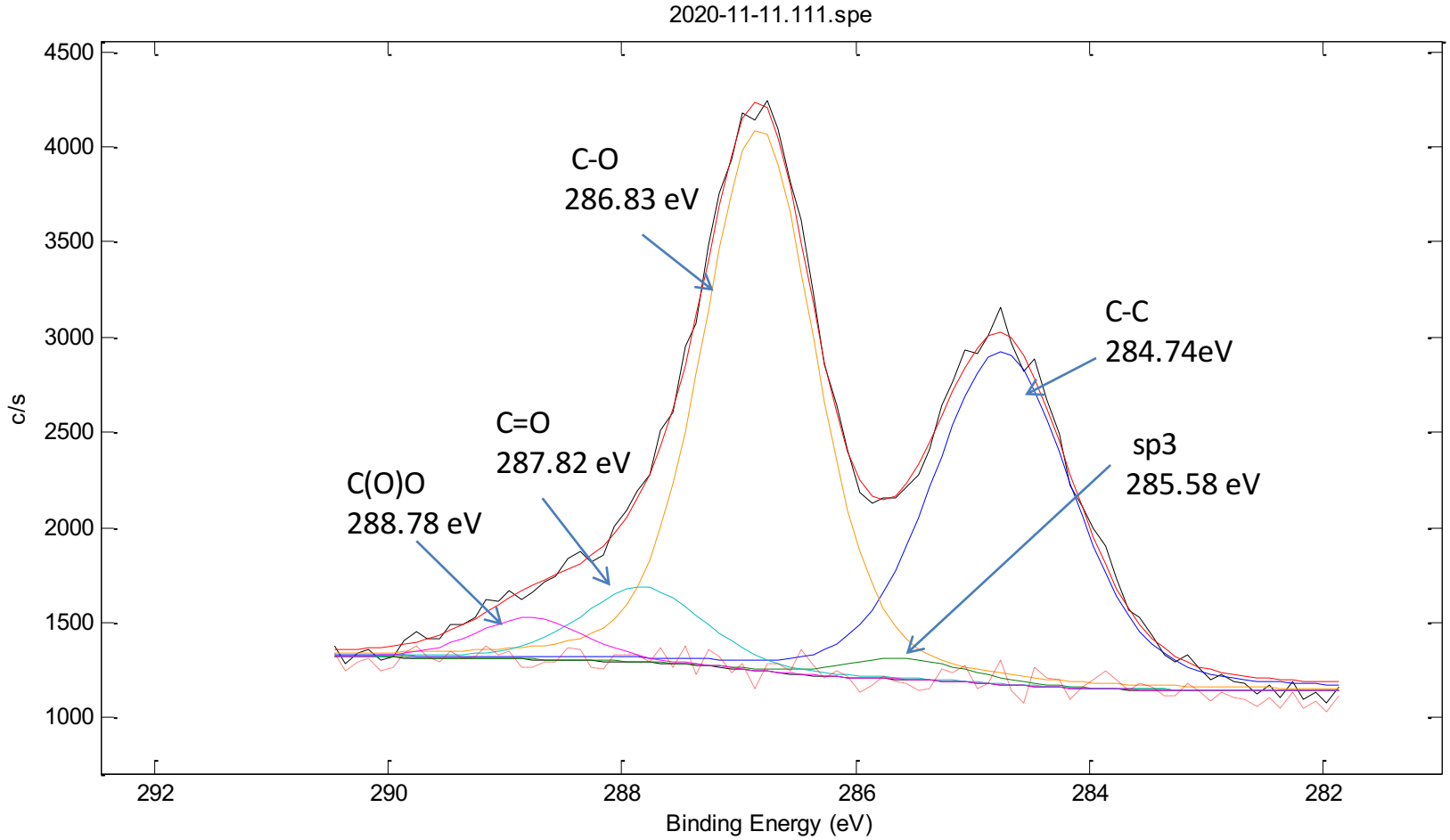

Atomic Concentration Table

C-C	sp3	C-O	C=O	C(O)O
37.55	2.09	49.49	7.37	3.50

2020-11-11.111.spe: 2020-11-11 Company Name

2020 Nov 11 Al mono 24.3 W 100.0 µ 45.0° 112.00 eV 2.1428e+004 max 4.02 min

O1s/Point4: HGO/1 (Shft)

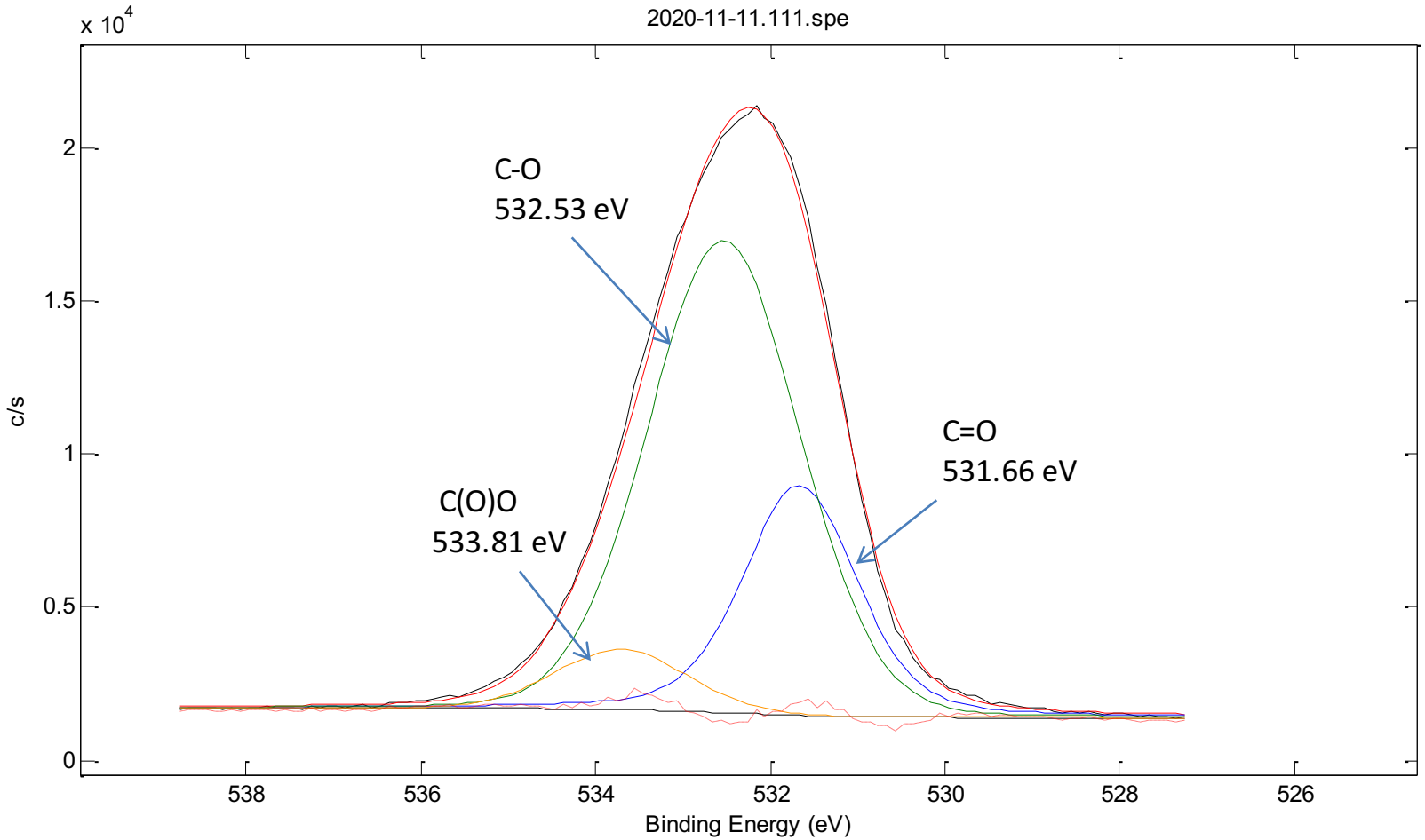

Atomic Concentration Table

C=O	C-O	C(O)O
26.87	65.83	7.30

2020-11-11.108.spe: 2020-11-11 Company Name

2020 Nov 11 Al mono 24.3 W 100.0 µ 45.0° 280.00 eV 1.4863e+004 max 8.01 min

Su1s/Point6: OGO/1

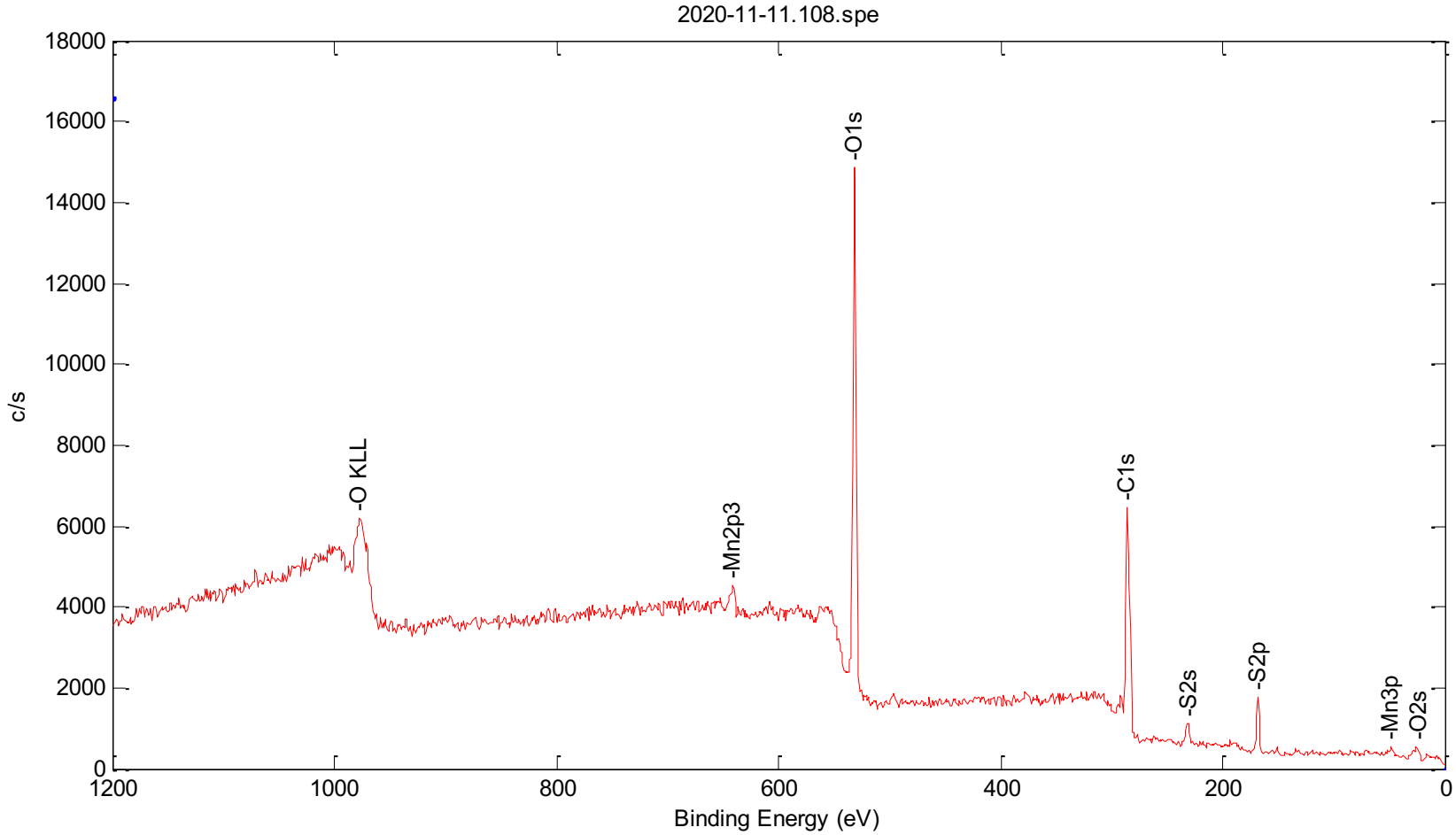

Atomic Concentration Table

C1s	O1s	S2p	Mn2p3
50.82	44.06	3.96	1.16

Weight % Table

C1s	O1s	S2p	Mn2p3
40.52	46.80	8.43	4.25

2020-11-11.112.spe: 2020-11-11 Company Name

2020 Nov 11 Al mono 24.3 W 100.0 µ 45.0° 112.00 eV 4.1092e+003 max 4.02 min

C1s/Point6: OGO/1 (Shft)

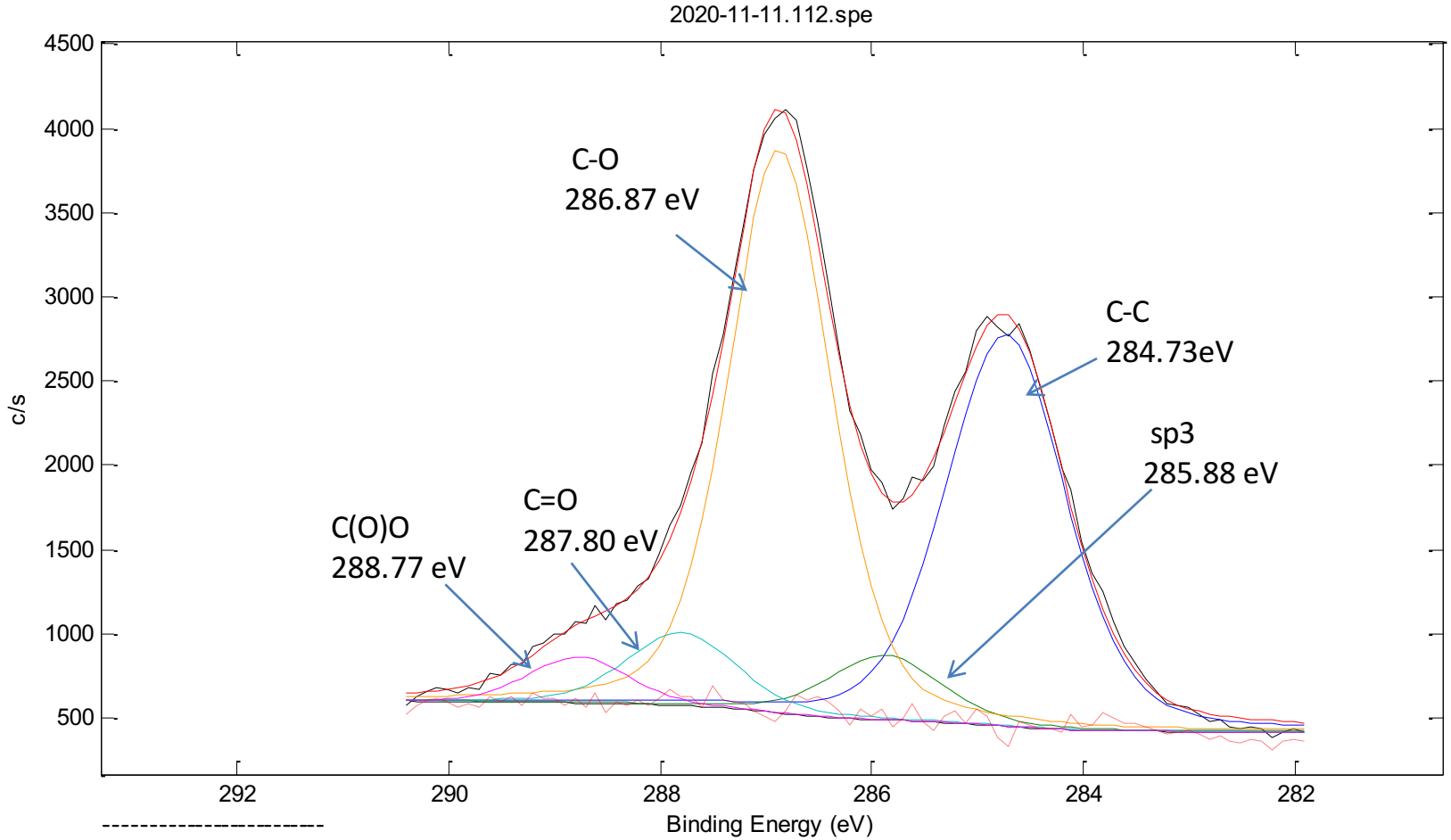

Atomic Concentration Table

C-C	sp3	C-O	C=O	C(O)O
37.83	5.85	46.42	6.40	3.51

2020-11-11.112.spe: 2020-11-11 Company Name

2020 Nov 11 Al mono 24.3 W 100.0 µ 45.0° 112.00 eV 8.9575e+003 max 4.02 min

O1s/Point6: OGO/1 (Shft)

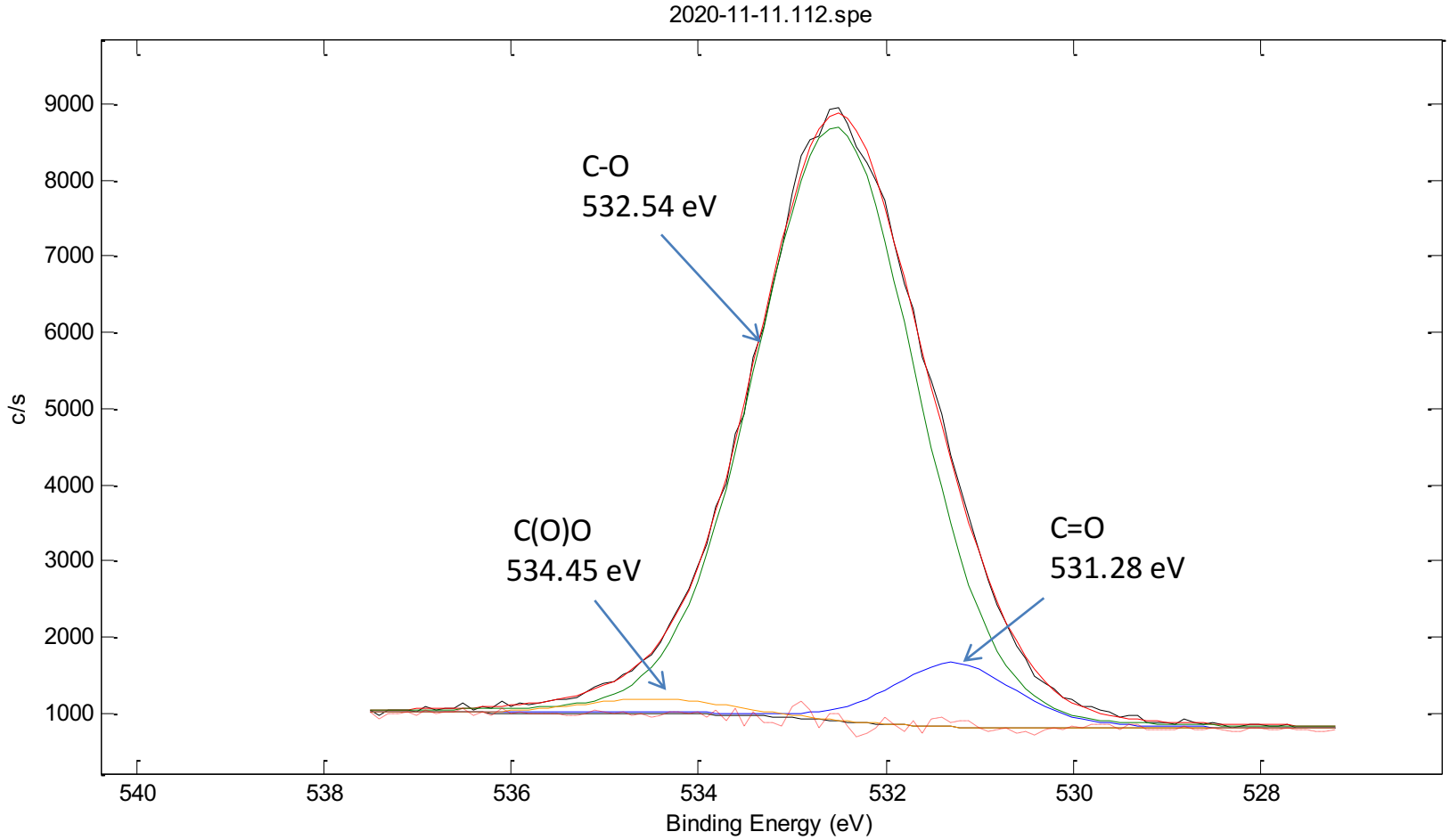

Atomic Concentration Table

C=O	C-O	C(O)O
8.30	89.67	2.04

2020-11-11.109.spe: 2020-11-11 Company Name

2020 Nov 11 Al mono 24.3 W 100.0 µ 45.0° 280.00 eV 3.7333e+004 max 8.01 min

Su1s/Point8: XGO/1

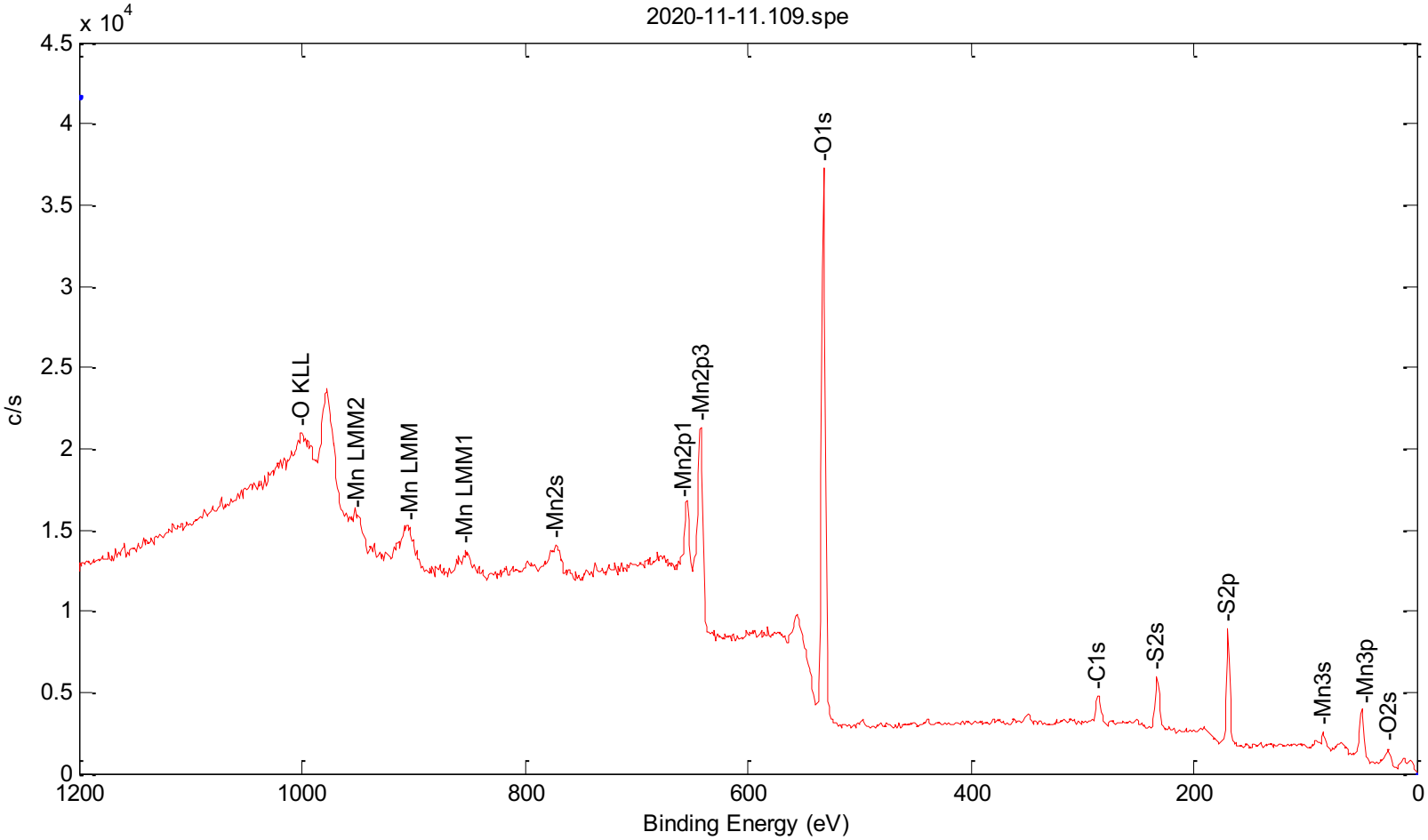

Atomic Concentration Table

C1s	O1s	S2p	Mn2p3
9.80	67.46	11.83	10.92

Weight % Table

C1s	O1s	S2p	Mn2p3
5.41	49.60	17.43	27.57

2020-11-11.113.spe: 2020-11-11 Company Name

2020 Nov 11 Al mono 24.3 W 100.0 µ 45.0° 112.00 eV 2.1500e+003 max 4.02 min

C1s/Point8: XGO/1 (Shft)

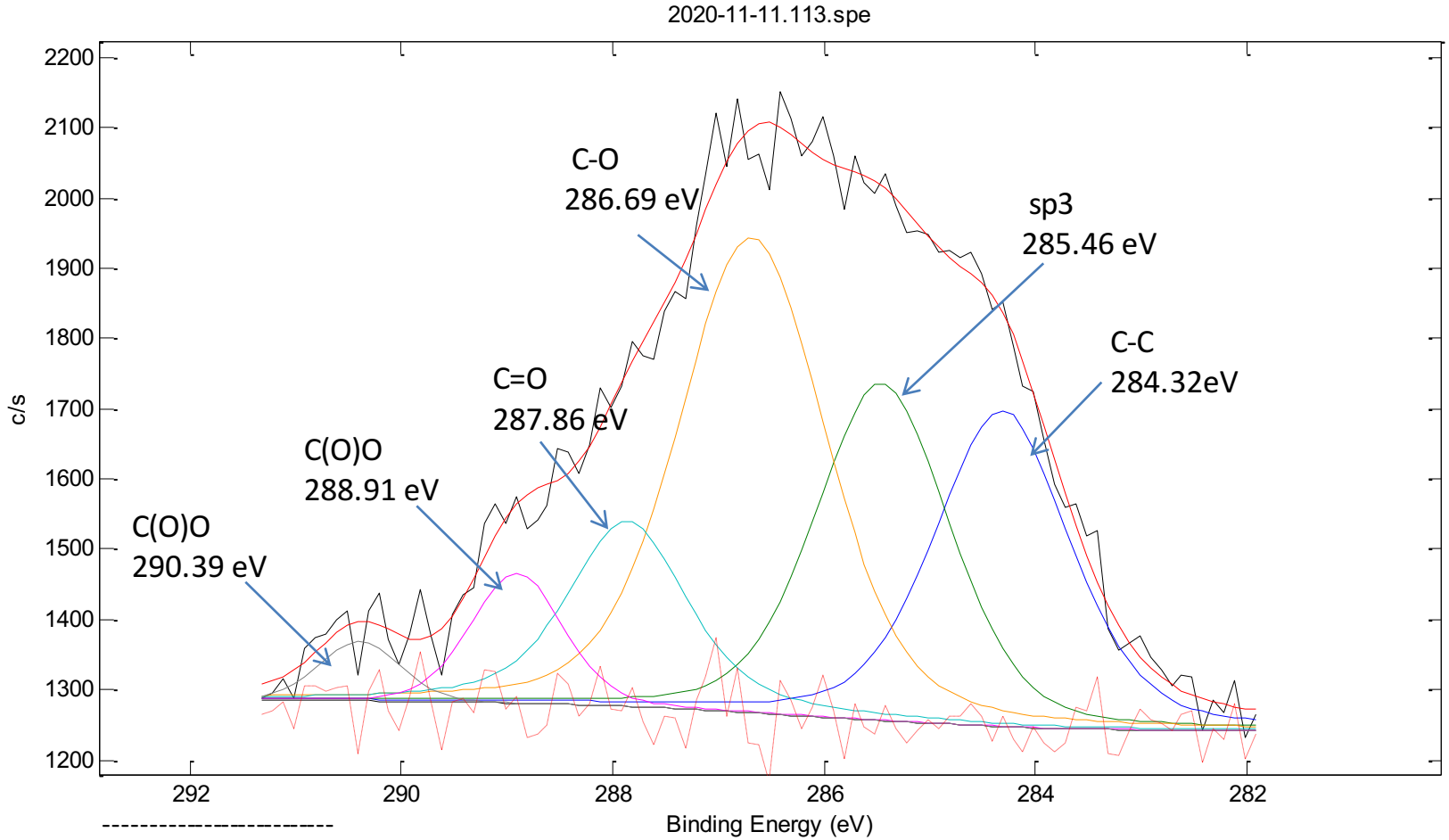

Atomic Concentration Table

C-C	sp3	C-O	C=O	C(O)O
22.64	23.22	35.89	12.43	5.82

2020-11-11.113.spe: 2020-11-11 Company Name

2020 Nov 11 Al mono 24.3 W 100.0 µ 45.0° 112.00 eV 1.6553e+004 max 4.02 min

O1s/Point8: XGO/1 (Shft)

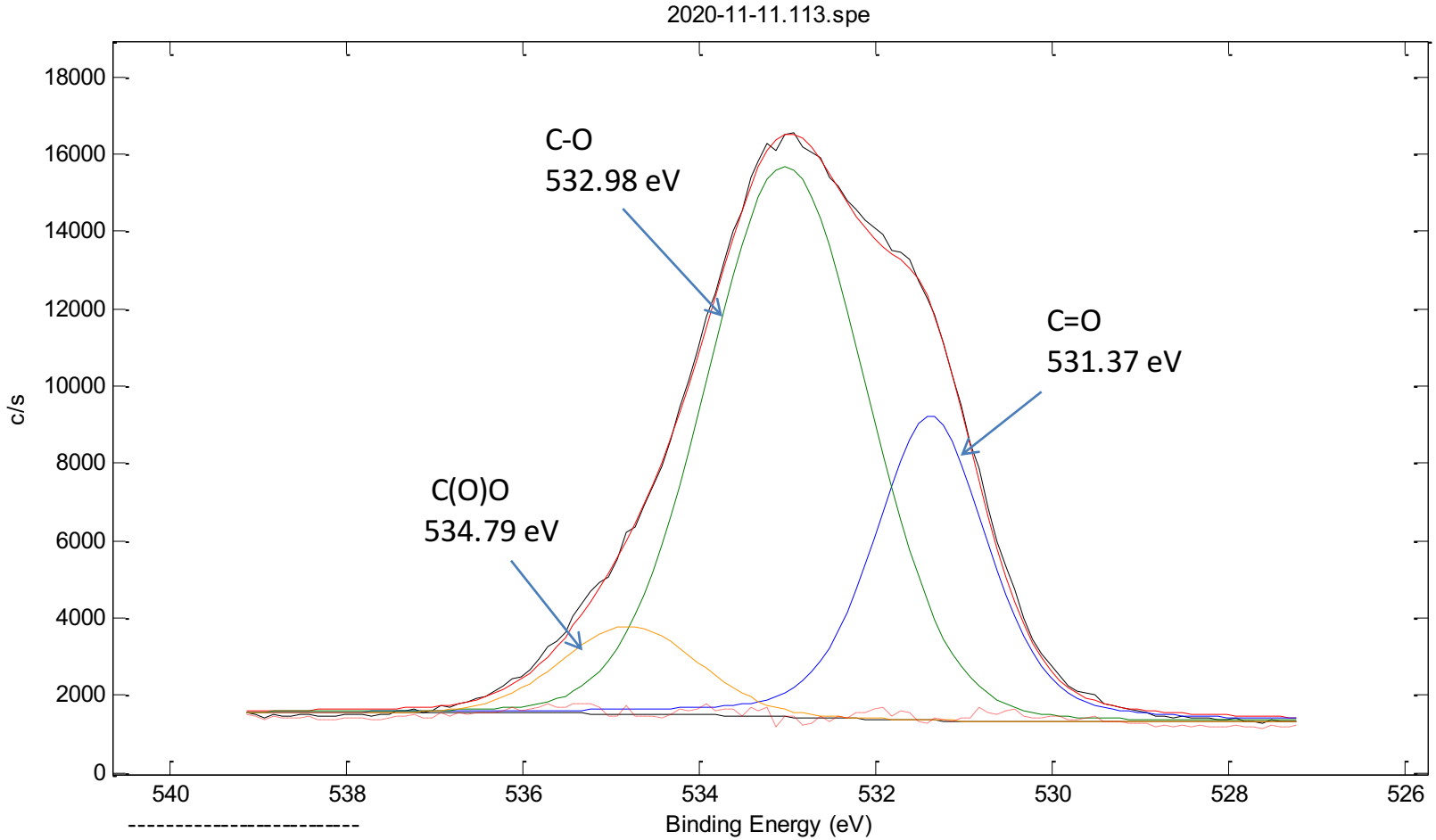

Atomic Concentration Table

C=O	C-O	C(O)O
27.66	63.76	8.59

Appendix 3: Compressive and flexural sample results

x axis = strain, y axis = stress (Mpa)

control

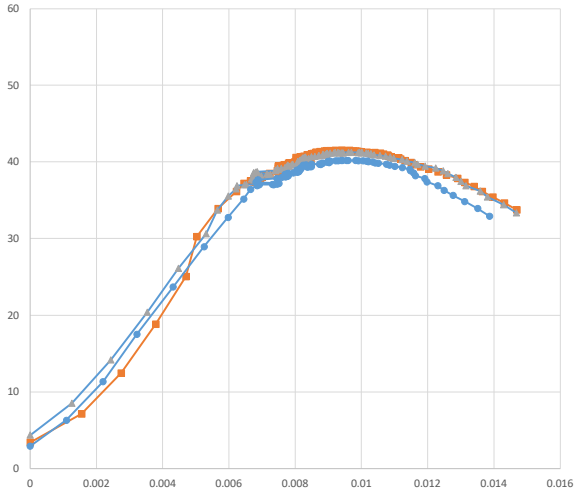

Ultimate stress for all samples

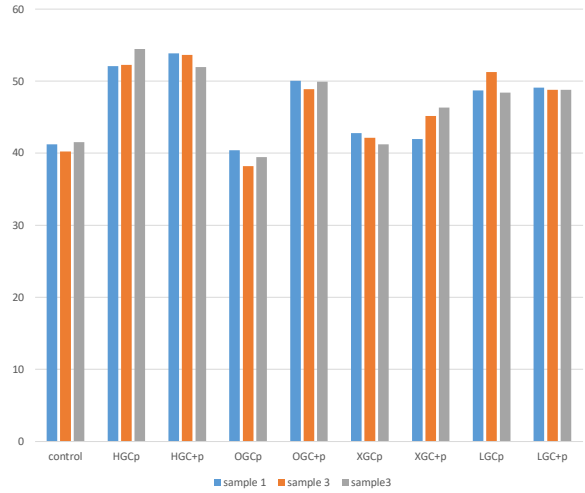

HGCp

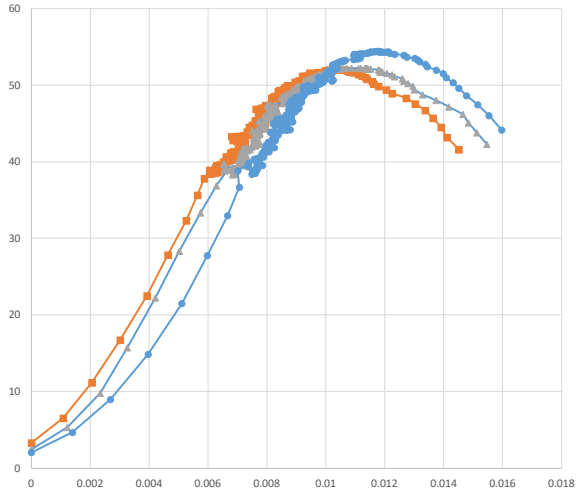

HGC+p

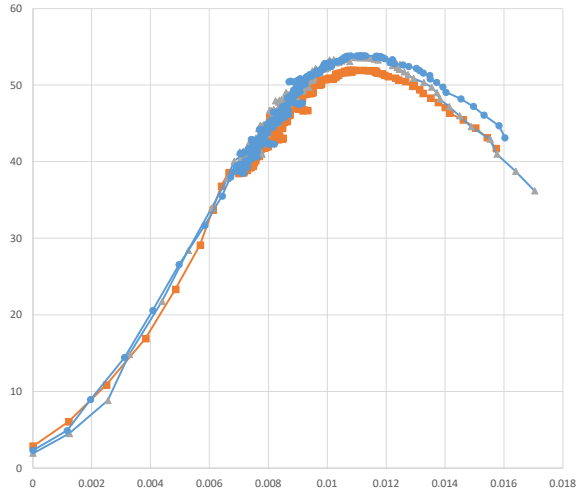

OGCp

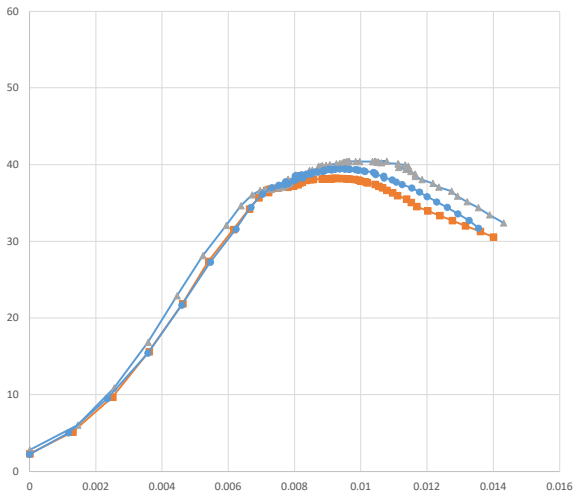

OGC+p

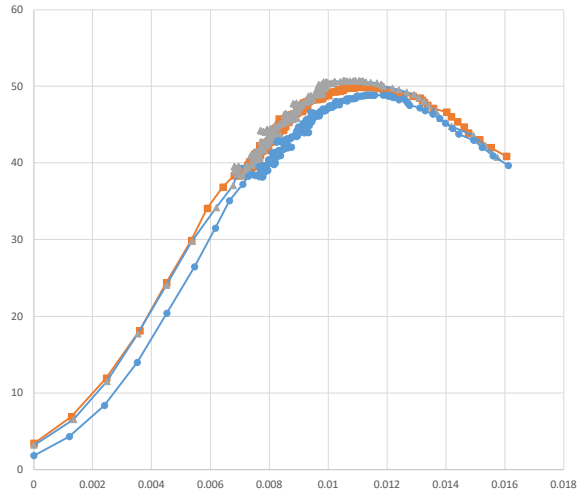

XGCp

XGC+p

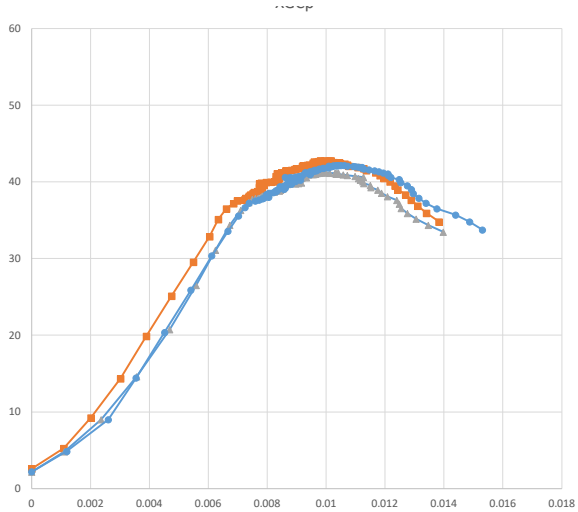
60
50
40
30
20
10
0
0
0.002
0.004
0.006
0.008
0.01
0.012
0.014
0.016
0.018

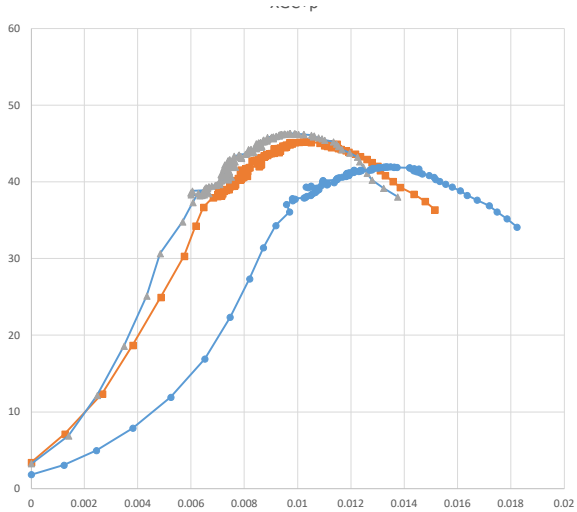
60
50
40
30
20
10
0
0
0.002
0.004
0.006
0.008
0.01
0.012
0.014
0.016
0.018
0.02

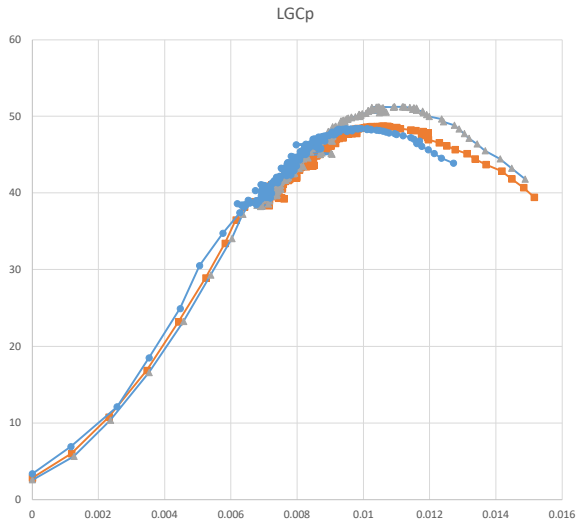
LGCp
60
50
40
30
20
10
0
0
0.002
0.004
0.006
0.008
0.01
0.012
0.014
0.016

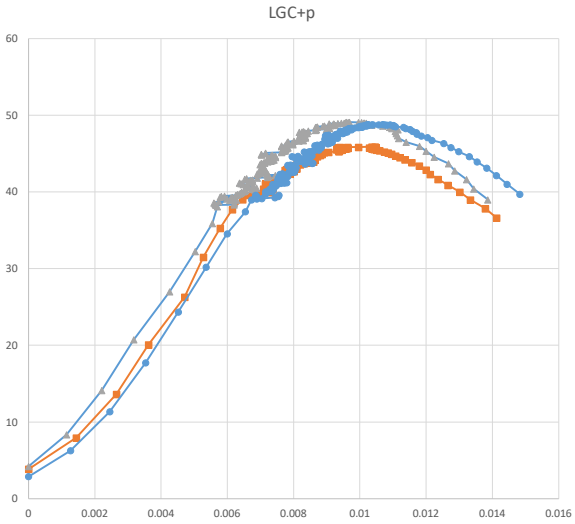
LGC+p
60
50
40
30
20
10
0
0
0.002
0.004
0.006
0.008
0.01
0.012
0.014
0.016

	sample	Peak Load (N)	Length (mm)	width (mm)	depth (mm)	σf (MPa)	%Δ σf
	1	48.15	225	23.52	14.5	3.29	
control	2	48.15	230	23.6	13.14	4.08	
	3	41.90	290	20	15	4.05	
	1	30.25	275	21.64	11.86	4.10	
HGC+p	2	49.86	210	21.2	12	5.15	36%
	3	170.38	100	20.4	14.1	6.30	
	1	28.63	345	20.5	14.2	3.58	
OGC+p	2	57.71	175	20.4	14.8	3.39	13%
	3	84.92	205	22.52	14.02	5.90	
	1	31.48	345	20.5	14.1	4.00	
XGC+p	2	38.10	275	20	13.5	4.31	35%
	3	114.30	155	21.1	13.32	7.10	
	1	46.92	165	20	11.6	4.32	
LGC+p	2	53.79	180	20	11.8	5.21	54%
	3	174.74	80	19.5	11.6	7.99	

$$\sigma_f = \frac{3FL}{2bd^2}$$

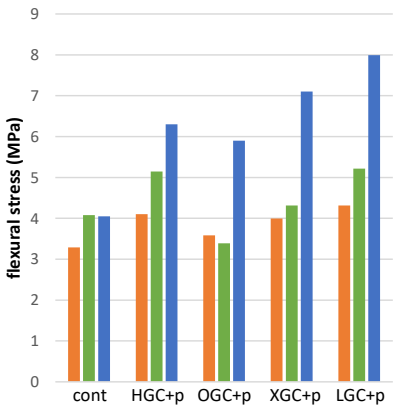

Appendix 4: XRD Rietveld Refinement Reports

Sample Information

C12 0				
File Name	C12.dia			
Instrument configuration	Aeris-fds-Pixcel1d-Medipix3.geq			
Wavelength	CU (1.5406 Å)			
Directory	C:/Users/Taimur/Documents/XRD/Raw Files			
Date of Refinement	Friday, January 08, 2021			
Operator	Taimur			
Statistics	R_{wp} = 48.42	R_{exp} = 45.72	χ^2 = 1.1216	GoF = 1.0591

Global GOALs

Parameter	Value	ESD
Qc3smumme	0.36	0.01
Qc3stbel	0.000000	0.000000
Qc4af	0.11	0.01
QPortlandite	0.005	0.003
QbetaC2S	0.045	0.008
QCSH	0.000000	0.000000
QCSH0625	0.000000	0.000000
QC3ACubic	0.018	0.004
QC3AOrt	0.000000	0.000000
Qcalcite	0.45	0.01
QSiC93R	0.014	0.007

Diffraction Pattern

C12 0

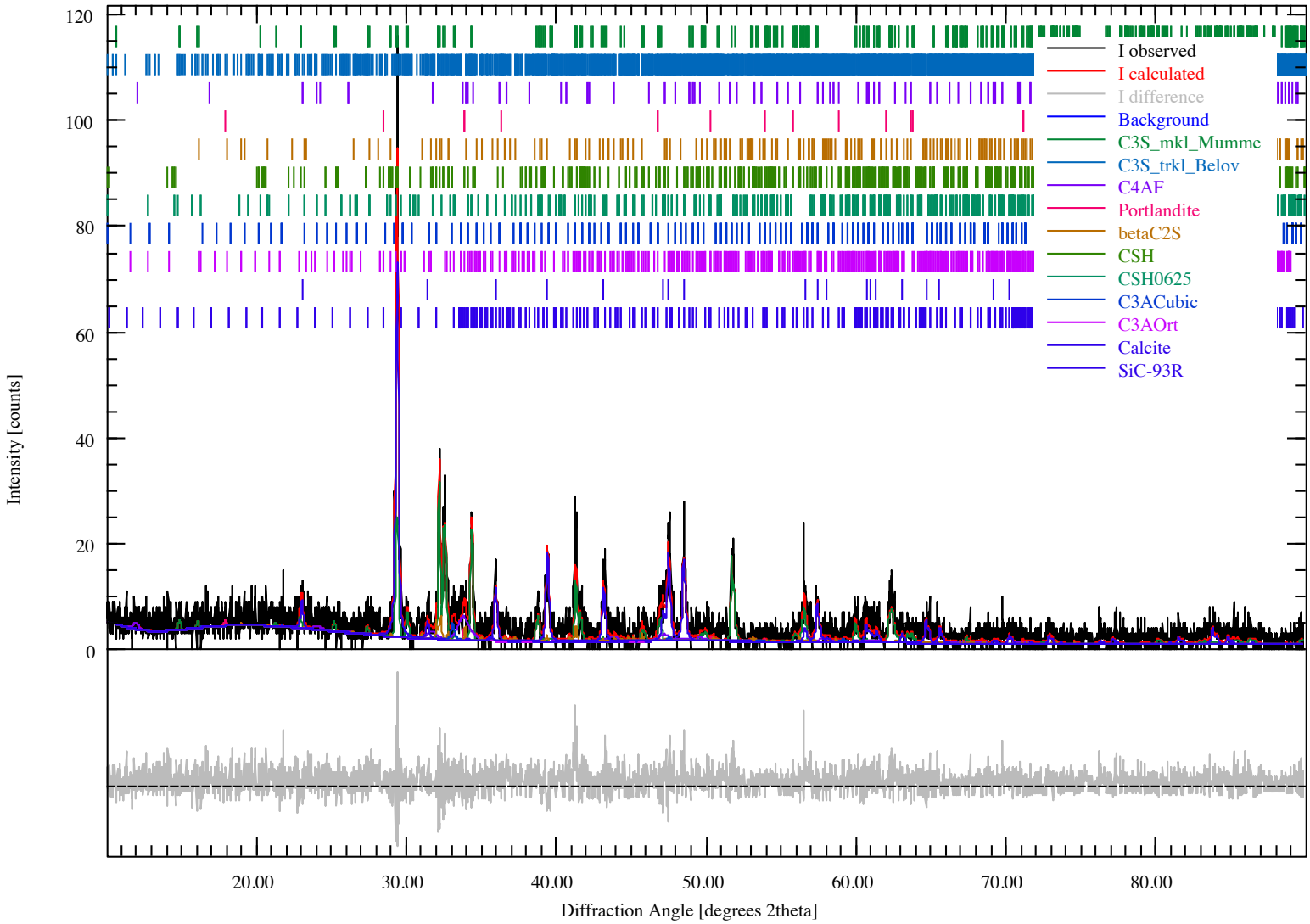
I observed
I calculated
I difference
Background
C3S_mkl_Mumme
C3S_trkl_Belov
C4AF
Portlandite
betaC2S
CSH
CSH0625
C3ACubic
C3AOrt
Calcite
SiC-93R
Intensity [counts]
Diffraction Angle [degrees 2theta]
0
20
40
60
80
100
120
20.00
30.00
40.00
50.00
60.00
70.00
80.00

Profex

Sample Information

C24 0				
File Name	C24.dia			
Instrument configuration	Aeris-fds-Pixcel1d-Medipix3.geq			
Wavelength	CU (1.5406 Å)			
Directory	C:/Users/Taimur/Documents/XRD/Raw Files			
Date of Refinement	Friday, January 08, 2021			
Operator	Taimur			
Statistics	R_{wp} = 49.32	R_{exp} = 46.63	χ^2 = 1.1187	GoF = 1.0577

Global GOALs

Parameter	Value	ESD
Qc3smumme	0.31	0.01
Qc3stbel	0.016	0.006
Qc4af	0.11	0.01
QPortlandite	0.020	0.004
QbetaC2S	0.057	0.009
QCSH	0.02	0.01
QCSH0625	0.006	0.004
QC3ACubic	0.004	0.003
QC3AOrt	0.022	0.006
Qcalcite	0.44	0.01

Diffraction Pattern

C24 0

C24.dia

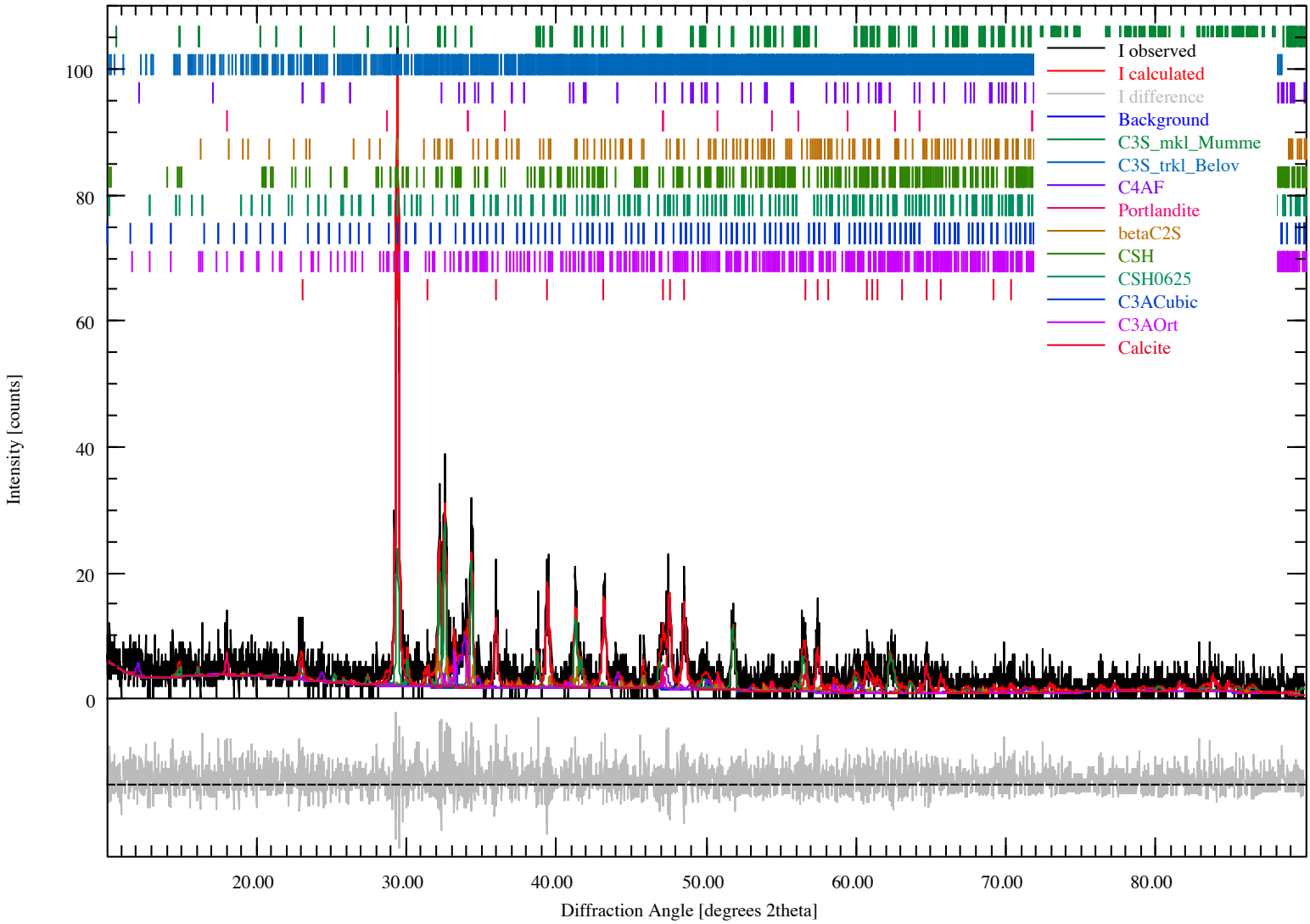
I observed
I calculated
I difference
Background
C3S_mkl_Mumme
C3S_trkl_Belov
C4AF
Portlandite
betaC2S
CSH
CSH0625
C3ACubic
C3AOrt
Calcite
Intensity [counts]
0
20
40
60
80
100
20.00
30.00
40.00
50.00
60.00
70.00
80.00
Diffraction Angle [degrees 2theta]

Sample Information

C28 0				
File Name	C28.dia			
Instrument configuration	Aeris-fds-Pixcel1d-Medipix3.geq			
Wavelength	CU (1.5406 Å)			
Directory	C:/Users/Taimur/Downloads/Raw Files			
Date of Refinement	Friday, January 08, 2021			
Operator	Taimur			
Statistics	R_{wp} = 41.85	R_{exp} = 39.93	χ^2 = 1.0985	GoF = 1.0481

Global GOALs

Parameter	Value	ESD
Qc3smumme	0.12	0.02
Qc3stbel	0.08	0.02
Qc4af	0.06	0.01
Qcalcite	0.48	0.03
Qportlandite	0.09	0.01
QbetaC2S	0.09	0.02
QCSH	0.06	0.03
QCSH0625	0.018	0.010
QC3ACubic	0.008	0.005
QC3AOrt	0.000000	0.000000

Diffraction Pattern

C28.dia

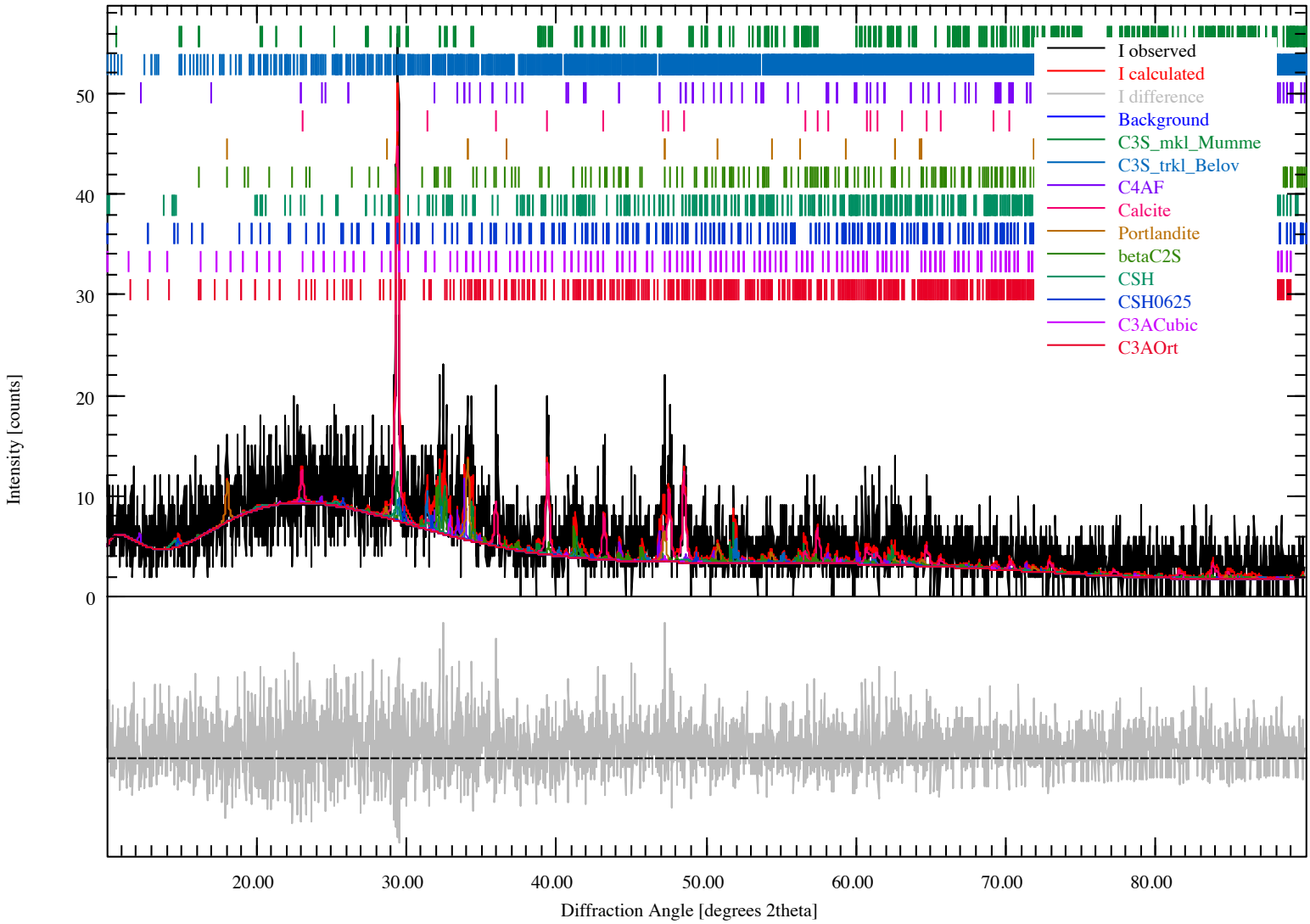
I observed
I calculated
I difference
Background
C3S_mkl_Mumme
C3S_trkl_Belov
C4AF
Calcite
Portlandite
betaC2S
CSH
CSH0625
C3ACubic
C3AOrt
Intensity [counts]
0
10
20
30
40
50
20.00
30.00
40.00
50.00
60.00
70.00
80.00
Diffraction Angle [degrees 2theta]

Sample Information

H12 0				
File Name	H12.dia			
Instrument configuration	Aeris-fds-Pixcel1d-Medipix3.geq			
Wavelength	CU (1.5406 Å)			
Directory	C:/Users/Taimur/Documents/XRD/Raw Files			
Date of Refinement	Friday, January 08, 2021			
Operator	Taimur			
Statistics	R_{wp} = 46.49	R_{exp} = 43.69	χ^2 = 1.1323	GoF = 1.0641

Global GOALs

Parameter	Value	ESD
Qc3smumme	0.32	0.01
Qc3stbel	0.000000	0.000000
Qc4af	0.06	0.01
QPortlandite	0.028	0.007
QbetaC2S	0.05	0.01
QCSH	0.016	0.006
QCSH0625	0.000000	0.000000
QC3ACubic	0.022	0.004
QC3AOrt	0.012	0.006
Qcalcite	0.49	0.01

Diffraction Pattern

H12 0

H12.dia

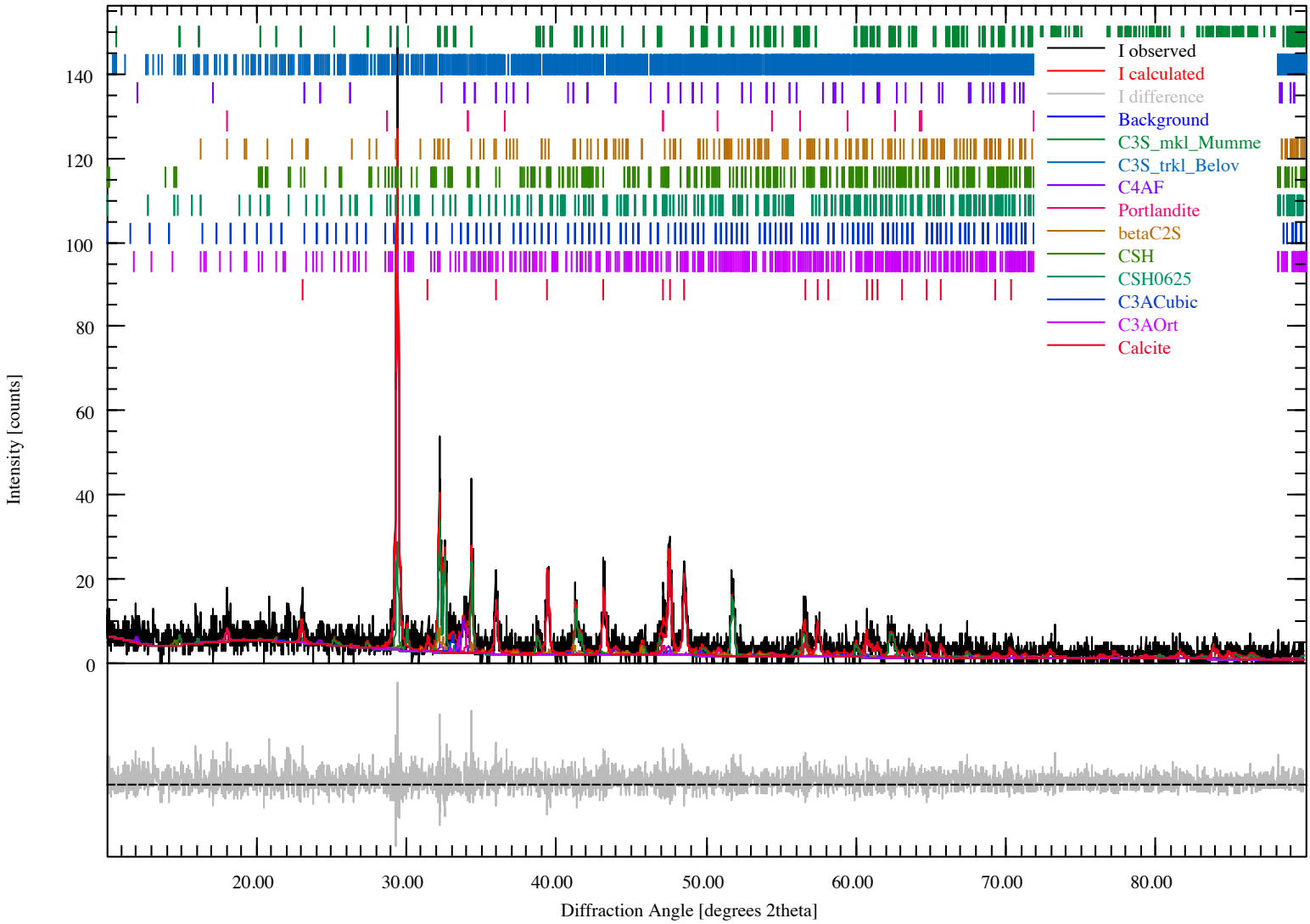
I observed
I calculated
I difference
Background
C3S_mkl_Mumme
C3S_trkl_Belov
C4AF
Portlandite
betaC2S
CSH
CSH0625
C3ACubic
C3AOrt
Calcite
Intensity [counts]
0
20
40
60
80
100
120
140
20.00
30.00
40.00
50.00
60.00
70.00
80.00
Diffraction Angle [degrees 2theta]

Sample Information

H24 0				
File Name	H24.dia			
Instrument configuration	Aeris-fds-Pixcel1d-Medipix3.geq			
Wavelength	CU (1.5406 Å)			
Directory	C:/Users/Taimur/Documents/XRD/Raw Files			
Date of Refinement	Friday, January 08, 2021			
Operator	Taimur			
Statistics	R_{wp} = 47.70	R_{exp} = 44.63	χ^2 = 1.1423	GoF = 1.0688

Global GOALs

Parameter	Value	ESD
Qc3smumme	0.15	0.01
Qc3stbel	0.048	0.009
Qc4af	0.039	0.007
QPortlandite	0.065	0.007
QbetaC2S	0.071	0.008
QCSH	0.010	0.006
QCSH0625	0.010	0.004
QC3ACubic	0.021	0.004
QC3AOrt	0.009	0.003
Qcalcite	0.57	0.01
QSiC93R	0.006	0.004

Diffraction Pattern

H24 0

H24.dia

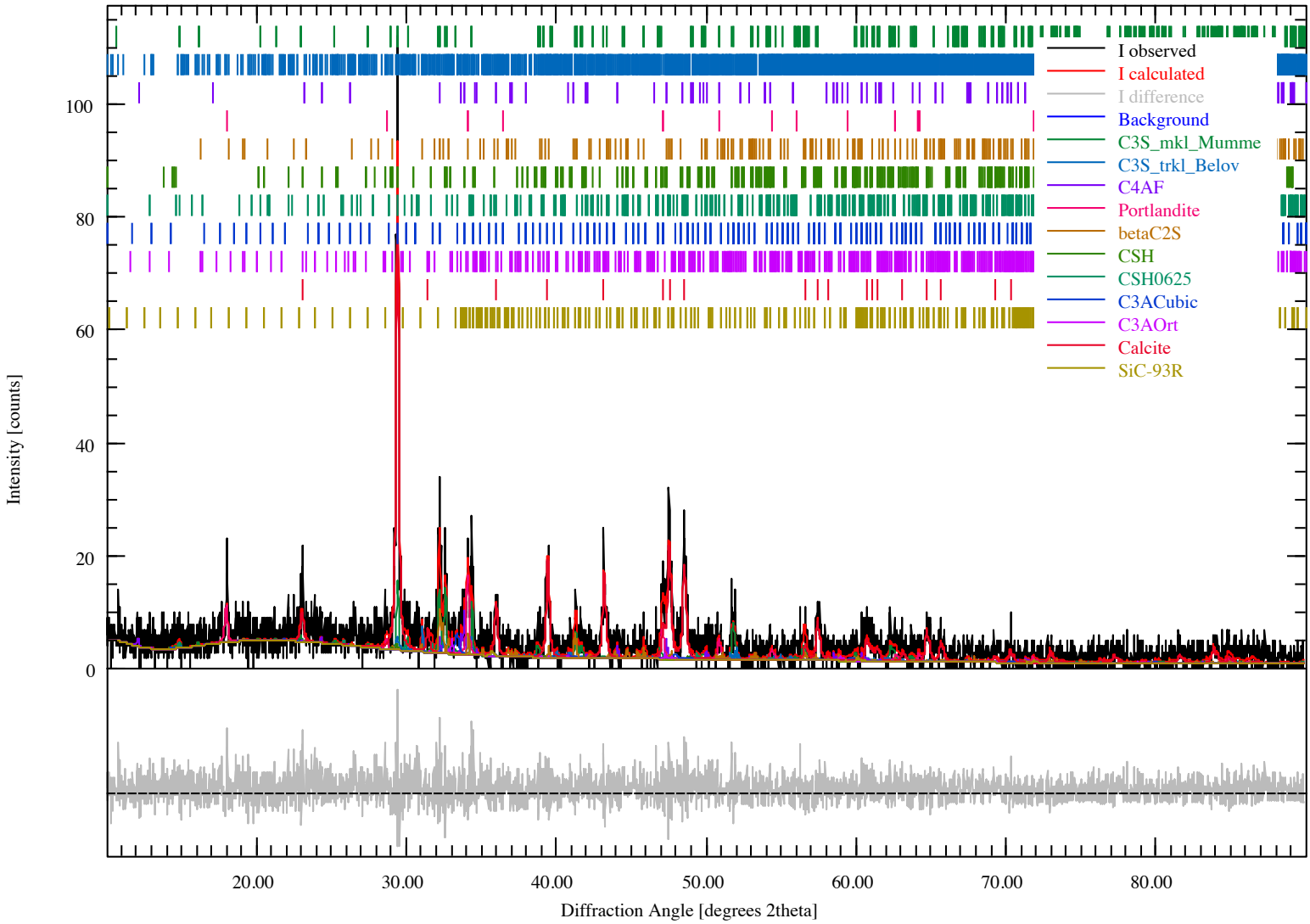
I observed
I calculated
I difference
Background
C3S_mkl_Mumme
C3S_trkl_Belov
C4AF
Portlandite
betaC2S
CSH
CSH0625
C3ACubic
C3AOrt
Calcite
SiC-93R
Intensity [counts]
0
20
40
60
80
100
20.00
30.00
40.00
50.00
60.00
70.00
80.00
Diffraction Angle [degrees 2theta]

Sample Information

H28 0				
File Name	H28.dia			
Instrument configuration	Aeris-fds-Pixcel1d-Medipix3.geq			
Wavelength	CU (1.5406 Å)			
Directory	C:/Users/Taimur/Downloads/Raw Files			
Date of Refinement	Friday, January 08, 2021			
Operator	Taimur			
Statistics	R_{wp} = 43.66	R_{exp} = 41.01	χ^2 = 1.1334	GoF = 1.0646

Global GOALs

Parameter	Value	ESD
Qc3smumme	0.11	0.01
Qc3stbel	0.07	0.01
Qc4af	0.036	0.008
Qcalcite	0.65	0.02
Qportlandite	0.051	0.008
QbetaC2S	0.06	0.01
QCSH	0.03	0.02
QCSH0625	0.000000	0.000000
QC3ACubic	0.006	0.004
QC3AOrt	0.01	0.01

Diffraction Pattern

H28 0

H28.dia

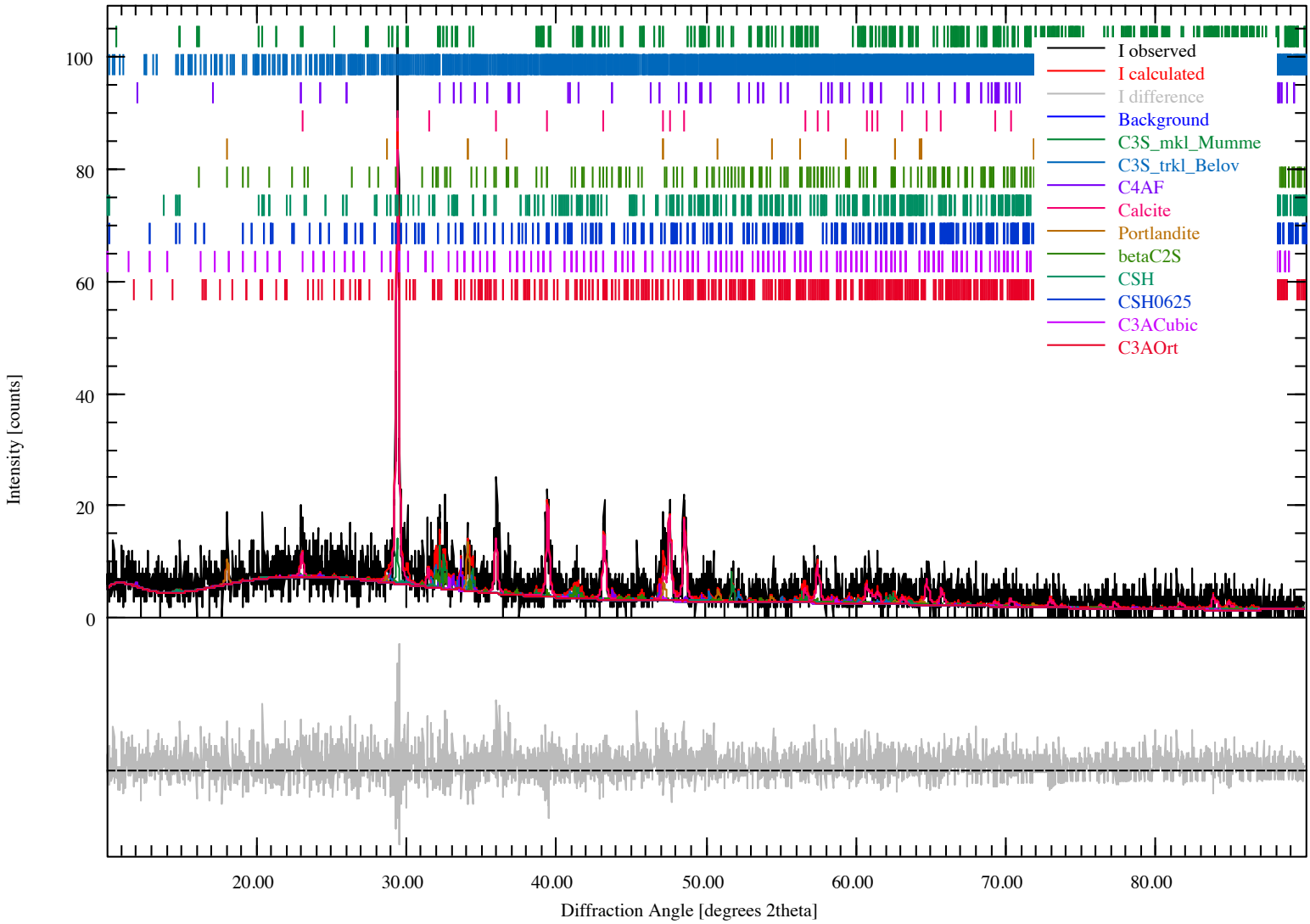
I observed
I calculated
I difference
Background
C3S_mkl_Mumme
C3S_trkl_Belov
C4AF
Calcite
Portlandite
betaC2S
CSH
CSH0625
C3ACubic
C3AOrt
Intensity [counts]
0
20
40
60
80
100
20.00
30.00
40.00
50.00
60.00
70.00
80.00
Diffraction Angle [degrees 2theta]

Sample Information

L12 0				
File Name	L12.dia			
Instrument configuration	Aeris-fds-Pixcel1d-Medipix3.geq			
Wavelength	CU (1.5406 Å)			
Directory	C:/Users/Taimur/Documents/XRD/Raw Files			
Date of Refinement	Friday, January 08, 2021			
Operator	Taimur			
Statistics	R_{wp} = 43.25	R_{exp} = 41.55	χ^2 = 1.0835	GoF = 1.0409

Global GOALs

Parameter	Value	ESD
Qc3smumme	0.26	0.02
Qc3stbel	0.000000	0.000000
Qc4af	0.09	0.01
QPortlandite	0.023	0.007
QbetaC2S	0.08	0.01
QCSH	0.028	0.010
QCSH0625	0.000000	0.000000
QC3ACubic	0.016	0.005
QC3AOrt	0.000000	0.000000
Qcalcite	0.50	0.01

Diffraction Pattern

L12 0

L12.dia

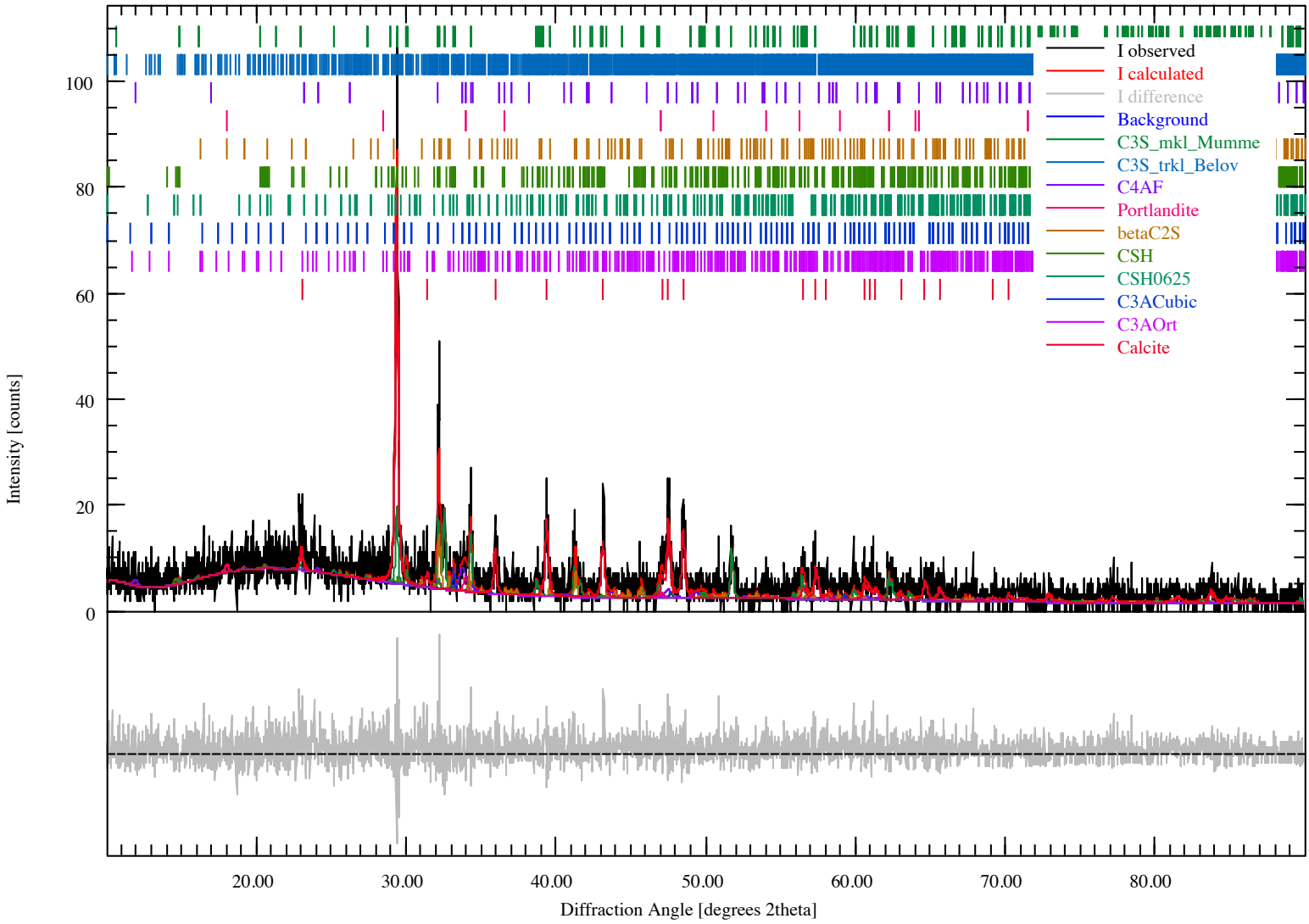
I observed
I calculated
I difference
Background
C3S_mkl_Mumme
C3S_trkl_Belov
C4AF
Portlandite
betaC2S
CSH
CSH0625
C3ACubic
C3AOrt
Calcite
Intensity [counts]
0
20
40
60
80
100
20.00
30.00
40.00
50.00
60.00
70.00
80.00
Diffraction Angle [degrees 2theta]

Sample Information

L24 0				
File Name	L24.dia			
Instrument configuration	Aeris-fds-Pixcel1d-Medipix3.geq			
Wavelength	CU (1.5406 Å)			
Directory	C:/Users/Taimur/Documents/XRD/Raw Files			
Date of Refinement	Friday, January 08, 2021			
Operator	Taimur			
Statistics	R_{wp} = 46.55	R_{exp} = 43.62	χ^2 = 1.1389	GoF = 1.0672

Global GOALs

Parameter	Value	ESD
Qc3smumme	0.19	0.01
Qc3stbel	0.027	0.007
Qc4af	0.059	0.009
QPortlandite	0.023	0.004
QbetaC2S	0.08	0.01
QCSH	0.000000	0.000000
QCSH0625	0.00	0.01
QC3ACubic	0.004	0.005
QC3AOrt	0.026	0.007
Qcalcite	0.59	0.01

Diffraction Pattern

L24.dia

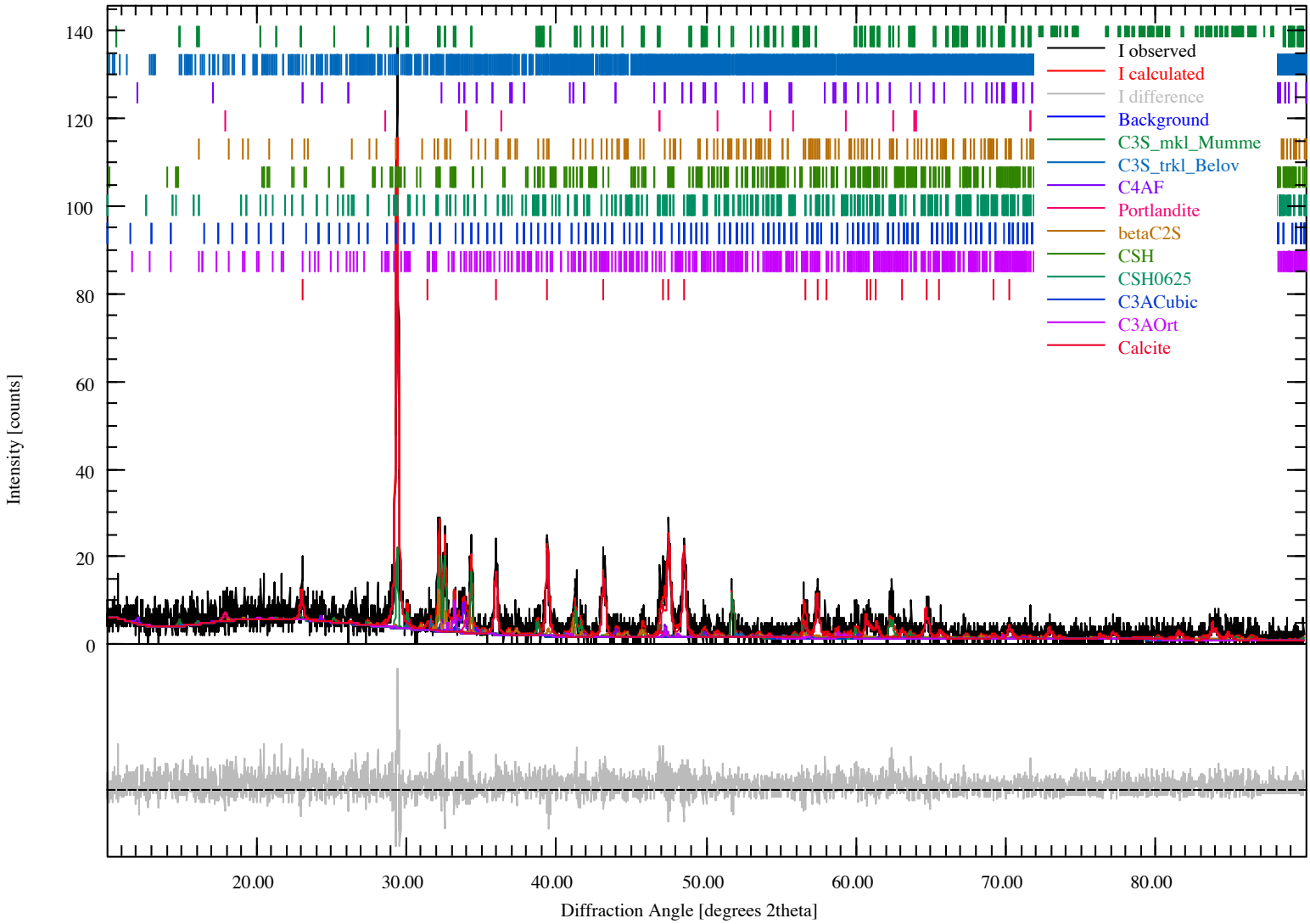
I observed
I calculated
I difference
Background
C3S_mkl_Mumme
C3S_trkl_Belov
C4AF
Portlandite
betaC2S
CSH
CSH0625
C3ACubic
C3AOrt
Calcite
Intensity [counts]
Diffraction Angle [degrees 2theta]
0
20
40
60
80
100
120
140
20.00
30.00
40.00
50.00
60.00
70.00
80.00

Sample Information

L28 0				
File Name	L28.dia			
Instrument configuration	Aeris-fds-Pixcel1d-Medipix3.geq			
Wavelength	CU (1.5406 Å)			
Directory	C:/Users/Taimur/Downloads/Raw Files			
Date of Refinement	Friday, January 08, 2021			
Operator	Taimur			
Statistics	R_{wp} = 45.53	R_{exp} = 43.09	χ^2 = 1.1165	GoF = 1.0566

Global GOALs

Parameter	Value	ESD
Qc3smumme	0.18	0.01
Qc3stbel	0.02	0.01
Qc4af	0.08	0.02
Qcalcite	0.56	0.02
Qportlandite	0.061	0.008
QbetaC2S	0.06	0.01
QCSH	0.01	0.02
QCSH0625	0.016	0.010
QC3ACubic	0.000000	0.000000
QC3AOrt	0.018	0.005

Diffraction Pattern

L28.dia

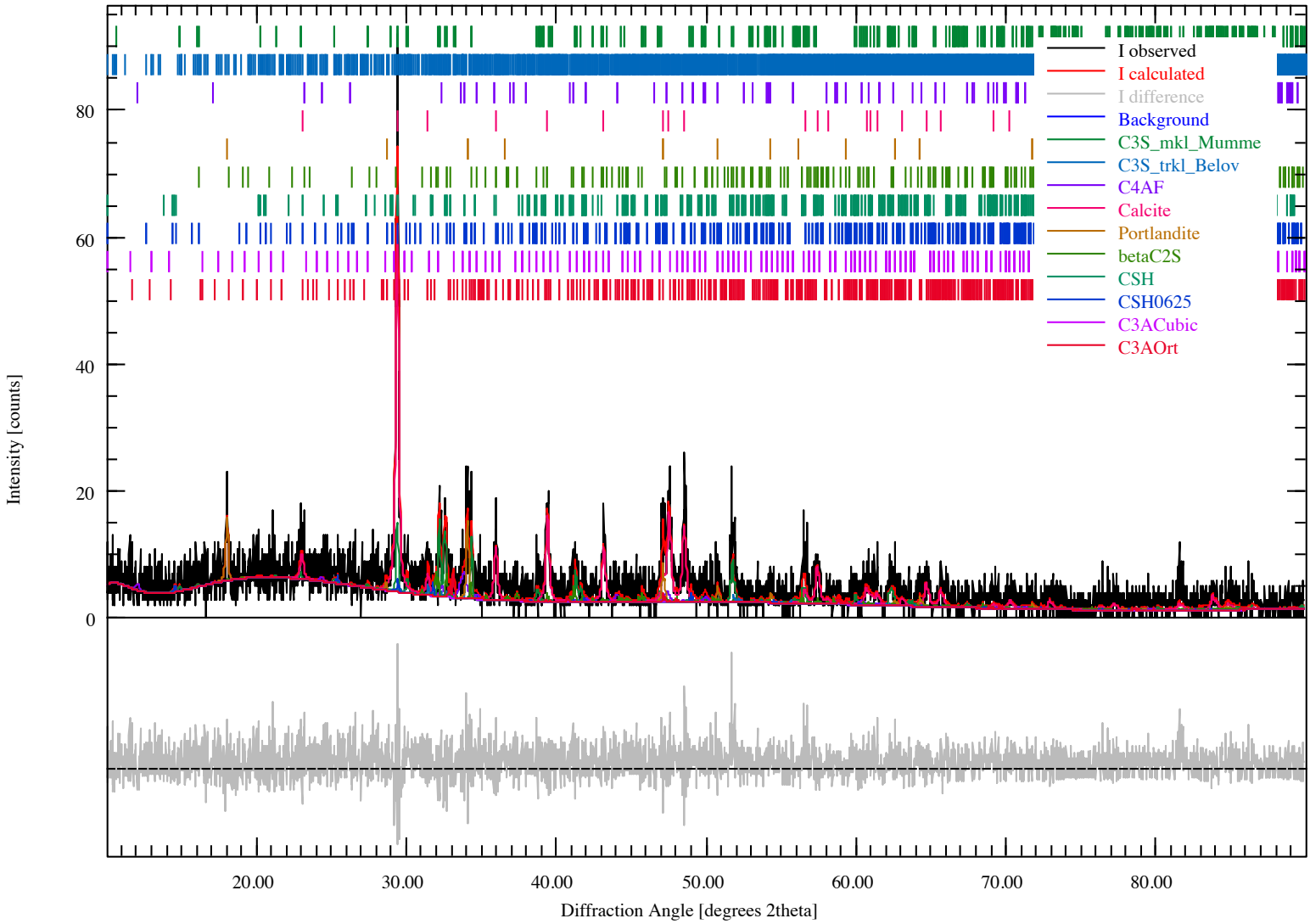
I observed
I calculated
I difference
Background
C3S_mkl_Mumme
C3S_trkl_Belov
C4AF
Calcite
Portlandite
betaC2S
CSH
CSH0625
C3ACubic
C3AOrt
Intensity [counts]
0
20
40
60
80
20.00
30.00
40.00
50.00
60.00
70.00
80.00
Diffraction Angle [degrees 2theta]

Profex

Sample Information

O12 0				
File Name	O12.dia			
Instrument configuration	Aeris-fds-Pixcel1d-Medipix3.geq			
Wavelength	CU (1.5406 Å)			
Directory	C:/Users/Taimur/Downloads/Raw Files			
Date of Refinement	Friday, January 08, 2021			
Operator	Taimur			
Statistics	R_{wp} = 47.69	R_{exp} = 44.51	χ^2 = 1.1480	GoF = 1.0714

Global GOALs

Parameter	Value	ESD
Qc3smumme	0.29	0.01
Qc3stbel	0.029	0.009
Qc4af	0.037	0.010
Qcalcite	0.53	0.01
Qportlandite	0.023	0.005
QbetaC2S	0.050	0.010
QCSH	0.000000	0.000000
QCSH0625	0.000000	0.000000
QC3ACubic	0.022	0.008
QC3AOrt	0.020	0.005

Diffraction Pattern

O12 0

O12.dia

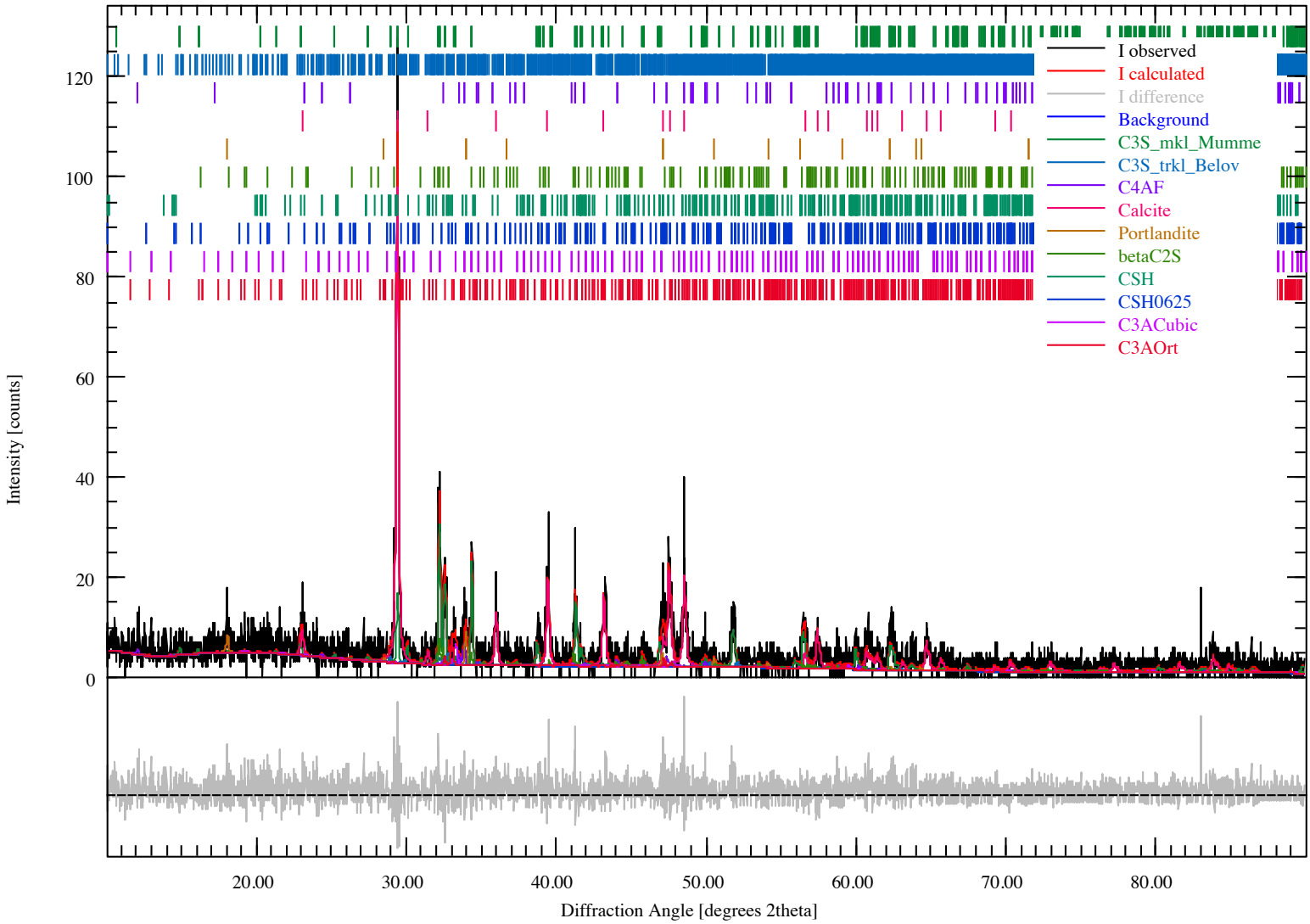
I observed
I calculated
I difference
Background
C3S_mkl_Mumme
C3S_trkl_Belov
C4AF
Calcite
Portlandite
betaC2S
CSH
CSH0625
C3ACubic
C3AOrt
Intensity [counts]
0
20
40
60
80
100
120
20.00
30.00
40.00
50.00
60.00
70.00
80.00
Diffraction Angle [degrees 2theta]

Profex

Sample Information

O24 0				
File Name	O24.dia			
Instrument configuration	Aeris-fds-Pixcel1d-Medipix3.geq			
Wavelength	CU (1.5406 Å)			
Directory	C:/Users/Taimur/Downloads/Raw Files			
Date of Refinement	Friday, January 08, 2021			
Operator	Taimur			
Statistics	R_{wp} = 45.88	R_{exp} = 44.35	χ^2 = 1.0702	GoF = 1.0345

Global GOALs

Parameter	Value	ESD
Qc3smumme	0.19	0.01
Qc3stbel	0.000000	0.000000
Qc4af	0.07	0.01
Qcalcite	0.66	0.01
Qportlandite	0.016	0.003
QbetaC2S	0.026	0.007
QCSH	0.017	0.008
QCSH0625	0.000000	0.000000
QC3ACubic	0.006	0.004
QC3AOrt	0.023	0.006

Diffraction Pattern

O24.dia

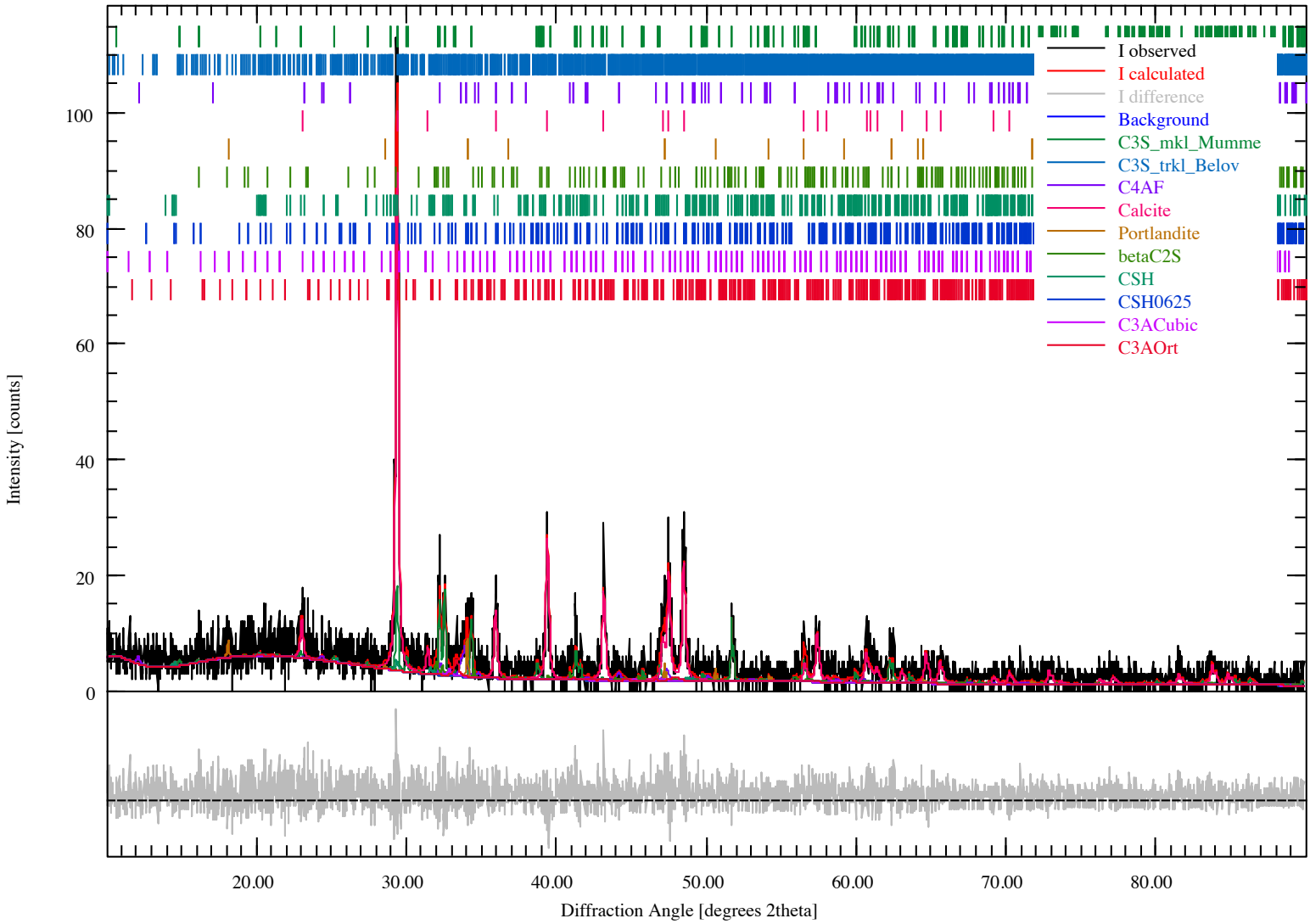
I observed
I calculated
I difference
Background
C3S_mkl_Mumme
C3S_trkl_Belov
C4AF
Calcite
Portlandite
betaC2S
CSH
CSH0625
C3ACubic
C3AOrt
Intensity [counts]
0
20
40
60
80
100
20.00
30.00
40.00
50.00
60.00
70.00
80.00
Diffraction Angle [degrees 2theta]

Profex

Sample Information

O28 0				
File Name	O28.dia			
Instrument configuration	Aeris-fds-Pixcel1d-Medipix3.geq			
Wavelength	CU (1.5406 Å)			
Directory	C:/Users/Taimur/Downloads/Raw Files			
Date of Refinement	Friday, January 08, 2021			
Operator	Taimur			
Statistics	R_{wp} = 43.95	R_{exp} = 42.06	χ^2 = 1.0919	GoF = 1.0449

Global GOALs

Parameter	Value	ESD
Qc3smumme	0.07	0.01
Qc3stbel	0.05	0.03
Qc4af	0.05	0.02
Qcalcite	0.62	0.03
Qportlandite	0.11	0.01
QbetaC2S	0.08	0.01
QCSH	0.000000	0.000000
QCSH0625	0.000000	0.000000
QC3ACubic	0.000000	0.000000
QC3AOrt	0.012	0.007

Diffraction Pattern

O28 0

O28.dia

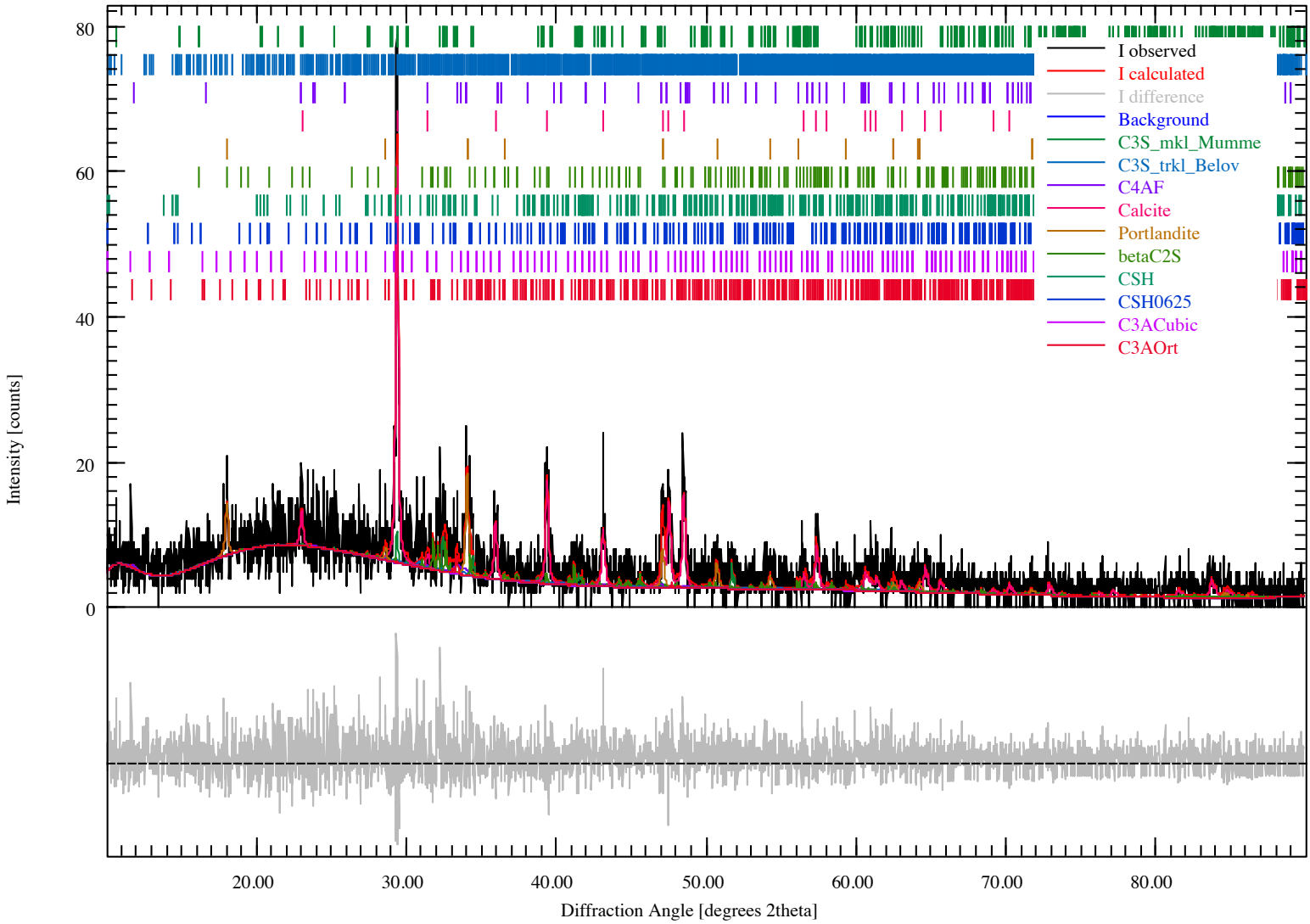
I observed
I calculated
I difference
Background
C3S_mkl_Mumme
C3S_trkl_Belov
C4AF
Calcite
Portlandite
betaC2S
CSH
CSH0625
C3ACubic
C3AOrt
Intensity [counts]
0
20
40
60
80
20.00
30.00
40.00
50.00
60.00
70.00
80.00
Diffraction Angle [degrees 2theta]

Sample Information

X12 0				
File Name	X12.dia			
Instrument configuration	Aeris-fds-Pixcel1d-Medipix3.geq			
Wavelength	CU (1.5406 Å)			
Directory	C:/Users/Taimur/Documents/XRD/Raw Files			
Date of Refinement	Friday, January 08, 2021			
Operator	Taimur			
Statistics	R_{wp} = 43.08	R_{exp} = 41.98	χ^2 = 1.0531	GoF = 1.0262

Global GOALs

Parameter	Value	ESD
Qc3smumme	0.36	0.01
Qc3stbel	0.020	0.008
Qc4af	0.043	0.005
QPortlandite	0.015	0.003
QbetaC2S	0.040	0.010
QCSH	0.021	0.009
QCSH0625	0.000000	0.000000
QC3ACubic	0.034	0.005
QC3AOrt	0.009	0.005
Qcalcite	0.46	0.01

Diffraction Pattern

X12 0

X12.dia

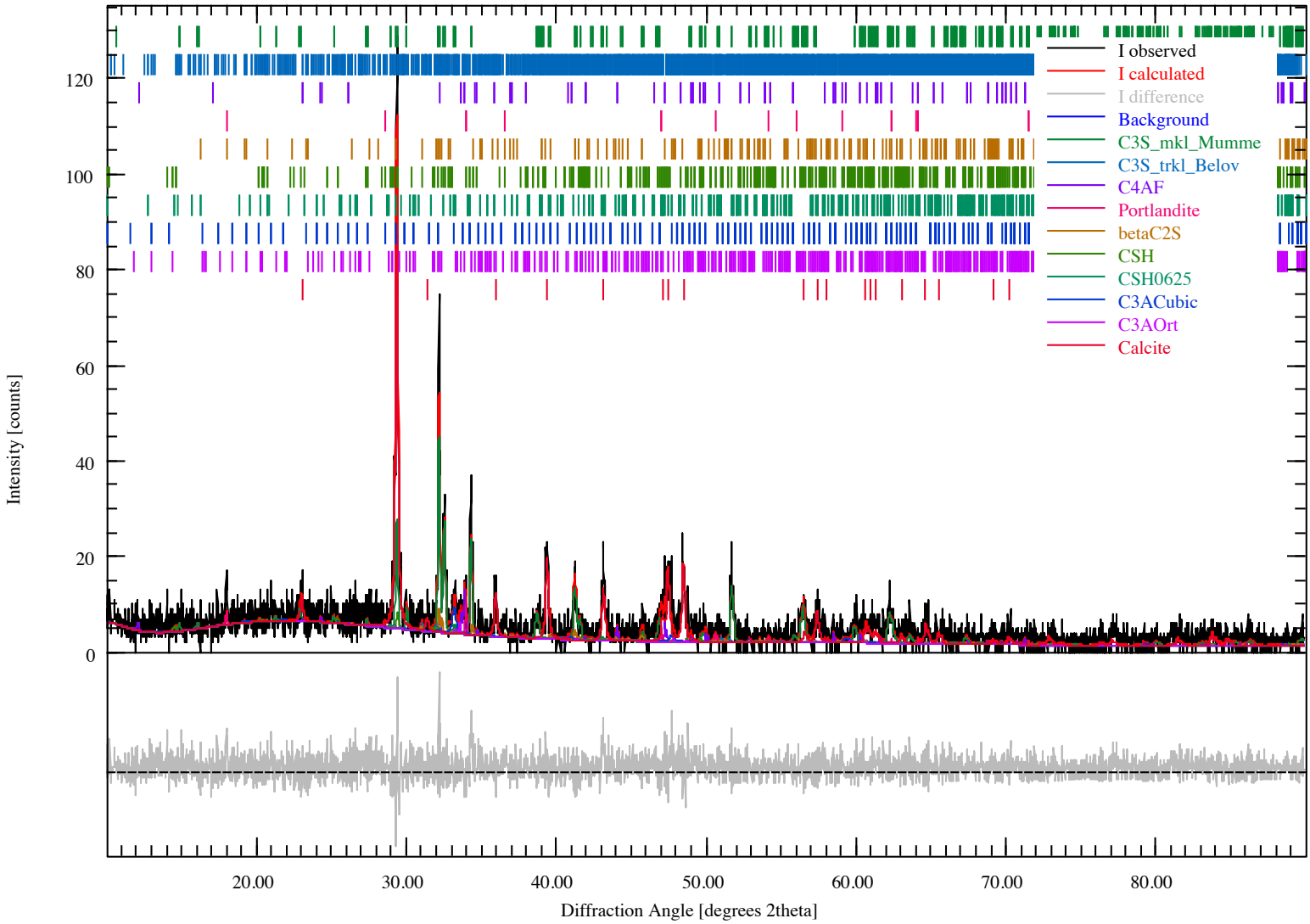
I observed
I calculated
I difference
Background
C3S_mkl_Mumme
C3S_trkl_Belov
C4AF
Portlandite
betaC2S
CSH
CSH0625
C3ACubic
C3AOrt
Calcite
Intensity [counts]
0
20
40
60
80
100
120
20.00
30.00
40.00
50.00
60.00
70.00
80.00
Diffraction Angle [degrees 2theta]

Sample Information

X24 0				
File Name	X24.dia			
Instrument configuration	Aeris-fds-Pixcel1d-Medipix3.geq			
Wavelength	CU (1.5406 Å)			
Directory	C:/Users/Taimur/Documents/XRD/Raw Files			
Date of Refinement	Friday, January 08, 2021			
Operator	Taimur			
Statistics	R_{wp} = 47.78	R_{exp} = 45.31	χ^2 = 1.1120	GoF = 1.0545

Global GOALs

Parameter	Value	ESD
Qc3smumme	0.13	0.01
Qc3stbel	0.09	0.02
Qc4af	0.06	0.01
QPortlandite	0.030	0.004
QbetaC2S	0.063	0.009
QCSH	0.04	0.01
QCSH0625	0.000000	0.000000
QC3ACubic	0.000000	0.000000
QC3AOrt	0.000000	0.000000
Qcalcite	0.59	0.02
QSiC93R	0.000000	0.000000

Diffraction Pattern

X24.dia

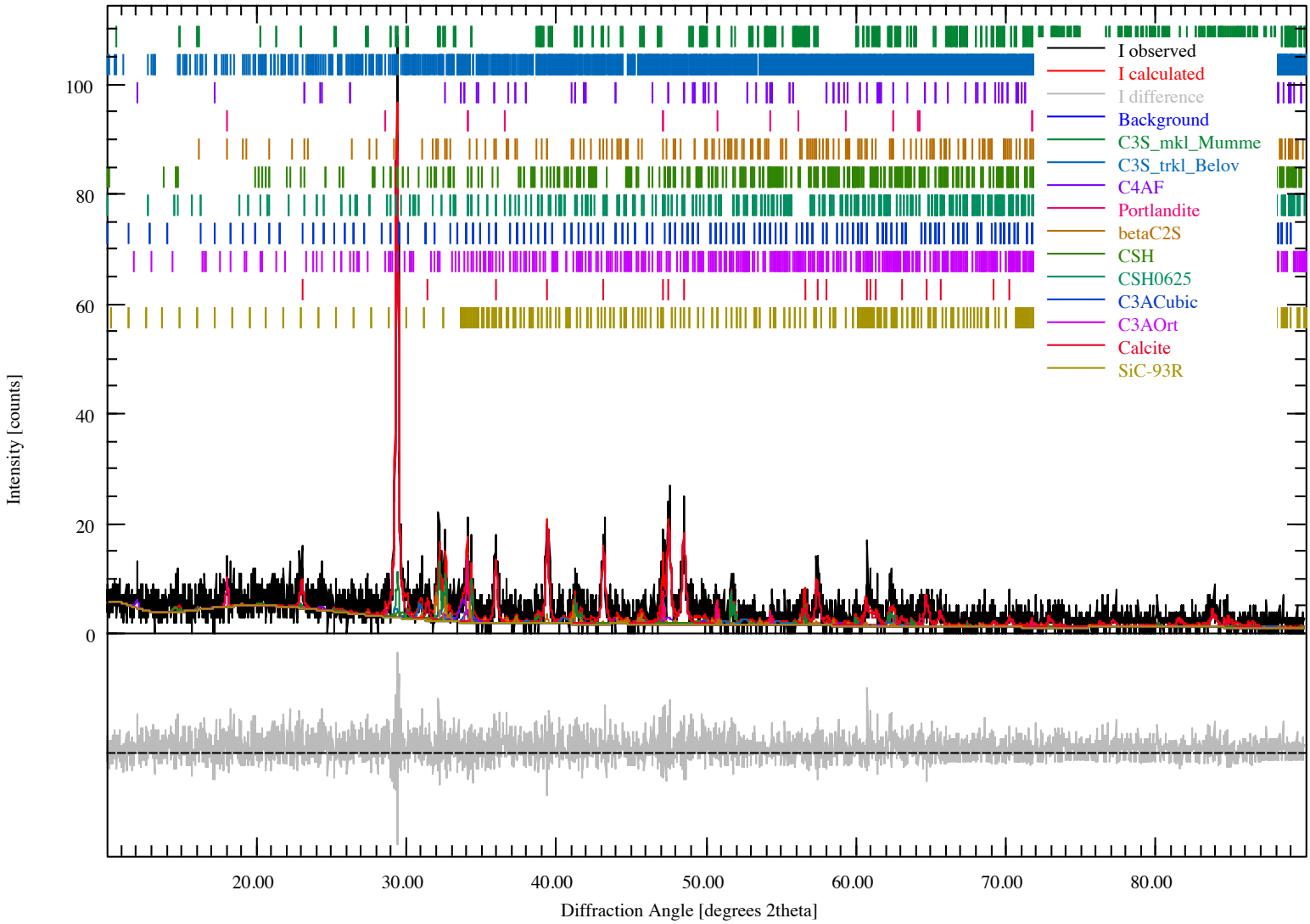
I observed
I calculated
I difference
Background
C3S_mkl_Mumme
C3S_trkl_Belov
C4AF
Portlandite
betaC2S
CSH
CSH0625
C3ACubic
C3AOrt
Calcite
SiC-93R
Intensity [counts]
0
20
40
60
80
100
20.00
30.00
40.00
50.00
60.00
70.00
80.00
Diffraction Angle [degrees 2theta]

Sample Information

X28 0				
File Name	X28.dia			
Instrument configuration	Aeris-fds-Pixcel1d-Medipix3.geq			
Wavelength	CU (1.5406 Å)			
Directory	C:/Users/Taimur/Downloads/Raw Files			
Date of Refinement	Friday, January 08, 2021			
Operator	Taimur			
Statistics	R_{wp} = 42.96	R_{exp} = 40.52	χ^2 = 1.1241	GoF = 1.0602

Global GOALs

Parameter	Value	ESD
Qc3smumme	0.000000	0.000000
Qc3stbel	0.07	0.01
Qc4af	0.07	0.02
Qcalcite	0.68	0.02
Qportlandite	0.054	0.009
QbetaC2S	0.08	0.01
QCSH	0.03	0.01
QCSH0625	0.021	0.009
QC3ACubic	0.000000	0.000000
QC3AOrt	0.000000	0.000000

Diffraction Pattern

X28.dia

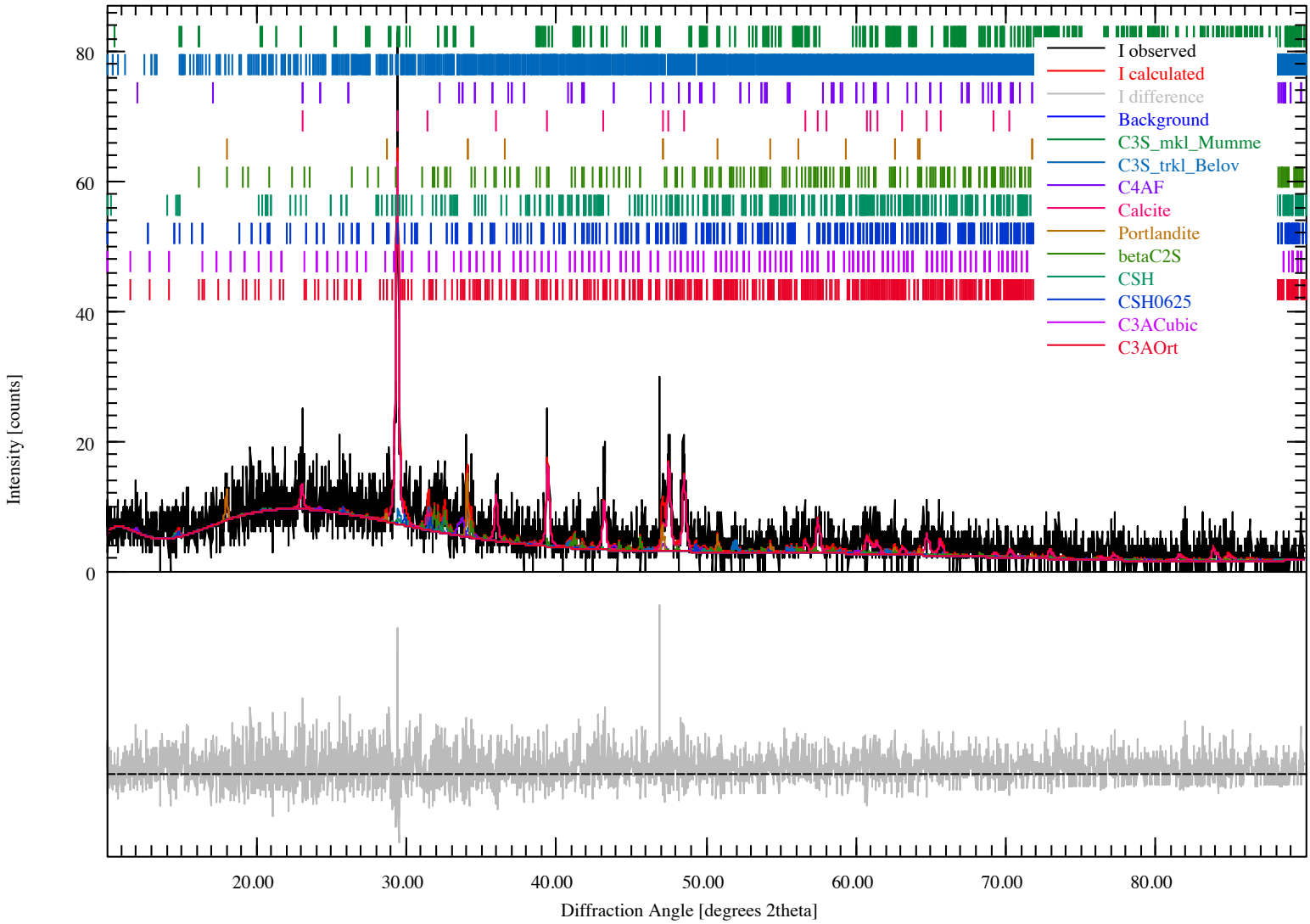
I observed
I calculated
I difference
Background
C3S_mkl_Mumme
C3S_trkl_Belov
C4AF
Calcite
Portlandite
betaC2S
CSH
CSH0625
C3ACubic
C3AOrt
Intensity [counts]
0
20
40
60
80
20.00
30.00
40.00
50.00
60.00
70.00
80.00
Diffraction Angle [degrees 2theta]